UNIVERSITÄT BONN
Physikalisches Institut

Development of a Benchmark Parameter Scan for Higgs Bosons in the NMSSM Model and a Study of the Sensitivity for $H \rightarrow AA \rightarrow 4\tau$ in Vector Boson Fusion with the ATLAS Detector

von
Iris Rottländer

Abstract: An evaluation of the discovery potential for NMSSM Higgs bosons of the ATLAS experiment at the LHC is presented. For this purpose, seven two-dimensional benchmark planes in the six-dimensional parameter space of the NMSSM Higgs sector are defined. These planes include different types of phenomenology for which the discovery of NMSSM Higgs bosons is especially challenging and which are considered typical for the NMSSM. They are subsequently used to give a detailed evaluation of the Higgs boson discovery potential based on Monte Carlo studies from the ATLAS collaboration. Afterwards, the possibility of discovering NMSSM Higgs bosons via the $H_1 \rightarrow A_1 A_1 \rightarrow 4\tau \rightarrow 4\mu + 8\nu$ decay chain and with the vector boson fusion production mode is investigated. A particular emphasis is put on the mass reconstruction from the complex final state. Furthermore, a study of the jet reconstruction performance at the ATLAS experiment which is of crucial relevance for vector boson fusion searches is presented. A good detectability of the so-called tagging jets that originate from the scattered partons in the vector boson fusion process is of critical importance for an early Higgs boson discovery in many models and also within the framework of the NMSSM.

Post address:
Nussallee 12
D-53115 Bonn
Germany

BONN-IR-2008-12
Bonn University
August 2008
ISSN-0172-8741

Angefertigt mit Genehmigung der Mathematisch-Naturwissenschaftlichen Fakultät
der Rheinischen Friedrich-Wilhelms-Universität Bonn

1. Gutachter: Prof. Dr. N. Wermes

2. Gutachter: Prof. Dr. M. Schumacher

Tag der Promotion: 31. 7. 2008

Erscheinungsjahr: 2008

Contents

1. Introduction

The wish to understand the world and the phenomena within it is deeply rooted in human culture. In this context, religion, philosophy and the natural sciences developed to address fundamental questions about the origin of the world and its inherent structure. High-energy particle physics is fundamental research dedicated to the exploration of the smallest, elementary constituents of matter and of the fundamental forces that our world is built from.

In the last 40 years, the so-called Standard Model of particle physics [1] was astoundingly successful in the prediction of fundamental particles and their interactions. The preliminary endpoint of a series of discoveries of formerly unknown fundamental particles was marked by the first observation of the top-quark at the CDF and D0 experiments at the Tevatron accelerator near Chicago in the year 1995 [2]. In precision measurements, eg. at the LEP accelerator near Geneva in Switzerland, the predictions of the Standard Model were confirmed partly to the level of quantum fluctuations [3]. However, not all questions of particle physics are answered yet.

For the imminent future, the Large Hadron Collider (LHC) [4] near Geneva and its experiments constitute one of the largest coordinated efforts ever to study the fundamental structure of nature. Currently, 7000 scientists from about 80 countries across the world prepare its start that is foreseen for the current year 2008. It is expected that at the energies reached in the proton-proton collisions at the LHC, unknown physical phenomena have to occur and will be observable.

One of the dedicated aims of the ATLAS [5, 6] and CMS [7] experiments at the LHC is to explore the unknown origin of mass of the fundamental particles for which a possible explanation is given by the so-called Higgs mechanism [8]. According to that theory, particles acquire mass by interaction with a scalar field that exists everywhere in the universe. The associated Higgs boson is the only yet undiscovered fundamental particle that is predicted by the Standard Model. Moreover, the underlying symmetries of nature are to be investigated.

This thesis is connected to both topics, as it deals with the ATLAS discovery potential for Higgs bosons in an extended supersymmetric model, the so-called Next-to-Minimal Supersymmetric Standard Model (NMSSM) [9]. Supersymmetry [10, 11] is a postulated, fundamental symmetry that links particles with different spin to each other. Supersymmetric theories postulate several Higgs bosons, for example, in the NMSSM, there are seven Higgs bosons in total. Although the existence of such a symmetry in nature could not yet be confirmed experimentally, it is appealing as it contains a possible explanation for dark matter in the universe, which is not accommodated within the Standard Model. Furthermore, it provides elegant solutions to some problems of the theory of the Standard Model.

Another focus of this work is the vector boson fusion process, that is the second largest production process for a Standard Model Higgs boson at the LHC. Due to the clear signature of vector boson fusion events, it is of paramount importance for an early Higgs boson discovery also in supersymmetric models. However, some of its typical features, such as the so-called tagging jets in the forward- and backward region of the detector, that are crucial for background suppression, need special experimental care to guarantee their good observability under realistic experimental conditions.

As this work was carried out before the start of the LHC, the presented studies are based on Monte Carlo simulations. During the preparation of a high-energy collider experiment, such simulations are important to develop efficient strategies for data analysis and for the reconstruction of the physics objects observed with the detectors. Moreover, the expectations from the Monte Carlo simulations can be compared to the measured situation at the experiment, which allows to draw conclusions on the underlying model realized in nature. One goal of this work is to determine regions in the multidimensional parameter space of the NMSSM for which it is not possible to find at least one Higgs boson with the current ATLAS search strategies. In a second step, this allows for the development of specialized analyses for the NMSSM. Otherwise, it cannot be guaranteed that the Higgs boson does not escape detection at the LHC if experimentally unfavorable parameter combinations are realized in nature.

The thesis is organized as follows:

In the first chapters, the basic principles of Higgs boson physics and of supersymmetry are explained and the main features of the Large Hadron Collider and the ATLAS experiment are reviewed. In the first part of this thesis, a general study of the detectability of one of the special features of vector boson fusion events, the so-called tagging jets in the forward- and backward region of the detector, is presented and different jet finding strategies are compared in detail in Chap. 4. The second part of this thesis deals with the discovery potential for the Higgs bosons of the NMSSM at the ATLAS experiment. At first, an overview of the current strategies for Higgs boson searches in ATLAS within the Standard Model and the Minimal Supersymmetric Standard Model (MSSM) is given and the overall discovery potential for Higgs bosons of these models is discussed. Subsequently, newly developed benchmark scenarios for the NMSSM, i.e. parameter combinations with experimentally challenging phenomenology in the Higgs sector, are introduced in Chap. 6. In Chap. 7, these scenarios are then used to evaluate the discovery potential for NMSSM Higgs bosons with the currently available ATLAS search strategies with the help of a scanning method. Since some gaps in the discovery potential for the Higgs bosons of the NMSSM are established by the scans of the benchmark scenarios, a possible new search specialized on the decay chain $H \rightarrow A_1 A_1 \rightarrow 4\tau \rightarrow 4\mu + 8\nu$, that can be important in extended models such as the NMSSM, is investigated in Chap. 8. A special focus is given to the Higgs boson mass reconstruction from the complex final state. A conclusion and appendices finalize the thesis.

2. Theoretical background

In this chapter, the theoretical concepts relevant to this work are shortly reviewed. Due to the complexity of the models, the description given here can only address the main aspects of the theory and assumes that some of the theoretical concepts are already known to the reader. More detailed discussions can be found in the references given in the respective sections.

2.1 The Standard Model of particle physics

First, the theoretical concepts of the so-called Standard Model of particle physics (SM) are described. All currently known fundamental particles and their interactions can be described by this model. Moreover, many parameters of the Standard Model were experimentally measured with high precision [3]. The predictions of the SM were confirmed, partly even to the level of quantum fluctuations. Although the Standard Model does not provide sufficient answers to all fundamental questions of particle physics, such as the nature of dark matter or the origin of the matter-antimatter asymmetry of the universe, it constitutes the basis of many extended theories which try to provide explanations to some of these issues, such as the supersymmetric theories which are addressed in Chaps. 2.2 and 2.3. The following description is in large parts based on Refs. [12, 13].

2.1.1 The electroweak sector

In modern quantum field theory, all fundamental interactions (except for gravity) between the fundamental, fermionic matter constituents are described by the exchange of bosonic field quanta. The strong interaction, whose field quanta are the massless gluons, is described by the $\mathrm{SU}(3)_\mathrm{C}$ gauge group in the framework of quantum chromodynamics. This theory is not reviewed here, as its details are not crucial for the understanding of this thesis.

The electroweak sector of the Standard Model was first described consistently in Refs. [1]. The gauge groups of the electroweak interaction have a $\mathrm{SU}(2)_{I_W} \times \mathrm{U}(1)_Y$ structure, which is broken down to a $\mathrm{U}(1)_\mathrm{EM}$ symmetry by electroweak symmetry breaking, as described in the following. Here, Y is the weak hypercharge, I_W the weak isospin, and I_W^3 its third component. These quantities are related to each other via

$$Q = \frac{Y}{2} + I_W^3 \tag{2.1}$$

With respect to the weak isospin, the left handed fermions can arranged in a doublet structure:

$$\begin{gathered} \begin{pmatrix} \nu_e \\ e \end{pmatrix}_L \begin{pmatrix} \nu_\mu \\ \mu \end{pmatrix}_L \begin{pmatrix} \nu_\tau \\ \tau \end{pmatrix}_L \\ \begin{pmatrix} u \\ d' \end{pmatrix}_L \begin{pmatrix} c \\ s' \end{pmatrix}_L \begin{pmatrix} t \\ b' \end{pmatrix}_L \end{gathered} \tag{2.2}$$

Right handed fermions are singlets under $\mathrm{SU}(2)_{I_W}$, since they are invariant under transformations of weak isospin, which means they do not couple to it. Both right handed and left handed

fermions couple to the weak hypercharge. A phenomenological consequence from this is that only the left handed doublets can interact via the exchange of $W^{\pm}$ bosons.

Initially, the bosons of the electroweak interaction are described by a massless isotriplet of $SU(2)_{I_W}$, $W_\mu^{1,2,3}$, and a massless isosinglet of $U(1)_Y$, B_μ. Also the fermions are initially massless. The kinetic energy of the B_μ field is usually called $B_{\mu\nu}$:

$$B_{\mu\nu} = \partial_\mu B_\nu - \partial_\nu B_\mu \tag{2.3}$$

The SU(2) generators T_i are proportional to the Pauli matrices σ_i.

$$T_i = \frac{1}{2}\sigma_i, \qquad i = 1,2,3 \tag{2.4}$$

Commonly, they are referred to in terms of the vector $\vec{T}$. Since the Pauli matrices do not commute with each other, the $\vec{W}_\mu$ fields have, in addition to their kinetic energy, also a contribution from their self-interaction:

$$\vec{W}_{\mu\nu} = \partial_\mu \vec{W}_\nu - \partial_\nu \vec{W}_\mu - g\vec{W}_\mu \times \vec{W}_\nu \tag{2.5}$$

With that, the Lagrangian density is [12]:

$$\begin{aligned} \mathcal{L} \;=\; & -\frac{1}{4}\vec{W}_{\mu\nu}\cdot\vec{W}^{\mu\nu} - \frac{1}{4}B_{\mu\nu}B^{\mu\nu} \\ & +i\bar{L}\gamma^\mu\partial_\mu L + i\bar{R}\gamma^\mu\partial_\mu R \\ & -g\bar{L}\gamma^\mu\vec{T}\cdot\vec{W}_\mu L \\ & -g'\frac{Y}{2}\bar{L}\gamma^\mu B_\mu L - g'\frac{Y}{2}\bar{R}\gamma^\mu B_\mu R \end{aligned} \tag{2.6}$$

Here, L is an arbitrary left handed fermionic $SU(2)_{I_W}$ doublet and R its corresponding right handed singlet. The parameters g and g' denote the respective coupling strengths.

To achieve local gauge invariance, i.e. invariance under the transformation

$$\begin{aligned} L \to L' &= e^{i\vec{\alpha}(x)\cdot\vec{T}+i\beta(x)Y}L \\ R \to R' &= e^{i\beta(x)Y}R \end{aligned} \tag{2.7}$$

the covariant derivative $D_\mu = \partial_\mu + igT^aW_\mu^a - ig'YB_\mu$ has to be used in the Lagrangian instead of ∂_μ. The parameters $\vec{\alpha}(x)$ and $\beta(x)$ are space-time dependent phases.

The first two terms in Eq. 2.6 describe the kinetic energy and self-interaction of the $W_\mu^{1,2,3}$ and B_μ fields and the two following terms the kinetic energies of left and right handed fermions. In the next row, the coupling of the left handed fermions to the weak isospin via the $W_\mu^{1,2,3}$ bosons with the coupling strength g is given. The last two terms describe the coupling of the fermions to the weak hypercharge via B_μ with the coupling strength g'.

The experimentally observed mass eigenstates of the field quanta of the electroweak sector are the neutral, massless photon (A_μ), the neutral, massive Z^0 boson (Z_μ) and the electrically charged massive $W^{\pm}$ bosons ($W_\mu^{\pm}$). The mass eigenstates are obtained from the mixing of the vector fields $W_\mu^{1,2,3}$ and B_μ:

$$W_\mu^{\pm} = \sqrt{\frac{1}{2}}\left(W_\mu^1 \mp iW_\mu^2\right) \tag{2.8}$$

$$A_\mu = B_\mu\cos\theta_W + W_\mu^3\sin\theta_W \tag{2.9}$$

$$Z_\mu = -B_\mu\sin\theta_W + W_\mu^3\cos\theta_W \tag{2.10}$$

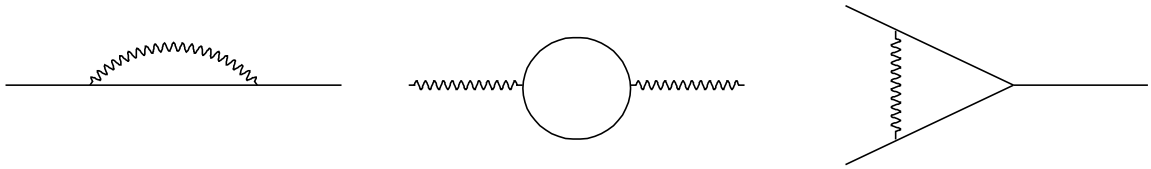

Fig. 2.1: Example higher order Feynman diagrams. Straight lines indicate fermions, wavy lines bosons. The momentum circulating in the loop can have arbitrary values.

Equations 2.9 and 2.10 arise only after spontaneous symmetry breaking as described in Chap. 2.1.2. The parameter θ_W with $\sin\theta_W \approx 0.231$ [14] is the weak mixing angle. The coupling constants g and g' are related to the elementary charge and the weak mixing angle via the equation:

$$g \sin\theta_W = g' \cos\theta_W = e \tag{2.11}$$

In perturbation theory, higher order terms with bosonic or fermionic loops arise (Fig. 2.1). For the calculation of physical quantities like cross sections, an integration over the momentum in the loop is necessary. This integration is logarithmically divergent. Predictions of the actual physical behavior are therefore not possible at first glance. By renormalization, mass and charge are redefined, so that they absorb the infinities of the theory. As a result, the quantities now depend on the energy scale that they are observed at. With the help of renormalization, the theory retains its predictive power also in the presence of loop diagrams.

As explained above, the Lagrangian density (Eq. 2.6) was constructed such that it is locally gauge invariant. If this prerequisite is fulfilled, the theory is also renormalizable. The existence of the vector fields $W_\mu^{1,2,3}$ and B_μ and their interactions results stringently from the requirement of local gauge invariance, since only the vector fields can compensate terms from the derivatives of the space-time dependent phases. Accordingly, the interactions are a direct result of local gauge symmetry.

2.1.2 Spontaneous symmetry breaking and Higgs mechanism

Introducing mass terms like:

$$\begin{aligned} \mathcal{L}_{M_W} &= \frac{M_W^2}{2} W_\mu^i W^{\mu i} \\ \mathcal{L}_{M_B} &= \frac{M_B^2}{2} B_\mu B^\mu \\ \mathcal{L}_{M_F} &= -M_F f \bar{f} \end{aligned} \tag{2.12}$$

into the Lagrangian density (Eq. 2.6) explicitly breaks local gauge symmetry. To obtain consistency with the experimental observations $M_{\mathrm{W}^\pm} = 80.403 \pm 0.029$ GeV and $M_{\mathrm{Z}^0} = 91.1876 \pm 0.0021$ GeV [14], the mechanism of spontaneous symmetry breaking is introduced into the Standard Model.

For the generation of masses, a scalar field ϕ is added to the theory[1]. Therefore, the Lagrangian density (Eq. 2.6) is extended by the following terms [12]:

$$\mathcal{L}_\phi = \left| \left(i\partial_\mu - g\vec{T} \cdot \vec{W}_\mu - g' \frac{Y}{2} B_\mu \right) \phi \right|^2 - V(\phi). \tag{2.13}$$

[1] A vector field is forbidden by the requirement of Lorentz invariance, since it would favor one of the spatial directions after obtaining a vacuum expectation value after the symmetry breaking.

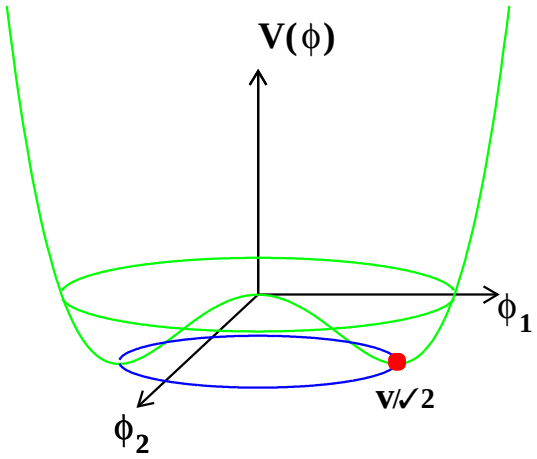

Fig. 2.2: The Higgs potential, projected to two degrees of freedom for better presentability. There is an infinite number of ground states, one of which is chosen randomly. The local maximum at $\phi = 0$ is not stable.

These are the kinetic energy and the interaction terms of the scalar field ϕ with $W_\mu^{1,2,3}$ and B_μ fields, also including a potential term:

$$V(\phi) = \mu^2 \phi^\dagger \phi + \lambda \left(\phi^\dagger \phi\right)^2 \tag{2.14}$$

Terms of higher order in ϕ would lead to a non-renormalizable theory. The modified Lagrangian density still has to be $\mathrm{SU}(2)_{I_W} \times \mathrm{U}(1)_Y$ gauge invariant. Furthermore, in order to describe the observed particle spectrum, the $\mathrm{SU}(2)_{I_W} \times \mathrm{U}(1)_Y$ symmetry, but not the $\mathrm{U}(1)_{\mathrm{EM}}$ symmetry, must be broken. Accordingly, the ground state must have non-vanishing weak hypercharge and isospin, but must not be electrically charged. The most simple choice for ϕ that fulfills these requirements is a scalar, complex isodoublet with weak hypercharge Y=1 and weak isospin $I_W = 1/2$:

$$\phi = \frac{1}{\sqrt{2}} \begin{pmatrix} \phi_1 + i\phi_2 \\ \phi_3 + i\phi_4 \end{pmatrix} \tag{2.15}$$

In Eq. 2.14, λ must be larger than zero, since the energy of the ground state should be finite. The choice $\mu^2 > 0$ yields a symmetric potential with a unique ground state at $\phi = 0$. This choice cannot generate any mass terms. In contrast to that, $\mu^2 < 0$ yields an infinite number of equally likely states of lowest energy with a non-vanishing expectation value v (Fig. 2.2). These states fulfill the condition:

$$\phi^\dagger \phi = \frac{1}{2}\left(\phi_1^2 + \phi_2^2 + \phi_3^2 + \phi_4^2\right) = -\frac{\mu^2}{2\lambda} = \frac{v^2}{2} \tag{2.16}$$

Nature randomly selects one of the minima of the potential as the physical ground state. By that, the symmetry of the system is spontaneously broken. One possible choice for the ground state, ϕ_0, that yields the correct mass relations and breaks $\mathrm{SU}(2)_{I_W} \times \mathrm{U}(1)_Y$ symmetry, is:

$$\phi_0 = \frac{1}{\sqrt{2}} \begin{pmatrix} 0 \\ v \end{pmatrix} \tag{2.17}$$

This choice also guarantees that the field ϕ_0 is invariant under the $\mathrm{U}(1)_{\mathrm{EM}}$ symmetry, as required, i.e. that

$$Q\phi_0 = 0 \tag{2.18}$$

with the electric charge generator $Q = I_W^3 + Y/2$. Accordingly, the ground state is electrically neutral.

For every broken generator of the presented theory, there exists a massless scalar Goldstone boson [15]. Since the original $\mathrm{SU}(2)_{I_W} \times \mathrm{U}(1)_Y$ symmetry is broken, but the Lagrangian density stays invariant under $\mathrm{U}(1)_{\mathrm{EM}}$ transformations, three Goldstone bosons are created. These bosons do not have any physical degrees of freedom. The expression for ϕ can be developed around the minimum by parameterizing the fluctuations of the vacuum in terms of the Goldstone fields $\vec{\theta}$ and a forth field h, which is the Higgs field [12]:

$$\phi(x) = \frac{1}{\sqrt{2}} e^{i\vec{\sigma}\cdot\vec{\theta}(x)/v} \begin{pmatrix} 0 \\ v + h(x) \end{pmatrix} \tag{2.19}$$

Via the so-called unitary gauge, the degrees of freedom if the Goldstone bosons can be transformed into the longitudinal degrees of freedom of the now massive weak bosons. This is called the Higgs mechanism [8]. Then, the Goldstone fields vanish from the theory, and Eq. 2.19 can be written as:

$$\phi(x) = \frac{1}{\sqrt{2}} \begin{pmatrix} 0 \\ v + h(x) \end{pmatrix} \tag{2.20}$$

This way, the term relevant for mass generation in the Lagrangian density (Eq. 2.13) is changed to [12]:

$$\left| \left(-ig\vec{T} \cdot \vec{W}_\mu - ig' \frac{Y}{2} B_\mu \right) \phi \right|^2 = \left(\frac{1}{2} vg \right)^2 W_\mu^+ W^{\mu-} + \frac{1}{8} v^2 \left[g W_\mu^3 - g' B_\mu \right]^2 \tag{2.21}$$

From this, Eqs. 2.9 and 2.10 for the mixing of the mass eigenstates Z_μ and A_μ as well as their masses can be extracted:

$$\begin{aligned} M_W &= \frac{1}{2} vg \\ M_Z &= \frac{1}{2} v \sqrt{g^2 + g'^2} \\ M_A &= 0 \end{aligned} \tag{2.22}$$

With the help of the expression for M_W and the Fermi coupling constant G_F, the vacuum expectation value of the potential, v, is determined to be 246 GeV [14]. The masses of the weak bosons are not equal due to the mixing. The ratio of their masses is given by the weak mixing angle:

$$\frac{M_W}{M_Z} = \cos\theta_W \tag{2.23}$$

Apart from this ratio, the theory does not make predictions on the absolute values of the masses of the $\mathrm{W}^\pm$ and Z^0 bosons.

In short, the breaking of the $\mathrm{SU}(2)_{I_W} \times \mathrm{U}(1)_Y$ symmetry gives masses to three of the vector bosons without destroying local gauge invariance. The process can be imagined as the interaction with a scalar, ubiquitary background field, the Higgs field. This field has a vacuum expectation value v, and its excitations can be understood as the Higgs boson. Invariance under the $\mathrm{U}(1)_{\mathrm{EM}}$ symmetry however remains. For this reason, one of the bosons, the photon, remains massless by construction. The experimental observations are well described by this theory.

In the Standard Model, the Higgs boson has the mass

$$M_h = v\sqrt{2\lambda} \tag{2.24}$$

and is electrically neutral. Its hypercharge is Y=1, the weak isospin $I_W^3 = -1/2$, and it is symmetric under CP-transformation (CP-even). The three-point couplings of the Higgs boson to bosons have the following strengths:

$$\mathrm{hWW} : \frac{2M_W^2}{v} \qquad \mathrm{hZZ} : \frac{2M_Z^2}{v} \qquad \mathrm{hhh} : \frac{3M_h^2}{v} \tag{2.25}$$

The following terms describe the coupling strengths of the four-point couplings:

$$\mathrm{hhWW} : \frac{2M_W^2}{v^2} \qquad \mathrm{hhZZ} : \frac{2M_Z^2}{v^2} \qquad \mathrm{hhhh} : \frac{3M_h^2}{v^2} \tag{2.26}$$

To also generate fermions masses, a $\mathrm{SU}(2)_{I_W} \times \mathrm{U}(1)_Y$ gauge invariant term can be included in the Lagrangian density [12]:

$$\mathcal{L}_{M_f} = -G\bar{L}\phi R + h.\ c. \tag{2.27}$$

i.e. an interaction of the fermion with the Higgs-field that causes a helicity flip. After symmetry breaking, ϕ can be substituted by Eq. 2.20 and G be chosen such that $M_f = Gv/\sqrt{2}$. The masses of the fermions M_f and their couplings to the Higgs boson are then given by:

$$\mathcal{L}_{M_f} = -M_f \bar{f} f - \frac{M_f}{v} \bar{f} f h \tag{2.28}$$

Since G is arbitrary, the masses of the fermions are not explicitly predicted by the theory. Equation 2.27 is valid for down-type fermions (charged leptons, down quark, strange quark, bottom quark). Masses for the up-type fermions (up quark, charm quark, top quark) are generated in the same way, but the charge conjugated field $\phi_c = i\sigma_2\phi^*$ must be used. Thus, the Higgs mechanism provides an elegant solution for the problem of mass generation.

Moreover, the existence of the Higgs boson would also solve a different problem of the theory. The scattering cross section of $\mathrm{W}^\pm$ bosons is proportional to the square of the center-of-mass energy and thus divergent for high energies. This can lead to a violation of the unitarity principle from energies of 1 to 2 TeV onwards. However, this divergence can be compensated for by the exchange of a scalar, neutral boson whose couplings are proportional to mass (Fig. 2.3). These requirements are fulfilled by the Higgs boson.

The Higgs boson is the last component of the Standard Model that is not yet experimentally observed. If it is discovered, the predictions of the Standard Model, such as the quantum numbers of the Higgs boson or its couplings to fermions and bosons need to be verified experimentally.

2.1.3 Bounds on the Higgs boson mass

Although the Higgs boson has not yet been observed experimentally, it is possible to give limits on its mass, which are derived both from theory and from experiment in the context of the Standard Model.

Unitarity

As was discussed above, one reason for the postulation of the Higgs boson are divergences that otherwise arise in the scattering of $\mathrm{W}^\pm$ bosons at high energy. For the scattering of longitudinally polarized $\mathrm{W}^\pm$ bosons, the scattering amplitude for s-waves can be given in the limit of small masses compared to the center-of-mass energy (see eg. [16]):

$$a_0 = -\frac{G_F M_h^2}{4\sqrt{2}\pi} \tag{2.29}$$

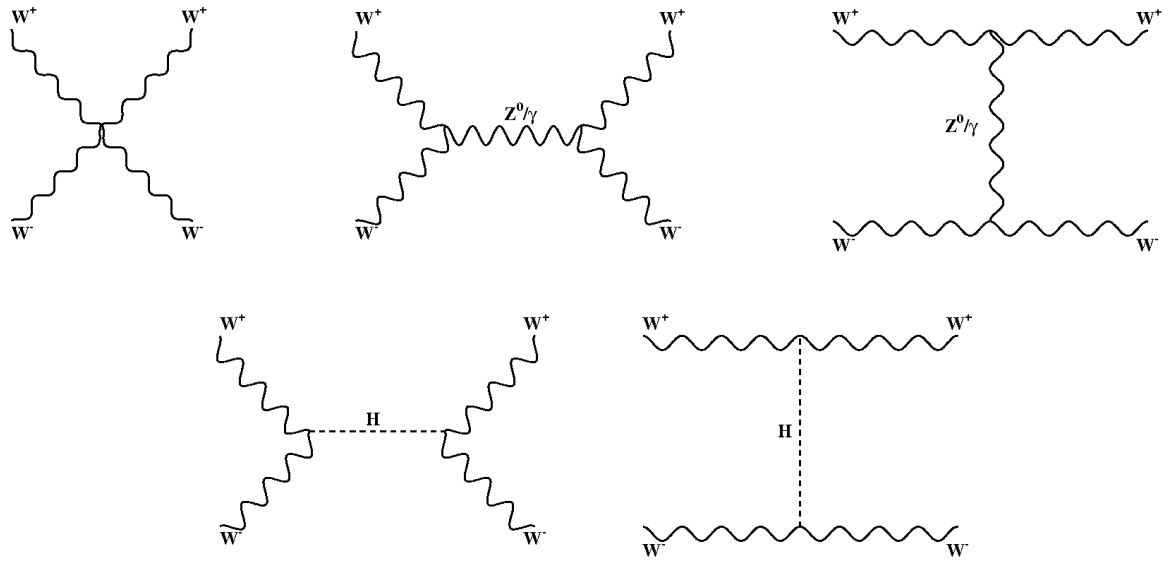

Fig. 2.3: Feynman diagrams for elastic W^+W^- scattering. Top row: Gauge boson exchange. These diagrams alone lead to violation of the unitarity principle at large energies. Bottom row: Higgs boson exchange. Addition of these diagrams to the theory can restore the unitarity of the process also at large energies.

Unitarity requires $|\mathcal{R}e(a_0)| \leq \frac{1}{2}$. From this it follows

$$M_h \leq \sqrt{\frac{2\sqrt{2}}{G_F}} \approx 850 \text{ GeV} \tag{2.30}$$

Also from other scattering processes, a mass limit of about 1 TeV can be derived [16, 17].

Triviality and Landau pole

The value of the parameter λ from Eq. 2.14 is energy dependent because of radiative corrections [16]. The diagram in the middle of Fig. 2.4 causes λ to be divergent for large center-of-mass energies, i.e. a so-called Landau pole occurs. Perturbation theory can be applied if λ is not arbitrarily large. If λ is required to be finite at an infinitively large energy scale Λ, it will have to approach zero at a small energy scale Λ_0. In that case, the Higgs boson couplings vanish and the theory is trivial as no symmetry breaking takes place. Consequently, there must be a largest scale Λ_{max} until which the theory is valid.

The Higgs boson mass ist given by $M_h = v\sqrt{2\lambda}$. Therefore, the choice of the scale Λ_{max} affects the bounds on the Higgs boson mass. When requiring a finite λ at Λ_{max}, the upper limit on the mass of the Higgs boson is given by (see eg. [16]):

$$M_h^2 \leq \frac{4\pi^2 v^2}{3 \log \frac{\Lambda_{max}}{v}} \tag{2.31}$$

Accordingly, if Λ_{max} is 1 TeV, the Higgs boson must be lighter than about 800 GeV, if Λ_{max} is at the Planck scale at 10^{19} GeV, the Higgs boson mass must be smaller than about 190 GeV.

Vacuum stability

Due to the contribution from the right hand diagram of Fig. 2.4, λ also depends on the top quark mass. If the Higgs boson mass is small compared to the top quark mass, the contribution

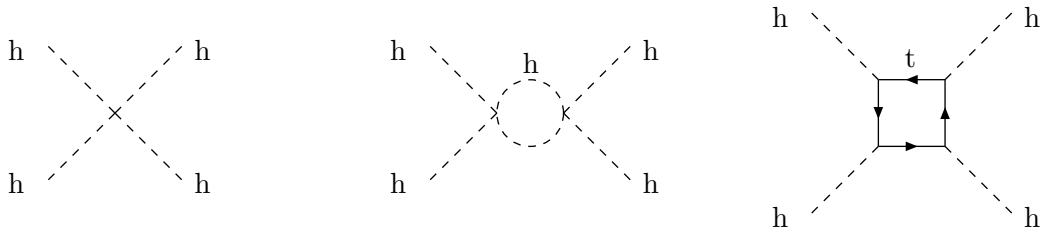

Fig. 2.4: Dominant Feynman diagrams for the Higgs boson self-interaction.

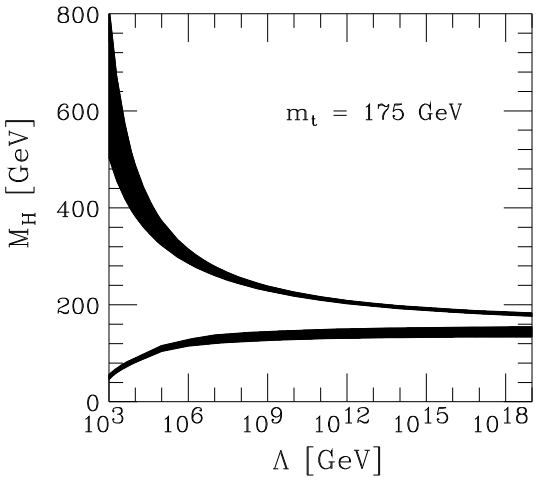

Fig. 2.5: Bounds on the Higgs boson mass in dependence on the maximal scale, until which the Standard Model remains valid. The upper bound is given by triviality , the lower bound by vacuum stability. The black bands show the theoretical uncertainties, between them, there is the allowed mass range [19].

from this diagram reduces λ to very small or even negative values. If λ turns to negative values, the lowest energetic state is not the minimum of Eq. 2.17, and in particular it can have infinite negative values. From the requirement for a stable local minimum, a lower bound on the Higgs boson mass can be derived [18].

The bounds on the Higgs boson mass from triviality and from vacuum stability are shown in Fig. 2.5. If the Standard Model is valid up to the Planck scale, the Higgs boson mass is restricted to values from 130 to 190 GeV. If the maximal scale is only 1 TeV, Higgs boson masses from about 50 to 800 GeV are allowed.

Experimental limits

Via direct searches, the experiments at the LEP[2] accelerator were able to exclude a Standard Model Higgs boson with a mass lower than 114.4 GeV with at least 95% confidence level [20].

All parameters of the Standard Model, except for the Higgs boson mass, were already measured experimentally. The Higgs boson mass depends on these quantities via loop corrections [21] and is especially sensitive to the mass of the heavy top quark. Therefore, a fit of these parameters to the predictions of the theory gives a prediction of the Higgs boson mass.

Figure 2.6 shows the results of such a fit (March 2008). In the fit, the current world average mass of the top quark of (172.6 ± 1.4) GeV [22] was used. The prediction for the Higgs boson mass, i.e. the minimum of the χ^2 curve, is 87^{+36}_{-27} GeV. The theoretical uncertainties, that are

[2] The Large Electron Positron Collider (LEP) ran from 1989 to 2000 at center-of-mass energies up to 209 GeV.

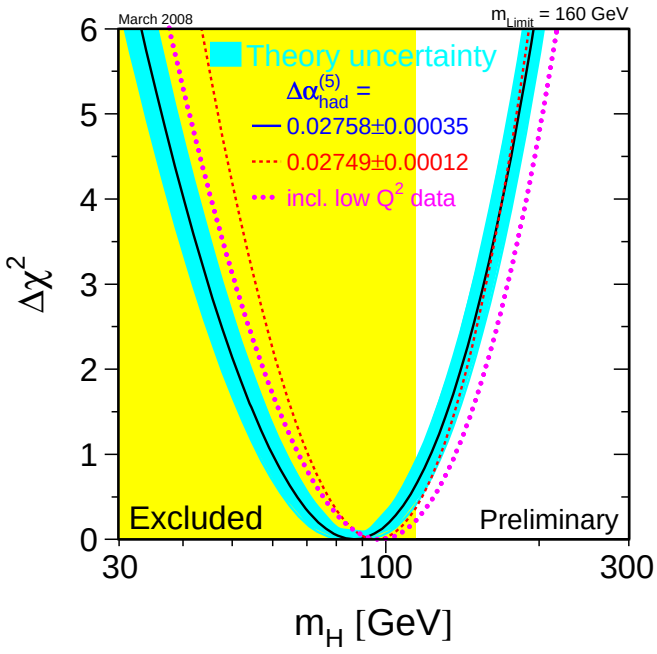

Fig. 2.6: The χ^2 distribution of a fit of the Standard Model parameters in dependence on the Higgs boson mass [3]. The highlighted region is excluded by direct searches. The blue (grey) band shows the theoretical uncertainty. The opening width of the parabola is determined by the experimental errors of the fitted parameters.

shown by the blue (grey) band, are not included in the errors. The upper bound for the Higgs boson mass is 160 GeV at 95% confidence level. When the theoretical uncertainty and the direct limit from the LEP searches are included, this bound increases to 190 GeV at 95% confidence level [3].

2.1.4 Problems of the Standard Model

In spite of the great successes of the Standard Model, this theory can for sure not provide the final answers to all questions of particle physics. For example, there is only an insufficient explanation for the matter-antimatter asymmetry and baryogenesis [23]. Furthermore, gravity is not contained in the Standard Model.

The mass of the Higgs boson is affected by various loop corrections, as for example in Fig. 2.8a. The contributions of single diagrams are of the same order of magnitude as the energy scale until which the Standard Model is valid (see eg. [24]). Commonly, this scale is assumed to be the Planck scale (10^{19} GeV). The natural mass of the Higgs boson accordingly lies at that scale, whereas theoretical and experimental limits on the Higgs boson mass show that it actually has to be of $\mathcal{O}(100)$ GeV. Technically, it is possible in the Standard Model to obtain such a low Higgs boson mass via mutual cancellation of different contributions, however, for this, large fine-tuning in every order of perturbation theory is needed without having a satisfactory explanation. This is called the naturalness problem [25].

Moreover, in the Standard Model, the vacuum expectation value of the Higgs field is the only mass scale to which all particle masses are related. If the Standard Model is to be valid

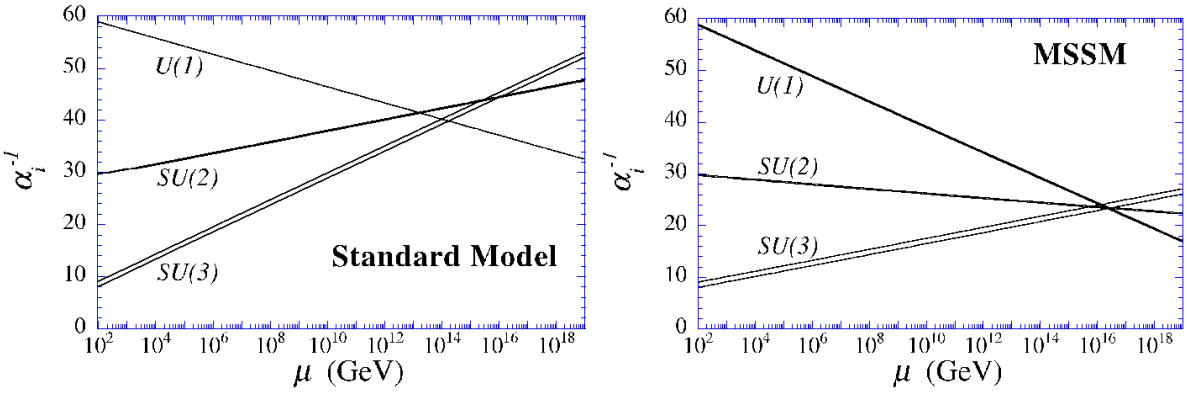

Fig. 2.7: The running of the inverse coupling constants with the energy scale μ in the SM and the MSSM [26].

until eg. the Planck scale, it is unclear why the electroweak scale is so much smaller. The obvious discrepancy between the two energy scales is called the hierarchy problem [25]. A natural solution to these problems is for example provided by supersymmetric theories.

Furthermore, the Standard Model only contains a description, but not an explanation of the $\mathrm{SU(3)_C} \times \mathrm{SU(2)}_{I_W} \times \mathrm{U(1)}_Y$ gauge structure. Also the different values of the coupling strengths remain unexplained. There are efforts to unify the gauge groups and couplings at the so-called Grand Unification scale (GUT scale). In the framework of the Standard Model, such a unification is not possible since the coupling constants do not meet in a single point at large energies. In contrast to that, the coupling constants meet in one point in supersymmetric theories (Fig. 2.7).

Moreover, the Standard Model does not present a sufficient explanation for the presence of dark matter in the universe. In supersymmetric theories, the lightest supersymmetric particle (LSP) could be stable due to an additional, conserved quantum number, the R-parity. The LSP, which is often the so-called neutralino, is a possible dark matter constituent if it is electrically neutral and colorless.

Taking all these issues into account, the Standard Model is regarded by many (see eg. Ref. [27]) as a low-energy approximation of a more fundamental theory. Due to the features mentioned above, supersymmetric theories offer an appealing possibility for such a theory.

2.2 Supersymmetry and the MSSM

Supersymmetry is a fundamental space-time symmetry that relates bosons to fermions. This concept first emerged in the context of string theory [10] in the early 1970s. Few years later, supersymmetric field theories were proposed [11]. Until today, the existence of supersymmetry in nature has not been experimentally proven. However, its phenomenology and implications have been studied in great detail both in theory and in experiment. The search for supersymmetry, and, if it should be discovered, the measurement of its model parameters, will be one of the main tasks at future collider experiments like the LHC[3] and the ILC[4]. In the following, a short outline of supersymmetry as it is described by the Minimal Supersymmetric Standard Model (MSSM) is given. The description is based on Refs. [28, 29].

A supersymmetry transformation with the operator Q_s turns a bosonic state into a fermionic

[3] The Large Hadron Collider, see Chap. 3.1.
[4] The International Linear Collider, a proposed electron-positron collider.

state and vice versa:

$$\begin{aligned} Q_s|\text{boson}\rangle &= |\text{fermion}\rangle \\ Q_s|\text{fermion}\rangle &= |\text{boson}\rangle \end{aligned} \tag{2.32}$$

Apart from the spin, the bosonic and fermionic states have the same quantum numbers, as Q_s commutes with the generators of the gauge transformations. If the commutation relations

$$\begin{aligned} \{Q_s, Q_s^\dagger\} &= P^\mu \\ \{Q_s, Q_s\} &= \{Q_s^\dagger, Q_s^\dagger\} = 0 \\ [P^\mu, Q_s] &= [P^\mu, Q_s^\dagger] = 0 \end{aligned} \tag{2.33}$$

hold, the theory is able to describe chiral fermions as they are observed in nature [28,30]. Here, P^μ is the four-momentum generator of space-time translations. Irreducible representations of this algebra are called supermultiplets and describe the single particle states. A supermultiplet contains both bosonic and fermionic states, i.e. the particles of the Standard Model and their superpartners. Apart from their spin which differs by 1/2, the Standard Model particles and their respective superpartners have the same quantum numbers. With the help of Eqs. 2.33, it can be shown that the number of bosonic and fermionic degrees of freedom in a supermultiplet must be equal (see eg. Ref. [28]):

$$n_B = n_F \tag{2.34}$$

Then, if the theory has only one supersymmetry operator Q_s (N=1 supersymmetry) and is renormalizable, only two types of irreducible supermultiplets exist: chiral (also named scalar) supermultiplets and gauge (also named vector) supermultiplets.

A chiral supermultiplet contains a Weyl fermion (spin 1/2) with two spin helicity states ($n_F = 2$), and two real scalars (each $n_B = 1$, spin 0), which can be described by one complex scalar field. The known fermions of the Standard Model and their postulated superpartners, the scalar sfermions (denoted by a prepended 's'), are described by chiral supermultiplets. Since right handed and left handed fermions ($\mathrm{f_R}, \mathrm{f_L}$) have different weak isospin and hypercharge quantum numbers, they have different superpartners which are denoted as $\tilde{\mathrm{f}}_\mathrm{R}$, $\tilde{\mathrm{f}}_\mathrm{L}$.

A gauge supermultiplet contains a massless vector boson ($n_B = 2$, spin 1) and the superpartner of this boson, a spin 1/2 Weyl fermion ($n_F = 2$). Masses can later be generated by electroweak symmetry breaking. The known Standard Model bosons and their postulated superpartners, the bosinos ($\tilde{V}$, denoted by the suffix 'ino'), are described by gauge supermultiplets.

As none of the currently known particles can be identified with a superpartner, the particle content of the SM is essentially doubled by supersymmetry. Because no new vector fields are added, the gauge interactions of the supersymmetric particles are identical to the known interactions of the Standard Model.

According to the above, the Higgs boson as a scalar particle is described by a chiral supermultiplet. Since the introduction of only one fermionic Higgsino would introduce unacceptable anomalies into the theory, the minimal number of Higgs supermultiplets is two, i.e. there have to be at least two Higgs doublets. Moreover, the second Higgs doublet with hypercharge $Y = -1$ is also needed to give masses to the up-type fermions, because in a supersymmetric theory, it is not possible to use the charge conjugated Higgs field for this as in the Standard Model (see eg. Ref. [29]).

Before symmetry breaking, there are eight degrees of freedom in the scalar components of the two Higgs doublet fields. After symmetry breaking, three correspond to Goldstone bosons and thus are absorbed by the longitudinal degrees of freedom of the massive vector bosons. The remaining five degrees of freedom form the five Higgs bosons of the MSSM: the two CP-even

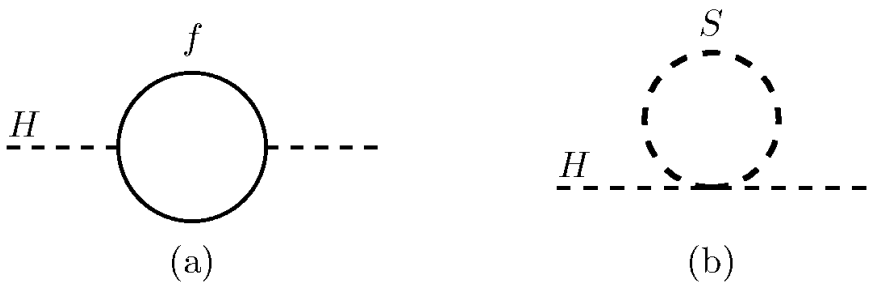

Fig. 2.8: One-loop quantum corrections to the Higgs boson mass a) due to a fermion f b) due to a scalar S [28].

scalars h, H (in order of mass), the pseudoscalar A[5] and the charged Higgs bosons $H^{\pm}$.[6]

The superpartners (interaction eigenstates) are not necessarily the physically observable mass eigenstates. The charged Winos and charged Higgsinos mix to the mass eigenstate charginos ($\tilde{\chi}^{\pm}_{1,2}$). There are four neutralinos ($\tilde{\chi}^{0}_{1,2,3,4}$) that are produced by the mixing of the Zino, the photino and the neutral Higgsinos. Moreover, the right and left handed[7] staus $\tilde{\tau}_{\mathrm{R,L}}$, stops $\tilde{\mathrm{t}}_{\mathrm{R,L}}$ and sbottoms $\tilde{\mathrm{b}}_{\mathrm{R,L}}$, which have the largest Yukawa couplings, are likely to mix to the $\tilde{\tau}_{1,2}$, $\tilde{\mathrm{t}}_{1,2}$ and $\tilde{\mathrm{b}}_{1,2}$ mass eigenstates. Mixing of the other sleptons is usually assumed to be negligible in the MSSM.

As mentioned earlier, the existence of supersymmetry naturally solves the so-called hierarchy problem described in Chap. 2.1.4. For each fermion loop contributing to the Higgs boson mass (Fig. 2.8, left hand side), additional contributions from the two scalars now enter the theory (Fig. 2.8, right hand side). If the Higgs boson coupling to the fermion (λ_f) and to the scalar (λ_S) are related as

$$\lambda_S = |\lambda_f|^2, \tag{2.35}$$

these diagrams cancel exactly to all orders of perturbation theory, as contributions from bosonic and fermionic loops have opposite sign. This condition (Eq. 2.35) is naturally fulfilled by the structure of supersymmetric theories (see eg. Ref. [29]).

According to Eq. 2.33, the squared mass operator $-P^2$ commutes with the operators Q_s, $Q_s^{\dagger}$. Hence, all particles have the same mass as their superpartners in unbroken supersymmetry (see eg. [28]). Since supersymmetric particles with such masses should already have been observed experimentally, supersymmetry must be broken. As the mechanism for supersymmetry breaking is unknown, usually terms that explicitly break supersymmetry and that parameterize the low-energy effects of the unknown breaking mechanism are included into the Lagrangian density. These supersymmetry breaking terms should be soft, i.e. of positive mass dimension, in order to guarantee that bosonic and fermionic loop corrections to the Higgs boson mass still cancel, i.e. the hierarchy problem is still solved after symmetry breaking.

The Langrangian of the MSSM can then be written as

$$\mathcal{L}_{\mathrm{MSSM}} = \mathcal{L}_g + \mathcal{L}_M + \mathcal{L}_H + \mathcal{L}_{Soft} \tag{2.36}$$

Here, $\mathcal{L}_g$ describes the pure gauge part of the model, $\mathcal{L}_M$ the matter part and $\mathcal{L}_H$ the Higgs doublets and the Yukawa couplings. While these parts of the Langrangian are supersymmetry

[5] The term 'pseudoscalar' is often used to refer to a CP-odd boson. Accordingly, the term 'scalar' refers to a CP-even boson. This convention is also used in this thesis.

[6] It is also possible to introduce a second Higgs doublet to the Standard Model without supersymmetry. This field then gives masses to the up-type fermions instead of the conjugated Higgs field.

[7] In this notation, the handedness is not a feature of the staus, stops and sbottoms that are scalar particles, but of the Standard Model particles of which they are the superpartners.

conserving, the soft supersymmetry breaking terms are collected in $\mathcal{L}_{Soft}$.

The interactions of the chiral and gauge supermultiplets and the quartic self-coupling of the Higgs fields are completely determined by the gauge symmetries and by supersymmetry, the interaction strengths by the gauge couplings. Only the so-called superpotential W_{MSSM} can be chosen freely. If the Lagrangian density is required to be invariant under the gauge symmetries and supersymmetry, and if lepton and baryon number violating processes are assumed to be forbidden, the superpotential has the following form [28]:

$$W_{\mathrm{MSSM}} = \bar{u}\mathbf{y_u}QH_u - \bar{d}\mathbf{y_d}QH_d - \bar{e}\mathbf{y_e}LH_d + \mu H_u H_d \tag{2.37}$$

H_u, H_d, Q, $\bar{u}$, $\bar{d}$, L and $\bar{e}$ denote the chiral superfields for the Higgs bosons, quarks and leptons. $\mathbf{y_u}$, $\mathbf{y_d}$ and $\mathbf{y_e}$ are the dimensionless 3×3 Yukawa coupling matrices. The parameter μ is the Higgs-Higgsino mass parameter of the MSSM and gives rise to the so-called μ-problem (see Chap. 2.2.2).

The same requirements as above lead to the following form of $\mathcal{L}_{Soft}$ [28]:

$$\begin{aligned}
\mathcal{L}_{Soft} \;=\; & -\frac{1}{2}\left(M_3\tilde{g}\tilde{g} + M_2\tilde{W}\tilde{W} + M_1\tilde{B}\tilde{B} + \; h.c.\right) \\
& -\tilde{Q}^\dagger \mathbf{M_Q^2}\tilde{Q} - \tilde{L}^\dagger \mathbf{M_L^2}\tilde{L} - \tilde{u}\mathbf{M_{\bar{u}}^2}\tilde{\bar{u}}^\dagger - \tilde{\bar{d}}\mathbf{M_{\bar{d}}^2}\tilde{\bar{d}}^\dagger - \tilde{\bar{e}}\mathbf{M_{\bar{e}}^2}\tilde{\bar{e}}^\dagger \\
& -\left(\tilde{\bar{u}}\mathbf{A_u}\tilde{Q}H_u - \tilde{\bar{d}}\mathbf{A_d}\tilde{Q}H_d - \tilde{\bar{e}}\mathbf{A_e}\tilde{L}H_d + \; h.c.\right) \\
& -m_{H_u}^2 H_u^* H_u - m_{H_d}^2 H_d^* H_d - (\mu B H_u H_d + \; h.c.)
\end{aligned} \tag{2.38}$$

The first line of Eq. 2.38 creates mass terms for the gauge fermions, the second line mass terms for the scalar superpartners of the Standard Model fermions. The third line contains trilinear interaction terms between three scalar particles. The last line describes additional terms to the Higgs potential. The $\mathbf{M^2}$ and $\mathbf{A}$ parameters are 3×3 matrices that allow for mixing between the families. Usually, the masses of the supersymmetric particles are assumed to be at a common, characteristic scale M_{susy}. Supersymmetry is broken by $\mathcal{L}_{Soft}$, because it involves only scalars and gauginos and not their respective superpartners, the known Standard Model particles.

In principle, fast proton decay via $p \to e^+\pi^0$ is possible in a general supersymmetric theory[8]. To achieve consistence with the observed decay time for that decay mode of the proton which is larger than 10^{32} years [28], a new multiplicative, conserved quantum number, the R-parity, is postulated in the MSSM:

$$R = (-1)^{3B+L+2S} \tag{2.39}$$

Here, B is the baryon number, L the lepton number and S the spin. All Standard Model particles have even R-parity, their superpartners have odd R-parity. Assuming R-parity is conserved, supersymmetric particles can only be produced in pairs. Moreover, the lightest supersymmetric particle (LSP) cannot decay to Standard Model particles and is therefore stable. The LSP is therefore a candidate for dark matter, however, it must be electrically neutral and may not carry color to be in agreement with astrophysical observation [25, 31].

2.2.1 The MSSM Higgs sector

As stated in the previous chapter, two Higgs doublets H_d, H_u with opposite hypercharge are needed for anomaly cancellation and to generate masses for down-type and up-type fermions in the MSSM.

$$H_d = \begin{pmatrix} H_d^0 \\ H_d^- \end{pmatrix} \; (Y{=}1), \qquad H_u = \begin{pmatrix} H_u^+ \\ H_u^0 \end{pmatrix} \; (Y{=}\text{-}1) \tag{2.40}$$

[8] The corresponding terms do not appear in the here given superpotential of Eq. 2.37, as lepton and baryon number conservation was required.

The scalar potential can be derived from the superpotential and the soft supersymmetry breaking terms [29]:

$$V = \frac{1}{8}\left(g^2 + g'^2\right)\left(|H_d|^2 - |H_u|^2\right)^2 + \frac{1}{2}g^2|H_d^\dagger H_u|^2 + \mu^2\left(|H_d|^2 + |H_u|^2\right) + V_{Soft} \tag{2.41}$$

In contrast to the SM, the quartic Higgs self-couplings are not free parameters in the MSSM, but are given by the gauge couplings. Without the terms in V_{Soft}, the potential would have a trivial minimum V=0 for H_u=H_d=0. Thus, without breaking supersymmetry, also the $\mathrm{SU(2)}_{I_W} \times \mathrm{U(1)}_Y$ symmetry remains unbroken. For this reason, the supersymmetry breaking terms contained in V_{Soft} are added to the potential.

$$V_{Soft} = m_{H_d}^2|H_d|^2 + m_{H_u}^2|H_u|^2 + \mu B\left(H_d \cdot H_u + h.c.\right) \tag{2.42}$$

Here, $m_{H_d}^2$, $m_{H_u}^2$ and B are soft supersymmetry breaking parameters. In order to break $\mathrm{SU(2)}_{I_W} \times \mathrm{U(1)}_Y \rightarrow \mathrm{U(1)_{EM}}$ in the desired way, the vacuum expectation values of the Higgs fields have to be non-zero:

$$\langle H_d \rangle = \frac{1}{\sqrt{2}}\begin{pmatrix} v_1 \\ 0 \end{pmatrix} \qquad \langle H_u \rangle = \frac{1}{\sqrt{2}}\begin{pmatrix} 0 \\ v_2 \end{pmatrix} \tag{2.43}$$

Here, the two expectation values v_1 and v_2 can always be chosen positive and real. With these expressions, mass terms for the Z^0 and $\mathrm{W}^\pm$ can be derived [29]:

$$\begin{aligned} M_W &= \frac{1}{2}\left(\sqrt{v_1^2 + v_2^2}\right) g \\ M_Z &= \frac{1}{2}\left(\sqrt{v_1^2 + v_2^2}\right)\sqrt{g^2 + g'^2} \end{aligned} \tag{2.44}$$

The squared sum of the vacuum expectation values is fixed by the known value of the $\mathrm{W}^\pm$ boson mass and by G_F (i.e. $\sqrt{v_1^2 + v_2^2} \approx 246$ GeV), but their ratio $\tan\beta$ is a free parameter:

$$\tan\beta = \frac{v_2}{v_1}. \tag{2.45}$$

The MSSM Higgs sector is often described in terms of $\tan\beta$. As $v_1 = v\cos\beta$ and $v_2 = v\sin\beta$ are real and positive, β is restricted to

$$0 < \beta < \pi/2. \tag{2.46}$$

A minimum of the Higgs potential with the features described above is obtained under the conditions [29]:

$$-2B\mu = \left(m_{H_d}^2 - m_{H_u}^2\right)\tan 2\beta + M_Z^2 \sin 2\beta \tag{2.47}$$

$$\mu^2 = \frac{m_{H_u}^2 \sin^2\beta - m_{H_d}^2 \cos^2\beta}{\cos 2\beta} - \frac{1}{2}M_Z^2 \tag{2.48}$$

As mentioned before, the two Higgs doublets describe three Goldstone bosons $\mathrm{G}^\pm$, G^0, two CP-even neutral Higgs bosons h, H, a CP-odd Higgs boson A and two charged Higgs bosons $\mathrm{H}^\pm$. These mass eigenstates are mixtures of the real and imaginary components of the fields with equal electric charge and CP quantum numbers [29]:

$$H^0 = \left(\sqrt{2}\Re H_d^0 - v_1\right)\cos\alpha + \left(\sqrt{2}\Re H_u^0 - v_2\right)\sin\alpha \tag{2.49}$$

$$h^0 = -\left(\sqrt{2}\Re H_d^0 - v_1\right)\sin\alpha + \left(\sqrt{2}\Re H_u^0 - v_2\right)\cos\alpha \tag{2.50}$$

ϕ	$g_{u\bar{u}\phi}$	$g_{d\bar{d}\phi}$	$g_{VV\phi}$
h	$\cos\alpha/\sin\beta$	-$\sin\alpha/\cos\beta$	$\sin(\beta-\alpha)$
H	$\sin\alpha/\sin\beta$	$\cos\alpha/\cos\beta$	$\cos(\beta-\alpha)$
A	$1/\tan\beta$	$\tan\beta$	0

Tab. 2.1: The couplings of the neutral MSSM Higgs bosons to the known fermions and gauge bosons relative to their Standard Model value.

$$A^0 = \sqrt{2}\left(\Im H_d^0 \sin\beta + \Im H_u^0 \cos\beta\right) \tag{2.51}$$
$$G^0 = \sqrt{2}\left(-\Im H_d^0 \cos\beta + \Im H_u^0 \sin\beta\right) \tag{2.52}$$

$$H^\pm = \sin\beta H_d^\pm + \cos\beta H_u^\pm \tag{2.53}$$
$$G^\pm = -\cos\beta H_d^\pm + \sin\beta H_u^\pm \tag{2.54}$$

The mixing angle of the CP-even Higgs bosons, α, is related to β via

$$\tan 2\alpha = \frac{M_A^2 + M_Z^2}{M_A^2 - M_Z^2}\tan 2\beta \tag{2.55}$$

By evolving the Higgs potential around its minimum, Born level expressions for the Higgs boson masses can be extracted [29]:

$$M_{H,h}^2 = \frac{1}{2}\left(M_A^2 + M_Z^2 \pm \sqrt{\left(M_A^2 + M_Z^2\right)^2 - 4M_Z^2 M_A^2 \cos^2 2\beta}\right) \tag{2.56}$$

$$M_A = \frac{B\mu}{v_1 v_2}\left(v_1^2 + v_2^2\right) \tag{2.57}$$

$$M_{H^\pm} = \left(\frac{B\mu}{v_1 v_2} + \frac{1}{4}g_2^2\right)\left(v_1^2 + v_2^2\right) = M_A^2 + M_{W^\pm}^2 \tag{2.58}$$

By definition, h is the lighter and H the heavier CP-even scalar. The Goldstone bosons are massless and absorbed by the longitudinal degrees of freedom of the massive vector bosons.

From Eq. 2.56, it can be shown that at Born level:

$$M_h < M_Z|\cos(2\beta)|. \tag{2.59}$$

Thus, the mass of the lightest scalar is bound from above and cannot be arbitrarily large. At Born level, M_h lies below the Z^0 boson mass. These Born level mass equations are modified by radiative corrections. However, even with radiative corrections, M_h cannot be larger than about 135 GeV [32].

The electroweak parameters of the Standard Model and the values of β and α completely determine the couplings of the MSSM Higgs bosons to the known gauge bosons and fermions. An overview of the coupling sizes of the neutral Higgs bosons relative to the Standard Model is given in Tab. 2.1. At Born level, the Higgs boson couplings are parity conserving. Moreover, the couplings of the h and H bosons to vector bosons are pairwise complementary, i.e. if one of the couplings is suppressed, the other one is large due to their dependence on the mixing angles. In particular, the sum of the squared couplings of the scalar Higgs bosons to vector bosons is equal to the square of this coupling in the Standard Model. The couplings of the CP-even Higgs bosons to down-type fermions are enhanced at high $\tan\beta$ and moderate α. The coupling of the

pseudoscalar boson to down-type fermions is enhanced at large $\tan\beta$ independently of α.

The coupling of the charged Higgs boson to fermions is given by [29]:

$$g_{H^+ f_d \bar{f}_u} = \frac{g}{\sqrt{2} M_W} (M_u \cot\beta P_L + M_d \tan\beta P_R) \tag{2.60}$$

P_L and P_R are here the left and right handed projection operators, and $M_{u,d}$ the fermion masses. The coupling is large for small and for large values of $\tan\beta$.

Only two parameters are sufficient to describe the MSSM Higgs sector at Born level. Commonly, these are chosen to be $\tan\beta$ and M_A.

To get a better handle on the rich MSSM phenomenology and to test the power of Higgs boson searches in the framework of the MSSM, several benchmark scenarios for the MSSM Higgs sector were defined [33]. The following list gives two examples.

- The $M_h$max Scenario is defined in a way that the mass of the lightest scalar is maximized. This scenario has the least restrictions from LEP results.
- The CPX Scenario is defined to have maximized CP violation by loop corrections in the Higgs sector. Here, CP-odd and CP-even Higgs bosons mix. There is no bound on the mass of the lightest Higgs boson from LEP.

2.2.2 The μ-problem

The so-called μ-problem of the MSSM is a problem of naturalness related to the size of the Higgs-Higgsino mass parameter μ. As this parameter is not restricted by theory, it could in principle have any value from zero up to the Planck scale. However, μ is phenomenologically constrained to lie not far from the electroweak ($\mathcal{O}$(100 GeV)) or supersymmetry breaking scale ($\mathcal{O}$(1 TeV) if the hierarchy problem is to be solved) [34]. In principle, it is possible within the MSSM to simply fix the supersymmetry conserving parameter μ at a suitable scale, however, it seems unnatural that μ and the unrelated supersymmetry breaking scale should just by chance lie so close to each other. In fact, it would be more convincing to have a theory which actually links μ to the supersymmetry breaking scale and thus gives a natural explanation for its expected size. A possible solution for this problem is given in the framework of the NMSSM.

2.3 The NMSSM

In the Next-to-Minimal Supersymmetric Standard Model (NMSSM) [9], an additional neutral gauge singlet chiral superfield S is added to the MSSM. It contains in total four degrees of freedom, two scalar bosons and a spin 1/2 Weyl fermion. This choice respects the gauge invariance of the theory. The resulting model contains the entire particle spectrum of the MSSM with an additional neutral scalar boson, a neutral pseudoscalar boson and a neutral fermion ('singlino'). After symmetry breaking, the two additional scalars mix with the MSSM Higgs bosons to form the five neutral Higgs bosons of the NMSSM (in order of mass): three CP-even bosons H_1, H_2, H_3 and two CP-odd Higgs bosons A_1, A_2. The neutral fermion mixes with the four neutralinos of the MSSM. Thus, the model contains in total five neutral fermion states. Since no charged particles are added, the features of the other MSSM particles, including the charged Higgs bosons $H^\pm$, are only modified marginally. The description of the NMSSM given here is based on Refs. [29, 35, 36].

To solve the μ-problem, the term $\mu H_u H_d$ in the superpotential of the MSSM (Eq. 2.37) is replaced by the interaction term $\lambda S H_u H_d$. Here, the parameter λ is a dimensionless coupling

strength. If s, the bosonic component of S, has acquired a non-zero vacuum expectation value after symmetry breaking, an effective μ term is generated:

$$\mu = \lambda \langle s \rangle \tag{2.61}$$

The constraints which arise when the Higgs potential is minimized relate the vacuum expectation values of the three neutral scalar fields H_u^0, H_d^0 and s to their soft supersymmetry breaking masses [36]. Thus, μ can now be naturally expected to lie at the right scale.

However, this model still includes an additional global U(1) (Peccei-Quinn) symmetry which leads to an extra massless CP-odd scalar, the Peccei-Quinn axion [37]. Astrophysical and cosmological constraints heavily restrict the allowed parameter space for such a model. Especially, λ has to be smaller than 10^{-7} [38]. Accordingly, $\langle s \rangle$ has to be very large to generate a μ in the required range. Such a model would thus be unsatisfactory for solving the μ-problem [35]. In the MSSM, the Peccei-Quinn symmetry is explicitly broken by the existence of the μ-term. In the NMSSM, an additional term $\frac{1}{3}\kappa S^3$, which breaks the Peccei-Quinn symmetry, is included into the superpotential. Here, κ is a dimensionless coupling strength. The massless axion is thus avoided. The superpotential then reads [35]:

$$W_{\text{NMSSM}} = \bar{u}\mathbf{y_u} Q H_u - \bar{d}\mathbf{y_d} Q H_d - \bar{e}\mathbf{y_e} L H_d + \lambda S H_u H_d + \frac{1}{3}\kappa S^3 \tag{2.62}$$

The unification of the different gauge couplings as in Fig. 2.7 is also valid for the NMSSM, if the model is perturbatively treatable up to the unification scale, i.e. λ and κ should be reasonably small at that scale [29].

However, the theoretical framework of the NMSSM gives rise to the so-called domain wall problem [39]. The model possesses a discrete Z_3 symmetry, i.e. observables are unchanged when the fields Φ are transformed as $\Phi \rightarrow e^{i2\pi/3}\Phi$. For this symmetry, there exist three separate but degenerate vacua. During the electroweak phase transition in the early universe, different causally separated parts of space could have acquired different vacuum states. These parts are separated by so-called domain walls. The existence of such domain walls would lead to large anisotropies in the cosmic microwave background, which are not in agreement with observation [40]. However, this problem can be solved by adding additional terms which explicitly break the Z_3 symmetry. These terms must obey certain conditions to keep the model consistent. Details can be found in the literature (see eg. Refs. [35, 41]). If these terms are suitably chosen, their effect on the low-energy phenomenology as described in this thesis is negligible [35]. For this reason, they are not taken into account in the following.

To summarize, the NMSSM is an appealing theory for the description of nature since it presents solutions to several problems of the Standard Model and the MSSM:

- It solves the hierarchy problem and the naturalness problem of the SM.
- It provides for a dark matter candidate.
- It allows for gauge coupling unification at the GUT-scale.
- It solves the μ-problem of MSSM.

On the other hand, the cosmological domain wall problem is introduced, but can solved by adding further terms to the model that do not affect the low-energy phenomenology.

2.3.1 The NMSSM Higgs sector

Symmetry breaking in the NMSSM is analogous to the MSSM. With the modified superpotential of Eq. 2.62, the Higgs potential is given by [35]:

$$\begin{aligned} V = &\frac{1}{8}\left(g^2+g'^2\right)\left(|H_d|^2-|H_u|^2\right)^2+\frac{1}{2}g^2|H_d^\dagger H_u|^2 \\ &+|\lambda S|^2\left(|H_d|^2+|H_u|^2\right)+|\lambda H_u H_d+\kappa S^2|^2+V_{Soft} \end{aligned} \tag{2.63}$$

with

$$V_{Soft}=m_{H_d}^2|H_d|^2+m_{H_u}^2|H_u|^2+m_{H_S}^2|S|^2+\left(\lambda A_\lambda S H_u H_d+\frac{1}{3}\kappa A_\kappa S^3+h.c.\right) \tag{2.64}$$

A_λ and A_κ are trilinear, supersymmetry breaking coupling parameters of the dimension of a mass. By convention, the parameters λ, κ, A_λ and A_κ are chosen to be real.

After symmetry breaking, the two Higgs fields gain vacuum expectation values v_1 and v_2 as in the MSSM. Moreover, the bosonic component of S also gains a vacuum expectation value

$$\langle s\rangle=\frac{1}{\sqrt{2}}v_s \tag{2.65}$$

The expressions for the mixing of the component fields to the mass eigenstates of the neutral Higgs bosons are relatively lengthy and are thus not explicitly given here. More details can be found eg. in Ref. [35]. Also exact expressions for the Higgs boson masses in the NMSSM are partly very complex. Approximations for the Born level masses of the neutral Higgs bosons are given by [35]:

$$\begin{aligned} M_{H_{2/1}}^2 \approx\ & \frac{1}{2}M_Z^2+\frac{1}{4}\kappa v_s(4\kappa v_s+\sqrt{2}A_\kappa) \\ & \pm\frac{1}{2}\sqrt{\left(M_Z^2-\frac{1}{2}\kappa v_s(4\kappa v_s+\sqrt{2}A_\kappa)\right)^2+\cot^2\beta_s\left(2\lambda^2v_s^2-M_A^2\sin^2 2\beta\right)^2} \end{aligned} \tag{2.66}$$

$$M_{H_3}^2 \approx M_A^2\left(1+\frac{1}{4}\cot^2\beta_s\sin^2 2\beta\right) \tag{2.67}$$

$$M_{A_1}^2 \approx -\frac{3}{\sqrt{2}}\kappa v_s A_\kappa \tag{2.68}$$

$$M_{A_2}^2 \approx M_A^2\left(1+\frac{1}{4}\cot^2\beta_s\sin^2 2\beta\right) \tag{2.69}$$

Here, β_s is defined by the relation $\tan\beta_s=v_s/\sqrt{v_1^2+v_2^2}$. M_A is given by

$$M_A^2=\frac{\lambda v_s}{\sin 2\beta}\left(\sqrt{2}A_\lambda+\kappa v_s\right). \tag{2.70}$$

Since there is no additional mixing of the charged Higgs bosons, the exact expression for heir mass can be given more easily:

$$M_{H^\pm}^2=M_A^2+M_W^2-\frac{1}{2}\lambda^2\left(v_1^2+v_2^2\right) \tag{2.71}$$

The above Born level mass equations are then modified by radiative corrections. In the NMSSM, the pseudoscalar A_1 can be significantly lighter than the lightest scalar. Therefore, $H_1 \rightarrow A_1 A_1$

decays are possible in some parts of the parameter space [42].

The Born level bound on the mass of the lightest scalar NMSSM Higgs boson is given by:

$$M_{H_1}^2 \leq M_Z^2 \left(\cos^2 2\beta + \frac{2\lambda^2 \sin^2 2\beta}{g^2 + g'^2} \right) \tag{2.72}$$

The largest H_1 masses are obtained for small $\tan\beta \approx 1 - 2$. Including radiative corrections, the mass should be smaller than about 145 GeV [43].

At Born level, the pure singlet states have no couplings to the gauge bosons and fermions of the Standard Model. The couplings of the neutral Higgs bosons are basically given by the expressions of the MSSM multiplied with a 'dilution factor' which describes the admixed fraction of the singlet state. Although a Standard Model Higgs boson with mass below 114.4 GeV is ruled out by the LEP experiments, lighter Higgs bosons of other models are still allowed if their couplings to the Z boson are reduced. The couplings of the charged Higgs bosons to the known gauge bosons and fermions are at Born level identical to the MSSM couplings. However, the Higgs boson couplings to sparticles may be modified by terms that depend on λ and κ.

In the NMSSM, the Higgs sector can at Born level be described by six parameters. Usually, the first four parameters are chosen to be the newly introduced coupling parameters. While λ and κ are dimensionless Yukawa couplings of the gauge singlet field, A_λ and A_κ describe the trilinear couplings and have the dimension of a mass. Moreover, usually μ and $\tan\beta$, which is defined as in the MSSM, are chosen as free parameters.

If λ and κ approach zero and A_λ and A_κ are not arbitrarily large, the interactions of the singlet field with the MSSM Higgs fields vanish. Then, no mixing between the Higgs fields and the singlet field takes place, i.e. the singlet field decouples. The decoupled singlet field itself has no gauge couplings. If it does not mix nor interact with the Higgs fields, its bosonic component has no influence on the observable phenomenology. In this so-called decoupling limit, the MSSM phenomenology is fully retrieved in the Higgs sector. However, in some cases, the distinction of the two models still might be possible via the neutralino sector [44].

2.3.2 The constrained NMSSM

The unconstrained NMSSM as described above possesses a large number of free, unmeasured parameters, including the various mass parameters for gauginos, Higgs bosons and sfermions as well as the six parameters of the Higgs sector. However, some mechanisms for supersymmetry breaking predict a unification of the soft supersymmetry breaking parameters at the GUT scale. Such unification conditions significantly reduce the number of free parameters. For the MSSM, the widely studied mSUGRA[9] scenario is an example for such a theory [45]. Here, the gaugino masses, the scalar masses and the trilinear couplings are unified at the GUT scale. Similarly, it is also possible to build a corresponding model for the NMSSM [46].

This model then should have unified gaugino masses $M_{1/2}$, unified scalar masses m_0 and unified trilinear couplings A_0 at the GUT scale:

$$M_{1,2,3} \equiv M_{1/2}, \qquad m_{\tilde{f}_i} = m_{H_i} = m_S \equiv m_0, \qquad A_\tau = A_t = A_b = A_\lambda = A_\kappa \equiv A_0 \tag{2.73}$$

These supersymmetry breaking parameters can then be evolved to the supersymmetric scale via the renormalization group equations.

However, Ref. [47] argues that the Higgs sector of this fully constrained NMSSM has very

[9] mSUGRA means minimal supergravity. The theory includes the graviton and its supersymmetric partner, the gravitino. Supersymmetry breaking is mediated from a hidden sector to the supersymmetry sector by gravity.

much resemblance to constrained MSSM models in the unexcluded parameter region. Therefore, a relaxation of the complete unification is proposed, allowing for $m_S^2 \neq m_0^2$ and $A_\kappa \neq A_0$:

$$M_{1,2,3} \equiv M_{1/2}, \qquad m_{\tilde{f}_i} = m_{H_i} \equiv m_0, \qquad A_\tau = A_t = A_b = A_\lambda \equiv A_0 \tag{2.74}$$

This can be motivated by the possibility that the singlet sector could be of special origin[10]. Details can be found in the literature. Then, also regions with $H_1 \rightarrow A_1 A_1$ decays are contained in the model, that is in this thesis referred to as the constrained NMSSM (cNMSSM). It only depends on the six unmeasured parameters λ, $\tan\beta$, A_κ, A_0, M_0 and $M_{1/2}$. Moreover, the sign of μ can be chosen freely.

Many theorists favor the cNMSSM over the unconstrained case as a small number of free parameters is generally desirable for a fundamental theory.

[10] Also for the MSSM, models with relaxed unification requirements exist, see eg. Ref. [48].

3. The experiment

In this chapter, the experimental setting of this thesis is presented. At first, a brief overview of the Large Hadron Collider [4] is given. Afterwards, the ATLAS ('A Toroidal LHC Apparatus') detector and its components is reviewed, based on the very detailed description in Ref. [6]. In the last part, the basic principles of the Monte Carlo simulation of high-energy particle interactions are explained.

3.1 The Large Hadron Collider

The Large Hadron Collider (LHC) is a proton-proton collider which is currently being built at CERN[1], the European laboratory for particle physics. It is constructed inside the tunnel formerly used for the LEP accelerator with a circumference of about 27 km. In this ring, two proton beams containing 2808 bunches of up to $1.1 \cdot 10^{11}$ protons will circulate in opposite directions and collide with a center-of-mass energy of 14 TeV about 40 million times per second. First collisions at the LHC are expected for 2008. At first, the LHC will be run at a luminosity of $2 \cdot 10^{33}\mathrm{cm}^{-2}\mathrm{s}^{-1}$ during the so-called low luminosity phase, and will later go on to its design luminosity of $10^{34}\mathrm{cm}^{-2}\mathrm{s}^{-1}$. Such high interaction rates are needed because the rates of many physically interesting processes are expected to be small. For the low luminosity phase, about five collisions, for the design luminosity phase, about 25 collisions per bunch crossing are expected. Additionally, it is planned to collide heavy ions, particularly lead nuclei, at a center-of-mass energy of 5.5 TeV per nucleon pair at a luminosity of $10^{27}\mathrm{cm}^{-2}\mathrm{s}^{-1}$.

To accelerate protons up to energies of 7 TeV, the existing accelerator facilities at CERN, that consist of the Linac, the Booster, the Proton Synchrotron (PS) and the Super Proton Synchrotron (SPS) (Fig. 3.1) are used. Initially, the protons are obtained from a hydrogen source and are then accelerated up to energies of 50 MeV in the Linac. Afterwards, they are successively accelerated to higher energies of 1.4 GeV in the Booster, 25 GeV in the PS and 450 GeV in the SPS. Then they are injected into the LHC ring where they reach their final energy.

For particle acceleration in the LHC ring, eight superconducting RF-cavities per beam are used as they provide large accelerating fields with minimal energy loss. Each cavity provides 2 MV of acceleration voltage, summing up to a total 16 MV per beam. The cavities operate at 400 MHz, which is the second harmonic of the SPS frequency. The bunch spacing is 25 ns or about 7 m, which corresponds to ten RF periods. The cavities are operated at a temperature of 4.5 K.

As two beams of particles with the same charge are accelerated in opposite directions, two independent magnet channels are required. These share the same yoke and cryostat system. To achieve the necessary bending power to keep the proton beams on track, superconducting magnets are utilized. In total, 9593 magnets, among them 1232 dipole magnets made from copper-clad niobium-titanium cables with a peak field of 8.33 T, make up the magnet system. The superconducting magnets are operated at a temperature of 1.9 K. Such low temperatures are obtained by cooling with superfluid helium. For thermal insulation, the magnets are placed

[1] Conseil Europeén pour la Recherche Nucléaire

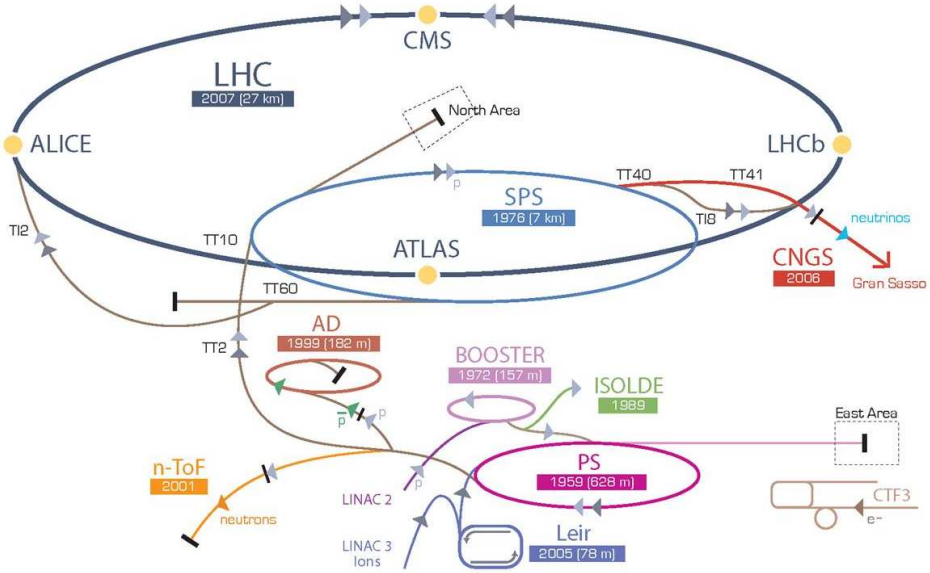

Fig. 3.1: The CERN accelerator system. The LHC ist the last ring in a complex chain of particle accelerators. The LINAC-Booster complex, PS and SPS are used to for pre-acceleration of protons that are afterwards injected into the LHC ring. Other accelerator facilities are the Antiproton Decelerator (AD), the Clic Test Facility (CTF3), the CERN Neutrinos to Gran Sasso (CNGS) experiment, the Isotope Separator Online Device (Isolde), the Low Energy Ion Ring (Leir), and the Neutrons Time-of Flight experiment (n-ToF).

inside a vacuum vessel. The superconducting current of the dipoles is 11700 A.

Also the beam pipe is evacuated to an ultra-high vacuum with a pressure of only 10^{-13} atm to avoid collisions of the proton bunches with residual gas molecules.

At the four interaction points at the LHC ring, the experiments LHCb [49], ALICE [50], ATLAS [5, 6] and CMS [7] are located. While LHCb and ALICE focus on the specific topics of b-physics and heavy ion physics, ATLAS and CMS are multi-purpose detectors that were designed to explore a wide range of physics at the LHC. This thesis has been carried out using simulations for the ATLAS experiment.

3.2 The ATLAS detector

ATLAS is one of the two multi-purpose experiments at the LHC. The detector is sketched in Fig. 3.2. As typical for detectors in high-energy physics, it has a cylindrical symmetry with different subsystems positioned in layers around the interaction point. In total, the detector has a diameter of 22 m, a length of 42 m and weighs approximately 7000 tons.

To cope with the huge event rates at the LHC and to disentangle rare events containing interesting physics from the overwhelmingly large QCD background processes, a reliable identification and precise measurement of muons, electrons, photons and jets from b-quarks and from τ-leptons are required. Also a good measurement of the escaped momentum from non-interacting particles such as neutrinos or neutralinos, commonly referred to as 'missing momentum', is needed. To meet these aims, the ATLAS detector has to provide for:

- an efficient tracking system for a good momentum resolution of charged particles and for the observation of secondary vertices,

Detector component	Required resolution	η coverage	
		Measurement	Trigger
Tracking	$\sigma_{p_T}/p_T = 0.05\% p_T \oplus 1\%$	± 2.5	-
EM calorimetry	$\sigma_E/E = 10\%\sqrt{E} \oplus 0.7\%$	± 3.2	± 2.5
Hadron calorimetry			
barrel & end-cap	$\sigma_E/E = 50\%\sqrt{E} \oplus 3\%$	± 3.2	± 3.2
forward	$\sigma_E/E = 100\%\sqrt{E} \oplus 10\%$	$3.1 < \eta < 4.9$	$3.1 < \eta < 4.9$
Muon Spectrometer	$\sigma_{p_T}/p_T = 10\%$ at $p_T = 1$ TeV	± 2.7	± 2.4

Tab. 3.1: General performance goals of the ATLAS detector. The unit for p_T and E is 'GeV'.

- a very good electromagnetic calorimetry system for the measurement of photons and electrons,
- a large acceptance in pseudorapidity and an almost full azimuthal coverage of the calorimeters for a correct measurement of particle showers and of the missing momentum,
- an excellent muon system
- and a highly efficient trigger and data acquisition system.

An overview of the performance goals of the ATLAS detector is shown in Tab. 3.1. In the following, the coordinate system used to describe the highly relativistic particles at the ATLAS experiment is briefly reviewed. Then, an overview of the most important detector components and their working principles is given.

3.2.1 Coordinate system

The ATLAS detector uses a cartesian, right handed coordinate system. The z-axis is defined by the beam direction. The x- and y-axes accordingly lie in the plane perpendicular to the beam pipe. The positive x-axis is defined as pointing from the interaction point to the center of the LHC ring, whereas the positive y-axis points upwards.

Due to a better practicability, the position of particles in the detector is commonly not given by x-, y- and z-coordinates, but in terms of the azimuthal angle ϕ, which describes the direction in the plane perpendicular to the beam pipe, and the pseudorapidity η. The pseudorapidity is given by the polar angle θ between the beam pipe and the direction of flight of the particle:

$$\eta = -\ln \tan \frac{\theta}{2}. \tag{3.1}$$

It has the advantage that differences of the pseudorapidity are invariant under a Lorentz boost along the beam axis. Since in a hadron collision, only the center-of-mass energy of the entire hadron, but not of the interacting partons is known, events generally have an unknown Lorentz boost in z-direction parallel to the beam pipe. However, the momenta perpendicular to the beam pipe should be balanced. For this reason, at hadron colliders, often the transverse momentum

$$p_T = \sqrt{p_x^2 + p_y^2} \tag{3.2}$$

is used[2], since it only takes into account the momentum components which are unaffected by the unknown boost. For the same reason, only the missing transverse momentum, but not the total missing momentum can be measured, as the escaped momentum in z-direction is unknown.

[2] Since energy depositions are measured in the calorimeters, often also the analoguely defined transverse energy (E_T, E_{Tmiss}) is used.

	Pixel	**SCT**	**TRT**
Pseudorapidity range	$\|\eta\| < 2.5$	$\|\eta\| < 2.5$	$\|\eta\| <\sim 2.0$
Radial extension [mm]	45.5<R<242	251<R<610	554<R<1106
Intrinsic accuracy (barrel)	Rϕ: 10µm, z: 115µm	Rϕ: 17µm, z: 580µm	Rϕ: 130µm per straw
Intrinsic accuracy (end-caps)	Rϕ: 10µm, R: 115µm	Rϕ: 17µm, R: 580µm	Rϕ: 130µm per straw
Read-out channels	$80.4 \cdot 10^6$	$6.3 \cdot 10^6$	$0.351 \cdot 10^6$

Tab. 3.2: Characteristic parameters of the components of the Inner Detector.

3.2.2 The Inner Detector

The purpose of the Inner Detector is the exact identification of the tracks of charged particles close to the interaction point. The cavity of the Inner Detector is surrounded by a superconducting solenoid magnet. The bending of the directions of flight of charged particles in the field of 2 T allows for a measurement of their momentum and charge.

The main challenge of track finding in the LHC environment is the large expected track density. Every 25 ns, about 1000 particles produced in the collisions will traverse the Inner Detector [6]. The precision of the track finding should be sufficient for the identification of secondary vertices, which is crucial for b-tagging. For this, a fine detector granularity is needed.

The ATLAS tracking system consists of the Pixel Detector, the Silicon Microstrip Detector and the Transition Radiation Tracker (Fig. 3.3). An overview of the main parameters of these three detector components is given in Tab. 3.2.

The Pixel Detector

The Pixel Detector is the innermost detector component and has the highest spatial resolution of the three components of the tracking system (see Tab. 3.2). It consists of 1744 pixel modules that have 47232 pixels each[3]. In total, the Pixel Detector has about 80.4 million read-out channels.

In principle, each pixel cell acts like a reverse-biased diode. When a charged particle traverses the depleted silicon material, it creates ionization charges that are collected by the electric field and can then be read-out. The read-out chip is connected via bump-bonding to each pixel cell.

The Pixel Detector covers the pseudorapidity range $|\eta| < 2.5$. In the barrel region, the pixel modules are arranged in three concentric cylinders around the beam axis, and in each end-cap region in three pixel disks perpendicular to the beam. Typically, three pixel layers are crossed by each track, so that the pixel system provides for three high-precision hits in close proximity to the interaction point. This is crucial for the b-tagging performance.

The Silicon Microstrip Tracker (SCT)

The next component of the Inner Detector is the Silicon Microstrip Tracker (SCT). Its working principle is similar to the Pixel Detector. In the barrel region, it consists of four layers, in the

[3] For reasons of space, eight pixels in each column of the front-end chip are connected to only four read-out channels ('ganged pixels'), thus leading to a total of 46080 read-out channels.

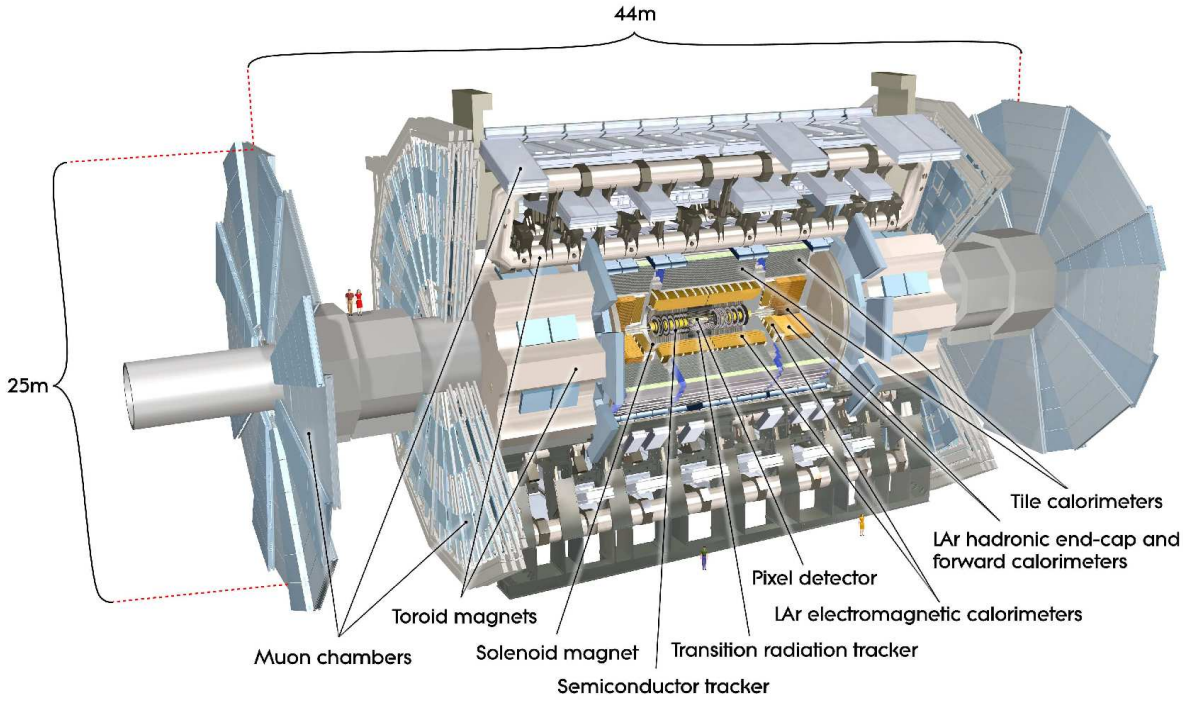

Fig. 3.2: Cut-away view of the ATLAS detector.

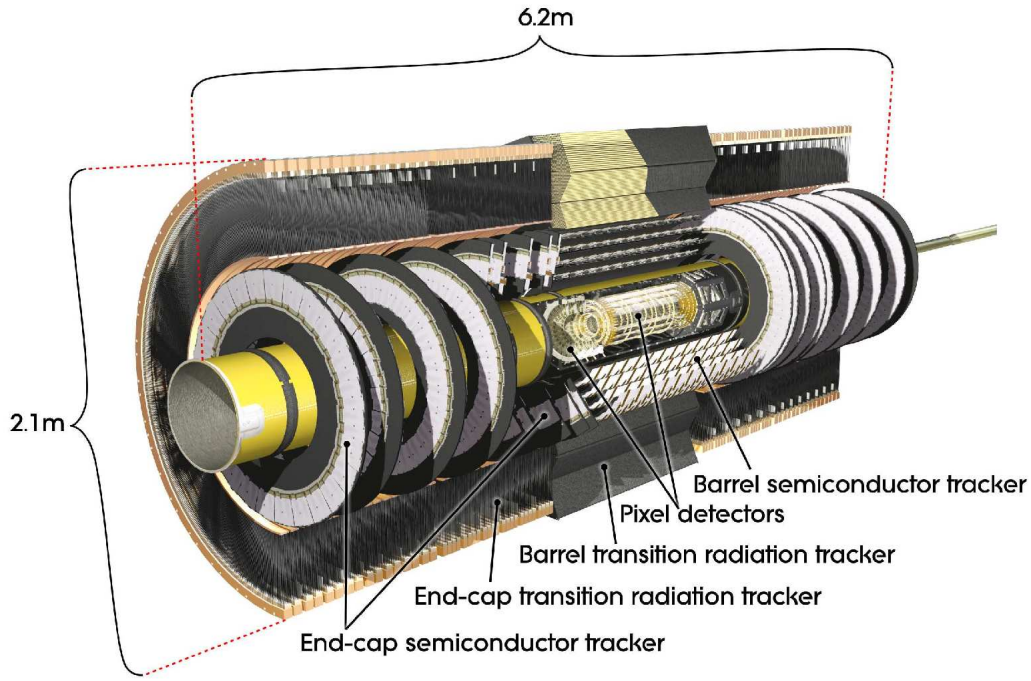

Fig. 3.3: Cut-away view of the ATLAS Inner Detector.

end-cap regions of nine wheels. Also the SCT covers the pseudorapidity range $|\eta| < 2.5$. In total, 15912 sensors with 768 strips of 12 cm length are used. In each layer and wheel, the silicon microstrips are arranged in two joint sets. In the barrel, the first set runs parallel to the beam axis, in the end-cap region, it runs radially, for a measurement of Rϕ. The second set is nearly parallel to the first set but with a small angle of $\sim$40 mrad between them. This geometry makes it possible to also measure the z-coordinate in the barrel and the radial coordinate in the end-cap, even though no pixels, but strips are used. A charged particle traversing the SCT typically hits eight silicon strips. Thus, four track points are measured.

To avoid a large increase of the noise levels after irradiation of the detector, the silicon systems of the ATLAS tracker, i.e. the Pixel Detector and the SCT, are run at a low temperature of about -5°C to -10°C.

The Transition Radiation Tracker (TRT)

In total, seven high-precision hits per track can be obtained by the silicon detectors. Because more silicon layers would cause a degradation of the spatial resolution due to multiple scattering and would also be cost-intensive, additional track points are measured by a cost-efficient system with low material budget. This system is the Transition Radiation Tracker (TRT). It consist of straw tubes of 4 mm diameter that are filled with a gas mixture of 70% Xe, 27% CO_2 and 3% O_2 with 5-10 mbar over-pressure. The sensitive element that measures the ionization charges created by charged particles traversing the gas mixture is a gold-plated tungsten wire.

Additionally, there are varying dielectric boundaries between the straw tubes. When an electron enters this material, it produces transition radiation that can be detected in the xenon-based gas mixture of the straw tubes. This enhances the electron identification capabilities of the ATLAS detector in the region $|\eta| < 2.0$.

In the barrel region, the straw tubes are arranged parallel to the beam axis and have a length of 144 cm, with their wires divided into two halves. In the end-cap region, the tubes are 37 cm long and are arranged radially in wheels. Depending on the position of a track in the detector, on average additional 36 hits per track are provided by the TRT.

3.2.3 The calorimeters

When hadrons, photons or electrons enter a dense material, they create showers of particles with decreasing energy due to bremsstrahlung, pair creation processes, interactions with nuclei, decays of unstable particles etc. For thick enough absorber materials, the energy of the initial particle is deposited completely in the material. This is exploited in the calorimeters for the precise measurement of the energy and position of photons, electrons and hadronic jets as well as the measurement of the missing transverse momentum. The measurement takes place active material, where a fraction of the deposited energy is transformed into a measurable signal proportional to the initial energy. Active material and absorbers are typically positioned in an alternating manner to allow for a measurement of the shower in different stages.

In ATLAS, the Electromagnetic Calorimeter covers the range $|\eta| < 3.2$. The Hadron Calorimeter has two distinct parts, the central Tile Calorimeter at $|\eta| < 1.7$, and the End-cap Calorimeter at $1.5 < |\eta| < 3.2$. The forward detector region with $3.1 < |\eta| < 4.9$ is covered by the Forward Calorimeter. A sketch of the calorimeters is shown in Fig. 3.4. An overview of the calorimeter parts, the number of their longitudinal layer and their η-coverage is given in Tab. 3.3. The granularity depending on calorimeter type, layer and pseudorapidity is listed in Tab. 3.4.

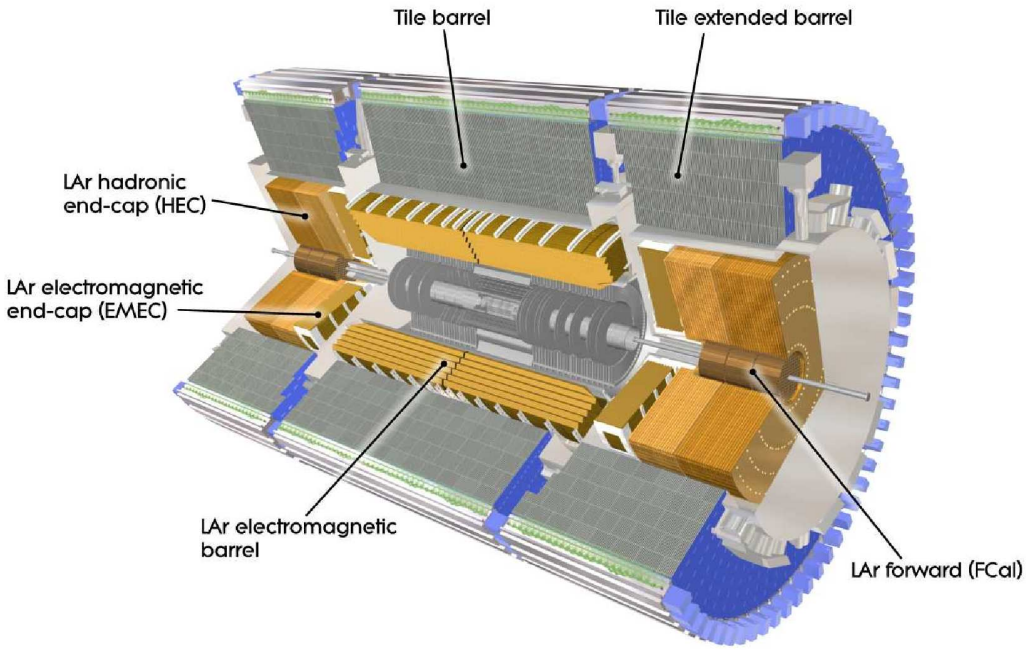

Fig. 3.4: Cut-away view of the ATLAS calorimeter system.

The Electromagnetic Calorimeter

As the radiation lengths of electromagnetically interacting particles are smaller than the interaction lengths of hadrons, the development of electromagnetic showers from photons and electrons takes place earlier in the calorimeter than the development of hadronic showers. Therefore, electromagnetic showers are typically fully contained in the Electromagnetic Calorimeter, which is placed closer to the interaction point than the Hadronic Calorimeters.

The Electromagnetic Calorimeter of the ATLAS experiment uses liquid argon (LAr) as active material. The particles from the shower ionize the liquid argon. Thus, free electrons are created, which are transferred to the kapton electrodes with the help of a strong electric field. The electrodes are placed on an accordion-like structure which allows for complete calorimeter coverage without any gaps or cracks. The absorber material is lead. The lead thickness in the absorber plates has been optimized depending on η with regard to an optimal energy resolution in the calorimeter.

The Electromagnetic Calorimeter is divided into the barrel part at $|\eta| < 1.475$ and two endcap parts at $1.375 < |\eta| < 3.2$. All parts consist of two or three longitudinal layers depending on η (see Tab. 3.3). In the region where the Electromagnetic Calorimeter is behind the Inner Detector ($|\eta| < 2.5$), it has a very fine granularity (see Tab. 3.4) ideally suited for the precision measurement of electrons and photons. The coarser granularity in the rest of the electromagnetic calorimeter is sufficient for jet reconstruction and missing momentum measurement.

In the central region with $|\eta| < 1.8$, the electromagnetic calorimeter is preceded by a presampler, which consists of an additional active LAr layer, to correct for the energy loss in the preceding solenoid magnet and the cryostat.

Calorimeter part	Layers	η-coverage
Presampler barrel	1	$\lvert\eta\rvert < 1.52$
Presampler end-cap	1	$1.5 < \lvert\eta\rvert < 1.8$
EM barrel	3	$\lvert\eta\rvert < 1.35$
	2	$1.35 < \lvert\eta\rvert < 1.475$
EM end-cap	2	$1.375 < \lvert\eta\rvert < 1.5$
	3	$1.5 < \lvert\eta\rvert < 2.5$
	2	$2.5 < \lvert\eta\rvert < 3.2$
Tile barrel	3	$\lvert\eta\rvert < 1.0$
Tile extended barrel	3	$0.8 < \lvert\eta\rvert < 1.7$
LAr hadronic End-cap	4	$1.5 < \lvert\eta\rvert < 3.2$
LAr forward	3	$3.1 < \lvert\eta\rvert < 4.9$

Tab. 3.3: Pseudorapidity coverage and number of longitudinal layers of the calorimeter subsystems.

The Hadron Calorimeters

The Hadron Calorimeters are placed at larger radii than the Electromagnetic Calorimeter. Together with the Electromagnetic Calorimeter, they are used for the measurement of hadronic showers and the missing momentum.

The central part of the ATLAS Hadron Calorimeters is the so-called Hadronic Tile Calorimeter which is divided into a barrel and an extended barrel part. It is made of plastic scintillator plates, the so-called tiles, that are used for the measurement of the energy deposition. Steel absorbers are used to ensure a good development of the showers. Particles that traverse the scintillators excite the atoms in the scintillator material which then emit light. This light is read out with the help of wavelength shifting fibers, transferred to photomultipliers and then transformed into an electric signal.

In the end-cap region, also the Hadronic End-cap Calorimeter (HEC) is built from liquid argon, as here, a larger radiation density is expected, and the liquid argon has a larger radiation hardness than the plastic scintillators. Copper plates are used as absorbers. The Hadronic End-cap Calorimeter slightly overlaps in η with the Tile Calorimeter and Forward Calorimeter for a better coverage of the transition regions.

The Forward Calorimeter

The Forward Calorimeter (FCal) is integrated in the end-cap cryostats. Since the expected radiation level in the forward region of the detector is high, the active material of the ATLAS Forward Calorimeter was chosen to be liquid argon for reasons of radiation hardness. It consists of three modules in each end-cap: the first module, which is closest to the interaction point, uses copper, which is optimal for heat removal, as an absorber and is optimized for the measurement of electromagnetic showers, the second and third module are made of tungsten and were designed to measure predominantly hadronic showers. Tungsten was chosen here as it is very dense and can thus guarantee that the showers are fully contained in the calorimeter.

In each module, there is a metal matrix with regularly spaced longitudinal channels, in which the electrodes which are made of concentric rods and tubes parallel to the beam axis are located. The LAr is filled in the gap between the rod and the tube.

Unlike the other calorimeter types, the granularity of the Forward Calorimeter is not chosen within a $\Delta\eta \times \Delta\phi$, but within a Δx $\times$ Δy grid (see Tab. 3.4). This translates into a varying,

Calorimeter part	**Granularity**	**η-range**
Granularity in $\Delta\eta \times \Delta\phi$		
Presampler barrel	0.025×0.1	$\lvert\eta\rvert < 1.52$
Presampler end-cap	0.025×0.1	$1.5 < \lvert\eta\rvert < 1.8$
EM barrel, 1st layer	$0.025/8 \times 0.1$	$\lvert\eta\rvert < 1.4$
	0.025×0.025	$1.4 < \lvert\eta\rvert < 1.475$
EM barrel, 2nd layer	0.025×0.025	$\lvert\eta\rvert < 1.4$
	0.075×0.025	$1.4 < \lvert\eta\rvert < 1.475$
EM barrel, 3rd layer	0.050×0.025	$\lvert\eta\rvert < 1.35$
EM end-cap, 1st layer	0.050×0.1	$1.375 < \lvert\eta\rvert < 1.425$
	0.025×0.1	$1.425 < \lvert\eta\rvert < 1.5$
	$0.025/8 \times 0.1$	$1.5 < \lvert\eta\rvert < 1.8$
	$0.025/6 \times 0.1$	$1.8 < \lvert\eta\rvert < 2.0$
	$0.025/4 \times 0.1$	$2.0 < \lvert\eta\rvert < 2.4$
	0.025×0.1	$2.4 < \lvert\eta\rvert < 2.5$
	0.1×0.1	$2.5 < \lvert\eta\rvert < 3.2$
EM end-cap, 2nd layer	0.050×0.025	$1.375 < \lvert\eta\rvert < 1.425$
	0.025×0.025	$1.425 < \lvert\eta\rvert < 2.5$
	0.1×0.1	$2.5 < \lvert\eta\rvert < 3.2$
EM end-cap, 3rd layer	0.050×0.025	$1.5 < \lvert\eta\rvert < 2.5$
Tile barrel, 1st & 2nd layer	0.1×0.1	$\lvert\eta\rvert < 1.0$
Tile barrel, 3rd layer	0.2×0.1	$\lvert\eta\rvert < 1.0$
Tile extended barrel, 1st & 2nd layer	0.1×0.1	$0.8 < \lvert\eta\rvert < 1.7$
Tile extended barrel, 3rd layer	0.2×0.1	$0.8 < \lvert\eta\rvert < 1.7$
LAr hadronic end-cap	0.1×0.1	$1.5 < \lvert\eta\rvert < 2.5$
LAr hadronic end-cap	0.2×0.2	$2.5 < \lvert\eta\rvert < 3.2$
Granularity in Δx $\times$ Δy (cm)		
FCAl1	3.0×2.6	$3.15 < \lvert\eta\rvert < 4.30$
	$\sim 4\times$ finer	$3.10 < \lvert\eta\rvert < 3.15$
		$4.30 < \lvert\eta\rvert < 4.83$
FCAl2	3.3×4.2	$3.24 < \lvert\eta\rvert < 4.50$
	$\sim 4\times$ finer	$3.20 < \lvert\eta\rvert < 3.24$
		$4.50 < \lvert\eta\rvert < 4.82$
FCAl3	5.4×4.7	$3.32 < \lvert\eta\rvert < 4.60$
	$\sim 4\times$ finer	$3.29 < \lvert\eta\rvert < 3.32$
		$4.60 < \lvert\eta\rvert < 4.75$

Tab. 3.4: Granularity of the different calorimeter sub-systems depending on η-range.

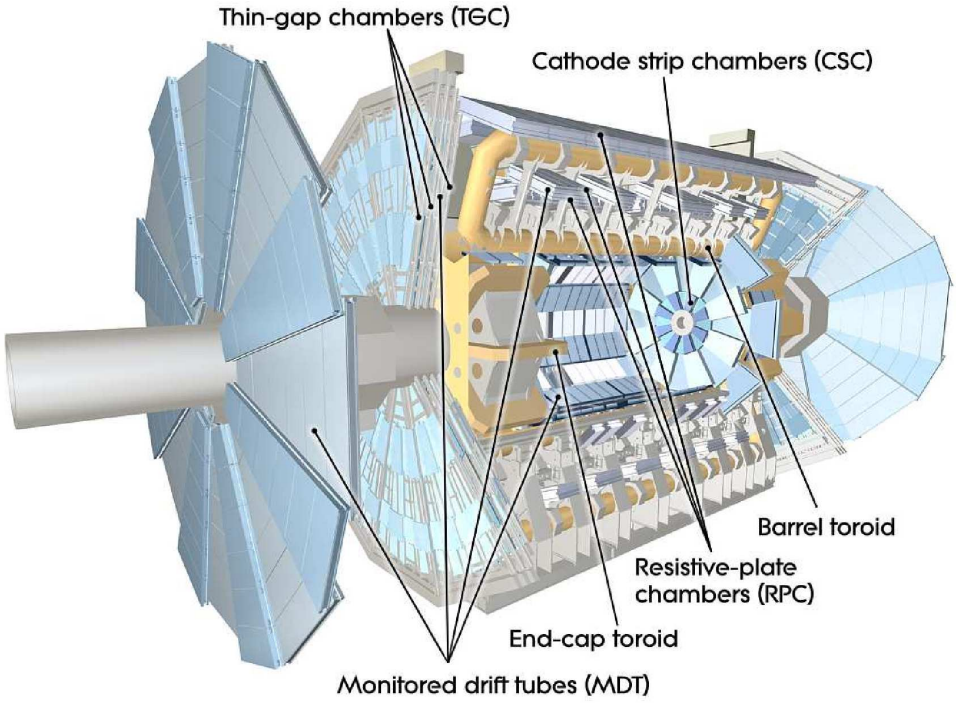

Fig. 3.5: Cut-away view of the ATLAS muon system.

complex and sometimes rather coarse granularity structure ($\sim 0.2 \times 0.2$) in $\Delta\eta \times \Delta\phi$ units.

3.2.4 The Muon Spectrometer

The Muon Spectrometer is designed for the identification and momentum measurement of muons. The muons interact only minimally with the calorimeter material. Therefore, they are the only particle type that routinely traverses the entire calorimeter system and reaches the Muon Spectrometer which is the outermost part of the ATLAS detector.

A special feature of the ATLAS muon system is three superconducting air-core toroid magnets arranged with eightfold azimuthal symmetry around the calorimeters. The large barrel toroid magnet bends the muon tracks in the central region with $|\eta| < 1.4$. Tracks with $1.6 < |\eta| < 2.7$ are bent by two smaller end-cap toroids. In the transition region between the barrel and end-cap magnets, there is a combination of fields originating from the barrel and the end-cap toroids. This magnet configuration provides a field which is mostly orthogonal to the muon trajectories and minimizes the traversed material and thus the degradation of the resolution due to multiple scattering. This concept for the magnet system was one of the major design choices for the ATLAS detector and also gave it its name ('toroidal').

The Muon Spectrometer consists of two parts: the Muon Precision Tracking System and the Muon Trigger System. In the barrel region, the Muon Spectrometer consists of three cylindrical layers around the beam axis, and of three layers each in the end-cap region. A sketch of the ATLAS muon system is shown in Fig. 3.5.

The Muon Precision Tracking System

The precision measurement of muon tracks is performed by the Muon Precision Tracking System. It consists of two types of chambers, the Monitored Drift Tubes (MDT), and the Cathode Strip Chambers (CSC).

The MDTs with a diameter of 3 cm cover most of the η-range. They consist of tubes that are filled with a gas mixture of 93% Ar and 7% CO_2. Electrons resulting from the ionization of the gas are collected by a central tungsten-rhenium wire.

In the innermost layer in the region $2 < |\eta| < 2.7$, large event rates put high demands on the muon detectors. As the MDTs cannot be used here, CSCs are chosen instead. These are multiwire proportional chambers with their cathodes segmented into strips.

The Muon Trigger System

The Muon Trigger System in the pseudorapidity range $|\eta| < 2.4$ is able to deliver track information within a few tens of nanoseconds after the passage of the muon. It is made of Resistive Plate Chambers (RPC) in the barrel and Thin Gap Chambers (TGC) in the end-cap regions. Apart from triggering, these chambers also provide for bunch crossing information and measure the track coordinate in the direction perpendicular to the bending plane of the magnet system measured by the Muon Precision Tracking System.

3.2.5 Trigger and data acquisition

The proton bunches at the LHC cross at a rate of 40 MHz. In the design luminosity phase, about 25 inelastic collisions per bunch crossing are expected, leading to an expected interaction rate of about 1 GHz. However, technology and resource limitations restrict the recordable data rate to about 200 Hz. To ensure that the recorded data contain a large fraction of interesting physics events, an efficient trigger system is required. To achieve this goal, triggering in ATLAS is done in three steps. Each trigger level imposes harder requirements on the event and thus refines the trigger decision:

- The Level-1 Trigger uses the Muon Trigger System and reduced granularity information from all calorimeters to look for high-p_T muons, electrons, photons and jets as well as for large missing momentum and large total transverse momentum. The decision if an event is kept is made in less than 2.5 µs. If interesting objects are identified in an event, the Level-1 Trigger defines a 'region of interest', the information on which is passed on to the next trigger step. Thus, the event rate is reduced to about 75 kHz.

- The Level-2 Trigger uses all available detector data on the regions of interest it receives from the Level-1 Trigger, which is about 2% of the total event data. It reduces the event rate to about 3.5 kHz with a processing time of approximately 40 ms.

- The Event Filter is the final stage of the ATLAS trigger. It uses algorithms similar to the offline analysis concepts. The time needed for the final trigger decision is about four seconds, the final event rate about 200 Hz. Selected events have an average size of about 1.5 MByte.

The Level-2 Trigger and Event Filter are jointly referred to as the High Level Trigger.

The data acquisition is based on sub-detector specific front-end systems. These include buffers in which the data from all events is stored until the Level-1 Trigger decision is taken. After an event is accepted, the event data is sent to the following level of the read-out chain with the help of the Read-out Drivers, that collect and multiplex data from several front-end data streams. In the first stage of the Data Acquisition System, the event data is temporarily stored in local buffers until the Level-2 Trigger decision is taken. Afterwards, selected events are transferred to the Event Filter and, if accepted, written to permanent storage. Furthermore, the Data Acquisition System allows for configuration, control and monitoring of the hardware and software components used in the data taking.

3.3 Monte Carlo Simulation

As measured data from the LHC is not yet available, this work was carried out with the help of Monte Carlo simulations of interactions in proton-proton collisions. The production of Monte Carlo samples is generally performed in several steps:

- At first, the so-called hard interaction, i.e. the process of interest[4], is generated from the matrix element, which describes the probability of an interaction in dependence on the momenta and energies of the interacting particles. The actual probability of momentum and energy of the incoming particle is given by parton distribution functions. The phase space can be restricted by generator cuts to the relevant regions to save computing time. Commonly, the events are assigned a weight in the generation process which describes the probability of their phase space point. To obtain unweighted events, each event is either rejected or kept for the final Monte Carlo sample with the probability given by its weight.

- After the generation of the hard interaction, additional interactions of the same proton collision (underlying event) are added to the event. Such interactions can be parameterized according to different models. In some cases, also pile-up, i.e. interactions from other proton-proton collisions than the hard event, which might also arise from an earlier or later bunch crossing, are added. Moreover, the decays of unstable particles, the parton shower, initial and final state radiation and the hadronization are performed. After this step, the event generation is finished. In this thesis, particles from the event generation step will be referred to as 'truth particles' or 'true particles'. Event generators commonly used are Pythia [51] and Herwig [52].

- Then, the interaction of the generated particles with the ATLAS detector is simulated. This includes eg. hits in the Inner Detector and the muon chambers and the showering and energy deposition in the calorimeters.

- At last, the signals from the detector are reconstructed to obtain a description of physical objects such as electrons, muons, photons or jets. For this aim, clustering of the energy depositions in the calorimeter, jet- and track finding as well as the lepton identification and the calculation of the missing transverse momentum are performed.

- Often, a filter that selects only interesting events for storage is applied. This is not obligatory, but helps to reduce the number of events which have to be processed and thus to minimize computing times and required storage.

Currently, two validated approaches for the simulation of the response of the ATLAS detector are available in the ATLAS software framework. The full detector simulation with GEANT [53] simulates the ATLAS detector and the reconstruction of the physics objects from the available data as exactly as possible. Therefore, the detector simulation and reconstruction are performed separately and are very time-consuming (up to several minutes per event).

Often, a large number of Monte Carlo events needs to be produced in a reasonably short time. For this task, usually ATLFAST [54] ist used. ATLFAST contains only basic information about the detector geometry, as for example the pseudorapidity coverage of the Inner Detector and the calorimeters, and the calorimeter granularity. Other effects, as for example the shower shape in the calorimeters, are not taken into account. ATLFAST uses a parameterization of the detector response that was obtained from representative processes and was optimized to be in good agreement with the full detector simulation.

[4] In the following also referred to as hard event, hard process or hard scattering.

Part I

General studies for optimal jet reconstruction

4. Jet reconstruction studies

Vector boson fusion processes have a paramount importance for Higgs boson discovery at the LHC in the frameworks of the SM, MSSM and NMSSM. In the context of this thesis, a contribution to the efforts of the ATLAS collaboration to guarantee a good signal-to-background ratio for the vector boson fusion searches, also under realistic experimental conditions, has been made. The quality of the jet reconstruction, in particular in the forward region of the ATLAS detector, is studied.

In the vector boson fusion process, the incoming quarks are scattered off the massive vector bosons to form the tagging jets. These jets preferably lie in the forward and backward detector region and provide additional means for background suppression (Fig. 4.1). A reliable identification of jets as close as 0.85° to the beam pipe ($|\eta| \approx 4.9$) is desirable. Since often at least one of the tagging jets lies in the central region of the calorimeter, the jet identification is studied over the full η range of the ATLAS detector.

The forward pseudorapidity region $3.1 < |\eta| < 4.9$ is covered by the Forward Calorimeter, which has a complex and sometimes rather coarse granularity structure (see Chap. 3.2.3). Moreover, jets in the very forward region may partially lie in the beam pipe and may thus not be fully contained in the calorimeters. For these reasons, jet identification in the forward region is expected to be more difficult than in other parts of the calorimeter.

The presence of underlying event and pile-up cannot be neglected in vector boson fusion analysis strategies, as the searches depend on quantities that are sensitive to additional energy depositions in the calorimeters. Mainly the central jet veto [55], the correct identification of the tagging jets, also in the very forward region, and the unbiased measurement of the missing momentum, as a mismeasurement can introduce a shift and a broadening of the Higgs boson mass resolution in the $H \rightarrow \tau\tau$ channels [56], are affected. For this reason, all ATLAS vector boson fusion analyses currently are restricted to the low-luminosity phase, where only about five collisions per bunch crossing are expected [4].

The results of Chap. 7 will show that in the NMSSM, it might be helpful in some parts of the parameter space to extend the vector boson fusion searches to the design luminosity phase in order to guarantee the discovery of at least one Higgs boson. Due to the high pile-up levels of about 25 collisions per bunch crossing, this needs special experimental care. Although such high pile-up levels are not studied here, a good understanding of the behavior of jet identification and other experimental issues of the vector boson fusion analyses at low pile-up levels is necessary before going to higher luminosities.

At first, a general overview of jet reconstruction strategies at the ATLAS experiment is given in this chapter. Then, a detailed evaluation of the performance of different reconstruction algorithms for jets in vector boson fusion events is presented. Also the effects of pile-up at a low luminosity are described.

4.1 Jet identification in ATLAS

In this section, the different strategies for jet identification that are currently used by the ATLAS collaboration are summarized. At a collider experiment, the final state partons produce

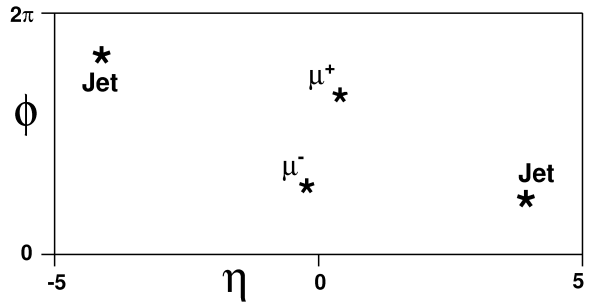

Fig. 4.1: The typical signature of the vectpr boson fusion process. The decay products of the Higgs boson, here two muons from τ-lepton decays, lie in the central region of the detector. The two tagging jets lie in the forward and backward region of the detector.

collimated jets of particles in a showering process. The energy from these particles is deposited in the calorimeter cells. Ideally, a jet identification strategy should collect all energy depositions originating from one parton, and exclude all others. In practice, this mapping of the jets to the partons is only possible approximately. In ATLAS, the first step of the jet identification is the grouping of a number of calorimeter cells into clusters. As a next step, these clusters are combined to jets. The calibration of the jets to the right energy scale currently takes place at the cell level.

4.1.1 Clustering algorithms

There are two clustering algorithms currently in use in ATLAS. One produces calorimeter towers with a fixed sized. The other approach uses a more dynamical algorithm to build the so-called topological clusters which can have a varying size depending on the energy depositions and the calorimeter geometry.

Calorimeter towers

The calorimeter towers [6] are based on a fixed $\Delta\eta \times \Delta\phi = 0.1 \times 0.1$ grid. Energy depositions from cells in the longitudinal direction are summed up. If a calorimeter cell is not fully contained in one cell of the grid, only the fraction of the energy corresponding to the overlap area is added to the tower. All cells are treated like this, independently of the energy deposition.

Towers with negative energy entries, as they can arise from noise fluctuations, cannot be used as input for a jet finding algorithm, because these algorithms only accept four-momentum vectors with a positive energy as valid input. Therefore, they are combined with neighboring towers until the energies of all towers are positive. As this is noise cancellation, but not suppression, the noisy cells still contribute to the jet finding. Every cell is included in a calorimeter tower.

Topological clusters

The formation of the topological clusters [6,57] (also referred to as topo clusters in the following) starts from all calorimeter cells that reach a certain energy threshold in order to ensure the significance of the energy deposition. This threshold is given in terms of σ_{cell}, the average level of the total noise in the cell, including electronic noise and pile-up. Currently, a threshold of $|E_{\text{cell}}| > 4 \cdot \sigma_{\text{cell}}$ is used in ATLAS. From these seed cells on, all neighboring cells in three dimensions, also if these lie in parts different of the calorimeter, are added to the cluster. All added cells which have energies above a lower threshold, typically $|E_{\text{cell}}| > 2 \cdot \sigma_{\text{cell}}$, are regarded

as secondary seed cells. All neighbors of these cells are also added to the cluster. This procedure is repeated iteratively. At the end, all cells above a third energy threshold that are surrounding the cluster are added to it. This third threshold is typically very low. Currently, ATLAS uses no threshold ($|E_{\text{cell}}| > 0 \cdot \sigma_{\text{cell}}$). After that step, the cluster formation is finished.

Then, a splitting algorithm is applied to the clusters. It looks for clusters with more than one local maximum in the energy depositions. This way a large cluster is split into smaller clusters with one maximum each, along the lines of minimal energy depositions which separate the maxima. Thus clusters of variable size are produced.

The formation of topological clusters has an inherent noise suppression, since cells with low energy depositions are likely not to be added to any cluster and are thus not taken into account. The noise contribution to jets built from topological clusters can therefore be several GeV less than for jets built from towers [6]. However, the topological clusters might be more sensitive to long range noise correlations or to pile-up effects than the towers.

4.1.2 Jet algorithms

Jet identification in ATLAS relies on the experiences at the Tevatron [58]. Currently, two different jet algorithms are used by the collaboration [6].

The seeded cone algorithm

The seeded cone algorithm starts from all cluster objects with a transverse energy above a certain seed threshold ($E_T = 1$ GeV in ATLAS). The algorithm adds the four-momentum vectors of all cluster objects that are within a cone of size $R = \sqrt{(\eta_i - \eta_j)^2 + (\phi_i - \phi_j)^2}$ around these seed objects. It also calculates η and ϕ from that four-momentum sum. If these correspond to the η and ϕ of the seed within errors, the axis of the cone is regarded as stable, and the jet is kept. Otherwise, the cone axis is shifted to the calculated η and ϕ, and the procedure is iterated until a stable axis is found. If no stable axis is found in ten iterations, the cone is not taken into account. In ATLAS, currently cone algorithms with R=0.4 and R=0.7 are used.

The jets found by the algorithm all have equal cone size, but they may overlap. Therefore in the next step, an additional split/merge algorithm is run. If the transverse energy shared between two jets is larger than 50% of the transverse energy of the jet with the lower energy, the two jets are merged. Otherwise, the cluster objects are uniquely assigned to the jet which is nearer in η and ϕ. After this step, the jet formation is finished. In the ATLAS software framework, only jets with $p_T > 7.5$ GeV are stored.

However, this jet algorithm is sensitive to low-energetic radiation between two jets, because it can cause the merging of two jets that would otherwise have been separated. Moreover, since the jet formation starts from a seed, it is also sensitive to collinear splitting of energy depositions in the calorimeter, i.e. an energy deposition larger than the seed threshold might be assigned to two clusters which then both might remain below the threshold. This means the seeded cone jet algorithm is neither infrared nor collinear safe. This is unsatisfactory, however, the algorithm is still used as it is fast and the jets are easy to calibrate. There exist also modified algorithms such as the seedless cone algorithm or the midpoint algorithm, which improve the infrared and collinear behavior of the cone algorithm. However, these algorithms are slower and not yet validated within the ATLAS software framework.

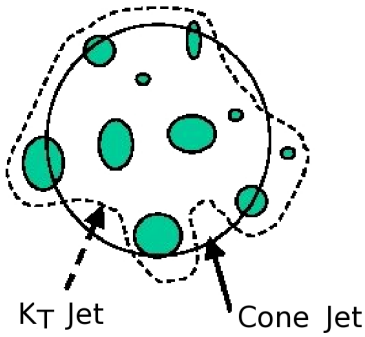

Fig. 4.2: Sketch of a cone jet and a k_T jet. The dots represent the cluster objects.

The k_T algorithm

The k_T algorithm is a successive recombination algorithm [59]. For every pair of the input clusters, it calculates the quantity d_{ij}:

$$d_{ij} = \min\left(p_{T,i}^2, p_{T,j}^2\right) R_{ij}^2 \tag{4.1}$$

Again, R_{ij} is a distance in the η-ϕ space. The algorithm has its name from the fact that for a small angle between the directions of the clusters, d_{ij} is approximately equal to the square of their their relative transverse momentum $k_T^2(ij)$. The d_{ij} are therefore small if two clusters have a similar momentum vector.

Also the quantity d_i is calculated for all clusters:

$$d_i = p_{T,i}^2 D^2 \tag{4.2}$$

The parameter D determines the jet size. In ATLAS, currently D=0.4 for narrow and D=0.6 for wide jets is used. The algorithm selects the smallest element in the set of all d_{ij} and d_i. If this element is a d_{ij}, the clusters i and j are combined by addition of their four-momentum vectors. The new cluster is added to the set of all clusters, the original clusters i and j are removed from it. If the smallest element is a d_i, the corresponding cluster d_i is regarded as a jet and removed from the set of all clusters.

As d_{ij} can only be the smallest element of the set, if it is smaller than both d_i and d_j, it then follows that for this case:

$$\min(p_{T,i}^2, p_{T,j}^2) R_{ij}^2 < \min(p_{T,i}^2, p_{T,j}^2) D^2 \tag{4.3}$$

Thus, D can be interpreted as the maximal distance $D = \sqrt{(\eta_i - \eta_j)^2 + (\phi_i - \phi_j)^2}$ of two clusters that can be merged. It also defines the minimal distance of two jets. However, two objects (towers / topo clusters) in the same jet may have a separation larger than D, because each of the objects can have a distance of D to the center-of gravity of the jet (at the time when the objects are merged to the jet).

The procedure is iterated until every cluster is contained in a jet. The resulting jets can have different sizes, but they cannot overlap. In ATLAS, only jets with $p_T > 7.5$ GeV are stored. More details on the implementation of the algorithm can be found in Ref. [60].

In contrast to the cone jet algorithm, the k_T algorithm is both infrared and collinear safe.

4.1.3 Truth jets

All jet algorithms described above can take any four-momentum vectors as input. For this reason, it is also possible in Monte-Carlo simulation to define jets based on truth particles (see

Chap. 3.3) [6]. In ATLAS, these are built from stable particles on the generator level within $|\eta| < 5$. These particles can be hadrons, electrons and photons from the hard interaction, from initial and final state radiation as well as from the underlying event. The interaction of these particles with the detector material or its magnetic field is not taken into account. These jets are referred to as "truth jets" and, although they will of course not be present in measured data, they are useful for the validation of the ATLAS calibration and jet identification strategies.

4.1.4 Calibration

ATLAS uses a cell based calibration method, similar to the method developed for the H1[1] calorimeter [61]. All cells contained in jets are multiplied by a weight w which depends on the energy density $\rho_i = E_i/V_i$ deposited in the cell, and on the location of the cell in the calorimeter $\vec{X}_i$. The weights are obtained by comparing the energies of uncalibrated, reconstructed cone 0.7 tower jets over the entire η and p_T spectrum to the expected energy of nearby cone 0.7 truth jets with the help of the weighting function:

$$\frac{\partial \chi^2}{\partial w(\rho_i \vec{X}_i)} = \frac{\partial}{\delta w(\rho_i, \vec{X}_i)} \left(\sum_{\text{matched jets}} \frac{((E_{rec} + E_{DM}) - E_{truth})^2}{E_{truth}} \right) = 0 \qquad (4.4)$$

The energy loss in the dead material between the electromagnetic barrel and the Tile Calorimeter E_{DM} is assumed to be proportional to the geometric mean of the sum of the energies of the cells in the last compartment of the electromagnetic barrel calorimeter and the corresponding sum in the first compartment of the Hadronic Tile Calorimeter, $E_{DM} = \alpha\sqrt{E_{EMB3}E_{TILE0}}$. The factor α is also determined from Eq. 4.4. As detector effects are not taken into account in the formation of the truth jets, the above weights correct for these effects by construction. One example for such a detector effect that is corrected for by the weights is the influence of the solenoid magnetic field on the tracks of charged particles with a p_T of ∼400 MeV or less. These are bent so much that the particles do not reach the calorimeters and thus do not contribute to the reconstructed jets.

The above calibration depends on the type of cluster object (tower / topo cluster) used as input for the jet algorithm, and the jet algorithm itself. The calibration weights are obtained for cone tower jets with R=0.7. To compensate for the differences, additional factors depending on $|\eta|$ and p_T are multiplied to all jets obtained with other jet algorithms [6].

4.2 Jet reconstruction studies

4.2.1 Monte Carlo samples

For many of the previous studies of the ATLAS discovery potential for Higgs bosons that will be described in Chap. 5, the fast detector simulation ATLFAST [54] is used. However, for a decent description of the jet reconstruction performance, ATLFAST is not sufficient, as many details of the detector geometry and the reconstruction algorithms are not contained in the ATLFAST parameterization. Therefore, the full GEANT [53] simulation of the ATLAS detector is used in the study presented here. It provides a detailed description of the calorimeters, also including the distribution of dead material and gaps in the detector.

An overview of the used samples is given in Tab. 4.1. All samples are taken from the ATLAS

[1] One of the experiments at HERA, an electron-proton collider in Hamburg, Germany.

Process	Generator	Events	Pile-up
VBF, H$\rightarrow\tau\tau\rightarrow$2l+4$\nu$	Herwig	49400	none
VBF, H$\rightarrow\tau\tau\rightarrow$2l+4$\nu$	Herwig	36750	10^{33}cm^{-2}s^{-1}

Tab. 4.1: Used Monte Carlo samples with their number of events. The samples are taken from the common ATLAS Monte Carlo production.

Monte Carlo production. Here, the vector boson fusion process[2] with subsequent H$\rightarrow\tau\tau\rightarrow$2l+4$\nu$ decay is studied. This process is chosen, as the H$\rightarrow\tau\tau$ channel is, together with the H$\rightarrow$WW channel, the most important decay mode for vector boson fusion analyses. In this study, as for the current CSC[3] effort, the generator Herwig[4] [52] is used for the description of the vector boson fusion process. Both, a sample without and a sample with pile-up, are available. The pile-up level in the latter sample corresponds to a luminosity of 10^{33}cm^{-2}s^{-1}, which is half the expected luminosity of the low luminosity phase of the LHC. This level was chosen to be produced by the ATLAS collaboration as for the starting phase of the LHC, it is not expected that the nominal luminosity is achieved directly.

4.2.2 Important definitions and procedures

Definition of efficiency and purity

Jet identification efficiency and purity are defined to obtain a quantitative measure of jet identification performance. Efficiency is defined as the fraction of truth jets found at the reconstruction level, and purity as the fraction of reconstructed jets that have a corresponding truth jet:

$$\text{efficiency} = \frac{\text{number of truth jets with matched reconstructed jet}}{\text{total number of truth jets}} \tag{4.5}$$

$$\text{purity} = \frac{\text{number of reco. jets with matched truth jet}}{\text{total number of reco. jets}} \tag{4.6}$$

In this study, these quantities are defined with regard to the truth jets. In principle, a matching could also be performed to the partons from the hard event. However, truth information on these partons differs from generator to generator and also depends on the version used. For example, the partons can be listed before or after final state radiation. Thus, such a matching would introduce an artificial dependence of the results on the Monte Carlo generator. This is avoided by using truth jets.

The above definitions for the efficiency and the purity are only meaningful if the same jet algorithm is used on truth and on reconstruction level. Therefore, in the following, cone jets from topological clusters and towers are always matched to cone truth jets with the same size parameter R. The same holds for the k$_\mathrm{T}$ jet algorithms and the D parameter.

It is possible to calculate efficiencies and purities only in a certain p_T or η window. Then, for

[2] In a previous study, the efficiency/purity distributions for jets from vector boson fusion and from QCD dijet production were compared. The performance is found to be very similar for jets of the same p_T and η. Only with the cone tower jet algorithms, the VBF events showed a slightly higher efficiency in the forward region for low-p_T jets. Only jets from the hard process were affected. A possible reason for this might be the different structure of gluon jets. The outgoing partons in the vector boson fusion process are always quarks.

[3] Computing System Commissioning, an effort to test the ATLAS computing system and data processing chain.

[4] In a previous study, no significant differences in the efficiency/purity distributions for jets of the same p_T and η between samples produced with Herwig and Pythia [51] were observed, although Pythia uses a completely different parton shower parametrization than Herwig.

Jet Algorithm	**ΔR for Matching**
Cone, R=0.4	0.25
Cone, R=0.7	0.50
$\mathrm{K_T}$, D=0.4	0.25
$\mathrm{K_T}$, D=0.6	0.40

Tab. 4.2: ΔR values used for the matching between truth and reconstructed jets. The optimal matching parameter depends on the size parameter of the jet algorithm.

the efficiency calculation, the p_T or η cut is only applied to the truth jets, with no requirement on the reconstructed jets, and vice versa for purity calculation. Else, the quality of the calibration and the spatial resolution influence the efficiency and purity dependences on η and p_T, as it is for example possible that a truth jet with p_T slightly above a p_T threshold belongs to a reconstructed jet with a p_T slightly below the same threshold. All jets are required to be within $|\eta| < 5.0$ to be considered for analysis. As in previous studies of Higgs boson detection from vector boson fusion production [62], jets must at least have $p_T > 20$ GeV, also here, $p_T > 20$ GeV is frequently required.

In this study, the experimental errors on the efficiencies and purities are obtained from Eqs. 4.7 and 4.8, which are commonly used for the calculation of binomial errors.

$$\sigma_{\text{efficiency}} = \sqrt{\frac{\text{efficiency} \cdot (1 - \text{efficiency})}{\text{Total number of truth jets}}} \tag{4.7}$$

$$\sigma_{\text{purity}} = \sqrt{\frac{\text{purity} \cdot (1 - \text{purity})}{\text{Total number of reco. jets}}} \tag{4.8}$$

The matching algorithm

The matching between truth and reconstructed jets is done by requiring that the distance between the matched jet pair is smaller than a certain $\Delta R = \sqrt{\Delta\eta^2 + \Delta\phi^2}$. The ΔR values used (see Tab. 4.2) are chosen such that the shape and absolute value of the efficiency and purity are stable under small variations of ΔR. With this method, different ΔR values are obtained for each jet algorithm, that are typically slightly smaller than the size parameter of the jet.

When smaller ΔR values are chosen, a large dependence of efficiencies and purities on small variations of ΔR is observed, which is not desirable. An example for the cone jet algorithm with R=0.4 run on topo clusters is given in Figs. 4.3 and 4.4. For ΔR values larger than approximately the size parameter of the jet algorithm, the probability of matching unrelated objects increases. This is visible in the distribution of the ΔR separation of cone truth jets from their nearest reconstructed cone jet as an increase of matched pairs at a separation approximately corresponding to the size parameter (Fig. 4.5). For a ΔR separation smaller than the size parameter, the probability of matching unrelated objects is small. This underlines that a matching parameter slightly smaller than the size parameter of the jet algorithm is reasonable.

For the $\mathrm{k_T}$ algorithms, a pronounced dip in the ΔR separation of truth jets from reconstructed jets is not observed as the jet size is here not fixed as for cone jets (Fig. 4.6). However, the slopes of the distributions become flatter for large separations.

In some cases, more than one jet fulfills the ΔR requirement for the matching to another jet. Then, only the jet pair with the smallest separation in ΔR is considered matched. Each jet can only be matched once.

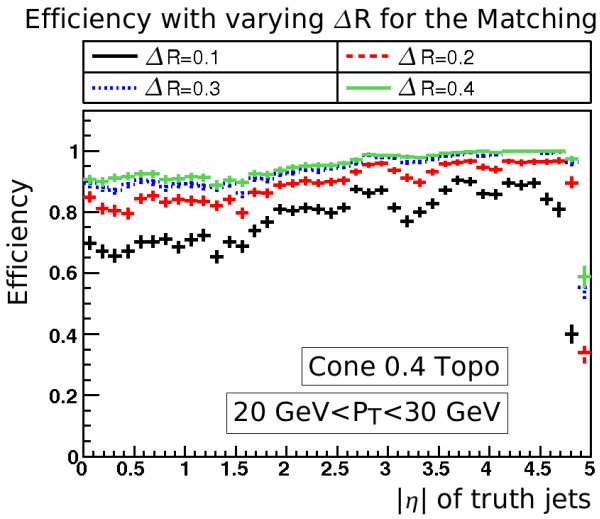

Fig. 4.3: Efficiencies for the cone 0.4 topo jet algorithm and varying ΔR for the matching for the Herwig VBF sample without pile-up. For a better visibility of the differences, only truth jets in the mass window 20 GeV $< p_T <$ 30 GeV are considered.

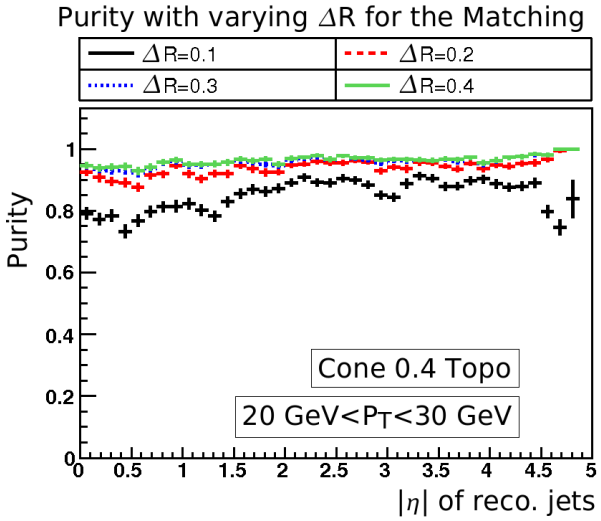

Fig. 4.4: Purities for the cone 0.4 topo jet algorithm and varying ΔR for the matching for the Herwig VBF sample without pile-up. For a better visibility of the differences, only reconstructed jets in the mass window 20 GeV $< p_T <$ 30 GeV are considered.

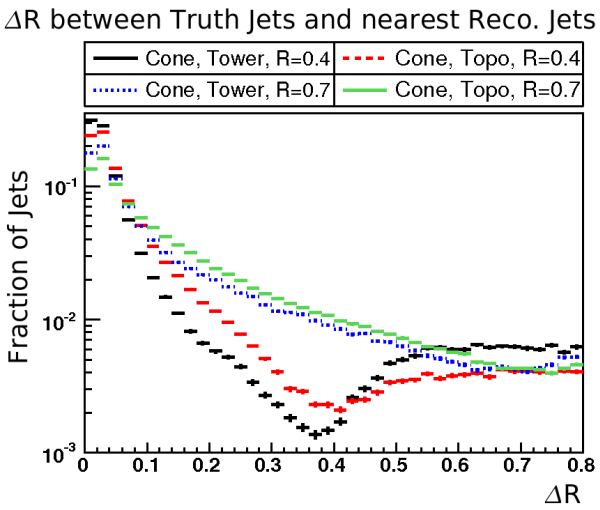

Fig. 4.5: ΔR between the truth jets and the nearest reconstructed jet for different cone jet algorithms for the Herwig VBF sample without pile-up. The histograms are normalized to 1. The increase in matched jet pairs for separations larger than the size parameter of the jet is due to the matching of unrelated objects.

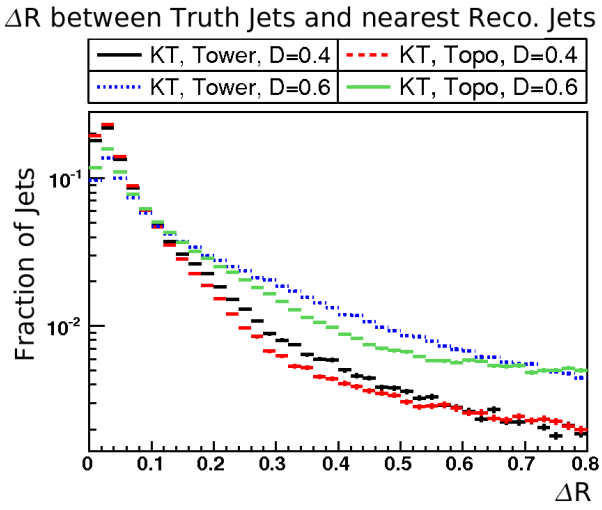

Fig. 4.6: ΔR between the truth jets and the nearest reconstructed jet for different k_T jet algorithms for the Herwig VBF sample without pile-up. The histograms are normalized to 1. As the size of k_T jets is not fixed as for cone jets, there is no pronounced dip in the distribution at a separation of about the size parameter.

Overlap removal with electrons

The jet algorithms used do not distinguish between different physical sources of the cluster or truth objects they use as an input. Therefore, not only hadronic parton showers, but also showers originating from an electron or photon are combined into jets.

To ensure that only hadronic jets are considered in this study, truth jets and reconstructed jets that are found by the jet algorithm are only taken into account if no true electron from a τ-lepton decay is found within $\Delta R = 0.1$ of the jet. This assumes that for the H$\rightarrow\tau\tau\rightarrow$2l+4$\nu$ samples, the electrons from the τ-lepton decays are the only significant source of isolated[5] electrons. This procedure is referred to as "overlap removal" in the following. It is not possible to use all the truth electrons of the event for the overlap removal, as also most of the hadronic jets contain a number of electrons from the shower development.

As truth information will not be available in measured data, it might seem appealing to do the overlap removal for the reconstructed jets with reconstructed electrons instead. However, the jet reconstruction efficiency and purity then become dependent on the details of the electron identification. Electrons that are not found by the identification algorithm used are misidentified as hadronic jets, but cannot be matched to a hadronic jet on truth level. As a consequence, the jet purity decreases.

An example of this behavior of the jet purity for the Herwig VBF sample without pile-up is shown in Fig. 4.7. In this plot, the overlap removal for truth jets is done with truth electrons, but for the reconstructed jets, the overlap removal is performed both with truth electrons and with different reconstructed electron objects[6] defined by the ATLAS collaboration [6]. When reconstructed electrons are used, the purity clearly mirrors the features of the electron identification. Only the central region with $|\eta| < 2.7$ is affected by this, as a lepton filter that forces the two leptons from the τ-lepton decay to lie in this region is applied to the sample. For example, the loose electron identification algorithm has softer cuts than the tight electron algorithm, therefore finds more electrons, and the jet purity is higher. Also regions in the detector where the electron identification efficiency is small can be seen as dips in the purity distribution. For example in the purity curve for the loose electrons, the transition regions between electromagnetic barrel and end-cap ($1.37< |\eta| <1.52$) [6] and the end of the Inner Detector at $|\eta|$=2.5 are visible.

Truth jets from the hard process

An interesting issue for jet physics in vector boson fusion processes is the correct identification of the tagging jets, i.e. the jets that originate from the partons of the hard process. In order to study this, truth jets are defined to originate from the hard process if a parton from the hard interaction is found within the same ΔR that is used for the matching between reconstructed and truth jets. It is possible to only use these truth jets from the hard process in the matching between reconstructed and truth jets for efficiency calculation. By this twofold matching, the influence of different parton definitions is reduced. About 73% to 80% of the truth jets with $p_T > 20$ GeV can be assigned to the hard process with this procedure.

On the other hand, the calculation of purities for these jets is not meaningful, as for this aim, it would be necessary to define jet objects that could be labeled as 'reconstructed jets from

[5] The term 'isolated' here means 'not being part of a hadronic shower'.

[6] For identification of 'loose electrons', some cuts on the shower shape of the electron candidate and a very loose matching to a track in the inner detector are done. For a 'medium electron', the shower shape cuts are refined, and quality cuts on the track match are added. 'Tight electrons' have harder cuts on the quality of the matched track, a E/p requirement and also use information from the Transition Radiation Tracker [6].

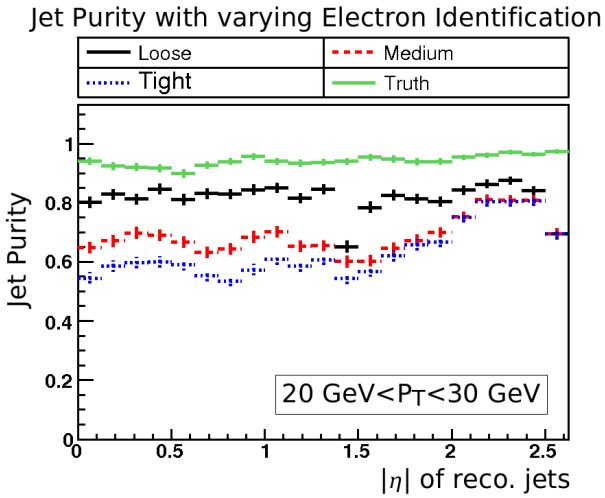

Fig. 4.7: Jet purities for the cone 0.4 topo jets for the Herwig VBF sample without pile-up. Electron objects from different identification algorithms (loose, medium and tight electrons as defined by the ATLAS collaboration [6]) and true electrons are used in the overlap removal. For a better visibility of the differences, only reconstructed jets in the mass window 20 GeV $< p_T <$ 30 GeV are considered.

	Cone R=0.4	**Cone R=0.7**	**K_T, D=0.4**	**K_T, D=0.6**
Input	**Mean Number of Jets per Event with p_T >10 GeV**			
Truth	3.2 ± 0.01	4.6 ± 0.01	3.0 ± 0.01	3.7 ± 0.01
Towers	2.4 ± 0.01	3.9 ± 0.01	3.6 ± 0.01	5.2 ± 0.01
Topo clusters	3.0 ± 0.01	4.5 ± 0.01	3.2 ± 0.01	3.9 ± 0.01
Input	**Mean Number of Jets per Event with p_T >20 GeV**			
Truth	2.0 ± 0.01	2.4 ± 0.01	2.0 ± 0.01	2.1 ± 0.01
Towers	1.8 ± 0.01	2.3 ± 0.01	1.9 ± 0.01	2.1 ± 0.01
Topo clusters	1.9 ± 0.01	2.3 ± 0.01	1.9 ± 0.01	2.1 ± 0.01

Tab. 4.3: Jet multiplicities (p_T >10/20 GeV) for different jet algorithms and input objects to these jet algorithms for the Herwig VBF sample without pile-up.

the hard process'. This would require that these jets can be matched to truth jets from the hard process. As the purity is defined as the percentage of reconstructed jets that can be matched to a truth jets, the purity of such 'reconstructed jets from the hard process' would be 100% by definition. This is also in agreement with intuition, as jets from the hard process cannot at the same time originate from detector noise or other sources that reduce the purity. For these reasons, only the efficiencies for jets from the hard process, but not the purities, are studied in this thesis.

4.2.3 Jet multiplicities

In the following sections, four jet algorithms (cone with R=0.4 and R=0.7 and k_T with D=0.4 and D=0.6) with both towers and topological clusters as input objects are compared. For a more condensed notation, abbreviations like 'cone 0.4 tower jet algorithm' are used to describe the combination of jet algorithm, size parameter and cluster object. The size parameters used

are in a sensible range. Significantly smaller size parameters lead to a meaningless behavior when they approach the dimension of the cluster objects. For larger jet sizes, the danger of combining predominantly noise contributions to jets is heavily enhanced, and the number of jets, especially in the central region, where only little energy is needed to reconstruct a jet with a certain p_T, is increased.

The number of jets that are detected in an event depends on the jet algorithm and the cluster objects used. An overview of the observed jet multiplicities for the Herwig VBF sample without pile-up is given in Tab. 4.3. In principle, two jets from the hard scattering process are expected in the events. Additionally, jets from initial and final state radiation as well as from the underlying event or detector noise can occur. On the other hand, not all partons might be detected experimentally as jets.

Generally, jet algorithms with large size parameters yield a larger number of jets than algorithms with a small size parameter, as they can collect a higher number of cluster objects, and thus more easily accumulate a p_T sufficient to pass the respective thresholds. This effect is more pronounced for jets with low p_T. This affects the performance of the typical central jet veto of vector boson fusion analyses, as the performance of the veto degrades if central jets are produced in abundance by the jet algorithm. However, this aspect is not studied in detail here, as the focus of this work is put on the performance of the jet reconstruction.

Among the truth jets, the cone 0.7 algorithm yields the largest number of jets. Its large cone size can collect a large number of truth particles and thus the jets pass the given p_T thresholds more easily. On the reconstruction level, the k_T 0.6 tower jet algorithm produces the largest number of jets with $p_T > 10$ GeV. Its variable size and the large size parameter seem to be more efficient than a fixed-size cone in combining small energy deposits or noise contributions in the calorimeters into a jet. For jets with p_T >20 GeV, the cone 0.7 tower jet algorithm has the largest multiplicity.

When jets with low p_T >10 GeV are included, the jet algorithms, when run on topo clusters, better reproduce the multiplicity predictions from the truth jets. However, for p_T >20 GeV, the tower jets show a similarly good agreement. Generally, the jet multiplicities of all jet algorithms under investigation seem reasonable.

4.2.4 The p_T and η spectra

In Fig. 4.8, an overview of the p_T and η distributions of the different jet algorithms is shown. The η spectrum of the truth jets is smoother than the spectrum of the reconstructed jets, as it is not influenced by the detector geometry. Due to the nature of the vector boson fusion process, the jets are preferably produced around $|\eta| \approx 2.5$. In the η spectra of the reconstructed jets, the degradation of the jet identification performance in the difficult transition region between Hadronic End-Cap and Forward Calorimeter at $|\eta| \approx 3.2$ and the transition region between electromagnetic barrel and end-cap calorimeters at $|\eta| \approx 1.5$ can be observed. In these regions, there is a large amount of dead material. Energy deposited in this material cannot be measured by the calorimeters, which hampers the jet reconstruction.

A larger number of jets is found in the central detector region when large size parameters are used, in particular with the cone 0.7 jet algorithm. It was already mentioned previously that large jet sizes can more easily collect enough energy contributions, i.e. from noise or from low-energy truth particles, to pass a given p_T threshold. As in the central detector region, a certain p_T corresponds to less energy than in the forward region. Here the effect from such an accumulation is most pronounced. As explained before, the production of low-p_T jets in the central region has an impact on the performance of the central jet veto.

For the k_T algorithms, the increase of the number of jets in the central region with increasing

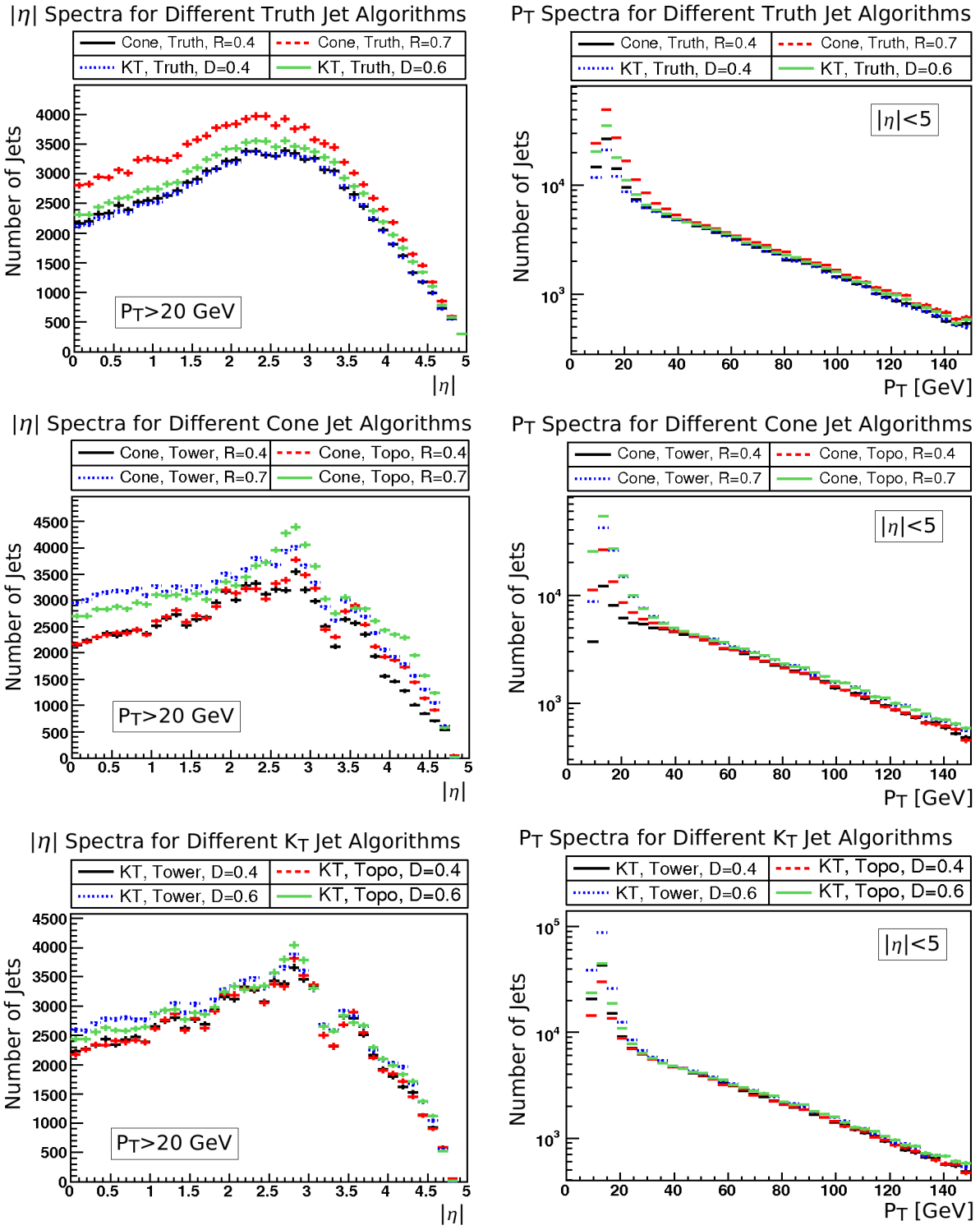

Fig. 4.8: $|\eta|$ and p_T spectra for different jet algorithms for the Herwig VBF sample without pile-up. Left hand column: $|\eta|$ spectra for jets with $p_T < 20$ GeV. Right hand column: p_T spectra for jets with $|\eta| < 5$. First row: Different jet algorithm run on truth objects. Second row: Different cone jet algorithms run on towers and topological clusters. Last row: Different k_T jet algorithms run on towers and topological clusters.

size parameter is not as pronounced as for the cone jet finders, since in contrast to the cone jets, the size of the k_T jets varies anyway in dependence of the neighboring energy depositions. The number of objects included into the k_T jets therefore seems not to vary as strongly with the size parameter.

In the forward region, the number of jets found by the cone topo jet algorithm is larger than with the cone tower jet algorithm for a fixed size parameter. Possible reasons for this are discussed in Chap. 4.2.5.

In the p_T spectra, there is a large number of jets at low p_T values below 20 to 30 GeV. In this region, many jets originate from the underlying event, radiation or collected detector noise. The jets with high p_T to a large fraction originate from the partons from the hard event.

Generally, for the k_T algorithm and for small p_T, the number of jets built from towers is slightly larger than the number of jets built from topological clusters. Here, the jet reconstruction profits from the built-in noise suppression of the topological clusters, which suppresses the formation of jets predominantly from noise, that could otherwise be collected by the k_T algorithm. However, for cone jet algorithms, the effect is reversed. A possible explanation for this might be that the topo clusters may become larger than the fixed-size towers. To include a large cluster in a jet, only its center-of-gravity must be inside the cone radius. Thus, the cone topo jets might contain more energy depositions outside the actual cone radius than cone tower jets, and thus more easily reach a certain p_T.

4.2.5 Efficiencies for different jet algorithms

The jet identification efficiencies of different cone and k_T jet algorithms run on different cluster objects are shown in Fig. 4.9. The dependence of the efficiency on the pseudorapidity is shown both for all jets with $p_T > 20$ GeV and for jets within the mass window 20 GeV $< p_T <$ 30 GeV, as for low-p_T jets, some features are more pronounced. In the spectra, a decrease of the efficiency in the transition region between Hadronic End-Cap and the Forward Calorimeter at $|\eta| \approx 3.2$ is observable.

For the cone algorithms using towers, a distinct drop of the efficiencies in the forward region, especially at low p_T, can be observed. This drop is more pronounced for the smaller cone size R=0.4. The cone topo and the k_T jet finders are not affected by this. The origin of this drop is not yet completely clarified. One possible reason for this behavior is the usage of a seed in the cone algorithms. In ATLAS, $E_T > 1$ GeV for the seed object is required. In the forward region, this corresponds to a larger energy than in the central detector region. If no cluster object passes the seed threshold, no jet is reconstructed and the efficiency decreases. As the topo clusters tend to be larger in the forward region than the calorimeter towers [63], they have less difficulties passing that threshold. The k_T algorithm is unaffected as it does not use a seed. However, this cannot explain why a small cone size is affected to a larger extent than a large cone size.

An alternative explanation for the efficiency drop in the forward region is that the cone size in the forward region is too small to fully accommodate the jets [64]. Such an effect might arise from the relatively coarse granularity in the forward region, that has no influence on the formation of the truth jets. Then, it is difficult for the fixed-size cone algorithms to collect enough energy in a jet to pass the minimal p_T of 7.5 GeV required for storage of a jet by the reconstruction algorithms. This explains why small cone sizes are more severely affected. The topo cluster jets with their variable and in the forward region relatively large size can compensate for the too small cone size, and the size of the k_T jets is not fixed anyway. This issue is not fully

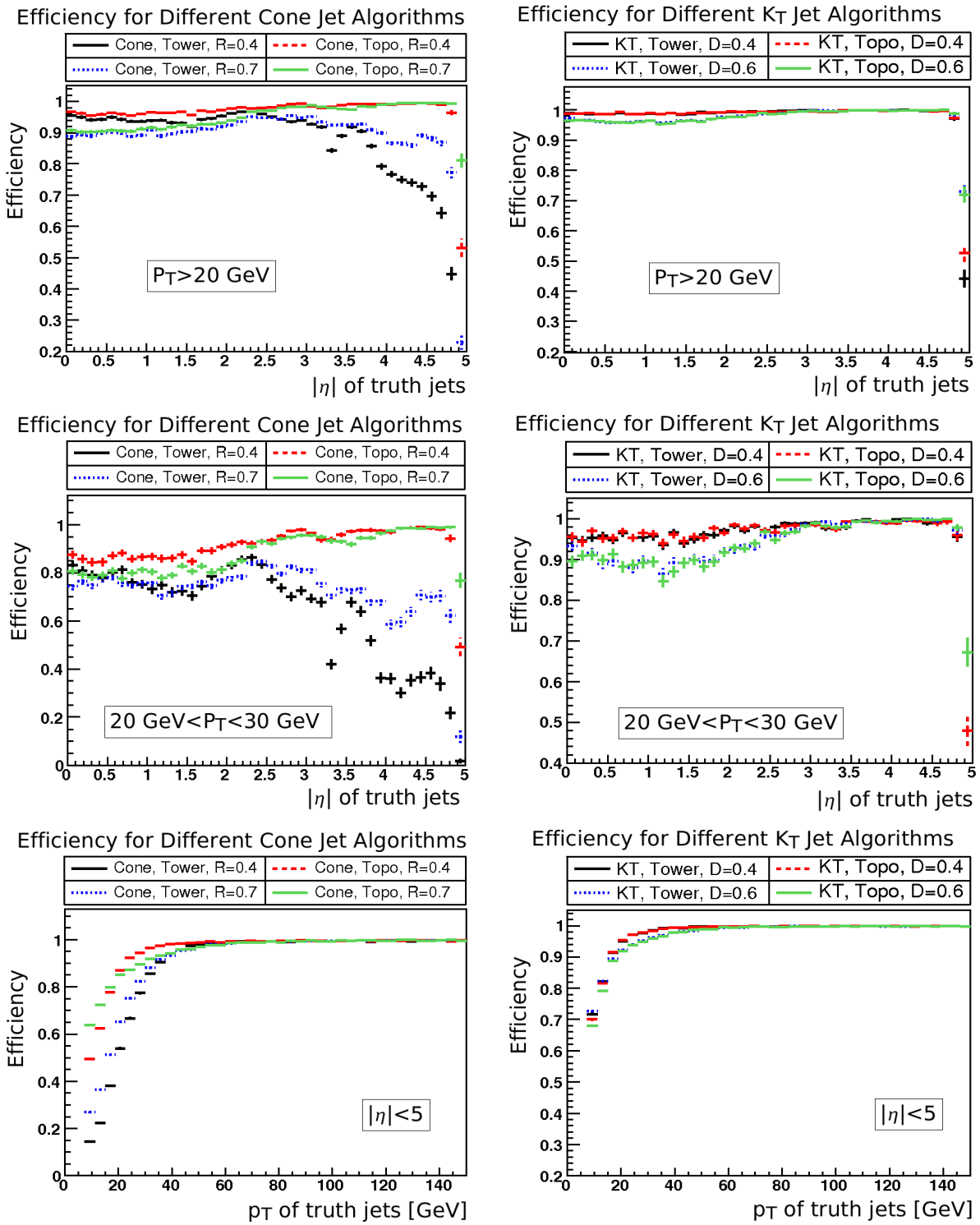

Fig. 4.9: Efficiencies of different jet algorithms for the Herwig VBF sample without pile-up. Left hand column: Cone jet algorithms. Right hand column: K_T jet algorithms. First row: Efficiencies in dependence on $|\eta|$ of the truth jets for truth jets with $p_T < 20$ GeV. Second row: Efficiencies in dependence on $|\eta|$ of the truth jets for truth jets within the p_T window 20 GeV $< p_T <$ 30 GeV. Last row: Efficiencies in dependence on the p_T of the truth jets for truth jets with $|\eta| < 5$.

understood yet and is the subject of ongoing studies[7].

In the central detector region, the efficiencies of jet algorithms with large size parameters are smaller than with small size parameters. For jet algorithms other than the cone tower jet finders, the efficiencies in the forward region are generally larger than in the central region. Jets in the central region have smaller energy depositions than jets with the same p_T in the forward region. The jet algorithms generally have problems finding such jets. For the k_T algorithms, the effect is smaller than for the cone algorithms. Among the cone jet finders, the cone 0.4 topo algorithm has the best performance in the central region. The efficiencies for the k_T jet finders with size parameter D=0.4 are close to 100%, also in the central region.

Generally, the efficiency is lower for jets with low p_T than for jets with high p_T. In the efficiency distributions in dependence on the transverse momentum, the cone tower jet algorithms show especially small efficiencies at low p_T, which is due to the drop of the efficiency in the forward region for low p_T jets. Among the cone jet finders, the cone 0.4 topo jet algorithm has the best overall performance for small p_T values $\gtrsim$ 20 GeV. For the k_T algorithms, the differences in the p_T dependence of the efficiencies are smaller. Here, the k_T 0.4 jet finders have the best performance due to their higher efficiencies in the central region. For large p_T, the efficiencies of all jet algorithms approach 100%.

In Tabs. 4.4 and 4.5, the overall efficiencies for all jets with $p_T > 20$ GeV and for low-p_T jets with 20 GeV $< p_T <$ 30 GeV are listed. The overall efficiencies are smallest for the cone tower jet finders due to the described drop in the forward region. For the other jet algorithms, the smaller jet sizes result in higher efficiencies due to the observed efficiency degradation in the central region. Generally, the efficiencies for the k_T algorithms are slightly higher than for the cone jet algorithms. In the low p_T window from 20 to 30 GeV, the largest efficiency (96.9%) is obtained with the k_T 0.4 topo jet finder, and, among the cone jet algorithms, with the cone 0.4 topo jet algorithm (91.8%). In principle, for the overall efficiencies also including higher p_T values, the same relations hold, however, the effect of the drop in the forward region for the cone towers is now slightly reduced. Again, the largest efficiency (99.1%) is obtained with both k_T 0.4 jet algorithms, and, among the cone jet algorithms, with the cone 0.4 topo jet algorithm (97.5%).

In vector boson fusion analyses, one of the main issues is the correct identification of the tagging jets originating from the scattered quarks. In a typical signal selection, these are identified with the two highest p_T jets, which are required to lie in different hemispheres of the detector. The exact implementation of the tagging jet selection may vary, however, all algorithms depend on the previous reconstruction of the tagging jets by the jet algorithms. Therefore, efficiencies for finding the truth jets from the hard event on reconstruction level are shown in Fig. 4.10. In general, the efficiencies are higher for finding these jets than for finding all jets. With the exception of the cone tower algorithms, all jet finders obtain efficiencies close to 100%, also in a low p_T window.

The drop of the efficiencies in the central region for jets with large size parameters is not present for the jets from the hard event. Moreover, the degradation of the efficiencies of the cone tower algorithms in the forward region is not as pronounced for the jets from the hard process. The remaining efficiency decrease in the forward region influences the efficiency distributions in dependence on p_T, where both cone tower jet finders show small efficiencies at low p_T.

All other jet algorithms show a similar performance for finding the jets from the hard process (Tab. 4.6). The maximal efficiency is achieved with the k_T 0.6 jet finders (99.8%), and, among the cone jet algorithms, for the cone 0.7 topo jet finder (99.7%). For jets from the hard event which have lower p_T between 20 and 30 GeV, the efficiency is maximal for the k_T 0.6 jet

[7] Effects from the calibration linked to the minimum jet p_T cut of 7.5 GeV have been excluded as a cause by this study.

Jet Algorithm	**Overall Efficiency ($p_T > 20$ GeV)**	**Overall Purity ($p_T > 20$ GeV)**
Cone, Tower, R=0.4	(91.0 ± 0.09)%	(98.2 ± 0.04)%
Cone, Topo, R=0.4	(97.5 ± 0.05)%	(98.2 ± 0.04)%
Cone, Tower, R=0.7	(91.3 ± 0.08)%	(95.8 ± 0.06)%
Cone, Topo, R=0.7	(94.9 ± 0.06)%	(96.9 ± 0.05)%
K_T, Tower, D=0.4	(99.1 ± 0.03)%	(98.5 ± 0.04)%
K_T, Topo, D=0.4	(99.1 ± 0.03)%	(98.9 ± 0.03)%
K_T, Tower, D=0.6	(97.9 ± 0.04)%	(97.2 ± 0.05)%
K_T, Topo, D=0.6	(97.9 ± 0.04)%	(98.5 ± 0.04)%

Tab. 4.4: Overall efficiencies and purities for different jet and cluster algorithms for the Herwig VBF sample without pile-up. For the efficiencies (purities), only truth jets (reconstructed jets) with $p_T > 20$ GeV are taken into account.

Jet Algorithm	**Efficiency (20 GeV $< p_T <$ 30 GeV)**	**Purity (20 GeV $< p_T <$ 30 GeV)**
Cone, Tower, R=0.4	(66.9 ± 0.33)%	(94.5 ± 0.19)%
Cone, Topo, R=0.4	(91.8 ± 0.20)%	(95.1 ± 0.16)%
Cone, Tower, R=0.7	(74.8 ± 0.25)%	(87.9 ± 0.20)%
Cone, Topo, R=0.7	(87.4 ± 0.19)%	(91.5 ± 0.17)%
K_T, Tower, D=0.4	(96.8 ± 0.13)%	(95.2 ± 0.15)%
K_T, Topo, D=0.4	(96.9 ± 0.12)%	(96.8 ± 0.13)%
K_T, Tower, D=0.6	(94.1 ± 0.16)%	(91.9 ± 0.18)%
K_T, Topo, D=0.6	(93.8 ± 0.16)%	(95.7 ± 0.14)%

Tab. 4.5: Low p_T efficiencies and purities for different jet and cluster algorithms for the Herwig VBF sample without pile-up. For the efficiencies (purities), only truth jets (reconstructed jets) inside the mass window 20 GeV $< p_T <$ 30 GeV are taken into account.

Jet Algorithm	**Efficiency (Hard Process)**	
	($p_T > 20$ GeV)	**(20 GeV $< p_T <$ 30 GeV)**
Cone, Tower, R=0.4	(95.4 ± 0.08)%	(75.0 ± 0.45)%
Cone, Topo, R=0.4	(99.3 ± 0.03)%	(97.5 ± 0.16)%
Cone, Tower, R=0.7	(98.7 ± 0.04)%	(91.7 ± 0.29)%
Cone, Topo, R=0.7	(99.7 ± 0.02)%	(99.0 ± 0.10)%
K_T, Tower, D=0.4	(99.7 ± 0.02)%	(98.4 ± 0.13)%
K_T, Topo, D=0.4	(99.7 ± 0.02)%	(98.6 ± 0.12)%
K_T, Tower, D=0.6	(99.8 ± 0.01)%	(99.2 ± 0.09)%
K_T, Topo, D=0.6	(99.8 ± 0.01)%	(99.2 ± 0.09)%

Tab. 4.6: Efficiencies for the truth jets from the hard event for different jet and cluster algorithms for the Herwig VBF sample without pile-up. For the efficiencies (purities), only truth jets (reconstructed jets) with $p_T > 20$ GeV and inside the mass window 20 GeV $< p_T <$ 30 GeV are taken into account.

algorithms (99.2%), and, among the cone jet finders, for the cone 0.7 topo jet finder (99.0%).

4.2.6 Purities for different jet algorithms

For a good performance of a jet algorithm, not only the efficiency of the jet reconstruction, but also its purity needs to be considered. Even if the jets from the hard event are correctly identified by the jet finder, a large number of additional jets from noise, pile-up or other effects complicate the selection of the tagging jets on the analysis level. In Fig. 4.11, purities obtained with different jet algorithms and cluster objects are shown.

For all jet algorithms, the purity in the forward region is high. In the central region, the purity decreases. This is due to the fact that noise contributions typically have low energy. Only a low energy is needed in the central region compared to the forward region to obtain a jet of a certain p_T.

Generally, the purity of jet algorithms with large size parameters is smaller than for small size parameters, as large jet sizes can more easily accumulate significant noise contributions. Moreover, the purities are higher for jet finders using topo clusters due to their inherent noise suppression, that is not present for calorimeter towers.

Among all cone jet algorithms, the overall purities for jets with $p_T > 20$ GeV (Tab. 4.4) are highest for the cone 0.4 jet finder (98.2%), and among all jet algorithms for the k_T 0.4 topo jet finder (98.9%). It is lowest for the cone 0.7 tower (95.8%) and k_T 0.6 tower jet algorithms (97.2%). The same relations with somewhat lower purities (88% to 97%) hold in case of jets with relatively low p_T between 20 and 30 GeV (Tab. 4.5).

4.2.7 Jet identification performance with pile-up

During the low-luminosity phase of the LHC, for which the current vector boson fusion analyses are designed, five interactions per bunch crossing are expected. Particles from interactions in other proton collisions than the hard event are called in-time pile-up. As the bunch spacing intervals at the LHC are smaller than the read-out time of the calorimeters, also energy depositions that originate from other bunch crossings can contribute (out-of-time pile-up). These additional energy depositions in the calorimeter can complicate the correct jet identification.

In the following, the effect of pile-up is studied with a Herwig VBF sample with a pile-up level that corresponds to a luminosity of $10^{33}\mathrm{cm}^{-2}\mathrm{s}^{-1}$, which is half the expected luminosity during the low luminosity phase of the LHC (two to three collisions per bunch crossing). It is important to first well understand the behavior of jet identification, but also of calibration and missing momentum measurement, in the presence of low pile-up levels, before going to higher pile-up levels, as expected for the low-luminosity phase, or even for the design luminosity phase. For the calculation of the efficiencies and purities, true particles from the pile-up are not taken into account in the formation of the truth jets, as it would be desirable to only reconstruct the jets from the main interaction. Jets from pile-up are usually not of physical interest. Therefore, the additional contributions from the pile-up particles can be regarded as a kind of noise.

A comparison of efficiencies with and without pile-up for the cone topo 0.4 jet algorithm is shown in the first row of Fig. 4.12. Only a small decrease of the efficiencies due to the pile-up, in particular in the central region, exists. The degradation of the efficiencies in the presence of pile-up is marginal, as the additional depositions in the calorimeters do not hinder the identification of other jets. This also holds for other jet algorithms and for the identification efficiencies of truth jets from the hard process.

Purities with and without pile-up for the cone topo and cone tower jet finders are shown in the second and third row of Fig. 4.12. The purities degrade in the presence of pile-up, as due

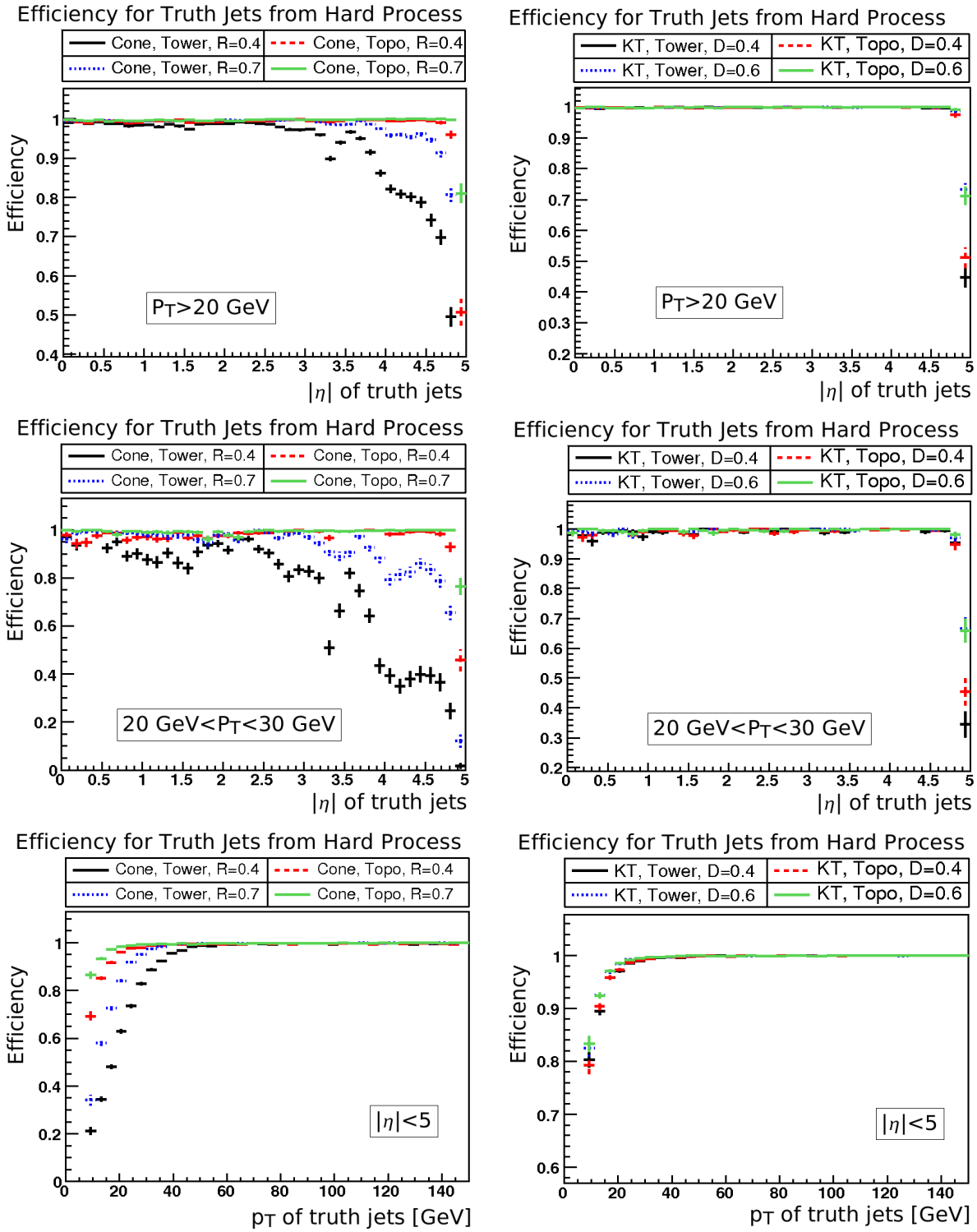

Fig. 4.10: Efficiencies for different jet algorithms for the Herwig VBF sample without pile-up. For all plots, only the truth jets from the hard process are taken into account. Left hand column: Cone jet algorithms. Right hand column: K_T jet algorithms. First row: Efficiencies in dependence on $|\eta|$ of the truth jets for truth jets with $p_T < 20$ GeV. Second row: Efficiencies in dependence on $|\eta|$ of the truth jets for truth jets within the p_T window 20 GeV $< p_T <$ 30 GeV. Last row: Efficiencies in dependence on the p_T of the truth jets for truth jets with $|\eta| < 5$.

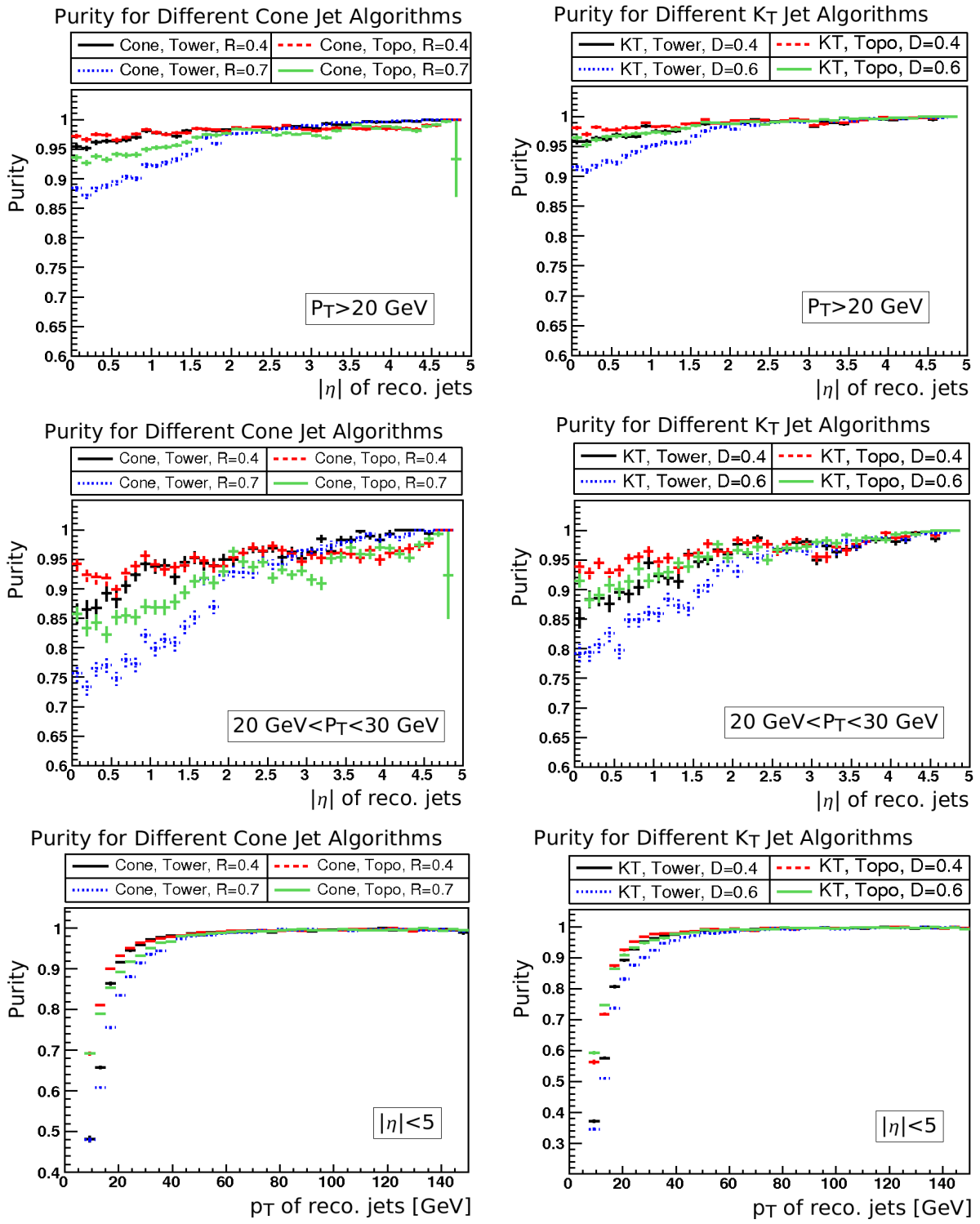

Fig. 4.11: Purities for different jet algorithms for the Herwig VBF sample without pile-up. Left hand column: Cone jet algorithms. Right hand column: K_T jet algorithms. First row: Purities in dependence on $|\eta|$ of the reconstructed jets for reconstructed jets with $p_T < 20$ GeV. Second row: Purities in dependence on $|\eta|$ of the reconstructed jets for reconstructed jets within the p_T window 20 GeV $< p_T <$ 30 GeV. Last row: Purities in dependence on the p_T of the reconstructed jets for reconstructed jets with $|\eta| < 5$.

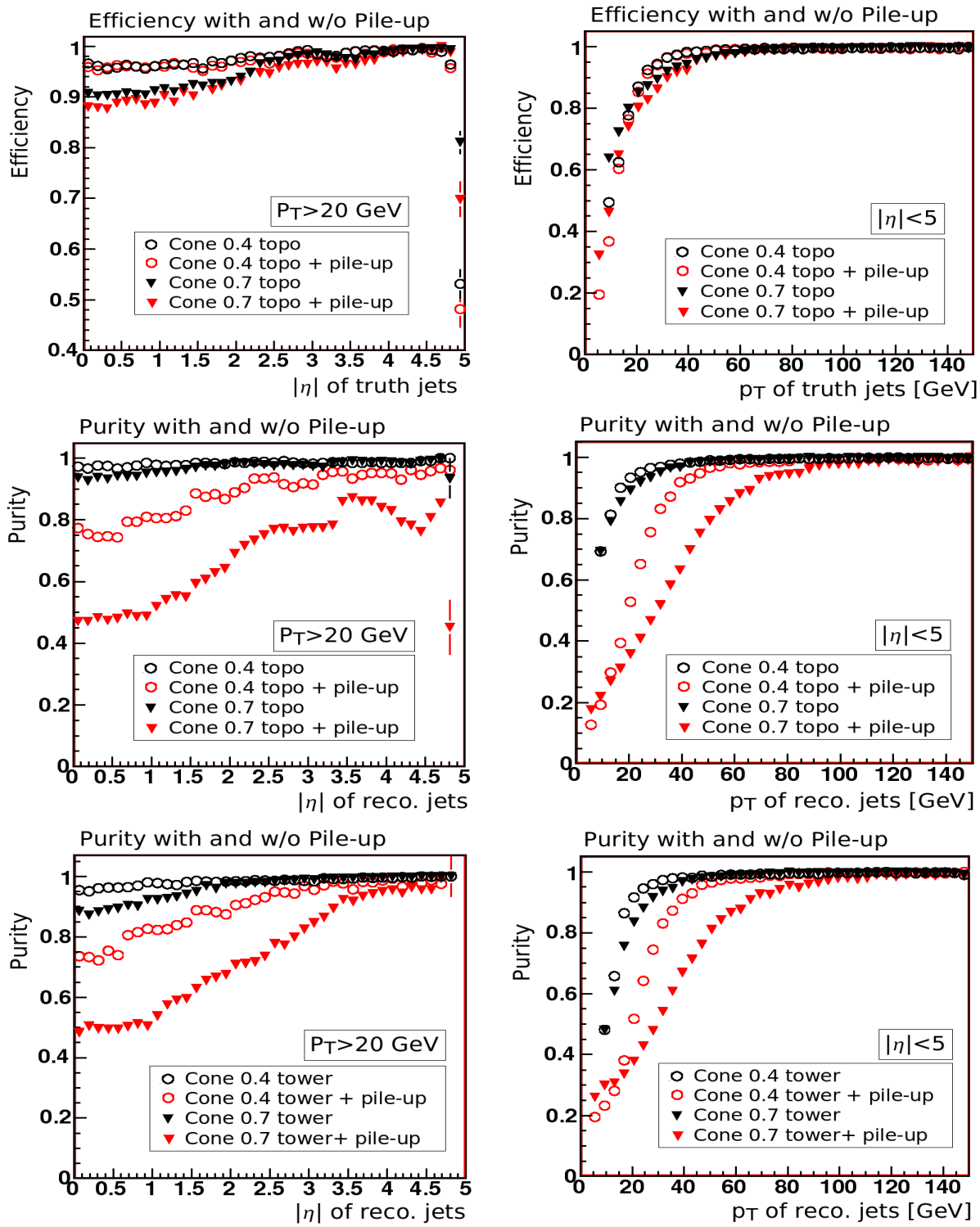

Fig. 4.12: Efficiency and purity for different cone jet algorithms for the Herwig VBF samples with and without pile-up. Left hand column: In dependence on $|\eta|$ for jets with $p_T < 20$ GeV. Right hand column: In dependence on p_T for jets with $|\eta| < 5$. First row: Efficiencies for the cone topo jet finders. Second row: Purities for the cone topo jet finders. Last row: Purities for the cone tower jet finders.

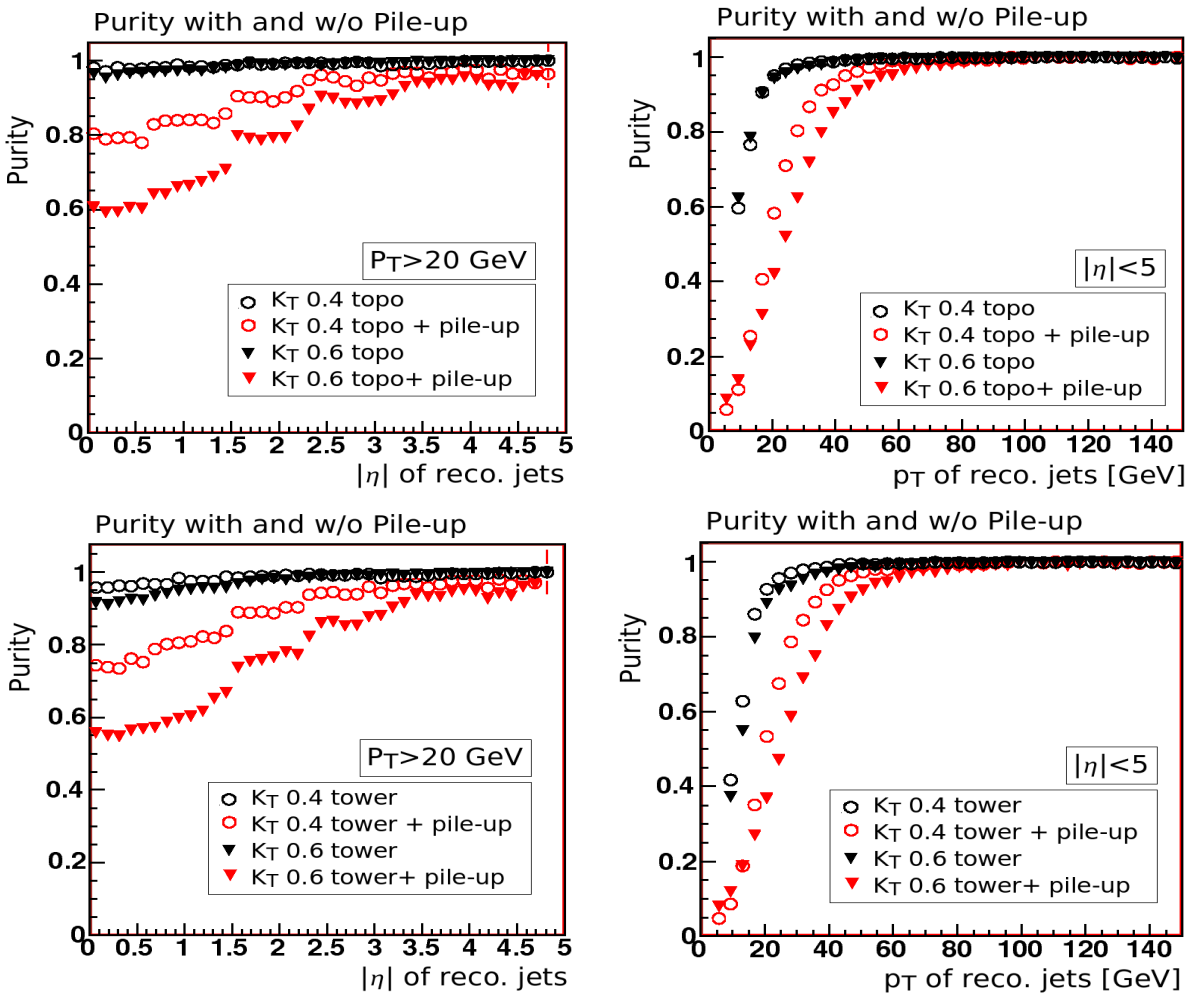

Fig. 4.13: Efficiency and purity for different k_T algorithms for the Herwig VBF samples with and without pile-up. Left hand column: In dependence on $|\eta|$ for jets with $p_T < 20$ GeV. Right hand column: In dependence on p_T for jets with $|\eta| < 5$. First row: Purities for the k_T topo jet finders. Last row: Purities for the k_T tower jet finders.

to the additional energy depositions in the calorimeters, jets that would not be present otherwise are now falsely identified by the jet algorithms on reconstruction level. The degradation is smaller for small size parameters, as large cone sizes can more easily collect a number of energy depositions sufficient to fake a jet. Moreover, for cone jet algorithms, the algorithms run on topo clusters have a larger degradation in the forward detector region. Topo clusters are expected to be sensitive to effects from pile-up [6], as with their variable size, they can combine more energy contributions from pile-up than the fixed-size towers. Their inherent noise suppression is not necessarily effective against pile-up noise, as the particles from pile-up may provide energy depositions that exceed the thresholds of the topo cluster formation.

In principle, the behavior is very similar for the k_T jet algorithms, but the purities are slightly higher (Fig. 4.13). However, as the k_T jets have a variable size anyway, the behavior of towers and topo clusters is very similar under the influence of pile-up in the forward region. In the central region, the purities are even slightly better for topo clusters than for towers.

Although the overall purities degrade significantly in the presence of pile-up, jets with low p_T are affected most. If only jets with p_T >30 GeV and jet algorithms with small size parameters

are considered, the achieved purities are larger than 80%.

4.2.8 Choosing the optimal jet finder

When choosing a jet finder, a good compromise between high efficiencies and purities is crucial. High efficiencies guarantee that physical objects like tagging jets or jets from radiation, that are important for the performance of the central jet veto, are correctly reconstructed. High purities allow for a reliable selection of the correct tagging jets on the analysis level and also for a good performance of the central jet veto. This is of special importance in the presence of pile-up.

Generally, the k_T jet algorithms show slightly higher efficiencies and purities than the cone jet algorithms. The k_T jet algorithms with a small size parameter D=0.4 show a better performance in the central region and in the presence of pile-up than those with a large size parameter. Results obtained with topological clusters and calorimeter towers are similar, with slightly higher purities for k_T topo jets in the central region. Thus, among the studied k_T algorithms, the k_T 0.4 topo jet finder is the best choice for jet reconstruction. Yet, no specialized calibration routines for k_T algorithms are currently available in the ATLAS software framework.

Among the studied cone jet algorithms, both the efficiencies and the purities are largest for the cone 0.4 topo jet algorithm for the case without pile-up. This jet finder has no efficiency drop in the forward region as the cone tower jet algorithms and has a better performance in the central region than jet algorithms with larger size parameters.

However, the cone 0.7 topo jet finder has a slightly better efficiency for truth jets from the hard process with $p_T > 20$ GeV than the cone 0.4 topo jet algorithm ($\sim$0.4% higher). Nevertheless, the cone 0.4 topo jet finder has higher purities and is, due to its smaller size, also expected to be more stable under the influence of pile-up.

As was shown in the previous section, topological clusters are in the forward detector region more sensitive to pile-up than calorimeter towers. However, the cone tower jet algorithms have a significant degradation of the efficiency in the forward region and therefore do not seem to be a good alternative. Consequently, among the cone jet algorithms studied here, the cone 0.4 topo jet finder is the optimal choice.

4.3 Conclusions on jet reconstruction

In this chapter, the most important jet reconstruction strategies of the ATLAS collaboration are reviewed and their performance is studied with the full ATLAS detector simulation. Adequate tools for a comparison of the performance of different jet algorithms are developed.

Depending on the jet algorithm, more than 91% of all jets with $p_T > 20$ GeV on truth level are reconstructed. The efficiencies for the tagging jets are even better than 95%. The purity is larger than 95% for all jet algorithms, but decreases significantly already for pile-up levels that correspond only to a relatively low luminosity. However, reasonable purities can still be obtained for jets with $p_T \gtrsim 30$ GeV if a suitable jet algorithm is chosen. The possibility of extending of the current vector boson studies to the design luminosity phase studies needs more studies. Here, timing information from the calorimeters might help to reduce the influence of out-of-time pile-up.

Most jet algorithms also show a good performance in the forward region, that a priori is expected to be challenging for jet reconstruction.

Generally, the k_T jet algorithms show a slightly better performance than the cone jet finders, but are currently not frequently used in ATLAS as no spezialized calibration routines are available yet. Among the studied k_T jet finders, the k_T 0.4 topo jet finder is the best choice for jet reconstruction.

As a result of this study, it is argued that, among the studied cone jet algorithms, the cone 0.4 topo jet finder constitutes an optimal choice for jet reconstruction in vector boson fusion events, as it shows a good performance both in the central and in the forward detector region and is relatively stable in the presence of noise and pile-up due to its small cone size. For many previous Higgs boson searches, the cone tower algorithm with size parameter R=0.7 was used by the collaboration as a standard. Recently, it was decided to use cone topo jets with size parameter R=0.4 in the current vector boson fusion studies of the CSC effort. This decision was based on this work and on similar studies [65].

Part II

Higgs boson searches within the NMSSM

5. Short review of Higgs boson searches in the SM and MSSM

In this chapter, at first the most important Higgs boson production processes at the LHC and the Higgs boson decays modes are shortly reviewed. Then, an overview of previous Monte Carlo studies evaluating the prospects of searches for Standard Model and MSSM Higgs bosons at the ATLAS experiment is given. Special emphasis is put on the vector boson fusion process since it is a main focus of this thesis.

5.1 Higgs boson production modes at the LHC

Gluon fusion

Gluon fusion (GGF) is the Higgs boson production process with the largest cross section at the LHC in the Standard Model (Fig. 5.1). Here, two energetic gluons strongly couple to the Higgs boson via a heavy quark loop (Fig. 5.2a). The top quark loop is dominant in the Standard Model. A direct coupling of the massless gluon to the Higgs boson is not possible. For the MSSM Higgs bosons, the cross section may be enhanced or suppressed compared to the Standard Model. Higher order corrections are especially important for this production mode as the k-factors[1] are in the range from 1.8 to 2.0 for this channel, depending on the Higgs boson mass [66, 67].

Vector boson fusion

In the vector boson fusion process (VBF), two weak gauge bosons are radiated off the incoming quarks and merge to give the Higgs boson (Fig. 5.2b). Both W and Z bosons contribute. Vector boson fusion is the second largest production process for a Standard Model Higgs boson at the LHC in a wide mass range (Fig. 5.1). It has a clear signature that can be used to efficiently suppress many background processes. Thus, in some cases a higher signal-to-background ratio than for the inclusive mode which is dominated by the more prevalent gluon fusion can be achieved. Two of the characteristic features of vector boson fusion analyses are described in the following:

Tagging Jets
The so-called tagging jets are produced from the quarks that are scattered off the merging massive vector bosons. They typically have high p_T and lie in different hemispheres in the forward- and backward region of the detector [69, 70]. A discussion of jet reconstruction for vector boson fusion is given in Chap. 4.

Central Jet Veto
The decay products of the Higgs boson typically lie in the central detector region [69, 70]. Since there is no color flow between the quarks in the vector boson fusion process, jet production in the central region is suppressed. In contrast, central emission is favored in

[1] The k-factor is the scale factor between the leading order and next-to-leading order cross section.

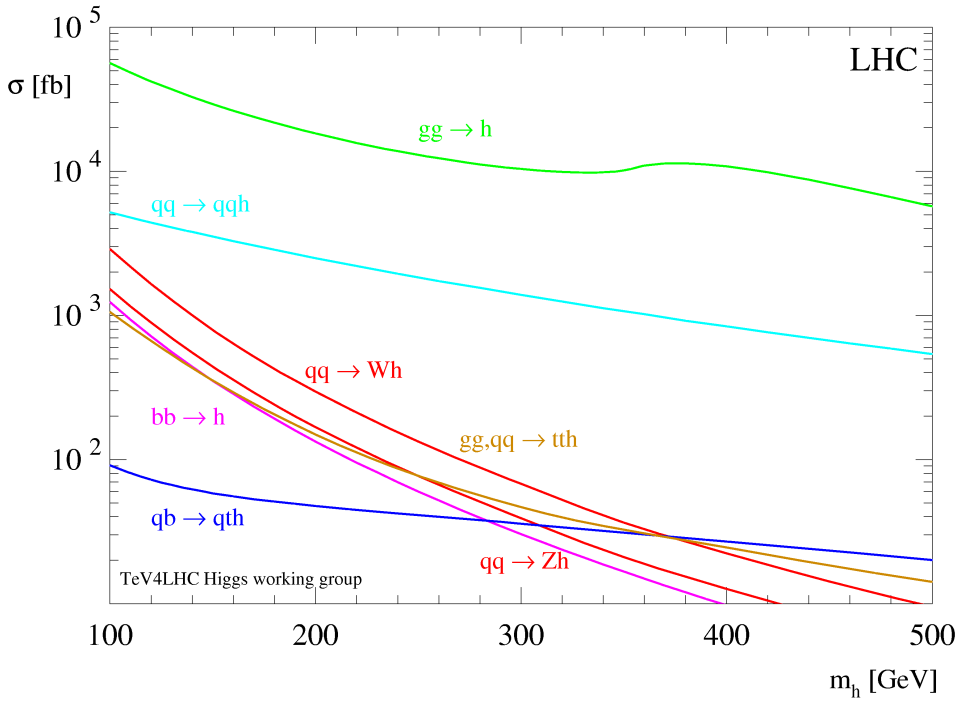

Fig. 5.1: Cross sections of the most important production processes for a SM Higgs boson at the LHC [68].

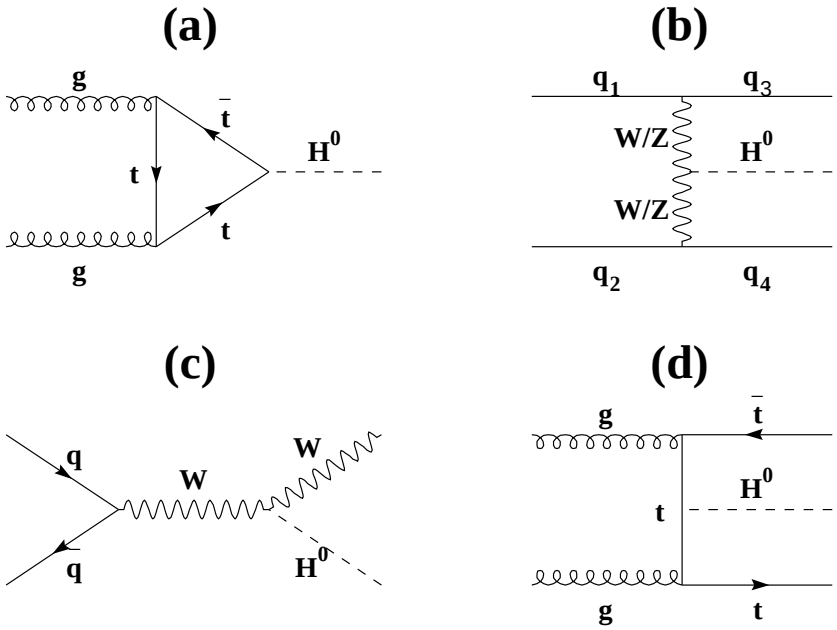

Fig. 5.2: Feynman diagrams for the production of a SM Higgs boson at the LHC: a) Gluon fusion b) Vector boson fusion c) Associated production with a W boson d) Associated production with a top quark pair.

QCD interactions which constitute important background processes at the LHC [69–71]. A veto on additional jets in the central region is therefore a powerful discriminant between vector boson fusion and QCD background processes such as $t\bar{t}$ production [62].

Underlying event and pile-up may produce activity in the calorimeters that does not originate from the vector boson fusion interaction. This leads to large uncertainties of jet tagging and the central jet veto in the presence of pile-up. Therefore, all vector boson fusion analyses presented here assume a data volume corresponding to the low luminosity phase of the LHC [62].

In extended models, like the MSSM and NMSSM, also pseudoscalar Higgs bosons are predicted. The coupling of pseudoscalar particles to the vector bosons vanishes at Born level, so for these Higgs bosons, the vector boson fusion production mode is negligible. The vector boson fusion cross sections of the scalar MSSM Higgs bosons may be reduced, but not enhanced, with respect to the Standard Model.

Associated production with massive vector bosons

It is also possible to radiate the Higgs boson off a massive vector boson produced from a quark-antiquark pair (WH, ZH production, Fig. 5.2c). The cross section for this production mode is relatively small, decreasing rapidly with decreasing Higgs boson mass (Fig. 5.1). Nevertheless, it is possible to exploit leptons from the vector boson decay for triggering and to obtain a clearer signature compared to the inclusive mode. Due to the vanishing coupling of pseudoscalar particles to vector bosons at Born level, also this mode is negligible for pseudoscalar Higgs boson production. Also the WH and ZH cross sections of the scalar MSSM Higgs bosons may be reduced, but not enhanced, with respect to the Standard Model.

Associated production with heavy quarks

In Higgs boson production in association with a top quark pair (ttH), the existence of two b-jets from the top quark decays can be exploited (Fig. 5.2d). In the MSSM, this process can be enhanced or reduced with respect to the Standard Model.

Also Higgs boson production in association with a bottom quark pair (bbH) is possible, but has a small cross section in the Standard Model (Fig. 5.1). However, in a supersymmetric scenario it may gain importance, since its rate can be enhanced for large $\tan\beta$ values [68].

Charged Higgs boson production

Many extended models of particle physics, such as the MSSM or NMSSM, predict the existence of charged Higgs bosons (see Chap. 2). Their dominant production processes depend on their mass:

Light charged Higgs bosons ($M_{H^\pm} < M_{top}$)
If the charged Higgs bosons are lighter than the top quark, they can be produced in top quark decays like $t \to H^+ b$ and $\bar{t} \to H^- \bar{b}$. Top quark pair production is then the largest source of charged Higgs bosons via the processes $t\bar{t} \to \bar{t} H^+ b$ and $t\bar{t} \to t H^- \bar{b}$ (Fig. 5.3).

Heavy charged Higgs bosons ($M_{H^\pm} > M_{top}$)
For charged Higgs bosons heavier than the top quark, the processes $gb \to tH^-$ and $g\bar{b} \to \bar{t}H^+$ as shown in Fig. 5.3 are the most important production mode.

Transition region ($M_{H^\pm} \approx M_{top}$)
If the mass of the charged Higgs bosons is approximately equal to the top quark mass, the

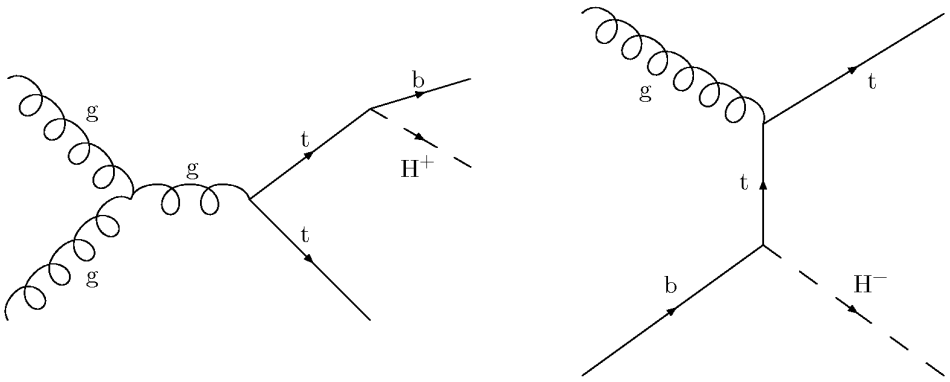

Fig. 5.3: Feynman diagrams for the most important production modes of charged Higgs bosons. Left: From a top quark decay, Right: Associated production with a top quark.

$t\bar{t}\rightarrow\bar{t}H^+b/t\bar{t}\rightarrow tH^-\bar{b}$ and $gb\rightarrow tH^-/g\bar{b}\rightarrow\bar{t}H^+$ processes are similar in cross section. In this region, Monte Carlo generation is more difficult than for smaller or larger masses of the charged Higgs bosons, and special procedures are needed [72–74]. A Monte Carlo event generator including such procedures has only been made available recently[2]. Therefore, the transition region is not taken into account by the most, currently available ATLAS Monte Carlo studies on the charged Higgs bosons.

The respective cross sections not only depend on the charged Higgs boson mass, but also on $\tan\beta$, since they are proportional to the square of the $tbH^\pm$ coupling of Eq. 2.60. Accordingly, they are sizeable for large and very small values of $\tan\beta$ and have a minimum around $\tan\beta \approx 7.5$. Also other model parameters influence the cross sections since radiative corrections are relevant, especially for large $\tan\beta$ [76].

5.2 Higgs boson decay modes

The coupling of the Higgs boson to a fermion pair is proportial to the fermion mass (Eq. 2.28). For this reason, the decay $H\rightarrow b\bar{b}$ is the most frequent decay channel of the Standard Model Higgs boson to fermions, followed by the decays $H\rightarrow\tau\tau$ and $H\rightarrow c\bar{c}$ (Fig. 5.4). Decays to strange quark pairs and to muons are very rare. The branching ratio of the Higgs boson to a top quark pair becomes sizeable if $M_H \gtrsim 2M_{top}$.

Also decays to bosons are relevant. Decays to the massive vector bosons W and Z are especially important, since these processes are possible also at Born level, in contrast to decays to massless gauge bosons. If the Higgs boson mass is larger than about 160 GeV, a pair of two on-shell bosons can be produced. Since the coupling of the Higgs boson to other bosons is proportional to the square of the boson mass (Eq. 2.25), these decay modes quickly become dominant in that region. At the dip in the branching ratio of $H\rightarrow ZZ$ at $2M_W$, a real W boson pair can be produced, so the $H\rightarrow WW$ mode is heavily enhanced. When the slightly heavier Z boson can also be produced on its mass shell, $H\rightarrow ZZ$ decays become more frequent again. Decays to the massless photons are only possible via loop diagrams with heavy particles and are therefore rare.

In the MSSM, the size of the branching ratios may be altered with respect to the Standard Model, because the respective couplings may be enhanced or suppressed.

[2] The event generator MATCHIG [75] includes the required matching algorithm.

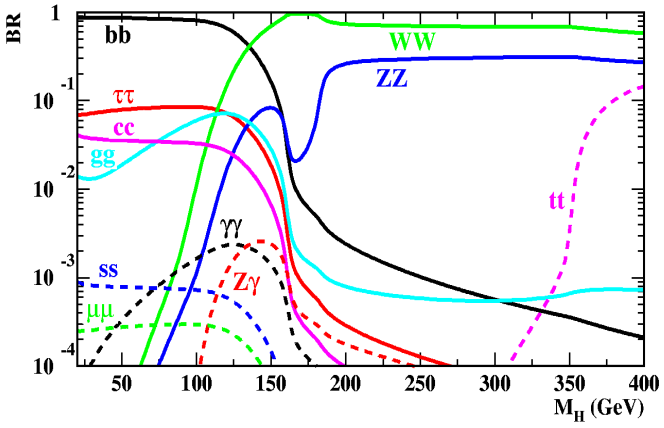

Fig. 5.4: Branching ratios of the dominant decay modes of the SM Higgs boson [16, 77].

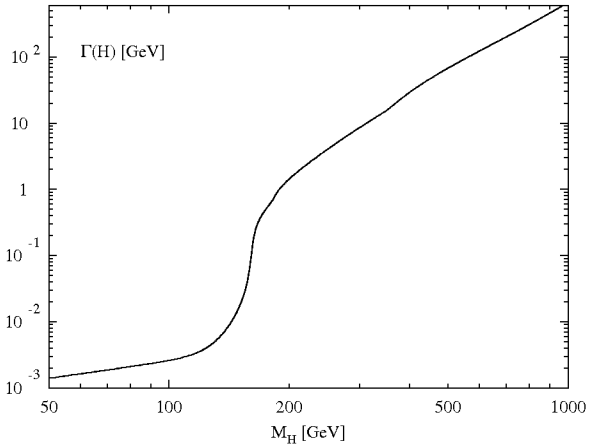

Fig. 5.5: Total decay width of the SM Higgs boson [16, 77].

The Higgs boson width continuously increases with the Higgs boson mass, becoming sizeable for masses around 160 GeV, when the decays to on-shell massive vector bosons is kinematically allowed (Fig. 5.5).

5.3 Standard Model searches

In the following, ATLAS search strategies for the Standard Model Higgs boson as they are specified in previous publications are reviewed. The results presented here are obtained with the fast detector simulation ATLFAST [54], unless otherwise noted. Aspects of some studies, eg. identification efficiencies, fake rates or mass resolutions, are evaluated using the full simulation based on GEANT [53]. For details, see the relevant references. Usually, a statistical significance of 5σ is considered sufficient for claiming a discovery. This corresponds to a probability of $2.88 \cdot 10^{-7}$ or less that the observed excess of events is only due to a statistical fluctuation of the background level.

Associated production with top quark pair, $H \rightarrow b\bar{b}$

Associated production with a top quark pair is the only production mode where the Higgs boson decay to a bottom quark pair might be visible at the ATLAS experiment. One of the W bosons from the top quark decays is required to decay leptonically to provide a lepton for triggering. The other W boson is required to decay to light quarks as the branching ratio is high. Thus, the final state contains four b-jets, two light jets, a lepton and missing momentum.

To reconstruct the Higgs boson mass, two of the four b-jets must be selected. To suppress the combinatorial background, a full reconstruction of the final state is performed, using a likelihood method to optimally assign the final state particles to W boson and top quarks decays. The four momentum vector of the leptonically decaying W boson is reconstructed despite the unknown p_z of the neutrino by using the known W boson mass as an input. The four momenta of the jet pair assigned to the W boson are rescaled to the W boson mass. Using the yet unassigned b-jet pair for M_{H} reconstruction, a mass resolution of 15.1 GeV (20.5 GeV) can be achieved for a Higgs boson mass of 120 GeV in the low (design) luminosity phase [78].

The main background process is $t\bar{t}$ production with additional jets. Using a cut analysis method, $\mathrm{S}/\sqrt{\mathrm{B}}$ values larger than 5σ are expected for Higgs boson masses $\lesssim$120 GeV, assuming a

data volume of 300 fb^{-1} [78]. However, this channel is very sensitive to systematic uncertainties, and also recent experience from CMS indicates that a discovery in this channel might be difficult [79].

Vector boson fusion, H→$\tau\tau$

The H→$\tau\tau$ channel allows access to a Higgs boson-fermion coupling in the decay. At the LHC, this is in the Standard Model otherwise only possible in the H→b$\bar{\text{b}}$ mode. For triggering, at least one high-p_T lepton in the final state is needed. For this reason, the decay chains H→$\tau\tau$→lh+3ν and H→$\tau\tau$→ll+4ν are considered. The typical vector boson fusion signature as described in Chap. 5.1 is exploited for suppression of the main background process, which is irreducible Z→$\tau\tau$ production from strong and electroweak processes. Also t$\bar{\text{t}}$ production and WW production in association with jets contribute [62].

In spite of the neutrinos in the final state, the reconstruction of the Higgs boson mass is possible by use of the collinear approximation [80, 81] with a similar procedure as described in Chap. 8.4. Thus, a mass resolution of 12 GeV is obtained for M_{H}=120 GeV. This channel is promising for a 5σ-discovery in a mass range from about 120 to 135 GeV with 30 fb^{-1}. Vector boson fusion is presumably the only production mode for with the H→$\tau\tau$ decay will be observable in the Standard Model [62].

Inclusive mode, H→$\gamma\gamma$

With this inclusive analysis, Higgs bosons from all production modes are selected. The inclusive cross section is dominated by the gluon fusion mode. The branching ratio of the Standard Model Higgs boson to two photons is at most only 0.22% at $\text{M}_{\text{H}} \approx 126$ GeV [77]. However, this decay channel has a clear and relatively rare signature and provides an excellent Higgs boson mass resolution ($\sigma = 1.31$ GeV at $M_{\text{H}} = 100$ GeV). The unknown position of the Higgs boson vertex leads to a slight smearing [5].

The main challenge of this analysis is to measure the small Higgs boson mass peak on top of a large irreducible $\gamma\gamma$ background. Therefore, excellent energy and spatial resolution of the electromagnetic calorimeters are needed, as well as a very low of systematic uncertainties on the background level. Moreover, processes with final state electrons and jets contribute to the background level if these particles are misidentified as isolated photons. Therefore, good photon identification and isolation algorithms and a realistic estimation of their fake rates are required.

Using a cut analysis methods with 100 fb^{-1} of integrated luminosity, $\text{S}/\sqrt{\text{B}}$ values larger than 5σ can be achieved in the mass range from about 105 to 145 GeV, where both the production cross section and the branching ratio of the Higgs boson to photons are relatively large [5].

Vector boson fusion, H→$\gamma\gamma$

This search exploits the typical features of the vector boson fusion process. The main background process is photon production in association with jets. As in Chap. 5.3, good photon identification and isolation algorithms are needed to suppress reducible background processes. The mass resolution is expected to be around 1.2%. Using a cut analysis method, a significance of 2.2σ can be achieved for a Higgs boson mass of 130 GeV with 30 fb^{-1} [82]. As a discovery channel for the Standard Model Higgs boson, vector boson fusion, H→$\gamma\gamma$ is therefore not competitive with the inclusive or associated production modes which reach significances above 5σ. However, in parts of the parameter space of the Small-α Scenario [33] of the MSSM, it contributes significantly to the discovery potential [83, 84].

Associated production, H→γγ

The total production cross sections of the Higgs boson in association with vector bosons (ZH, WH) or top quarks (ttH) are much smaller than for the inclusive mode. Nevertheless, requiring an additional lepton from massive vector boson decays in addition to the two photons from the Higgs boson decay substantially reduces the background rates. Another advantage of this analysis is that, unlike for the inclusive mode, the vertex position can be determined unambiguously with the help of the track from the charged lepton, which results in a slightly better mass resolution ($\sigma = 1.23$ GeV for $M_{\mathrm{H}} = 100$ GeV) [5].

The most important irreducible background process is $\mathrm{Z}\gamma\gamma$ production, but also $\mathrm{W}\gamma\gamma$, $\mathrm{t\bar{t}}\gamma\gamma$ and $\mathrm{b\bar{b}}\gamma\gamma$ production contribute. Events with misidentified leptons or photons, that might occur in processes like $\gamma\gamma$+jet, γl+jet, γ+2jets, l+2jets and 3jet production, need to be taken into account. Statistical significances around 4.3σ can be achieved in the mass range from about 100 to 120 GeV using a cut analysis method and a data volume of 100 fb^{-1} [5].

Gluon fusion, H→ZZ→4l

In this analysis, also the production of virtual Z bosons is taken into account, so this channel has a discovery potential for Higgs boson masses smaller than $2M_{\mathrm{Z}}$ as well. Both electrons and muons are considered in the final state. The total branching ratio of the decay chain depends on the Higgs boson mass and reaches values of maximal 0.14% for masses around 340 GeV [14, 77]. The mass resolution for relatively light Higgs bosons below 180 GeV ranges from 1.32 to 2.28 GeV, depending on the lepton flavors in the final state, the Higgs boson mass, and the luminosity. For Higgs bosons with $M_{\mathrm{H}} \gtrsim 300$ GeV, the natural line width dominates the mass resolution [5].

Main irreducible background processes are ZZ and $\mathrm{Z}\gamma$ production. Also the reducible processes $\mathrm{t\bar{t}}$, $\mathrm{Zb\bar{b}}$ are important, but can be suppressed by optimized isolation requirements on the leptons.

With a cut analysis method and 30 fb^{-1}, statistical significances larger than 5σ can be achieved for Higgs boson masses from 130 to 600 GeV, with a small gap around M_{H}=170 GeV. With 100 fb^{-1}, the entire mass range from 125 to 600 GeV can be covered. This search mode is expected to be robust even for higher masses [5].

Gluon fusion, H→WW→2l+2ν

In a mass region around 170 GeV, the H→ZZ* branching ratio is suppressed because the H→WW decay becomes kinematically possible. Then, the here presented search channel is of special importance. Virtual $\mathrm{W}^{\pm}$ bosons are taken into account in the analysis by slightly different cuts for Higgs boson masses below and above the production threshold. Both electrons and muons in the final state are taken into account [85].

Since Higgs boson masses near the production threshold of the W boson pair are considered, the decay products of the Higgs boson have relatively low p_T. The collinear approximation is therefore not usable. Instead, the transverse mass is calculated:

$$M_T = \sqrt{2\, p_{T,ll}\, p_{Tmiss}(1 - \cos\phi)} \tag{5.1}$$

In this equation, ϕ is the angle between the transverse dilepton momentum $p_{T,ll}$ and the missing transverse momentum p_{Tmiss}.

WW, $\mathrm{t\bar{t}}$ and Wt production are the dominant background channels for this search. Also WZ, ZZ and W+jet production are considered.

After applying a cut analysis, statistical significances larger than 5σ are predicted for this channel for the mass range from 150 to 190 GeV, using 30 fb^{-1} for the low luminosity or 100 fb^{-1} for the design luminosity phase [85].

Vector boson fusion, H→WW

This channel gives clean access to the Higgs boson coupling to W bosons both in the production and in the decay. The semileptonic H→WW→lνjj and the purely leptonic H→WW→lνlν decay modes provide the required lepton for triggering. Especially for the semileptonic mode, large background contributions have to be suppressed. These include $t\bar{t}$, W, Z, WW and ZZ production in association with jets as well as QCD multijet production. The vector boson fusion signature is exploited. As a complete mass reconstruction is not possible, the transverse mass from Eq. 5.1 is calculated [62].

With a cut analysis method, this channel is promising for a 5σ-discovery in a mass range from 125 to 190 GeV with 30 fb^{-1}. Only 5 fb^{-1} are needed in the mass region from 150 to 190 GeV [62].

Associated production with a W boson, H→WW→2l+2ν

This search is similar to the corresponding search strategy for the gluon fusion mode as described in Chap. 5.3. Especially, Higgs boson mass reconstruction is also not possible, and the transverse mass (Eq. 5.1) is used instead. Requiring a third lepton from the associated W boson in the final state significantly reduces the background rates. Main remaining background processes are WZ production and $t\bar{t}$ production where the third lepton originates from semileptonic bottom quark decays [5].

With a cut analysis method, statistical significances larger than 5σ are predicted for masses of about 160 to 170 GeV, assuming an integrated luminosity of 100 fb^{-1} [5].

ATLAS discovery potential for Higgs bosons of the SM

Figure 5.6 shows the ATLAS discovery potential for a Standard Model Higgs boson with a data volume of 30 fb^{-1} in the mass range from 100 to 200 GeV. Combined significances larger than 5σ are expected in the entire mass region shown. One of the two vector boson fusion modes H→$\tau\tau$ and H→WW is the most significant channel for every mass point between the LEP limit and 190 GeV, a mass region which is experimentally favored by the results of the electroweak precision measurements from LEP (see Chap. 2.1.3). This emphasizes the outstanding importance of the vector boson fusion searches for Higgs boson discovery at the LHC.

At higher Higgs boson masses, the H→ZZ mode guarantees the discovery of the Standard Model Higgs boson if it exists. Thus, with the searches described in the last chapter, the Standard Model Higgs boson will be observable with the ATLAS detector over the entire accessible mass range from the LEP exclusion limit of 114.4 GeV up to ∼1 TeV using 100 fb^{-1} [5].

5.4 MSSM Searches

In this chapter, ATLAS search strategies that were developed for MSSM Higgs bosons are reviewed. Apart from these analyses, also the previously described searches for the Standard Model Higgs bosons may be sensitive to MSSM Higgs bosons.

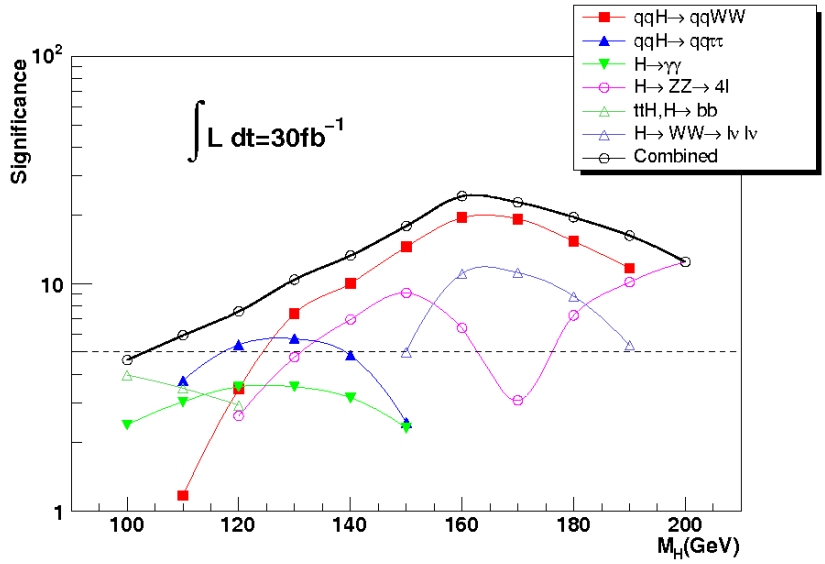

Fig. 5.6: Discovery potential for a Standard Model Higgs boson for different search channels and their combination in ATLAS with 30 fb^{-1} [86].

Gluon fusion and associated production with bottom quarks, H/A→$\tau\tau$

In the MSSM, the H/A→$\tau\tau$ decay may be strongly enhanced with respect to the Standard Model case. While at low tan β, gluon fusion is the dominant production mode, bbH/bbA production becomes important for large tan β. In this analysis, both production modes are considered in the cut analysis by a b-jet veto or a b-jet requirement respectively. The results are then combined. For $M_{\mathrm{A}} > 150$ GeV, the H and the A bosons are often degenerate in the CP-conserving MSSM, and their signal cross section can be added.

The decay chain H/A→$\tau\tau$→lνh is relevant for masses from 100 to ∼800 GeV. Since the production rates decrease with increasing Higgs boson mass, H/A→$\tau\tau$→hh decays are additionally studied for masses from 450 to 800 GeV to enhance the sensitivity of this channel. Good understanding of the trigger rates is crucial for the purely hadronic channel [87,88].

With the help of the collinear approximation, the invariant mass of the τ-lepton pair can be reconstructed. For Higgs boson masses of 150 GeV, a resolution of about 22 GeV can be achieved. For larger masses, the increasing natural line width has a significant influence on the mass resolution.

Z boson production with subsequent decay to a τ-lepton pair is the main reducible background process for this analysis. To suppress the most important reducible background processes from $\mathrm{t\bar{t}}$ and W+jet production, a good performance of the τ-jet identification is needed. Results for this search channel are only available for a low luminosity scenario.

Using a cut analysis method, statistical significances above 5σ can be achieved for Higgs boson masses of 100 GeV for tan $\beta \gtrsim 7.5$. For larger masses, larger tan β values are needed, for example for a Higgs boson mass of 700 GeV, tan β must be $\gtrsim 30$ to allow for a discovery [87,88].

Gluon fusion and associated production with bottom quarks, H/A→$\mu\mu$

Also the H/A→$\mu\mu$ decay is strongly enhanced with respect to the Standard Model case over a large range of the MSSM parameter space. The gluon fusion and the bbH/bbA production modes are taken into account by a b-jet veto or a b-jet requirement, similarly to the H/A→$\tau\tau$ search. Although the branching ratios of the Higgs bosons to muons are much smaller than the

branching ratios to τ-leptons, this channel is promising since it has a better mass resolution of about 2% [90].

Very low masses close to the Z boson mass are accounted for in a separate analysis for the associated channel only. The h and A boson are nearly degenerate in this mass region. Background events, as from $Zb\bar{b}$ production, are subtracted by estimating the shape of the invariant mass distribution of the muon pair with the help of a reference sample [89].

When using a cut analysis method, a Higgs boson with a mass of 150 GeV is expected to be observable in this channel at $\tan\beta \gtrsim 10$. For smaller or larger masses, larger $\tan\beta$ values are required for a discovery. For example, in case of a Higgs boson mass of 400 GeV, $\tan\beta \gtrsim 30$ is needed [90].

Inclusive mode, $A \to \gamma\gamma$

For the search in this channel, the same approach as for the Standard Model Higgs boson (Chap. 5.3) is used with the exception that the considered A boson masses are larger than 200 GeV. Therefore, the p_T thresholds have been adjusted to the larger masses. The width of the A boson is narrow in the studied MSSM scenarios, so that mass resolution is dominated by the experimental resolution of the electromagnetic calorimeter. For $M_A = 300$ GeV, the mass resolution is about 4.6 GeV [5].

This channel is promising for the discovery of a MSSM pseudoscalar Higgs boson at low $\tan\beta \lesssim 2$. Assuming a data volume of 100 fb^{-1}, A boson masses from about 260 GeV up to $2M_{top}$ can be discovered [5].

Gluon fusion, $H \to hh \to b\bar{b}\gamma\gamma$

With this decay mode, the h and H bosons might be observable simultaneously. The applied cuts include mass windows for both Higgs bosons. The final resolution for M_H is expected to be $\sigma = 9.6$ GeV for the mass combination $M_h = 98$ GeV, $M_H = 300$ GeV [5].

The production of bottom quark in association with a pair of photons is the main irreducible background process. The processes $bj\gamma\gamma$, $c\bar{c}\gamma\gamma$, $cj\gamma\gamma$ and $jj\gamma\gamma$ can contribute as well if one of the jets from the charm quarks or a light jet is misidentified as b-jet.

With this search mode, only $\tan\beta \lesssim 4$ are accessible using 300 fb^{-1} of integrated luminosity. The mass of the heavier Higgs boson H must be in the range $2M_h < M_H < 2M_{top}$ [5].

Gluon fusion, $A \to Zh \to b\bar{b}ll$

The discovery of the A and h bosons at the same time may be possible in this channel. Also here, a cut analysis including mass windows for both Higgs bosons is used. To improve the final mass resolution, the b-jet four-momenta are rescaled to the expected value of M_h. M_A resolutions around 8 GeV can thus be achieved [5].

The most important background processes are irreducible $Zb\bar{b}$ and reducible $t\bar{t}$ production. Also contributions from ZZ, Zjj and ZW production are investigated. Using the above described procedure and 300 fb^{-1} of integrated luminosity, the two Higgs bosons can be observed in this channel for $\tan\beta \lesssim 4$ and in the mass range 200 GeV $< M_A < 2M_{top}$ [5].

Light charged Higgs bosons, $H^{\pm} \to \tau^{\pm}\nu$

In this search, the Higgs boson is produced in the decay of a top quark pair. For Higgs bosons which are lighter than the top quark, the $H^{\pm} \to \tau^{\pm}\nu$ branching ratio can be nearly 100%.

There are two different analysis strategies for this channel, one of them requiring the W

boson from the second top quark decay to decay leptonically to provide a lepton for triggering. Then, the Higgs boson mass cannot be reconstructed, but its presence manifests in an excess of τ-leptons after the cut analysis. A good understanding of the τ-lepton identification efficiencies and fake rates is therefore crucial [5].

The other strategy looks for a hadronically decayed W boson, relying on the τ-jet trigger. The best fitting combination of two light jets from the W boson decay and a bottom quark in the event is used to reconstruct the top quark for background rejection. Then, the transverse mass of the $H^{\pm}$ is calculated [91].

The main background process for both searches is $t\bar{t}$ production with Standard Model-like decays. With the two analyses, significances $> 5\sigma$ can be obtained for masses $\lesssim 150$ GeV with a data volume of 30 fb^{-1}, largely independent of $\tan\beta$ [5, 91].

Heavy charged Higgs bosons, $H^{\pm}\rightarrow\tau^{\pm}\nu$

In Ref. [92], also the transition region described in Chap. 5.1 is taken into account for this search channel. Moreover, the study is performed with the full detector simulation. To suppress background processes like $t\bar{t}$, W+jets and QCD jet production, the top quark is reconstructed from its decay products. Additionally, the W boson is required to decay hadronically. The four momentum vectors of all jet pair combinations inside a mass window around the W boson mass are rescaled to the nominal M_{W} value. The best combination of a light jet pair and a bottom quark that is found in the event is then assumed to originate from the top quark decay. The cut analysis is optimized separately for a low, a medium and a high mass region. The Higgs boson mass cannot be reconstructed. A cut on the transverse mass is not performed.

It is found that a 5σ discovery can be expected in this channel for a Higgs boson mass of 180 GeV for $\tan\beta \gtrsim 20$ using 30 fb^{-1}. For larger masses, larger $\tan\beta$ values are required, for example if the Higgs boson mass is 550 GeV, $\tan\beta \gtrsim 40$ allow for a discovery using the same integrated luminosity. Higgs boson masses in the transition region smaller than the top quark mass are also observable, nearly independent of $\tan\beta$ [92].

Heavy charged Higgs bosons, $H^{+}\rightarrow t\bar{b}/H^{-}\rightarrow\bar{t}b$

In this analysis, one of the two top quarks in the final state is required to decay semileptonically to assure efficient triggering. The other top quark is required to decay purely hadronically. The two top quarks are reconstructed by finding the best assignment of light jet pair, rescaled to the nominal W boson mass, and one b-jet to the first top quark and of the lepton, missing momentum and another b-jet to the second top quark. Doing so, the z-component of the missing momentum is calculated from the known W boson mass. The third b-jet in the final state is used to calculate the Higgs boson mass. The mass resolution is about 37 GeV for $M_{\mathrm{H}^{\pm}} = 250$ GeV [72].

Apart from the combinatorial background, large QCD background contributions like $t\bar{t}b$ and $t\bar{t}q$ production have to be suppressed. An excellent performance of the b-tagging algorithm is needed to suppress reducible background contributions.

Using a cut analysis method, this channel is promising for discovery for $\tan\beta \lesssim 2.5$ or $\tan\beta \gtrsim 25$ and for masses $\lesssim 400$ GeV with 30 fb^{-1} of integrated luminosity [72]. However, in the large $\tan\beta$ region, the $H^{\pm}\rightarrow\tau^{\pm}\nu$ search channel is more significant .

ATLAS discovery potential for Higgs bosons of the MSSM

In Refs. [83, 84, 93], a global analysis of the ATLAS discovery potential for MSSM Higgs bosons using a procedure similar to the one described in Chap. 7.1 is given. All SM and MSSM searches

presented above are taken into account. The evaluation of the discovery potential is done in the five different MSSM benchmark scenarios. It is found that in all four CP-conserving scenarios, at least one Higgs boson will be visible over the entire $M_{\mathrm{A}}/\tan\beta$ plane. The results for the M_{h}max Scenario are given in Fig. 5.7. In a large region at intermediate $\tan\beta$ values, only the lightest scalar Higgs boson will be observable. In that region, the discrimination between Standard Model and MSSM will not be straightforward. However, in parts of the parameter space, such a discrimination will be possible by measuring the couplings and branching ratios of the observed Higgs boson [93, 94]. The region where the ratio R of the $\mathrm{h}\to\tau\tau$ and $\mathrm{h}\to\mathrm{WW}$ branching ratios that can both be measured in the VBF production mode deviates more than $\Delta = (R_{\mathrm{MSSM}} - R_{\mathrm{SM}})/\sigma_{\mathrm{exp}} = 1$ ($\Delta = 2$) from the Standard Model expectations are marked by red/dark grey (black) hatched areas in Fig. 5.7. The quantity σ_{exp} is the experimental error on the measurement of the ratio R.

Already with 30 fb^{-1}, it is possible to observe one scalar Higgs boson in the entire plane for the four CP-conserving benchmark scenarios using the vector boson fusion search channels only. The results for the M_{h}max Scenario are given in Fig. 5.8. Searches for other production modes need higher integrated luminosities for complete coverage of the $\mathrm{M_A}/\tan\beta$ plane.

In the CPX Scenario, the entire $\tan\beta/M_{\mathrm{H}^\pm}$ plane[3] can be covered with the exception of a small region at $\tan\beta \approx 5$ and $M_{\mathrm{H}^\pm} \approx 145$ GeV. In Ref. [95], a search for the decay chain $\mathrm{t\bar{t}}\to\mathrm{\bar{b}bW^\pm H^\pm}\to\mathrm{\bar{b}bl^\pm}\nu\mathrm{hW^\pm}\to\mathrm{\bar{b}b\bar{b}bl^\pm}\nu\mathrm{jj}$, where a light, neutral Higgs boson is produced in the decay of the charged Higgs boson, is proposed. This channel seems promising for covering the gap [96].

Accordingly, the ATLAS experiment has very good prospects to observe at least one Higgs boson of the MSSM if this model is realized in nature. Especially in the large and small $\tan\beta$ regions, also more than one Higgs boson is observable, which would be evidence for physics beyond the Standard Model.

5.5 Summary of the SM and MSSM searches

The prospects for finding a Standard Model or MSSM Higgs boson at the ATLAS experiment are very good. The results of the searches listed here are used as a basis for the evaluation of the ATLAS discovery potential for NMSSM Higgs bosons that is described in Chap. 7 of this work.

While this thesis is written, a major effort of the ATLAS collaboration is being made in order to evaluate the discovery potential of the most important search modes with the full detector simulation and a realistic detector design. Results from these so-called CSC[4] studies will be available in the course of the current year.

[3] As in this scenario, all neutral Higgs bosons mix, $M_{\mathrm{H}^\pm}$ is used instead of M_{A} as a free parameter.

[4] Computing System Commissioning, an effort to test the ATLAS computing system and data processing chain.

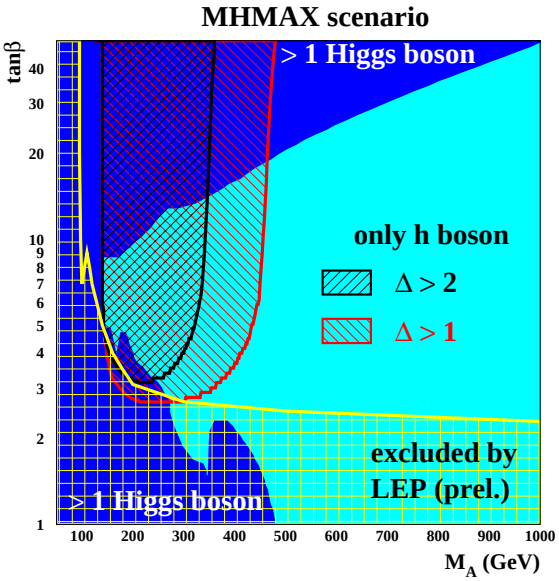

Fig. 5.7: 5σ discovery contours for different MSSM Higgs bosons in the $\tan\beta/M_{\mathrm{A}}$ plane of the M_{h}max Scenario with 300 fb^{-1} [93]. In the turquoise/light grey region, only the h boson, in the dark blue/dark grey region, more than one Higgs boson, are observable. For an explanation of Δ see the text.

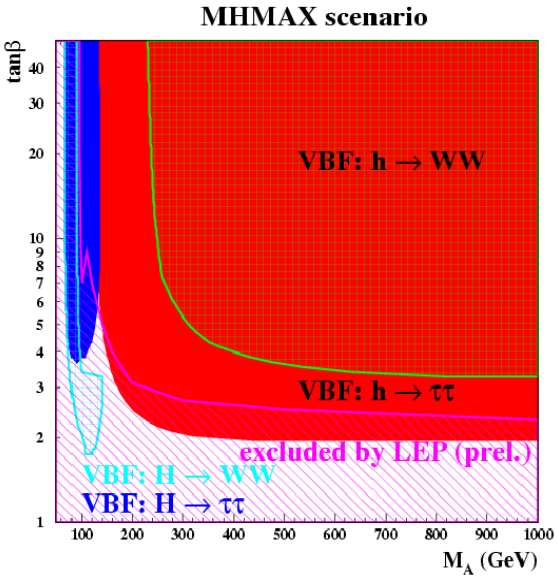

Fig. 5.8: 5σ discovery contours for Higgs boson searches in the vector boson fusion production mode in the $\tan\beta/M_{\mathrm{A}}$ plane of the M_{h}max Scenario with 30 fb^{-1} [83]. In the red/medium grey (dark blue/dark grey) region, the h(H)$\rightarrow\tau\tau$, in the green/light grey (turquoise/light grey)-hatched region, the h(H)$\rightarrow$WW decays are observable.

6. Development of benchmark scenarios for the NMSSM

6.1 Introduction to the benchmark scenarios

In the past, proposals for interesting points in the six-dimensional parameter space of the unconstrained NMSSM have been made [97–100]. A recent study also proposes benchmark points for the constrained NMSSM [47].

To evaluate the discovery potential for NMSSM particles such as the seven Higgs bosons at collider experiments like the LHC, it is furthermore desirable to define benchmark planes which include regions of typical and experimentally challenging NMSSM phenomenology. Unlike discrete points in the parameter space, planes provide a smooth variation of the model parameters and can give a better feeling for the position and size of regions of a certain phenomenology, also with respect to exclusion bounds, and for the dependence of the discovery potential on the model parameters. In the context of this thesis, six such parameter planes within three different scenarios for the Higgs sector of the unconstrained NMSSM and one plane for the cNMSSM are developed and studied. The number of planes proposed for the unconstrained NMSSM is larger than for the cNMSSM, because the constrained model allows only for a limited number of phenomenology types. All scenarios include one or more benchmark points from Refs. [47, 99, 100].

For the benchmark planes, only two of the six parameters of the Higgs sector of the unconstrained NMSSM are varied simultaneously, as variation of more parameters would lead to considerably longer program run times and the results would be difficult to visualize. Therefore, two-dimensional planes in the six-dimensional parameter space of the NMSSM Higgs sector are proposed. To further reduce the complexity of the parameter space to a manageable level, a choice of three sets of parallel planes is made. The four-point couplings λ and κ are varied simultaneously, as well as the three-point coupling parameters A_λ and A_κ, and the two remaining parameters μ and $\tan\beta$. This choice is arbitrary, as there is no preference from theory which combination of parameters to vary [101]. For example, also the λ/A_λ and κ/A_κ planes might be interesting. However, the current choice provides sufficient material for a detailed evaluation of the Higgs boson discovery potential.

For all scenarios of the unconstrained NMSSM presented in this chapter, a λ/κ plane is proposed as possible benchmark. A_λ/A_κ and $\mu/\tan\beta$ planes are proposed additionally if the allowed parameter region has interesting features not yet covered by previously proposed planes. For the constrained NMSSM, a $\lambda/A_{\kappa(\mathrm{GUT})}$ plane is chosen, as it includes three benchmark points from Ref. [47]. An overview of the proposed benchmark scenarios and planes is sketched in Fig. 6.1.

The parameter planes are scanned in a grid of typically 250×250 scan points. To calculate the NMSSM particle spectra and exclusion constraints for each scan point, the program package NMSSMTOOLS [102] is used. The programs NMHDECAY [103] for the unconstrained NMSSM and NMSPEC [104] for the constrained NMSSM are included in this package. Suitable looping and output routines are added to the programs where necessary. To extract the couplings of the neutral Higgs bosons to gluons[1], that include relevant radiative corrections, and the $\mathrm{H}^\pm\mathrm{tb}$

[1] As in the Standard Model, the NMSSM Higgs bosons cannot directly couple to massless particles, so that they can only couple to gluons via loops including massive particles. The dominant contributions come from top

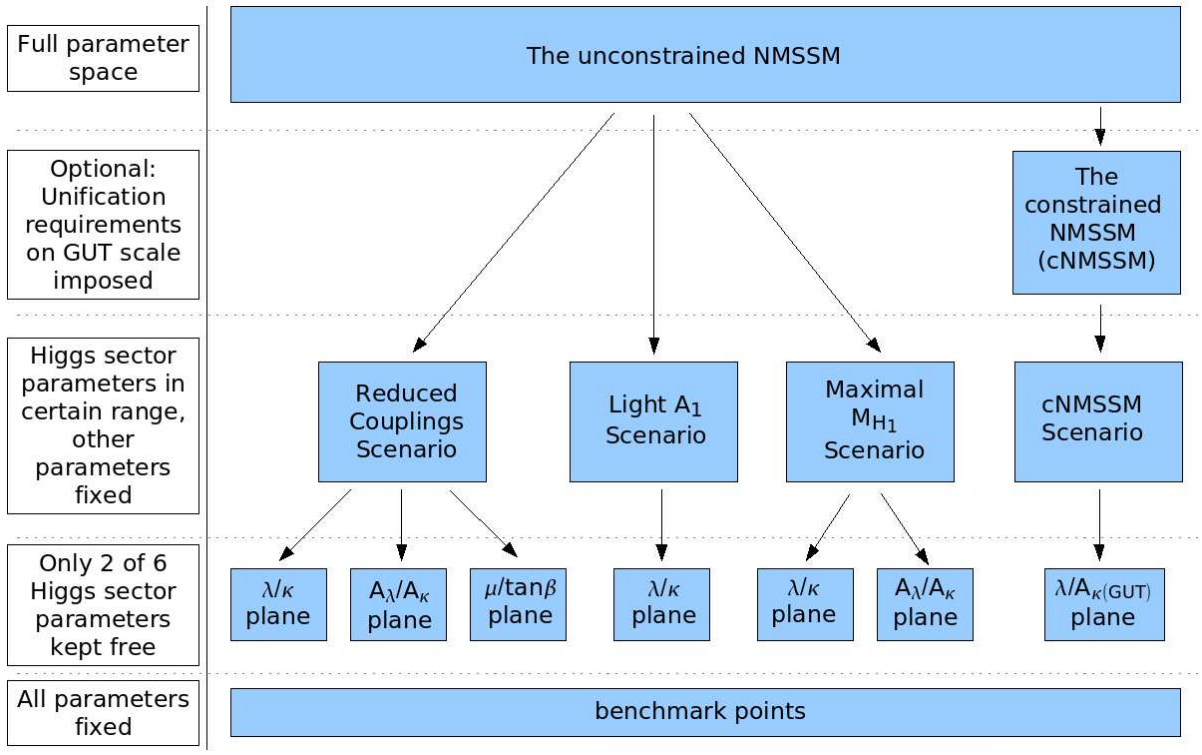

Fig. 6.1: Flowchart for the reduction of complexity in the parameter space of the NMSSM, including the benchmark scenarios and benchmark planes proposed in this thesis. All proposed benchmark scenarios include at least one benchmark point from previous publications [47, 99, 100].

coupling of the charged Higgs bosons that is not provided by NMSSMTOOLS, special procedures are developed. For details see Apps. A and B. The top quark mass is set to 172 GeV throughout this thesis. This is consistent with the current world average mass of the top quark of (172.6 ± 1.4) GeV [22].

6.1.1 Exclusion criteria

In the first step, different exclusion criteria are applied to each point of the scanning grid by the NMSSMTOOLS package. In this thesis, it is distinguished between constraints from theory and from experiment. The following cases lead to exclusion of a scan point from theoretical arguments:

- λ, κ, μ or $\tan\beta$ are identical to zero. In these cases, NMSSMTOOLS cannot calculate the particle spectra.
- Negative mass squares occur. In this case, NMSSMTOOLS cannot calculate the particle spectra.
- No electroweak symmetry breaking takes place. NMSSMTOOLS checks whether the physical minimum of the potential (i.e. where all vacuum expectation values are non-zero) is deeper than the local unphysical minima with vanishing H_u or H_d.

and bottom quarks.

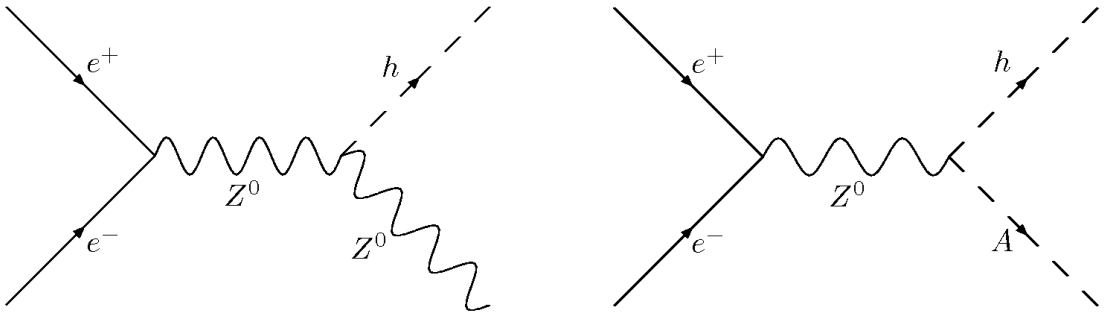

Fig. 6.2: Example Feynman diagrams for the production of Higgs bosons at LEP. Left hand side: hZ production. Right hand side: hA pair production.

- The Yukawa couplings λ, κ encounter a Landau pole below the GUT scale (see Chap. 2.1.3).
- The LSP carries electric or color charge.

Experimental constraints include:

- Limits on the masses of the neutralinos and on their couplings to the Z^0 boson. These limits are obtained from direct searches at the LEP experiment [105] and from the LEP limit on the invisible Z^0 width [38].
- Bounds from LEP and Tevatron[2] on the charged particle masses and the gluino mass [106, 107].
- Constraints on Higgs boson production rates and branching ratios from various channels studied at LEP, based on Ref. [108]. These include searches for hZ production (Fig. 6.2, left hand side) with subsequent Higgs boson decay to Standard Model particles or to a pair of light pseudoscalar Higgs bosons. Also the combined production of a scalar and a pseudoscalar Higgs boson (Fig. 6.2, right hand side) with various decays to Standard Model particles and in case of the scalar Higgs boson also to a pair of pseudoscalars is considered.
- Experimental constraints from b-physics on the measured branching ratios of rare decays and on the mass differences of the two mass eigenstates of the B_s^0 (ΔM_s) and of the B_d^0 (ΔM_d) [109]. These b-physics quantities can be affected by loop diagrams containing supersymmetric particles and/or Higgs bosons. Some examples are given in Figs. 6.3 and 6.4.

For all experimental constraints, a 95% confidence level exclusion is required. If both bounds from theory and from experiment lead to the exclusion of a scan point, this point is labeled as excluded by theory. Not in all proposed scenarios, each of the criteria listed above contributes to the exclusion bounds. The relevant exclusion criteria are listed in the descriptions of the scenarios. All constraints are taken into account separately, i.e. the limits are not combined by NMSSMTOOLS. Although a combination of different limits might lead to stricter exclusion bounds, its implementation is beyond the scope of this thesis.

[2] A proton-antiproton collider currently running at Fermilab, USA.

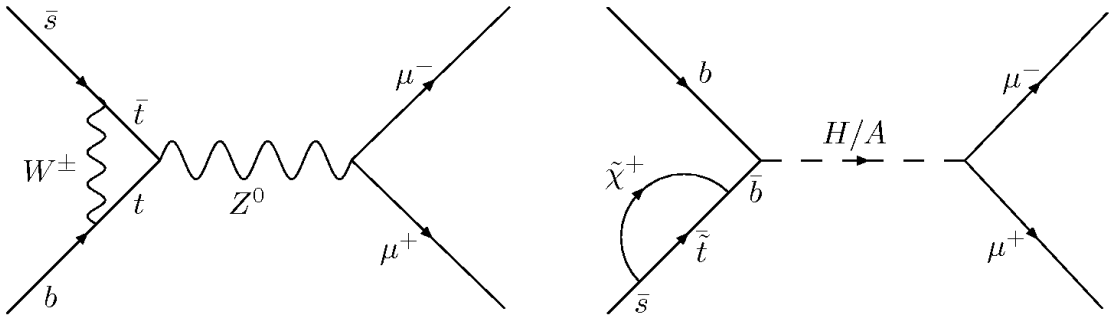

Fig. 6.3: Example Feynman diagrams for the $B_s \to \mu\mu$ process. Left hand side: The Standard Model process. Right hand side: Neutral current contribution in supersymmetric Models. This diagram is enhanced at large $\tan\beta$.

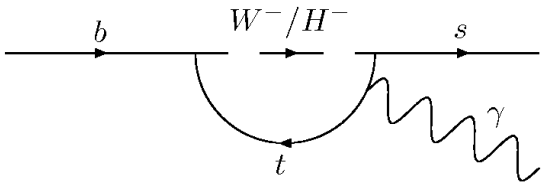

Fig. 6.4: Example Feynman diagram for the $b \to s\gamma$ process. In extended models, a charged Higgs boson can contribute in the loop. In supersymmetric models, also diagrams with a gluino/squark loop and a neutralino/squark loop exist.

6.2 The Reduced Couplings Scenario

Due to a possible mixing with the gauge singlet states (Chap. 2.3), the NMSSM Higgs bosons can have couplings to fermions or gauge bosons that are significantly smaller than in the Standard Model or the MSSM case. In the following, this will be referred to as reduced couplings[3]. A light scalar with reduced couplings and a mass below 114 GeV may still not be excluded by LEP, since the LEP mass limit assumes Standard Model-like couplings. Moreover, since the Higgs boson production cross sections are proportional to the square of the relevant coupling, reduced couplings can result in largely reduced signal rates. The discovery of such Higgs bosons might therefore be difficult.

In Ref. [99], a random scan of the six-dimensional parameter space of the Higgs sector of the unconstrained NMSSM is performed in order to find parameter points with interesting phenomenology. The first point from Tab. 6.1 has the lowest statistical significance found by this scan in a region without Higgs-to-Higgs decays. At this point, all Higgs bosons have similar masses ranging from about 90 to 160 GeV. The low discovery potential is at the one hand due to a rather low mass of the most Standard Model-like Higgs boson of about 114 GeV, on the other hand due to the small couplings of this Higgs bosons to fermions and vector bosons that are reduced to about 56-75% of their Standard Model values. This point is included in all proposed benchmark planes of this scenario.

[3] In the following, the term 'reduced couplings' only refers to the couplings of the Higgs bosons to vector bosons, up-type fermions and gluons, but excludes the couplings to bottom quarks unless otherwise noted. The couplings to bottom quarks are often enhanced with respect to the Standard Model, but are still too small to have an impact on the Higgs boson discovery potential for most of the here proposed benchmark planes with $\tan\beta$ values around 2 and 10.

NMSSM point	λ	κ	A_λ [GeV]	A_κ [GeV]	μ [GeV]	$\tan\beta$	Ref.
Reduced couplings	0.016	-0.0034	-70	-54	-284	5.7	[99]
Light $A_1 \to \tau\tau$	0.22	-0.1	-580	-2.8	-520	5.0	[99]
Maximal H_1 mass	0.678	0.067	1530	10	620	2.14	[100]

Tab. 6.1: Benchmark points from earlier publications that are covered by the proposed two-dimensional parameter planes for the unconstrained NMSSM.

NMSSM scenario	plane	λ	κ	A_λ [GeV]	A_κ [GeV]	μ [GeV]	$\tan\beta$
Reduced couplings	λ/κ	0 - 0.025	-0.005 - 0	-70	-54	-284	5.7
Reduced couplings	A_λ/A_κ	0.016	-0.0034	-500 - 0	-250 - 0	-284	5.7
Reduced couplings	$\tan\beta/\mu$	0.016	-0.0034	-70	-54	-350 - -50	1 - 50
Light A_1	λ/κ	0 - 0.55	-0.2 - 0.6	-580	-2.8	-520	5.0
Maximal M_{H_1}	λ/κ	0.52 - 0.72	0.01 - 0.09	1530	10	620	2.14
Maximal M_{H_1}	A_λ/A_κ	0.71	0.065	1530	10	620	2.14

Tab. 6.2: Parameter settings of the two-dimensional benchmark planes for three scenarios for the unconstrained NMSSM.

With the new version of NMHDECAY used for this thesis and a top quark mass of 172 GeV instead of 175 GeV as in the original publication, the point from Ref. [99] is labeled as excluded by LEP. The unexcluded points in its vicinity, eg. with $\lambda = 0.016$ and $\kappa = -0.0033$ or with $\lambda = 0.0165$ and $\kappa = -0.0034$, show a similar phenomenology with slightly less suppressed couplings (around 60-80% of the Standard Model values) and are not yet ruled out. Using such an unexcluded point as common point of the parameter planes would only marginally alter the phenomenology included in these planes, so for simplicity, the original point from Ref. [99] is kept.

For the Reduced Couplings Scenario of the unconstrained NMSSM, the mass parameters are chosen as $M_1 = 500$ GeV, $M_2 = 1$ TeV, $M_3 = 3$ TeV and $M_{\rm susy} = 1$ TeV as in Ref [99]. The trilinear soft supersymmetry-breaking parameters are set to $A_t = A_b = A_\tau = 1.5$ TeV. This choice is in principle arbitrary, but is appropriate to obtain the desired phenomenology. Moreover, with such a choice, the squarks and sleptons will be at the edge of the discovery reach of the LHC and the Higgs bosons might therefore be the only observable sign for new physics [99]. For an explanation of the parameters $M_{1/2/3}$, $M_{\rm susy}$ and $A_{t/b/\tau}$, see Chap. 2.2.

6.2.1 The λ/κ benchmark plane

Exclusion limits The parameter settings of this plane are given in the first row of Tab. 6.2. An overview of the allowed parameter region and the relevant exclusion criteria is given in Fig. 6.5. The white parameter region of Fig. 6.5 is not ruled out. The regions at large negative κ[4] and small λ and at small negative κ and large λ are theoretically inaccessible due to the occurrence of negative mass squares. There is also a band where no electroweak symmetry breaking takes place.

Among the experimental constraints, mainly the LEP bounds for the hZ process are im-

[4] In the following, terms like 'large κ' and 'small κ' will often be used to describe the position of regions inside the plane. Terms like 'large' and 'small' are then meant respectively to the κ range covered by the plane. The same is true also for the other Higgs sector parameters and other planes. Actually, the value of κ is in this plane very small compared to the full parameter space.

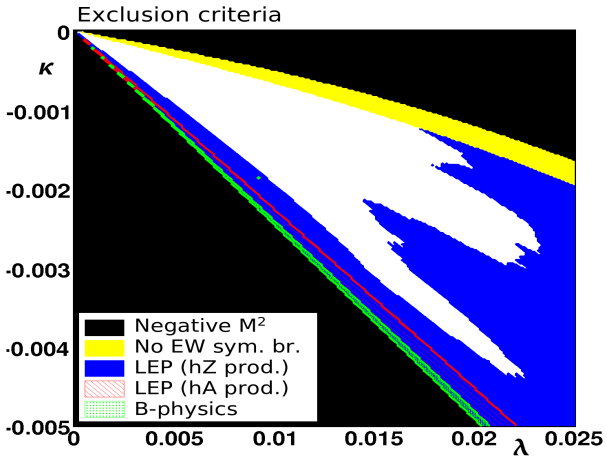

Fig. 6.5: Exclusion criteria in the Reduced Couplings Scenario, λ/κ plane.

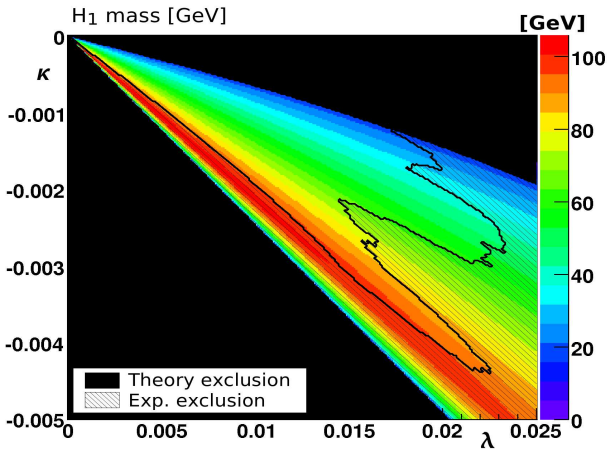

Fig. 6.6: H_1 mass (color coded) in the Reduced Couplings Scenario, λ/κ plane.

portant, especially those for the decay chains h→b$\bar{\text{b}}$ and h→2 jets. There are also smaller contributions from the hZ, h→$\tau\tau$ search and from a hZ search that is independent of the Higgs boson decay. In the region with large negative κ not yet ruled out by theory, also the searches for hA→4b, hA→2b2τ and hA→4τ contribute, as well as the bound on hA production from the measurement of the Z^0 width. The complicated shape of the experimentally excluded region mirrors the fact that LEP exclusion limits on the relevant Higgs boson production rates and branching ratios are measured separately for different Higgs boson mass assumptions and are thus influenced by different statistical fluctuations for each measurement. Also limits from the b-physics processes b→sγ and B_s→$\mu\mu$ and on the mass differences ΔM_s and ΔM_d apply in a small region.

Higgs boson masses and Higgs-to-Higgs decays In this plane, the masses of all seven Higgs bosons are smaller than about 300 GeV and thus in a range that is well accessible by the current ATLAS Higgs boson search strategies. The H_1 is very light with masses as low as about 20 GeV in an unexcluded region at small negative κ (Fig. 6.6). Since the H_2 has a mass around 115 to 120 GeV in the entire plane (Fig. 6.7), there is a region where the decay H_2→H_1H_1 is allowed (Fig. 6.10). In the white region of Fig. 6.10, the decay is forbidden. The light H_1 is composed to a large fraction of the gauge singlet state in the region where the H_2→H_1H_1 decay is allowed. The couplings of this state (i.e. λ, κ) are rather small in this scenario. For this reason, the H_2→H_1H_1 branching ratio is small for all parameter planes of the Reduced Couplings Scenario presented in this work. In the λ/κ plane, the branching ratio is at maximum 6% in the unexcluded region.

The A_1 mass ranges from about 55 to 100 GeV in the allowed parameter region (Fig. 6.8). The H_3, A_2, and $H^\pm$ bosons are approximately degenerate in the entire plane, but with small differences in mass for large negative κ. The mass of the H_3 ranges from about 150 to 300 GeV, the mass of the A_2 from about 140 to 300 GeV and the charged Higgs boson mass from about 165 to 300 GeV in the unexcluded region (Fig. 6.9). Only in the excluded region, the $H^\pm$ bosons are light enough to be produced in top quark decays.

Couplings Figures 6.11 to 6.13 show the couplings of the scalar Higgs bosons to vector bosons in terms of the couplings of a Standard Model Higgs boson of the same mass. They vary similarly to the couplings to up-type fermions (Figs. 6.14 to 6.16). Also the couplings to gluons show a similar pattern, although with some notable deviations (Figs. 6.17 to 6.19). These couplings are

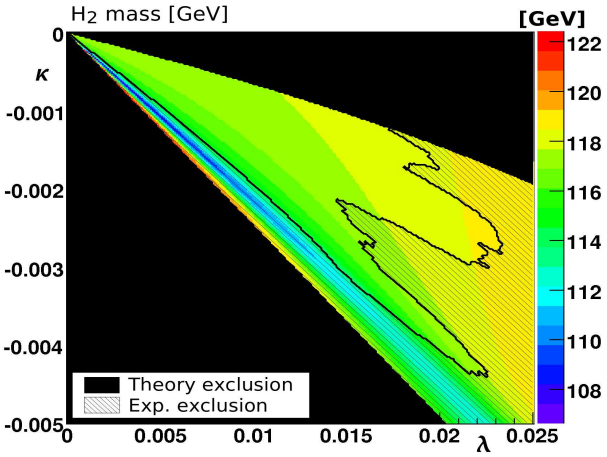

Fig. 6.7: H_2 mass (color coded) in the Reduced Couplings Scenario, λ/κ plane.

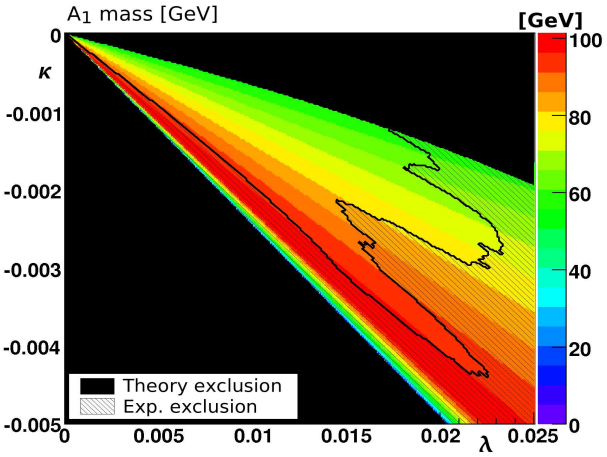

Fig. 6.8: A_1 mass (color coded) in the Reduced Couplings Scenario, λ/κ plane.

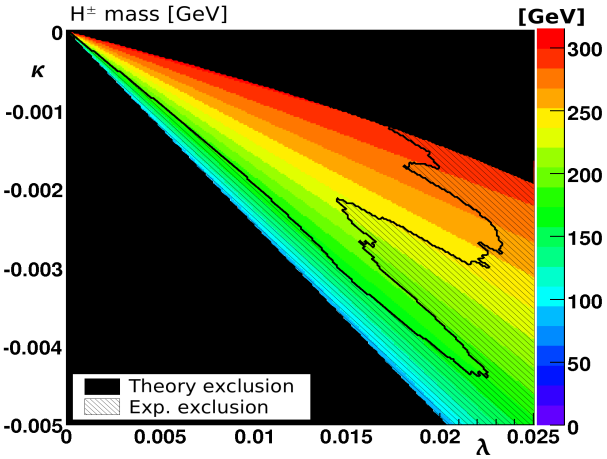

Fig. 6.9: $H^{\pm}$ mass (color coded) in the Reduced Couplings Scenario, λ/κ plane.

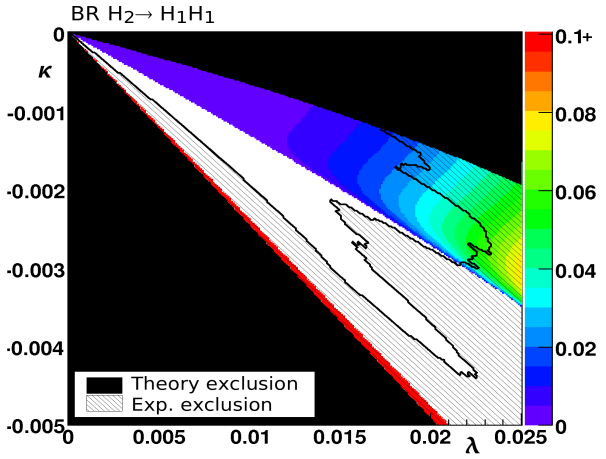

Fig. 6.10: $H_2 \rightarrow H_1H_1$ branching ratio (color coded) in the Reduced Couplings Scenario, λ/κ plane.

relevant for the Higgs boson discovery potential. The coupling to up-type fermions determines the size of the ttH production cross section, the coupling to gluons the size of the gluon fusion cross sections and the coupling to vector bosons influences the vector boson fusion and WH, ZH production cross sections. The similar behavior of the three couplings here and in other scenarios can be explained by the coupling sizes in Tab.2.1, the $\tan\beta$ value used and by the fact that the reduction of the couplings is in part determined by the mixing with the gauge singlet state. For the couplings to gluons, additional effects may occur due to the contribution from a bottom quark loop, which has a different dependence on the model parameters than the top quark loop. From here on, only the couplings to vector bosons will be given as example couplings when the other couplings are similar to them with respect to the Standard Model. Relevant exceptions will be noted.

Moreover, as can also be seen in this plane, the couplings of different Higgs bosons often vary inversely, eg. if the coupling of one scalar boson increases, the same coupling of another scalar boson decreases. A similar behavior exists also for the couplings of the h and H in the MSSM.

According to Tab. 2.1, in the MSSM, the couplings of one scalar Higgs boson varies with $\cos\alpha$ or $\cos(\beta-\alpha)$, while the couplings or the other scalar boson varies with $\sin\alpha$ or $\sin(\beta-\alpha)$. This is also the case for the NMSSM, but in addition, the inversely varying couplings can partly also be explained by a shifting of the admixed fraction of the singlet state from one Higgs boson to the other.

The couplings of the H_1 and H_3 are heavily suppressed in large parts of the parameter plane. They reach sizeable values only in the excluded region at large negative κ. The H_2 has Standard Model-like couplings in large parts of the parameter plane. However, its coupling to gluons remains somewhat below its Standard Model value, being largest for small negative κ. In the unexcluded region close to the benchmark point from Ref. [99], its coupling to vector bosons is reduced to about 80% of its Standard Model value, its coupling to up-type fermions to about 70% and its coupling to gluons even to about 60%. The couplings of the A_1 and A_2 are heavily suppressed in the entire plane. The combined cross section of the processes $gb\to tH^-$ and $g\bar{b}\to\bar{t}H^+$ stays below 0.35 pb (Fig. 6.20), since the intermediate $\tan\beta$ value of 5.7 does not yield a large $H^\pm tb$ coupling according to Eq. 2.60. In the white region of Fig. 6.20, the cross section cannot be calculated (see App. B).

Summary of the Reduced Couplings Scenario, λ/κ benchmark plane In the λ/κ benchmark plane of the Reduced Couplings Scenario, the H_2 is most promising for discovery. Although the other Higgs bosons have low masses, their couplings are heavily reduced in the allowed region and they accordingly have very small production rates. This plane is characterized by a region with a very light H_1 for small negative κ, where the $H_2\to H_1H_1$ decay is possible, but only with a small maximal branching ratio of 6%, a region with a purely Standard Model-like H_2 in the middle of the allowed parameter space, and a region with reduced couplings of the H_2 for large negative κ.

6.2.2 The A_λ/A_κ benchmark plane

Exclusion limits The parameters of this A_λ/A_κ plane can be found in the second row of Tab. 6.2. The allowed region is bound by the occurrence of negative mass squares at large negative $A_\kappa \approx -235$ GeV and at small negative $A_\lambda \approx -60$ GeV (Fig. 6.21). Positive values of the three-point coupling parameters A_λ, A_κ are excluded as well. For A_κ smaller than about -180 GeV, no electroweak symmetry breaking takes place.

Among the experimental constraints, again the LEP searches for hZ, $h\to b\bar{b}$ and hZ, $h\to 2$ jets give the most important limits, but there are also contributions from the hZ search independent of the Higgs boson decay, from searches for $hA\to 4b$ and $hA\to 2b2\tau$ and from the limits on hA production from the measurement of the Z^0 boson width. In a small region at small negative A_λ, also the experimental limit on the branching ratio of the $b\to s\gamma$ decay is relevant for this plane. In principle, it would be possible to extend the plane to A_λ values smaller than -500 GeV, but since no new model features would be included by that, this is not done in this work.

Higgs boson masses and Higgs-to-Higgs decays The mass of the lightest scalar H_1 primarily varies with A_κ from about 60 to 113 GeV in the unexcluded region (Fig. 6.22). As in the λ/κ plane, the H_2 has a mass around 120 GeV with significantly smaller values only in the excluded region (Fig. 6.23). Since the H_1 mass is not as small as in the λ/κ plane, the $H_2\to H_1H_1$ decay is only possible in a very restricted region around $A_\kappa \approx -175$ GeV and its branching ratio does not exceed 1.5% (Fig. 6.26). In the white region of Fig. 6.26, no decays of the H_2 to other Higgs bosons are allowed. The mass of the A_1 varies with A_κ as λ, κ, μ and $\tan\beta$ are kept fixed in this plane (Eq. 2.68). It varies inversely to the H_1 mass, i.e. it is small for small negative A_κ

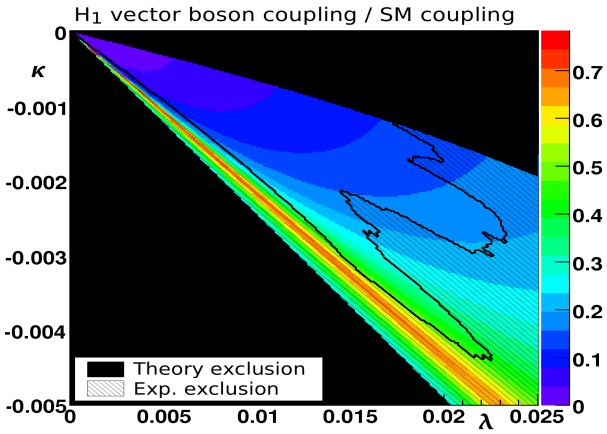

Fig. 6.11: H_1 vector boson coupling (color coded) in the Reduced Couplings Scenario, λ/κ plane.

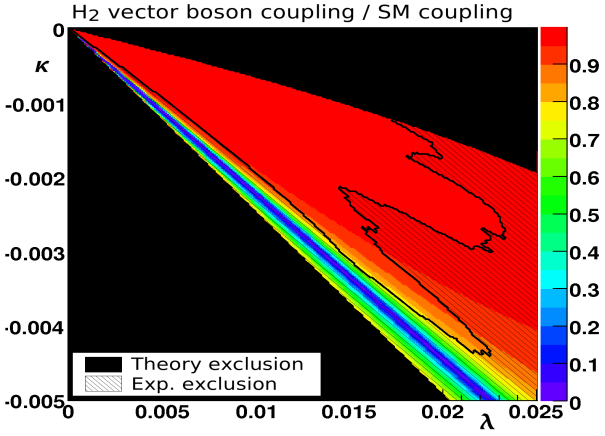

Fig. 6.12: H_2 vector boson coupling (color coded) in the Reduced Couplings Scenario, λ/κ plane.

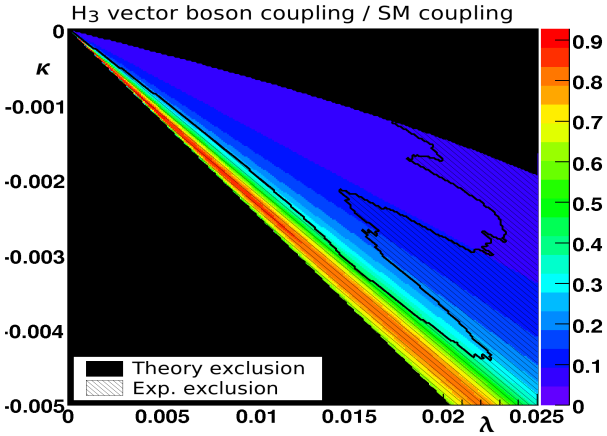

Fig. 6.13: H_3 vector boson coupling (color coded) in the Reduced Couplings Scenario, λ/κ plane.

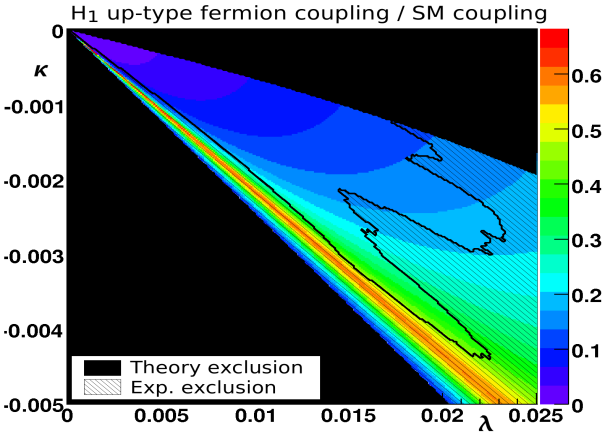

Fig. 6.14: H_1 up-type quark coupling (color coded) in the Reduced Couplings Scenario, λ/κ plane.

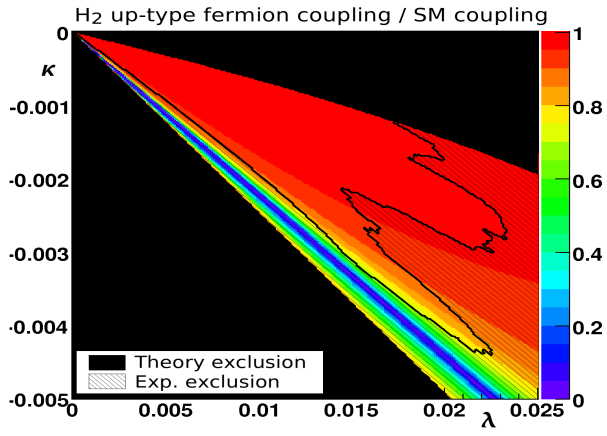

Fig. 6.15: H_2 up-type quark coupling (color coded) in the Reduced Couplings Scenario, λ/κ plane.

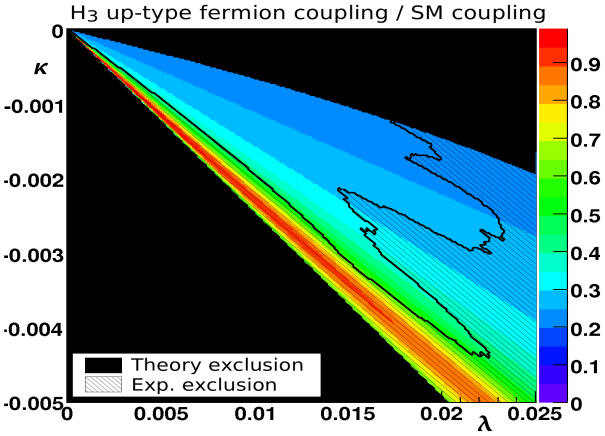

Fig. 6.16: H_3 up-type quark coupling (color coded) in the Reduced Couplings Scenario, λ/κ plane.

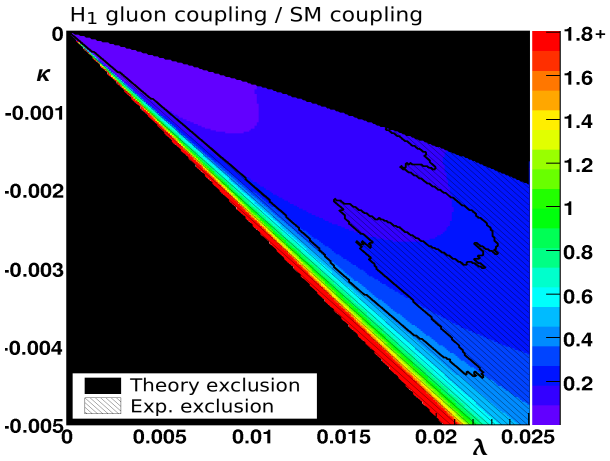

Fig. 6.17: H_1 gluon coupling (color coded) in the Reduced Couplings Scenario, λ/κ plane.

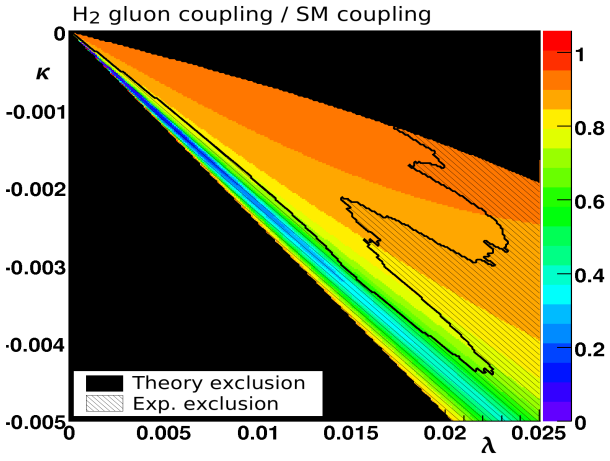

Fig. 6.18: H_2 gluon coupling (color coded) in the Reduced Couplings Scenario, λ/κ plane.

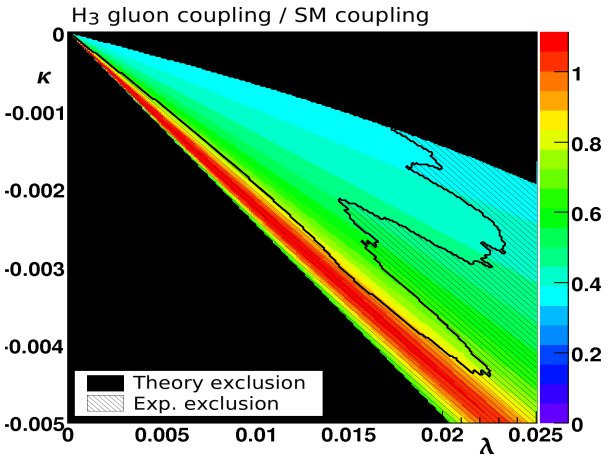

Fig. 6.19: H_3 gluon coupling (color coded) in the Reduced Couplings Scenario, λ/κ plane.

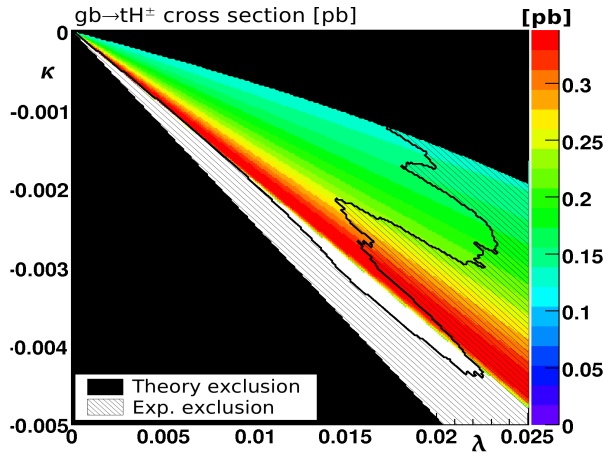

Fig. 6.20: $gb\to tH^-/g\bar{b}\to\bar{t}H^+$ cross section (color coded) in the Reduced Couplings Scenario, λ/κ plane.

(Fig. 6.24) and ranges from values close to zero to about 180 GeV in the unexcluded region. The decay chain $H_2\to A_1A_1$ with branching ratios smaller than 1% is negligible (Fig. 6.26). In contrast to the A_1, the masses of the heavier Higgs bosons H_3, A_2 and $H^\pm$ vary with A_λ as λ, κ, μ and $\tan\beta$ are kept fixed (Eqs. 2.67, 2.69, 2.71). These bosons are approximately degenerate in the entire parameter plane, but with some differences at small negative A_λ. The mass of the H_3 varies from about 155 to 850 GeV, the A_2 mass from about 145 to 850 GeV and the charged Higgs boson mass from about 165 to 850 GeV (Fig. 6.25). The $H^\pm$ bosons are light enough to allow for $t\to H^+b/\,\bar{t}\to H^-\bar{b}$ decays only in the excluded region at small negative $A_\lambda \gtrsim -70$ GeV.

Couplings In Figs. 6.27 to 6.29, the couplings of the scalar Higgs bosons to vector bosons are given as example couplings. In large parts of the parameter space, the H_2 has Standard Model-like couplings. However, its coupling to gluons stays below its Standard Model value in a large part of the parameter plane (Fig. 6.31). There are two unexcluded regions with

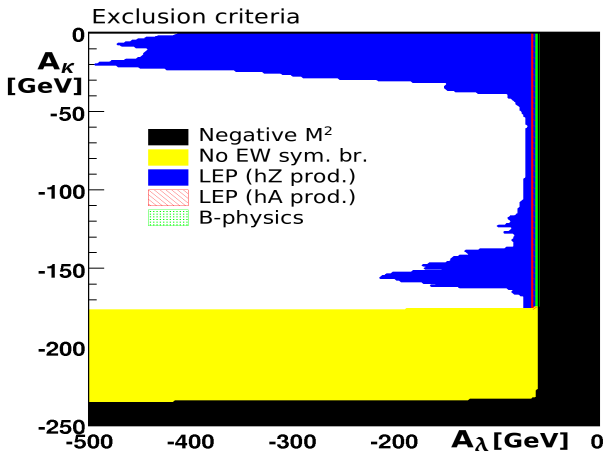

Fig. 6.21: Exclusion criteria in the Reduced Couplings Scenario, A_λ/A_κ plane.

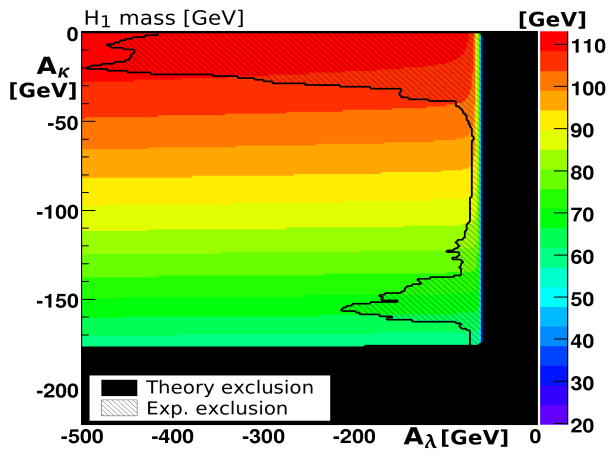

Fig. 6.22: H_1 mass (color coded) in the Reduced Couplings Scenario, A_λ/A_κ plane.

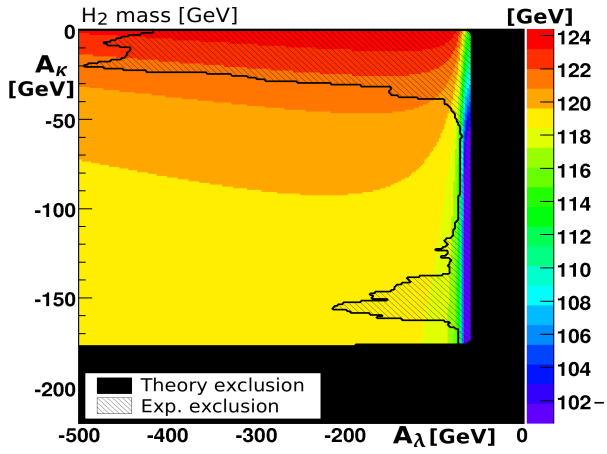

Fig. 6.23: H_2 mass (color coded) in the Reduced Couplings Scenario, A_λ/A_κ plane.

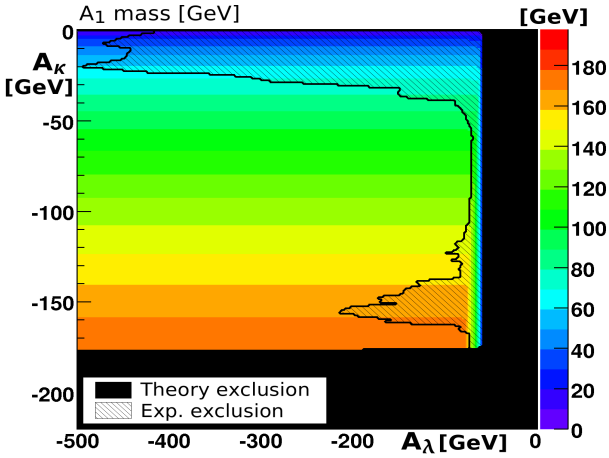

Fig. 6.24: A_1 mass (color coded) in the Reduced Couplings Scenario, A_λ/A_κ plane.

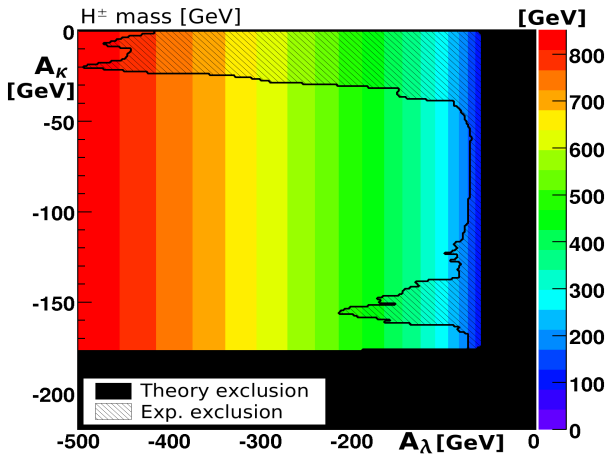

Fig. 6.25: $H^\pm$ mass (color coded) in the Reduced Couplings Scenario, A_λ/A_κ plane.

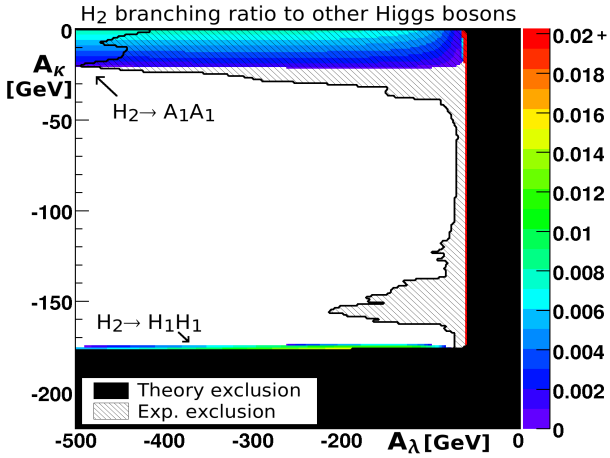

Fig. 6.26: H_2 branching ratio (color coded) to other Higgs bosons in the Reduced Couplings Scenario, A_λ/A_κ plane.

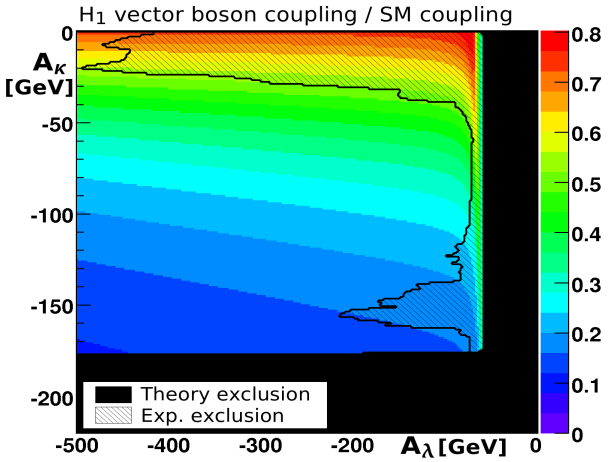

Fig. 6.27: H_1 vector boson coupling (color coded) in the Reduced Couplings Scenario, A_λ/A_κ plane.

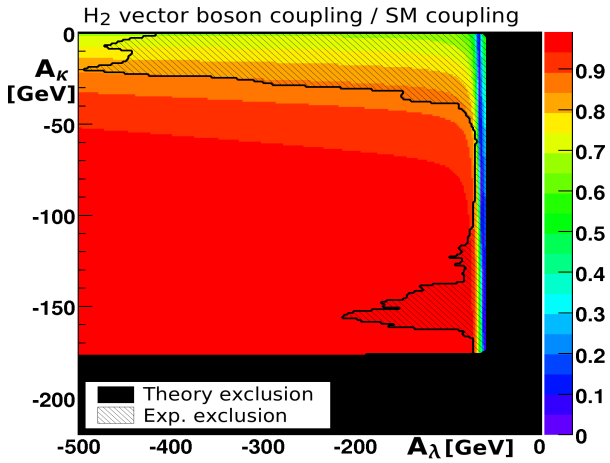

Fig. 6.28: H_2 vector boson coupling (color coded) in the Reduced Couplings Scenario, A_λ/A_κ plane.

reduced couplings of the H_2 which are not yet ruled out. The first one is located around the original point from Ref. [99] at small negative $A_\lambda \approx -70$ GeV, where its coupling to vector bosons reaches about 80% of its Standard Model value. The other region lies at small negative $A_\kappa \gtrsim -30$ GeV, where the H_2 couplings are reduced to values smaller than 70% of their Standard Model values. However, in the latter region, the couplings of the H_1, that are otherwise much reduced throughout the parameter plane, also reach about 70% of their Standard Model values (Figs. 6.27, 6.30). In this region, the H_1 mass is about 110 GeV, so that the discovery potential of the relevant Higgs boson searches is reasonably large for the H_1, too. Since the natural line widths of the H_1 and H_2 bosons are only about 2 MeV, it might be possible to observe the decay products of both the H_1 and H_2 separately in that region.

The couplings of the H_3 and the A_1 are reduced in the entire unexcluded region. However, they are Standard Model-like or enhanced in the excluded region at small negative $A_\lambda \gtrsim -70$ GeV. The couplings of the heavier pseudoscalar A_2 are negligible in the entire plane. Also in this plane, the cross section of the $gb \to tH^-/g\bar{b} \to \bar{t}H^+$ process is below 0.35 pb (Fig. 6.32). In the white region of Fig. 6.32, the cross section cannot be calculated (see App. B).

Summary of the Reduced Couplings Scenario, A_λ/A_κ benchmark plane Also in the A_λ/A_κ plane of the Reduced Couplings Scenario, the H_2 ist most promising for discovery. The $H_2 \to H_1H_1$ decay is allowed in parts of the plane, but has only a low branching ratio. This benchmark plane includes a region with reduced couplings similar to the one of the λ/κ plane. Additionally, there exists a region where the scalar Higgs bosons H_1 and H_2 both have reduced couplings and are in a mass range promising for discovery, so that they might be observable separately. For both of these bosons, the production cross sections are smaller than in the Standard Model, but as they are similar in mass, their contributions to some search modes might add up and help to retain a good discovery potential. Moreover, in this plane there is a larger variation of the Higgs boson masses than in the λ/κ plane.

6.2.3 The $\mu/\tan\beta$ benchmark plane

Exclusion limits This plane is presented here in order to also investigate the phenomenology at large $\tan\beta$. The relevant parameter settings are given in the third row of Tab. 6.2. In this

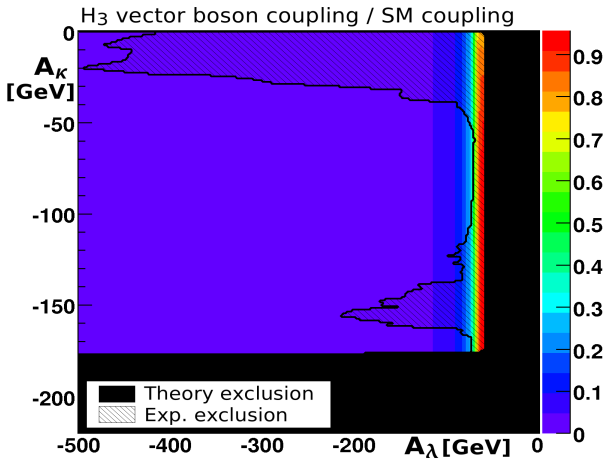

Fig. 6.29: H_3 vector boson coupling (color coded) in the Reduced Couplings Scenario, A_λ/A_κ plane.

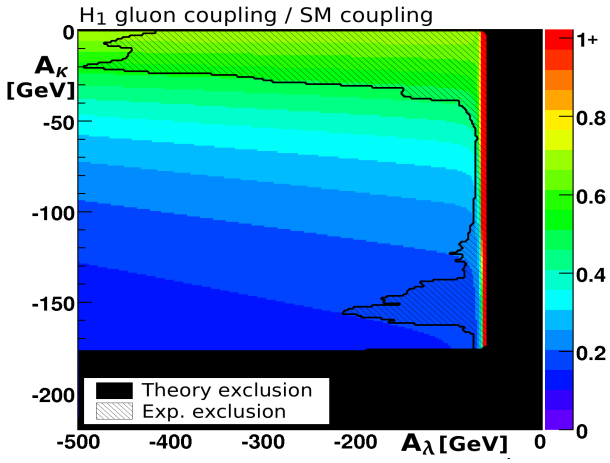

Fig. 6.30: H_1 gluon coupling (color coded) in the Reduced Couplings Scenario, A_λ/A_κ plane.

plane, there is a large and a small unexcluded region, the latter at large negative $\mu \approx -320$ GeV (Fig. 6.33). Too small and too large values of μ are unaccessible because negative mass squares occur. For small negative μ, there is no electroweak symmetry breaking. At very large and small $\tan\beta$, the presence of a Landau pole below the GUT scale leads to exclusion.

Since the Higgs-Higgsino mass parameter μ influences the masses of the charginos and neutralinos via their admixture of Higgsinos, too low $|\mu|$ values lead to exclusion because one or more of these particles have low masses that have already been ruled out experimentally. The LEP searches for hZ production with subsequent hZ$\to$b$\bar{\text{b}}$, hZ$\to\tau\tau$, hZ$\to$2jets decays and independent of the Higgs boson decay contribute mainly at small $\tan\beta$ and for large negative μ. Searches for hA production in the channels hA$\to$4b and hA$\to$2b2τ and the limit on hA production from the Z^0 boson width measurement also contribute in a smaller region of the parameter plane. In the plane presented here, exclusion bounds from b-physics are of importance, since the couplings of the charged and some neutral Higgs bosons to bottom quarks are enhanced for large $\tan\beta$. Above all, the measurement of the branching ratio of b$\to$sγ rules out large parts of the parameter space with $\tan\beta \gtrsim 25$. Also the measurements of the $B_s\to\mu\mu$ and $B^\pm\to\tau^\pm\nu$ branching ratios and of the mass difference ΔM_s are relevant for large negative values of μ and large $\tan\beta$.

Higgs boson masses and Higgs-to-Higgs decays The mass of the H_1 ranges from about 25 to 110 GeV in the unexcluded region (Fig. 6.34) and is thus again low. The H_2 has a mass of about 120 GeV in the allowed parameter region. Its mass is significantly lower only in a region at small $\tan\beta \lesssim 5$ already ruled out (Fig. 6.35). The mass of the A_1 varies from about 60 to 110 GeV in the allowed parameter region (Fig. 6.36). Unlike in the A_λ/A_κ plane, the H_1 and A_1 masses vary in the same direction, i.e. both increase with increasing $|\mu|$. The branching ratio of the H_2 to other Higgs bosons is well below 1% in the allowed parameter region (Fig. 6.38). In the white region of Fig. 6.38, such decays are not allowed at all. As before, the heavy Higgs bosons H_3, A_2 and $H^\pm$ are nearly degenerate in the entire parameter plane, reaching maximal masses for large $\tan\beta$ and medium μ values (Fig. 6.37). The smallest masses in the allowed region of about 130 GeV (105 GeV / 130 GeV) for the H_2 (A_2 / $H^\pm$) are obtained in the small unexcluded region at very negative $\mu \approx -320$ GeV and medium $\tan\beta$. Maximally, the masses reach values around 400 GeV in the unexcluded region.

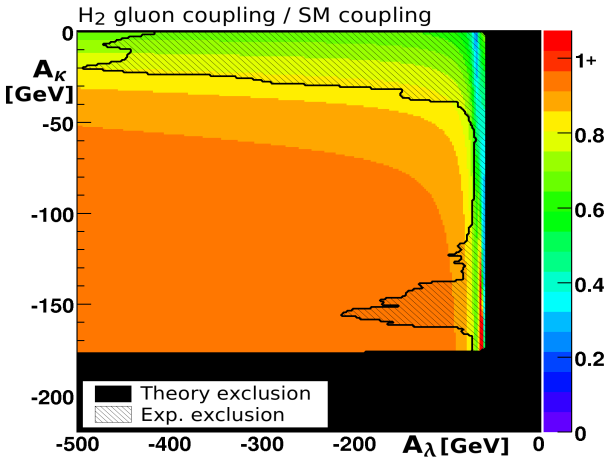

Fig. 6.31: H_2 gluon coupling (color coded) in the Reduced Couplings Scenario, A_λ/A_κ plane.

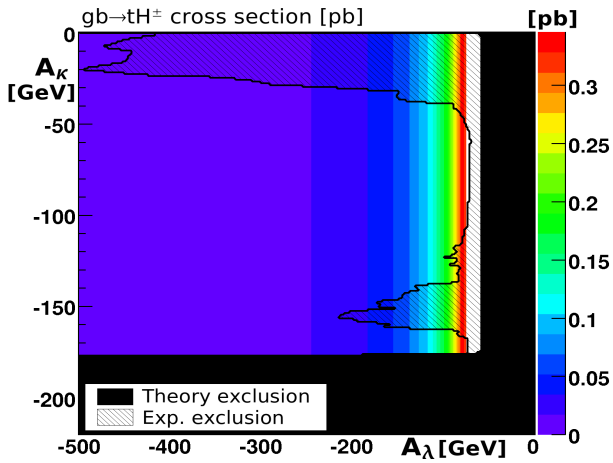

Fig. 6.32: $gb\to tH^-/g\bar{b}\to\bar{t}H^+$ cross section (color coded) in the Reduced Couplings Scenario, A_λ/A_κ plane.

Couplings Also in large parts of this plane, the H_2 has Standard Model-like couplings (Figs. 6.40, 6.43). In the unexcluded region around the point from Ref. [99], its couplings are reduced. The couplings of the H_1 and the H_3 are suppressed in large parts of the parameter plane (Figs. 6.39, 6.42, 6.41, 6.44). The couplings of the pseudoscalars A_1, A_2 to up-type fermions are heavily suppressed in the entire allowed region and are sizeable only at low $\tan\beta \lesssim 2$ which are already excluded experimentally.

The smallest couplings of the H_2 that are not yet ruled out can be found in the small unexcluded region at large negative $\mu \approx -320$ GeV. In this region, the coupling of the H_2 to vector bosons is only about 40-65% of its Standard Model value, the coupling of the H_1 about 30-50% and the one of the H_3 about 70-80%. In this region, the couplings of the scalars to gluons are larger than their couplings to vector bosons and their couplings to up-type fermions (respective to their Standard Model value) and may even be enhanced compared to the Standard Model case. Also the couplings of the pseudoscalars A_1 and A_2 to gluons are sizeable in this region (Figs. 6.45, 6.46). Since all Higgs boson masses in this small allowed region are well accessible by the existing SM and MSSM Higgs boson searches, all Higgs bosons can in principle contribute to the discovery potential in this region. This might help to retain a good discovery potential although the couplings of the scalar Higgs bosons to vector bosons and up-type fermions are reduced. Moreover, the charged Higgs bosons are light enough to be produced in the top quark decays $t\to H^+b$ and $\bar{t}\to H^-\bar{b}$.

For the mass degenerate bosons H_3 and A_2, the couplings to down-type fermions are heavily enhanced for large $\tan\beta$ (Figs. 6.48, 6.49). Then, the bbH_3/bbA_2 production mode becomes important. For the other Higgs bosons, the enhancement is not as large. As an example, the coupling to down-type fermions of the H_2 is given in Fig. 6.47. The production of the charged Higgs bosons via the $gb\to tH^-$ and $g\bar{b}\to\bar{t}H^+$ processes is enhanced in this scenario for large values of $\tan\beta$ and for large negative μ. Their combined cross section reaches values around 3.5 pb in the unexcluded region (Fig. 6.50). There is a minimum of the cross section ($\sim$0.28 pb) at $\tan\beta \approx 8.5$ and intermediate $\mu \approx -160$ GeV, which is not visible at the scale chosen for the figure. In the white region of Fig. 6.50, the cross section cannot be calculated (see App. B).

Summary of the Reduced Couplings Scenario, $\mu/\tan\beta$ benchmark plane In the $\mu/\tan\beta$ benchmark plane of the Reduced Couplings Scenario, there is a large region with a Standard

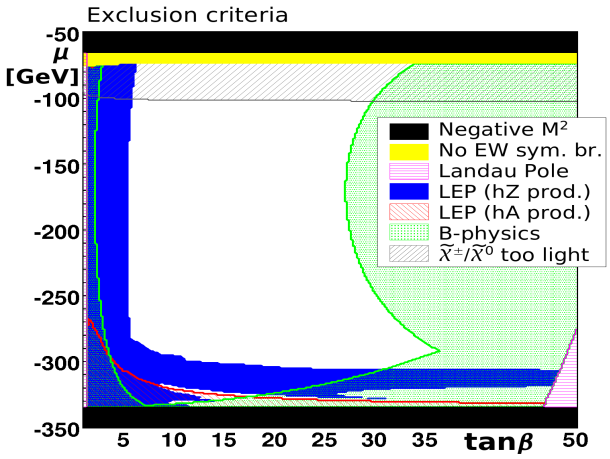

Fig. 6.33: Exclusion criteria in the Reduced Couplings Scenario, $\tan\beta/\mu$ plane.

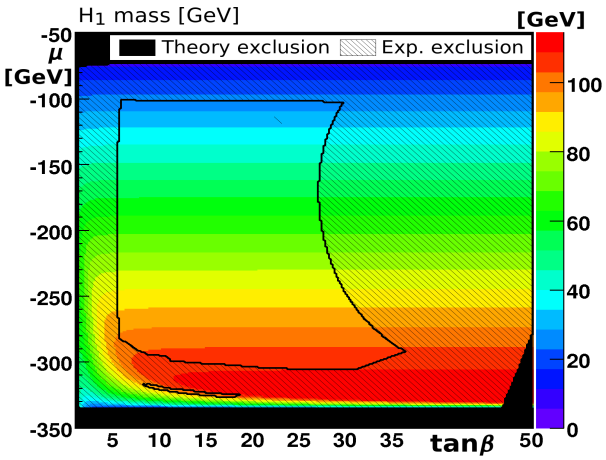

Fig. 6.34: H_1 mass (color coded) in the Reduced Couplings Scenario, $\tan\beta/\mu$ plane.

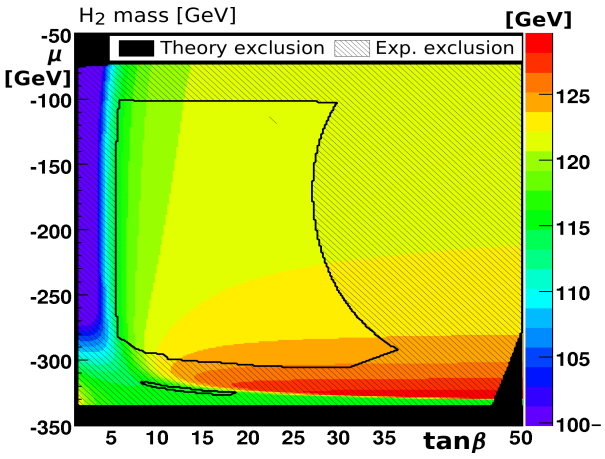

Fig. 6.35: H_2 mass (color coded) in the Reduced Couplings Scenario, $\tan\beta/\mu$ plane.

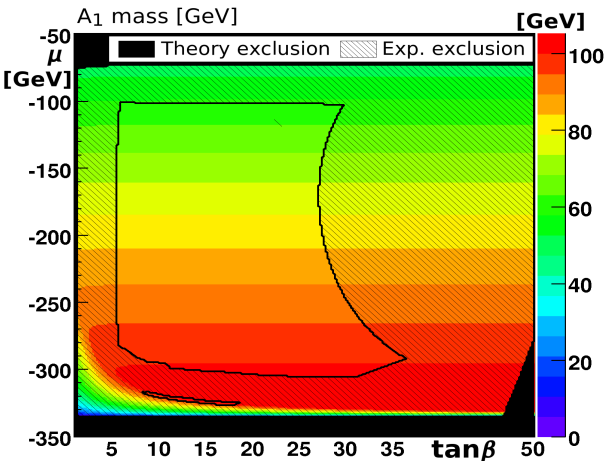

Fig. 6.36: A_1 mass (color coded) in the Reduced Couplings Scenario, $\tan\beta/\mu$ plane.

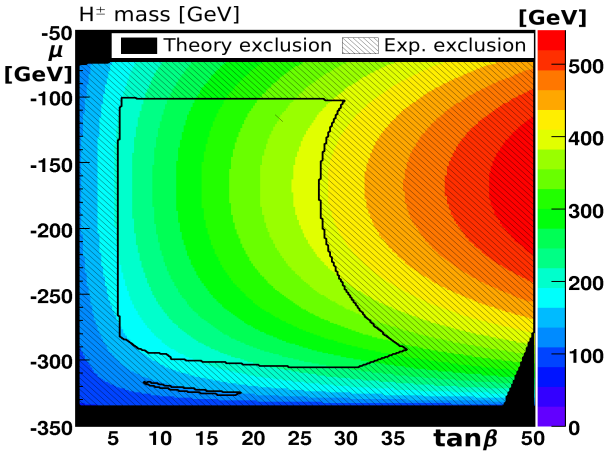

Fig. 6.37: $H^{\pm}$ mass (color coded) in the Reduced Couplings Scenario, $\tan\beta/\mu$ plane.

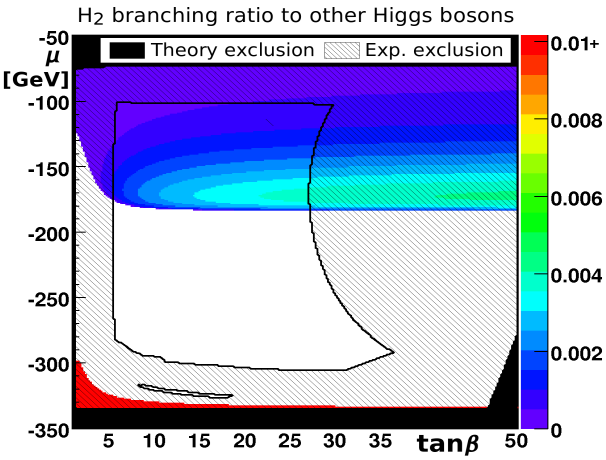

Fig. 6.38: H_2 branching ratio to other Higgs bosons (color coded) in the Reduced Couplings Scenario, $\tan\beta/\mu$ plane.

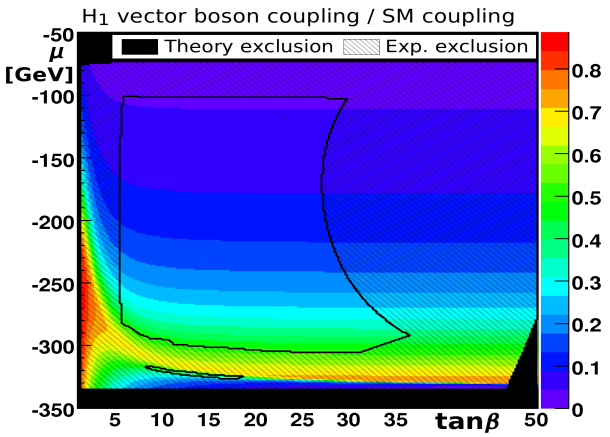

Fig. 6.39: H_1 vector boson coupling (color coded) in the Reduced Couplings Scenario, $\tan\beta/\mu$ plane.

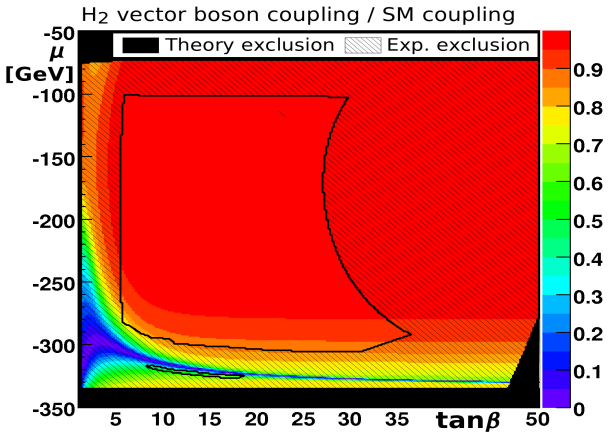

Fig. 6.40: H_2 vector boson coupling (color coded) in the Reduced Couplings Scenario, $\tan\beta/\mu$ plane.

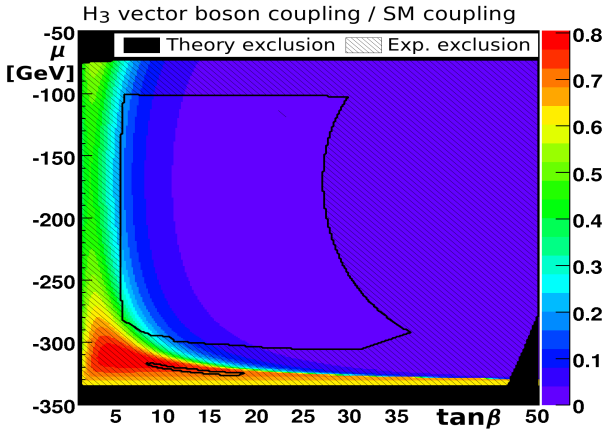

Fig. 6.41: H_3 vector boson coupling (color coded) in the Reduced Couplings Scenario, $\tan\beta/\mu$ plane.

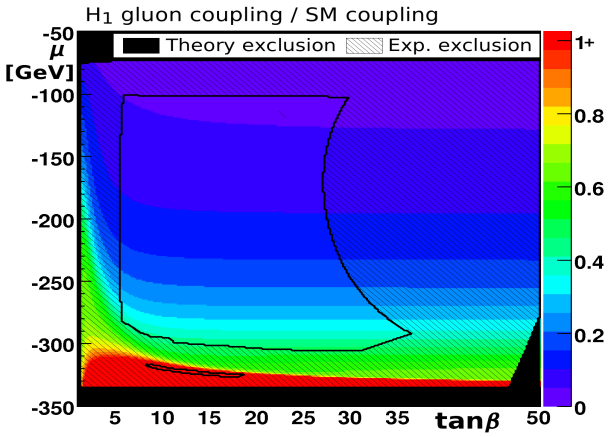

Fig. 6.42: H_1 gluon coupling (color coded) in the Reduced Couplings Scenario, $\tan\beta/\mu$ plane.

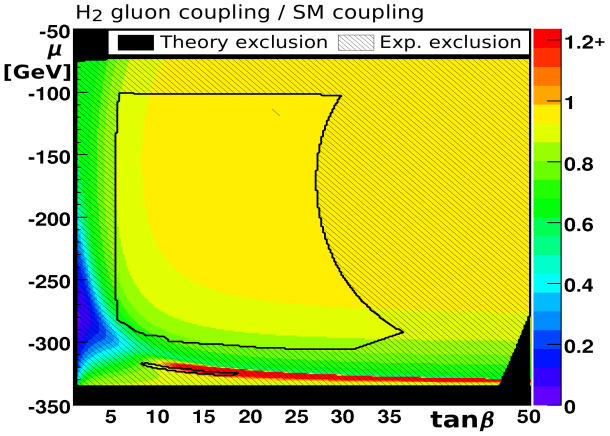

Fig. 6.43: H_2 gluon coupling (color coded) in the Reduced Couplings Scenario, $\tan\beta/\mu$ plane.

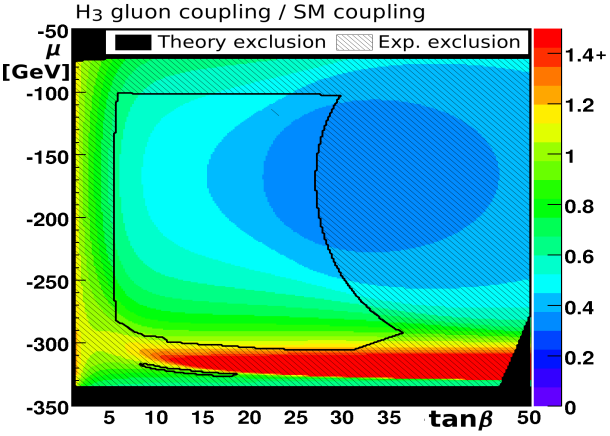

Fig. 6.44: H_3 gluon coupling (color coded) in the Reduced Couplings Scenario, $\tan\beta/\mu$ plane.

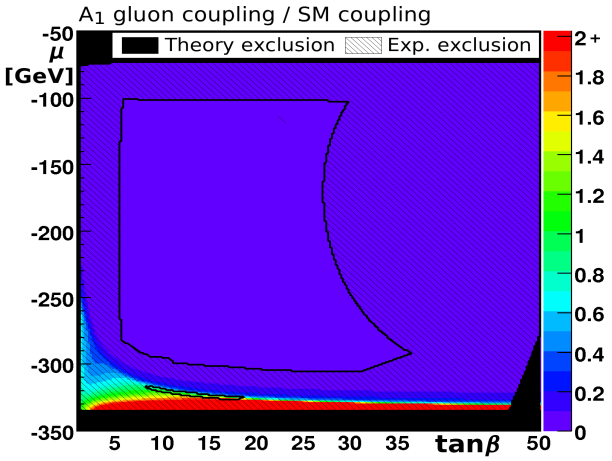

Fig. 6.45: A_1 gluon coupling (color coded) in the Reduced Couplings Scenario, $\tan\beta/\mu$ plane.

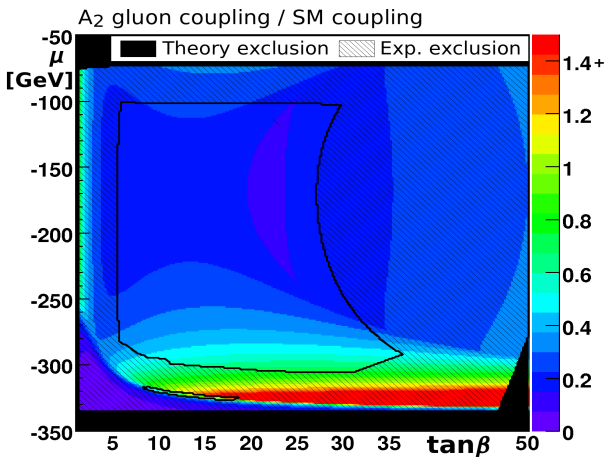

Fig. 6.46: A_2 gluon coupling (color coded) in the Reduced Couplings Scenario, $\tan\beta/\mu$ plane.

Model-like H_2, and also regions with reduced couplings of the H_2. Decays of the H_1 to other Higgs bosons are allowed in parts of the plane, but have only a low branching ratio. In one of these regions, all seven Higgs bosons might contribute to the discovery potential. At large $\tan\beta$, the bbH_3 and bbA_2 couplings are heavily enhanced compared to the Standard Model case, and also the $H^{\pm}tb$ coupling is large.

6.3 The Light A_1 Scenario

In the NMSSM, the lightest pseudoscalar boson A_1 can be very light and may thus be well below the H_1/H_2 masses. As there are no couplings of the CP-odd pseudoscalars to the weak gauge bosons at Born level, it is not possible to exploit the vector boson fusion production mode and the production in association with massive vector bosons for their discovery. Yet, in the NMSSM, the decay chain $H_{1/2}\rightarrow A_1A_1$ can be the dominant decay mode of the lightest scalars [42]. The decay of the A_1 to bottom quarks, and if this is kinematically forbidden, the decay to τ-leptons, is then dominant. The phenomenology of the Higgs sector thus depends on the A_1 mass.

The second point from Tab. 6.1 is included in this scenario for the unconstrained NMSSM. The lightest scalar Higgs boson has a mass of 90 GeV at that point. Although it has Standard Model-like couplings, it is not excluded by the LEP mass limit, since it may decay to the lightest pseudoscalar which has a mass of about 10 GeV. The decay chain $H_1\rightarrow A_1A_1\rightarrow 4\tau$ is dominant for that point.

For this scenario, the mass parameters are again chosen as $M_1 = 500$ GeV, $M_2 = 1$ TeV, $M_3 = 3$ TeV and $M_{\text{susy}} = 1$ TeV. The trilinear soft supersymmetry-breaking parameters are set to $A_t = A_b = A_\tau = 1.5$ TeV. This choice is the same as in Ref. [99] and in the Reduced Couplings Scenario.

For the Light A_1 Scenario, only the λ/κ plane is proposed as a benchmark because the A_λ/A_κ and $\mu/\tan\beta$ planes do not include new phenomenology types that are not covered by the already proposed planes.

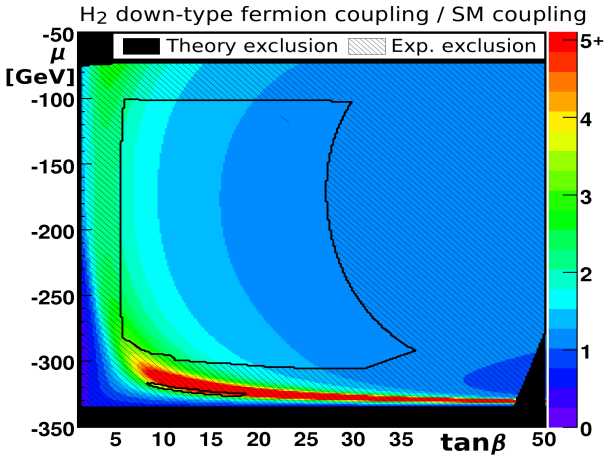

Fig. 6.47: H_2 up-type fermion coupling (color coded) in the Reduced Couplings Scenario, $\tan\beta/\mu$ plane.

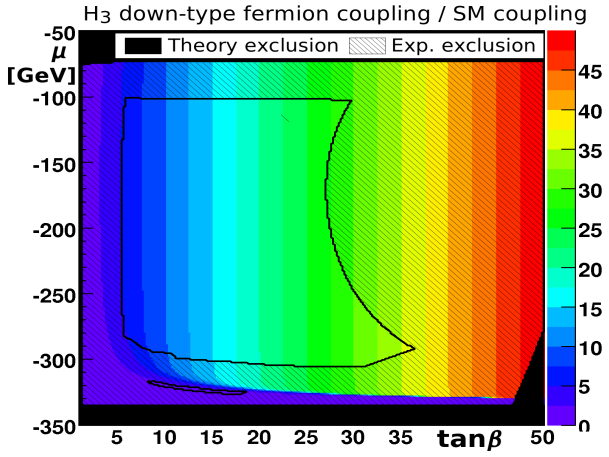

Fig. 6.48: H_3 up-type fermion coupling (color coded) in the Reduced Couplings Scenario, $\tan\beta/\mu$ plane.

6.3.1 The λ/κ benchmark plane

Exclusion limits The Light A_1 Scenario contains a λ/κ plane with parameters given in the forth row of Tab. 6.2. Two large parameter regions are not yet excluded (Fig. 6.51). Moreover, there is a small unexcluded band at $\lambda \approx 0.25$. The unexcluded regions are surrounded by large regions with negative mass squares. At large κ, also a region with a Landau pole below the GUT scale exists, as well as a region without electroweak symmetry breaking at large $\lambda > 0.37$ and intermediate $\kappa \approx 0.2$. Large regions are excluded by the LEP searches for hZ production with Higgs boson decays to Standard Model particles. Since the pseudoscalar A_1 is light in this scenario, also the LEP searches for the Higgs boson decay to a pseudoscalar pair, h→AA, are relevant. The most important constraints come from the hZ searches for h→$b\bar{b}$, h→$\tau\tau$, h→2 jets, h→AA→4b and independent of the decay. Also the limits for hZ, h→AA→jets, for hZ, h→AA→2b2τ and for pseudoscalar production from Z^0 decays, Z→AA→4τ, contribute in smaller regions. The hA production mode is not relevant for the limits in this scenario. There is also a small region with a very light A_1 that is excluded by b-physics constraints. With the scanning grid used here, it is only visible as four small dots around $\lambda \approx 0.2$ and $\kappa \approx -0.1$.

Higgs boson masses and Higgs-to-Higgs decays The lightest scalar H_1 has a mass around 120 GeV in the large parts of the unexcluded region, however, it can also be lighter, around 90 GeV, in small regions at intermediate $\lambda \approx 0.22$ (Fig. 6.52). The A_1 is very light with masses of maximally 65 GeV at very small $\kappa \approx -0.02$, and can also be significantly lighter than 10 GeV (Fig. 6.55). Accordingly, the decay $H_1 \to A_1A_1$ is possible in the entire allowed parameter plane with the exception of a tiny region at very small $\lambda \lesssim 0.05$ and $\kappa \approx -0.02$, which is shown in white in Fig. 6.57. In the unexcluded region at large λ and κ, the $H_1 \to A_1A_1$ decay reaches branching ratios above 90%. When the coupling parameters λ and κ decrease, also its branching ratio becomes smaller. The mass of the H_2 varies from about 400 GeV for negative $\kappa \gtrsim -0.1$ and small $\lambda \lesssim 0.1$ to about 1400 GeV at large λ and κ (Fig. 6.53). The other Higgs bosons are rather heavy (Figs. 6.54, 6.56), and the H_3, A_2 and $H^\pm$ bosons approximately degenerate for large λ. However, at negative $\kappa \gtrsim -0.1$ also the masses of the A_2 and $H^\pm$ bosons are as low as about 400 GeV in the allowed parameter space. The minimal H_3 mass in the unexcluded region is slightly shifted to smaller negative values of κ compared to the minimal A_2 and $H^\pm$ masses

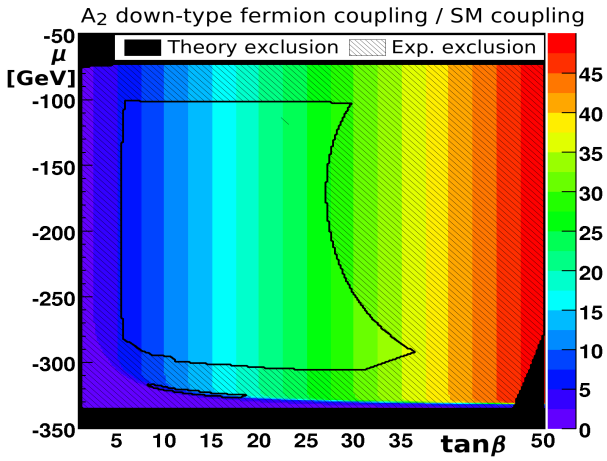

Fig. 6.49: A_2 up-type fermion coupling (color coded) in the Reduced Couplings Scenario, $\tan\beta/\mu$ plane.

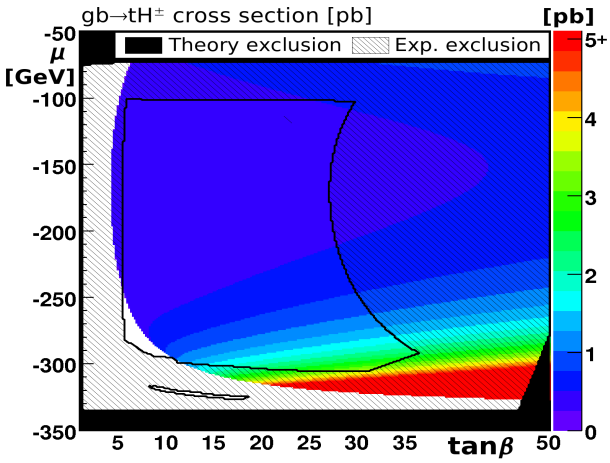

Fig. 6.50: $gb\to tH^-/g\bar{b}\to\bar{t}H^+$ cross section (color coded) in the Reduced Couplings Scenario, $\tan\beta/\mu$ plane.

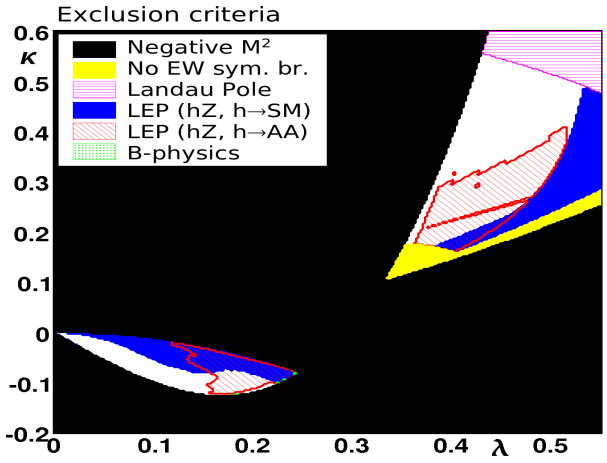

Fig. 6.51: Exclusion criteria in the Light A_1 Scenario, λ/κ plane.

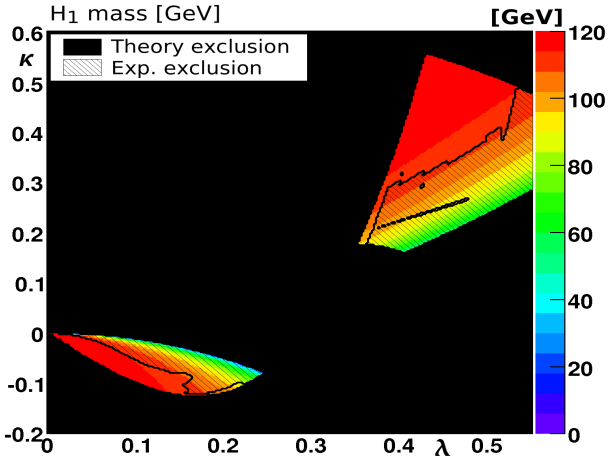

Fig. 6.52: H_1 mass (color coded) in the Light A_1 Scenario, λ/κ plane.

and is about 750 GeV.

For A_1 masses larger than $2m_b$, about 90% of the lightest pseudoscalar bosons decay to bottom quarks (Fig. 6.58). In these regions, the decay chains $H_1\to A_1A_1\to 4b$ and $H_1\to A_1A_1\to b\bar{b}\tau\tau$ are important. In bands close to the boundaries of the unexcluded region, the A_1 is so light that the decay chain $H_1\to A_1A_1\to\tau\tau\tau\tau$ prevails (Fig. 6.59). It is also possible to have such a light A_1 that the decay to a τ-lepton pair is kinematically forbidden. In such a case, the A_1 decays predominantly to lighter fermions. This phenomenology is present only in narrow bands that are barely visible at the scale chosen for the figure. In the small unexcluded band at $\lambda\approx 0.25$, the couplings of the A_1 to fermions are heavily suppressed. Therefore, decays to a bottom quark pair and to τ-leptons are very rare. Instead, the A_1 decays dominantly to two photons. The branching ratio of the $A_1\to\gamma\gamma$ decay is larger than 90% in the center of that region.

Couplings The couplings of the H_1 are Standard Model-like in the entire allowed parameter region (Fig. 6.60). The couplings of the H_2 are sizeable only in a small excluded region at κ

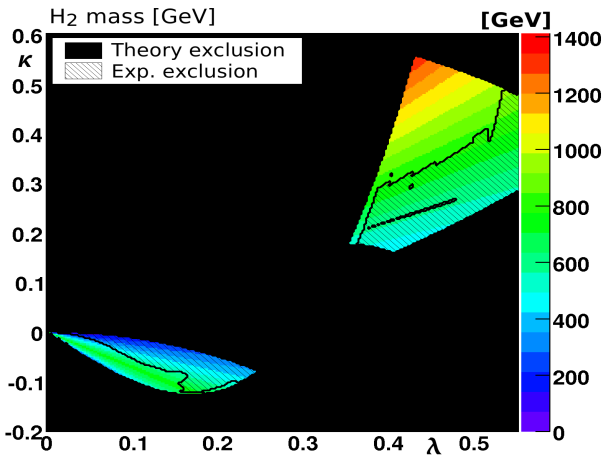

Fig. 6.53: H_2 mass (color coded) in the Light A_1 Scenario, λ/κ plane.

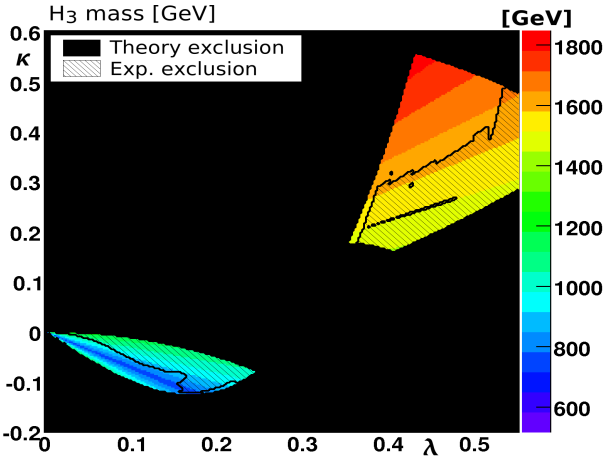

Fig. 6.54: H_3 mass (color coded) in the Light A_1 Scenario, λ/κ plane.

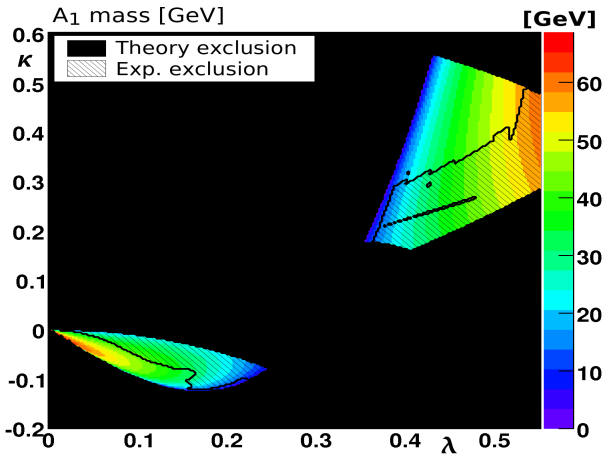

Fig. 6.55: A_1 mass (color coded) in the Light A_1 Scenario, λ/κ plane.

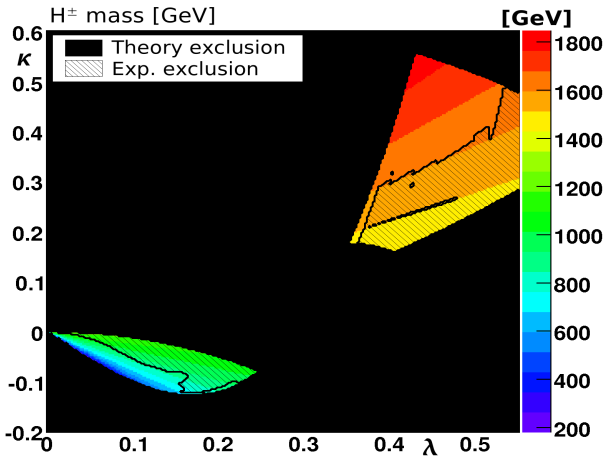

Fig. 6.56: $H^{\pm}$ mass (color coded) in the Light A_1 Scenario, λ/κ plane.

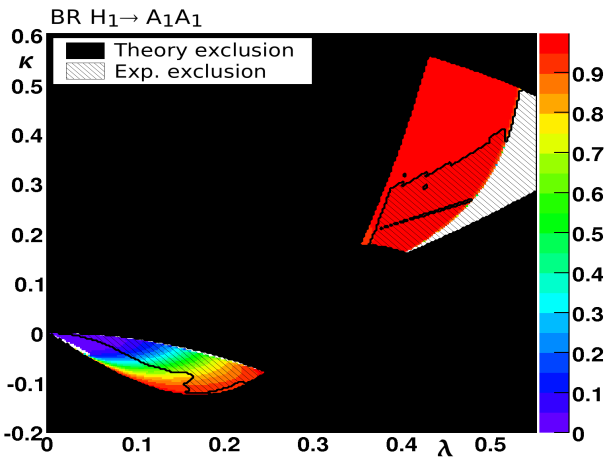

Fig. 6.57: $H_1 \to A_1A_1$ branching ratio (color coded) in the Light A_1 Scenario, λ/κ plane.

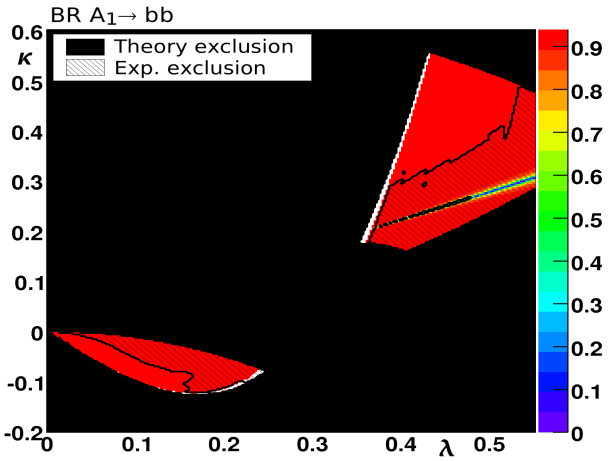

Fig. 6.58: $A_1 \to b\bar{b}$ branching ratio (color coded) in the Light A_1 Scenario, λ/κ plane.

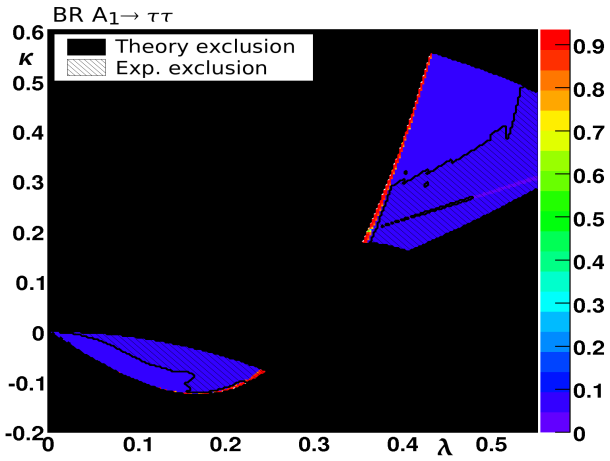

Fig. 6.59: $A_1 \to \tau\tau$ branching ratio (color coded) in the Light A_1 Scenario, λ/κ plane.

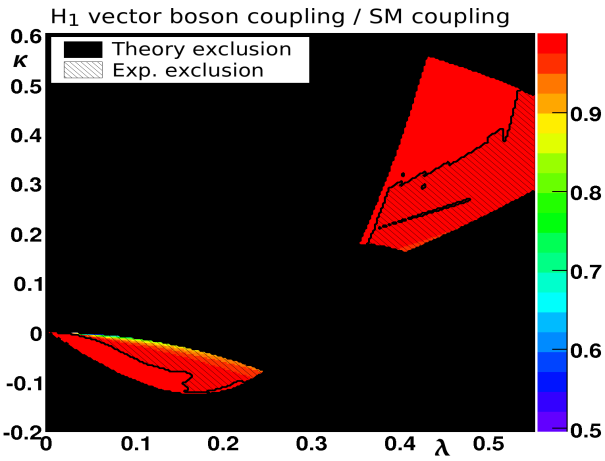

Fig. 6.60: H_1 vector boson coupling (color coded) in the Light A_1 Scenario, λ/κ plane.

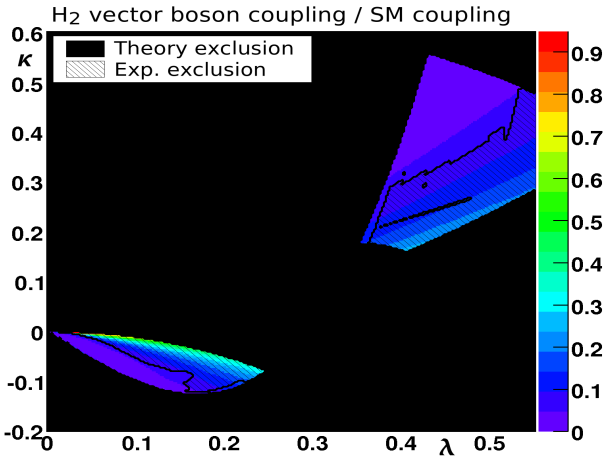

Fig. 6.61: H_2 vector boson coupling (color coded) in the Light A_1 Scenario, λ/κ plane.

values close to zero (Fig. 6.61). All other Higgs bosons have heavily suppressed couplings in the entire parameter plane. The cross section for the processes $gb \to tH^-$ and $g\bar{b} \to \bar{t}H^+$ is at maximum 0.35 pb for small λ and small negative κ, and is mostly even smaller than 0.1 pb.

Summary of the Light A_1 Scenario The Light A_1 Scenario is characterized by a scalar H_1 with Standard Model-like couplings and a mass around 120 GeV, but with frequent $H_1 \to A_1A_1$ decays. Regions with dominant decays of the A_1 to bottom quarks, to τ-leptons and to photons are covered.

Generally, these types of phenomenology are very sensitive to the value of A_κ. For example, $|A_\kappa|$ must be smaller than 5.5 GeV if the other parameters of the included point from Ref. [99] are kept in order to have such a light A_1 that $H_1 \to A_1A_1$ decays are still possible.

Moreover, the allowed parameter region around the included point from Ref. [99] point is heavily restricted by various exclusion criteria. Both in the A_λ/A_κ and the $\tan\beta/\mu$ planes including this benchmark point, only relatively small bands are still allowed (Figs. 6.62, 6.64). However, for a more central point, eg. λ=κ=0.45, the restrictions in these parameter planes are less severe (Figs. 6.63, 6.65).

6.4 The Maximal M_{H_1} Scenario

As described in Chap. 2.3.1, the mass of the lightest scalar Higgs boson is less constrained in the NMSSM than in the MSSM. References [43, 100] argue that in the NMSSM, its mass limit is about 10 GeV higher than in the MSSM. Reference [100] also states that the third parameter point of Tab. 6.1 is the point with the maximal H_1 mass found in a random scan of the Higgs sector parameters. While in the MSSM, the scalar mass is maximized for large $\tan\beta$ values, this maximal mass point is at a small $\tan\beta$ of 2.14. The mass value at this point is found to be 139.6 GeV by Ref. [100] with an assumed top quark mass of 178 GeV. This point is included in the λ/κ plane presented in the following. For comparison, the maximal mass of the lightest scalar Higgs boson of the MSSM found with NMHDECAY in the decoupling limit (see Chap. 2.3.1) is claimed to be 128.4 GeV by Ref. [100].

With the new version of NMHDECAY and a top quark mass of 172 GeV, the H_1 mass at this point is only 136.9 GeV. By shifting the original point to $\lambda \approx 0.71$ and $\kappa \approx 0.065$, an H_1 mass of 139.7 GeV can be recovered also with $M_{\text{top}} = 172$ GeV. To include the phenomenology at the maximal H_1 mass, this shifted point is included in all here presented planes instead of the original point from Ref. [100].

Generally, mass predictions depend on the theoretical approach, the corresponding renormalization scheme and on the included corrections of the program used to calculate the masses. NMHDECAY uses the effective field theory approach. Masses obtained with programs using the full diagrammatic approach can be up to 5 GeV larger. The differences between the two approaches are well understood [110].

For this scenario of the unconstrained NMSSM, the mass parameters are set to $M_1 = 150$ GeV, $M_2 = 300$ GeV, $M_3 = 1$ TeV and $M_{\text{susy}} = 1$ TeV according to the settings in Ref. [100]. These values roughly correspond to universal gaugino masses at the GUT scale. The trilinear soft supersymmetry-breaking parameters are chosen as $A_t = A_b = A_\tau = 2.5$ TeV. This choice maximizes the one loop radiative corrections to the Higgs boson mass and thus allows for a large M_{H_1} [100].

For the Maximal M_{H_1} Scenario, only the λ/κ and A_λ/A_κ planes are proposed as benchmarks because the $\mu/\tan\beta$ plane does not include new phenomenology that is not covered by the already proposed planes and is heavily restricted by the exclusion criteria.

6.4.1 The λ/κ benchmark plane

Exclusion limits The parameter settings for this plane are listed in the fifth row of Tab. 6.2. As can be seen in Fig. 6.66, the allowed parameter space in this plane is heavily constrained by requiring electroweak symmetry breaking. Large λ are excluded because of a Landau pole below the GUT scale. With the particle spectra and couplings of this plane, none of the experimental constraints apply.

Higgs boson masses and Higgs-to-Higgs decays For large κ, the mass of the lightest scalar H_1 is well above the MSSM bound (Fig. 6.67). As stated before, it is found that for the parameter settings used in this scenario, the H_1 mass is not maximized at the point suggested by Ref. [100], but instead around $\lambda \approx 0.71$ and $\kappa \approx 0.065$, where masses of nearly 140 GeV are obtained in the unexcluded region. For low κ, the H_1 mass decreases to values of about 95 GeV. The H_2 is in the mass range from about 135 to 195 GeV that is accessible at the LHC, being heaviest at large κ (Fig. 6.68). The pseudoscalar A_1 is light in the entire plane, its mass ranging from about 20 to 60 GeV (Fig. 6.69). Thus, the decay chains $H_1 \to A_1A_1 \to 4b/2b2\tau$ and $H_2 \to A_1A_1 \to 4b/2b2\tau$ are of importance (Figs. 6.71, 6.72). In principle, their branching ratios increase with κ, but in case

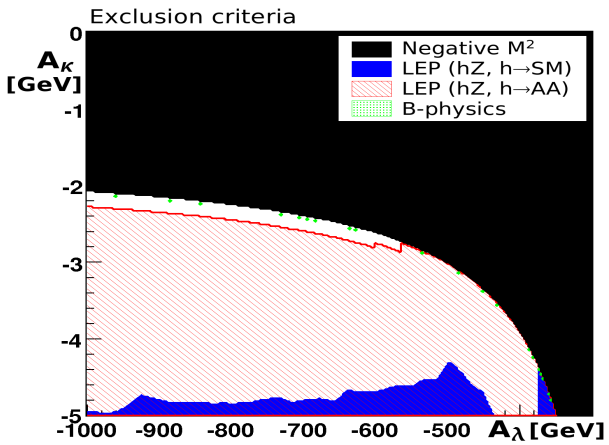

Fig. 6.62: Exclusion criteria in the Light A_1 Scenario, A_λ/A_κ plane with $\lambda = 0.22$ and $\kappa = -0.1$.

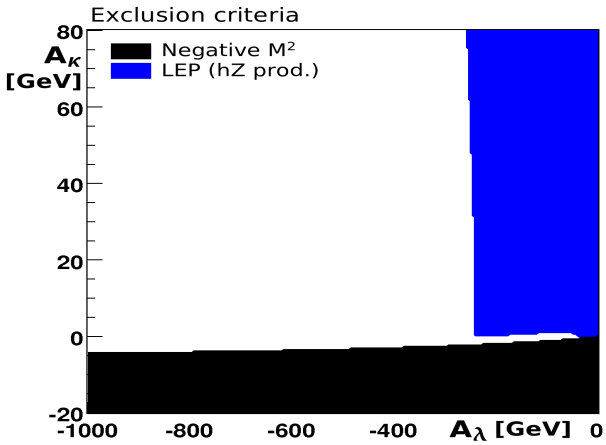

Fig. 6.63: Exclusion criteria in the Light A_1 Scenario, A_λ/A_κ plane with $\lambda = \kappa = 0.45$.

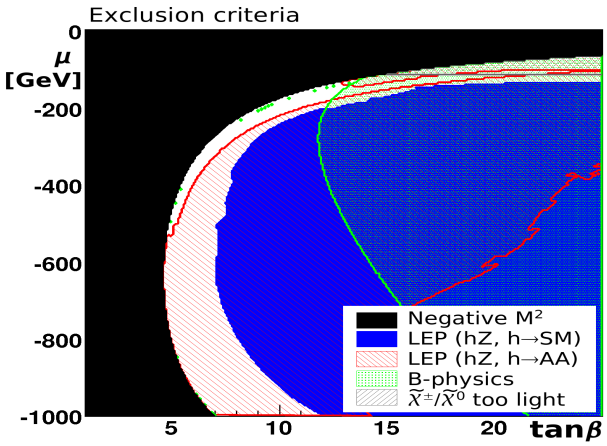

Fig. 6.64: Exclusion criteria in the Light A_1 Scenario, $\tan\beta/\mu$ plane with $\lambda = 0.22$ and $\kappa = -0.1$.

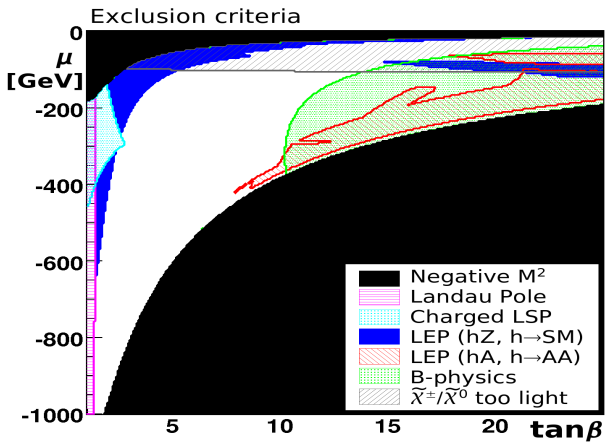

Fig. 6.65: Exclusion criteria in the Light A_1 Scenario, $\tan\beta/\mu$ plane with $\lambda = \kappa = 0.45$.

of the H_2 decrease again when the decays to the massive vector bosons become kinematically possible (Fig. 6.73). Also the coupling to vector bosons influences the branching ratio in that case. In the region where M_{H_1} is above the MSSM bound, the branching ratio of the $H_1 \to A_1 A_1$ decay is about 90%. The heavier Higgs bosons H_3, A_2 and $H^{\pm}$ are nearly degenerate and have masses larger than 1560 GeV in the entire parameter plane (Fig. 6.70).

Couplings The couplings of the H_1 are Standard Model-like for large κ, but are reduced to values of about 55% of the Standard Model values in the allowed parameter region at small λ and κ (Fig. 6.74). In contrast, the couplings of the H_2 are reduced for large κ, approaching zero in a small band around $\kappa \approx 0.06$ (Fig. 6.75). At small λ and κ, its couplings are about 80% of the Standard Model value. The couplings of the A_1 are suppressed below about 10%, the couplings of the heavier Higgs bosons H_3 and A_2 below 50% of their Standard Model values or less. The cross section of the processes $gb \to tH^-$ and $g\bar{b} \to \bar{t}H^+$ is about 0.23 pb and thus negligible.

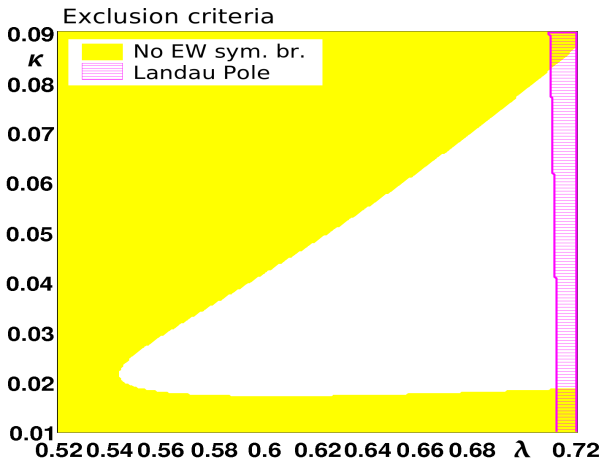

Fig. 6.66: Exclusion criteria in the Maximal M_{H_1} Scenario, λ/κ plane.

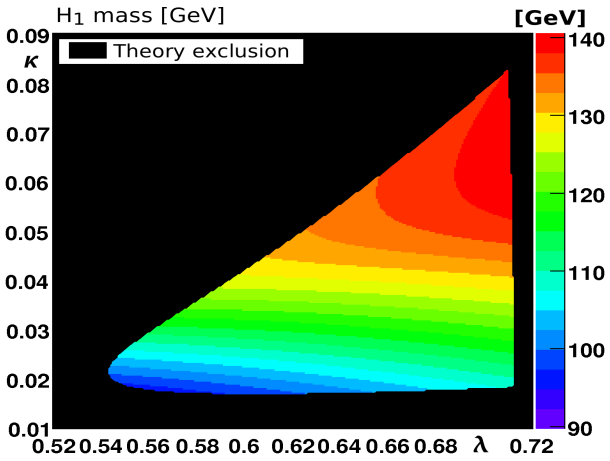

Fig. 6.67: H_1 mass (color coded) in the Maximal M_{H_1} Scenario, λ/κ plane.

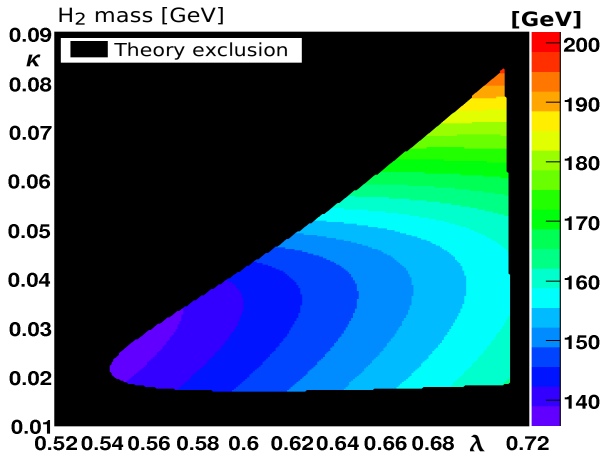

Fig. 6.68: H_2 mass (color coded) in the Maximal M_{H_1} Scenario, λ/κ plane.

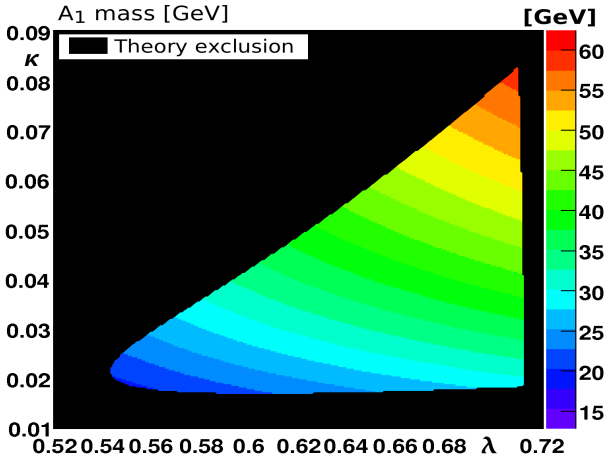

Fig. 6.69: A_1 mass (color coded) in the Maximal M_{H_1} Scenario, λ/κ plane.

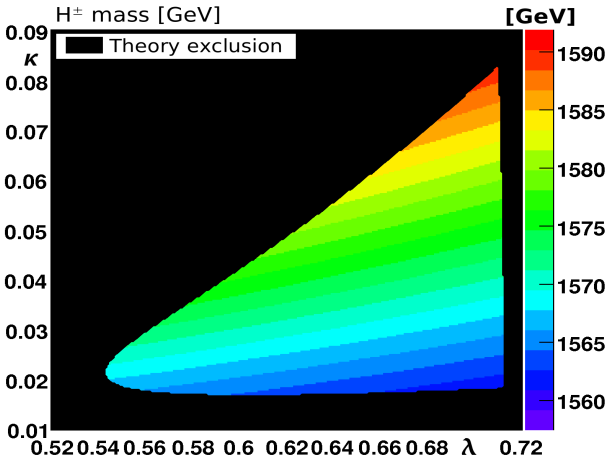

Fig. 6.70: $H^{\pm}$ mass (color coded) in the Maximal M_{H_1} Scenario, λ/κ plane.

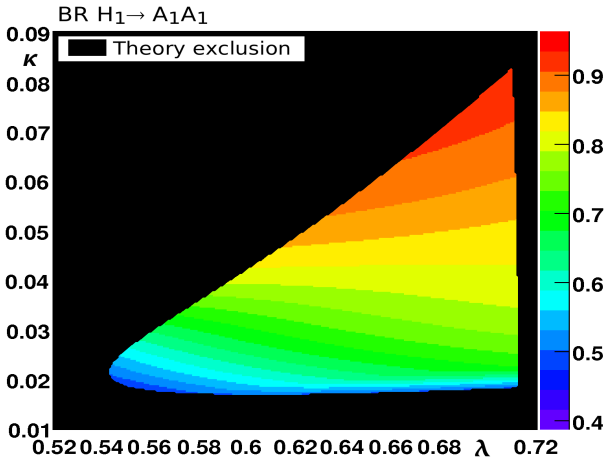

Fig. 6.71: $H_1 \to A_1 A_1$ branching ratio (color coded) in the Maximal M_{H_1} Scenario, λ/κ plane.

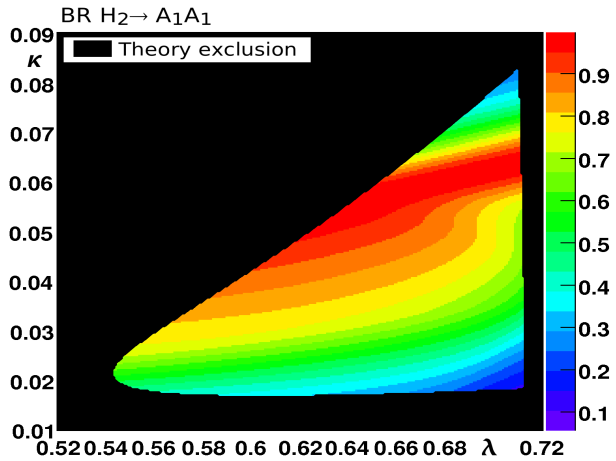

Fig. 6.72: $H_2 \to A_1A_1$ branching ratio (color coded) in the Maximal M_{H_1} Scenario, λ/κ plane.

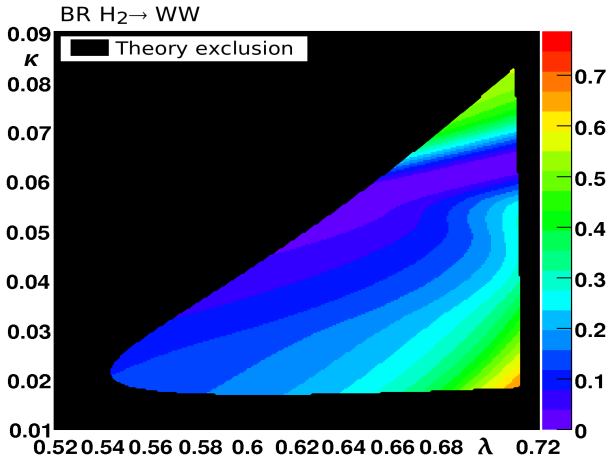

Fig. 6.73: $H_2 \to WW$ branching ratio (color coded) in the Maximal M_{H_1} Scenario, λ/κ plane.

Summary of the Maximal M_{H_1} Scenario, λ/κ benchmark plane The λ/κ plane of the Maximal M_{H_1} Scenario contains a region where the mass of the lightest scalar H_1 is maximal and thus above the MSSM mass bound. Also the H_2 has a mass that is well accessible by the current ATLAS search strategies. However, a discovery of the H_1 will be difficult due to the frequent $H_1 \to A_1A_1$ decay. Nevertheless, since there is a large variation of the branching ratios of the $H_1 \to A_1A_1$ and $H_2 \to A_1A_1$ decays and of the couplings of the H_1 and H_2, the effects of the simultaneous occurrence of these typical NMSSM features can be probed in this plane.

6.4.2 The A_λ/A_κ benchmark plane

Exclusion limits In the last row of Tab. 6.2, the parameters for this plane are listed. As shown in Fig. 6.76, this plane is bound by regions without electroweak symmetry breaking at small and at large negative A_κ as well as by regions with negative mass squares. The LEP searches for the hZ production mode and subsequent Higgs boson decays to Standard Model particles such as $h \to b\bar{b}$, $h \to \tau\tau$ and h→2jets are powerful experimental exclusion criteria. Also the decay mode independent search is relevant. In a small region, the limit on the branching ratio for h→AA leads to exclusion. Only one scan point of the scanning grid used here is excluded by the b-physics process $B_s \to \mu\mu$.

Higgs boson masses and Higgs-to-Higgs decays In the allowed region, the mass of the H_1 varies from the LEP limit of ∼114 GeV to the maximal mass bound of the NMSSM of about 140 GeV (Fig. 6.77). The maximal mass is achieved around $A_\lambda \approx 1530$ GeV. The H_2 is relatively light, its mass ranges from 140 to 200 GeV (Fig. 6.78). The mass of the lightest pseudoscalar A_1 is very sensitive to A_κ (Eq. 2.68) and varies from about 40 to 210 GeV in the allowed parameter region (Fig. 6.79). Thus, there is only a small band for $A_\kappa \gtrsim 0$ GeV with allowed $H_1 \to A_1A_1$ decay (Fig. 6.81, colored (grayish) region). The $H_2 \to A_1A_1$ decay is also only possible in a limited region (Fig. 6.82, colored (grayish) region). In contrast to the λ/κ plane, in the A_λ/A_κ plane a region where the H_1 is at its maximal mass and has no decay modes to other Higgs bosons is covered. The heavy Higgs bosons A_2, H_3 and $H^\pm$ are nearly degenerate in the entire parameter plane with masses around 1500 to 1600 GeV (Fig. 6.80).

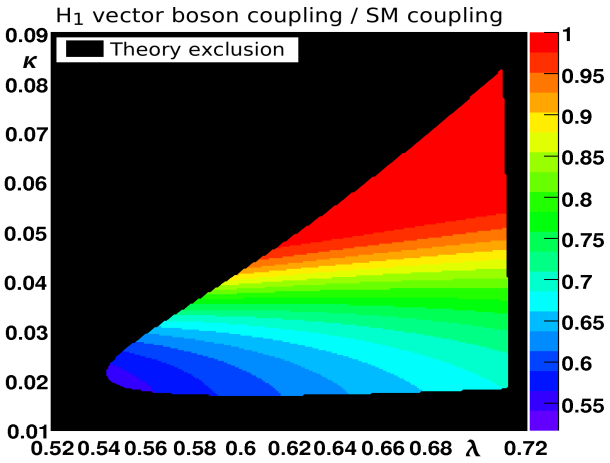

Fig. 6.74: H_1 vector boson coupling (color coded) in the Maximal M_{H_1} Scenario, λ/κ plane.

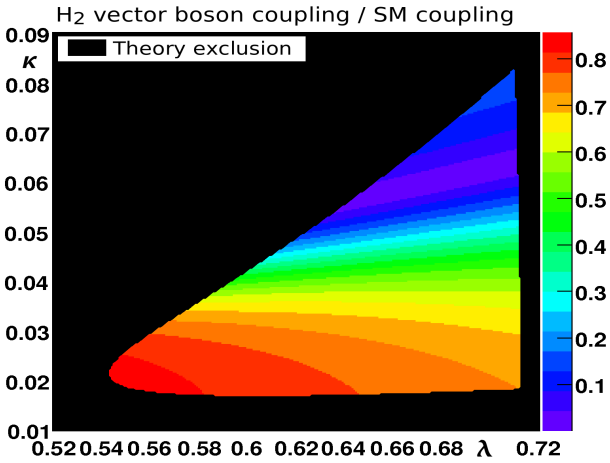

Fig. 6.75: H_2 vector boson coupling (color coded) in the Maximal M_{H_1} Scenario, λ/κ plane.

Couplings There is a significant variation of the Higgs boson couplings in the plane. The couplings of the H_1 are Standard Model-like in the maximal mass region at small negative $A_\kappa \gtrsim -190$ GeV (Fig. 6.83), whereas the H_2 couplings are suppressed there (Fig. 6.84). For larger negative A_κ, this pattern is reversed. The coupling of the H_3 to vector bosons and all couplings of the A_1 are heavily suppressed, whereas the couplings of the H_3 and A_2 to up-type fermions and to gluons are at about 50% of their Standard Model values in the entire plane. The $gb \to tH^-$ and $g\bar{b} \to \bar{t}H^+$ processes are negligible with a cross section below 0.25 pb.

Summary of the Maximal M_{H_1} Scenario, λ/κ benchmark plane The A_λ/A_κ plane of the Maximal M_{H_1} Scenario contains a region where the H_1 mass is at its maximally possible value. In this region, there are areas with and without $H_1 \to A_1A_1$ and $H_2 \to A_1A_1$ decays. Moreover, the H_1 and H_2 are quite light and thus well accessible by the current ATLAS searches. As the couplings these Higgs bosons vary inversely in the plane, they are likely to have discovery potentials in different areas. Thus, it can be investigated whether the entire plane can be covered and whether there are regions where both Higgs bosons are observable.

In the $\tan\beta/\mu$ plane around the included point from Ref. [100], the allowed parameter space of this scenario is heavily restricted (Fig.6.85).

6.5 The cNMSSM Scenario

As described in Chap. 2.3.2, the number of free parameters in the constrained NMSSM is reduced by the additional constraint of parameter unification at the GUT scale. λ at the supersymmetric scale[5] and $\tan\beta$ at the weak scale are still input parameters of NMSSMTOOLS as for the unconstrained model. A_κ at the GUT scale is also an input parameter and evolved to the supersymmetric scale with the help of the renormalization group equations (RGEs). A_λ is unified with the other trilinear couplings and thus is replaced by A_0 at the GUT scale. Accordingly, A_λ at the supersymmetric scale cannot be chosen independently of the other parameters. Its value is calculated by NMSPEC. Only the sign of μ at the weak scale, but not its absolute value, is an input parameter of the model. The absolute value of μ at the weak scale as well as κ at the

[5] The supersymmetric scale is defined by NMSPEC in terms of the squark masses.

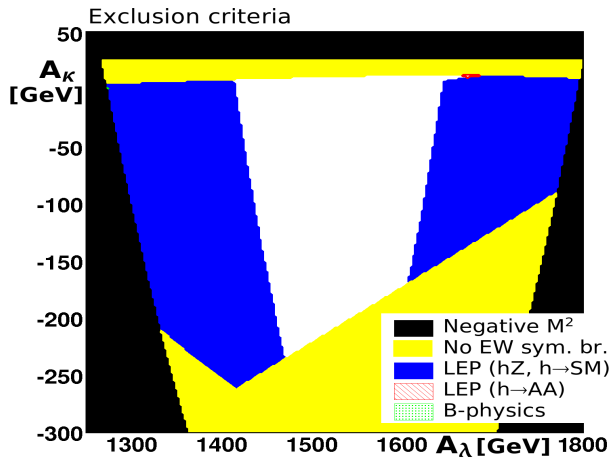

Fig. 6.76: Exclusion criteria in the Maximal M_{H_1} Scenario, A_λ/A_κ plane.

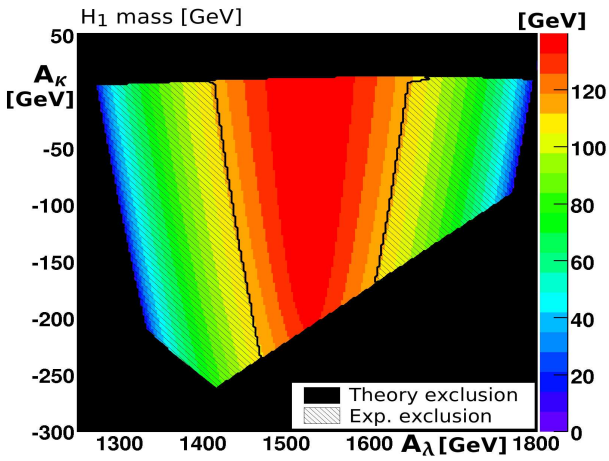

Fig. 6.77: H_1 mass (color coded) in the Maximal M_{H_1} Scenario, A_λ/A_κ plane.

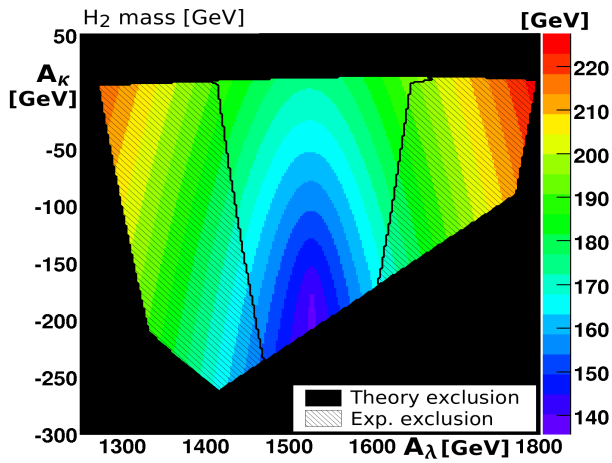

Fig. 6.78: H_2 mass (color coded) in the Maximal M_{H_1} Scenario, A_λ/A_κ plane.

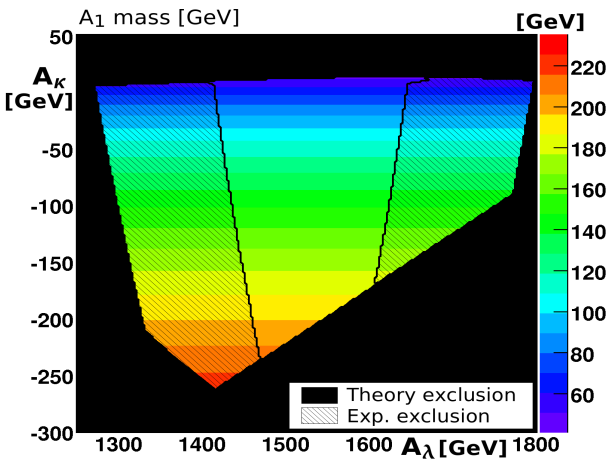

Fig. 6.79: A_1 mass (color coded) in the Maximal M_{H_1} Scenario, A_λ/A_κ plane.

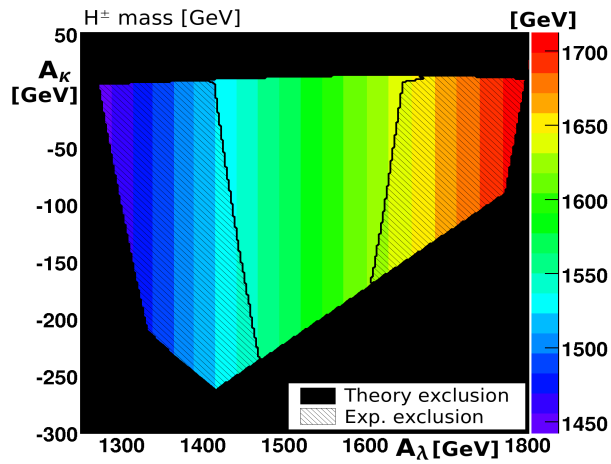

Fig. 6.80: $H^\pm$ mass (color coded) in the Maximal M_{H_1} Scenario, A_λ/A_κ plane.

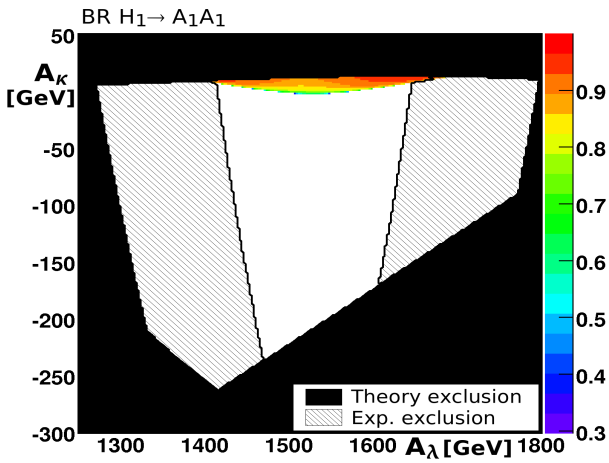

Fig. 6.81: $H_1 \to A_1A_1$ branching ratio (color coded) in the Maximal M_{H_1} Scenario, A_λ/A_κ plane.

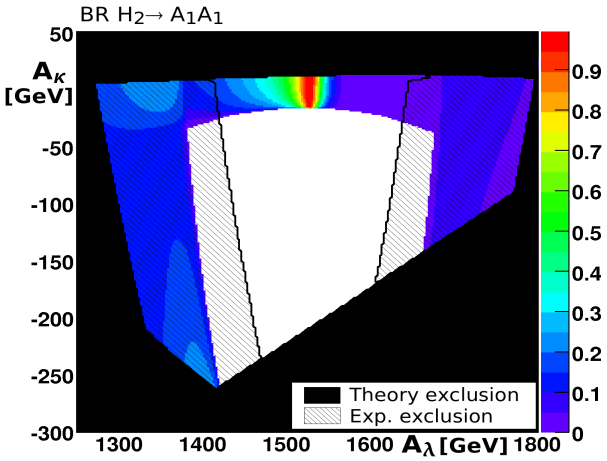

Fig. 6.82: $H_2 \rightarrow A_1A_1$ branching ratio (color coded) in the Maximal M_{H_1} Scenario, A_λ/A_κ plane.

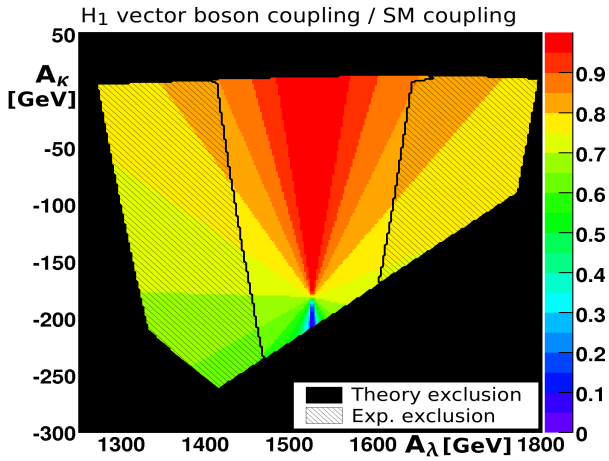

Fig. 6.83: H_1 vector boson coupling (color coded) in the Maximal M_{H_1} Scenario, A_λ/A_κ plane.

cNMSSM point	λ	$A_{\kappa(\mathrm{GUT})}$ [GeV]	A_0 [GeV]	$\tan\beta$	sign(μ)	M_0	$M_{1/2}$
Light $A_1 \rightarrow b\bar{b}$	0.1	-33.9	-1500	10	+	174	500
Light $A_1 \rightarrow \tau\tau$	0.1	-33.4	-1500	10	+	174	500
Light H_1, Light $A_1 \rightarrow \tau\tau$	0.4	-628.56	-1500	10	+	174	500

Tab. 6.3: Benchmark points from Ref. [47] that are covered by the proposed two-dimensional parameter plane for the constrained NMSSM.

supersymmetric scale are also calculated by NMSPEC.

In this thesis, λ and $A_{\kappa(\mathrm{GUT})}$ are varied to obtain a two-dimensional plane. With that choice, the three benchmark points from Tab. 6.3 which are proposed by Ref. [47] are included in the plane. All three points feature a very light A_1, so that the decay $H_1 \rightarrow A_1A_1$ is possible. At the first point, the A_1 has a mass around 40 GeV, therefore the decay chain $A_1 \rightarrow b\bar{b}$ is dominant. The other two points have an A_1 mass of about 10 GeV, resulting in a dominant $A_1 \rightarrow \tau\tau$ decay. The first two points have an H_1 mass of about 120 GeV, whereas for the third point, the H_1 mass is about 90 GeV. The sign of μ is chosen to be positive. With a negative sign of μ, a similar phenomenology would be obtained.

In contrast to the benchmark points on which the Reduced Couplings, the Light A_1 and the Maximal M_{H_1} Scenarios are based, the cNMSSM benchmark points used for the cNMSSM Scenario are in agreement with the allowed dark matter relic density [111], assuming that the LSP is the only dark matter constituent. However, this is not necessarily the case throughout this scenario. Nevertheless, a large part of the $\lambda/A_{\kappa(\mathrm{GUT})}$ plane is in agreement with the dark matter constraints.

Although this scenario does not include a new type of phenomenology that is not covered by the previously described benchmark planes, it is introduced here because the constrained NMSSM is favored over the unconstrained case. The phenomenology of other planes in this scenario, such as the $A_0/\tan\beta$ plane, is very similar to the $\lambda/A_{\kappa(\mathrm{GUT})}$ plane, which therefore can be considered sufficient to represent the cNMSSM Scenario.

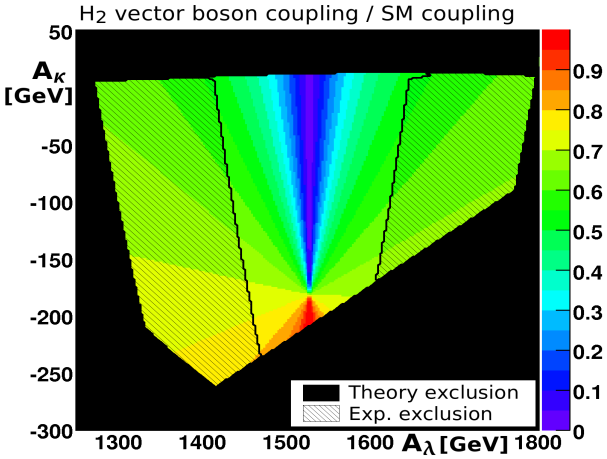

Fig. 6.84: H_2 vector boson coupling (color coded) in the Maximal M_{H_1} Scenario, A_λ/A_κ plane.

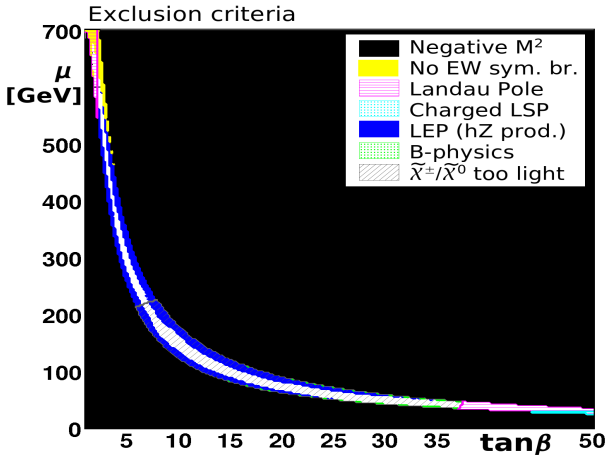

Fig. 6.85: Exclusion criteria in the Maximal M_{H_1} Scenario, $\tan\beta/\mu$ plane.

cNMSSM plane	λ	$A_{\kappa(GUT)}$ [GeV]	A_0 [GeV]	$\tan\beta$	sign(μ)	M_0	$M_{1/2}$
Full $\lambda/A_{\kappa(GUT)}$	0 - 0.5	-800 - 0	-1500	10	+	174	500
Restricted $\lambda/A_{\kappa(GUT)}$	0.096 - 0.102	-34 - -33	-1500	10	+	174	500

Tab. 6.4: Parameters of the proposed two-dimensional plane for the constrained NMSSM.

6.5.1 The $\lambda/A_{\kappa(\mathrm{GUT})}$ benchmark plane

Model parameters For the cNMSSM, the parameters κ, A_λ and A_κ at the supersymmetric scale and $|\mu|$ at the weak scale are output parameters of NMSPEC. Their evolvement in dependence on the input parameters is shown in Figs. 6.86 to 6.89. The values of κ and A_λ vary mainly with λ, whereas A_κ at the supersymmetric scale is influenced both by its value at the GUT scale, and, via the renormalization group equations, by λ. The parameter μ also shows a small variation with both λ and $A_{\kappa(\mathrm{GUT})}$.

Exclusion limits Parameter settings with small negative $A_{\kappa(\mathrm{GUT})}$ and large λ lead to negative mass squares and are thus inaccessible (Fig. 6.90). Positive $A_{\kappa(\mathrm{GUT})}$ values are excluded as well. For too large λ, electroweak symmetry breaking does not take place.

The part of the parameter plane with an H_1 mass smaller than 114 GeV is largely ruled out by LEP. However, there is a narrow allowed band between the blue (dark grey) and the black exclusion region which is barely visible at the chosen scale of the plot. In this band, the light scalar escaped exclusion due to its $H_1 \to A_1 A_1$ decays. The third point from Tab. 6.3 is located in such a region. There is also a narrow band with very low A_1 masses that is ruled out by b-physics constraints, as can be seen in Fig. 6.91, where only a restricted part of the plane including the first two points from Tab. 6.3 is shown. This restricted plane is also specified in Tab. 6.4. Due to the smallness of the band, the region excluded by b-physics is only visible as a line of dots.

Higgs boson masses and Higgs-to-Higgs decays In this plane, the mass of the H_1 is about 120 GeV in the unexcluded region (Fig. 6.92). The mass of the A_1 is mainly determined by the value of A_κ at the supersymmetric scale as in the scenarios before, and is therefore small in a

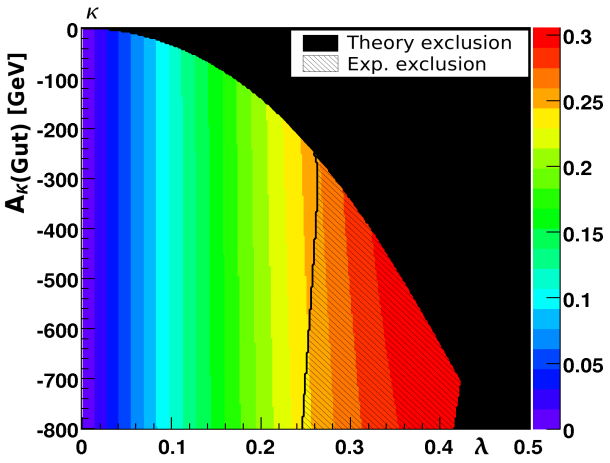

Fig. 6.86: κ (color coded) in the cNMSSM Scenario, $A_{\kappa(\mathrm{GUT})}/\lambda$ plane.

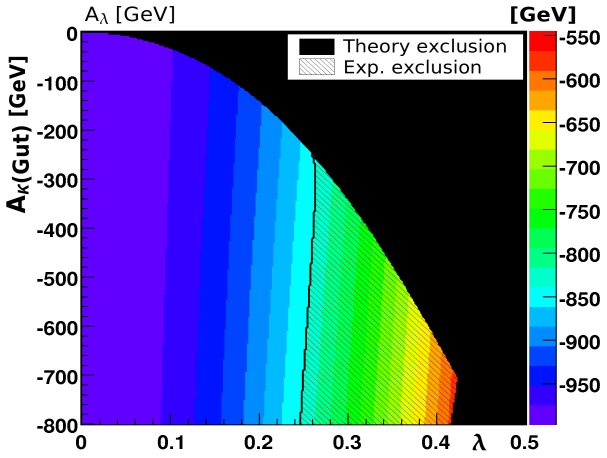

Fig. 6.87: A_λ (color coded) in the cNMSSM Scenario, $A_{\kappa(\mathrm{GUT})}/\lambda$ plane.

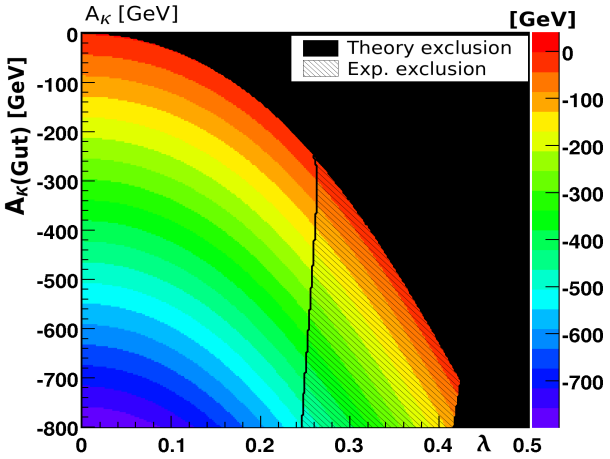

Fig. 6.88: A_κ (color coded) in the cNMSSM Scenario, $A_{\kappa(\mathrm{GUT})}/\lambda$ plane.

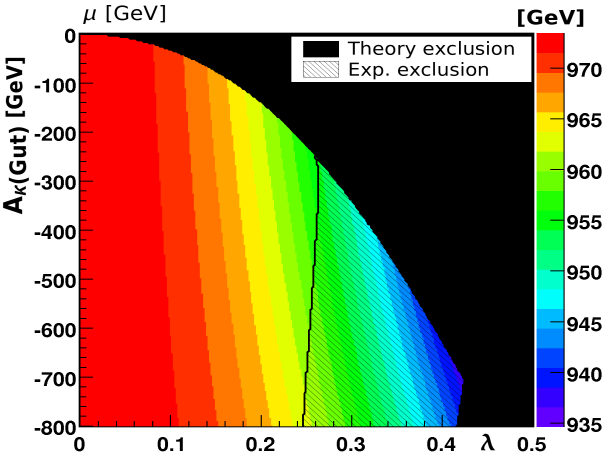

Fig. 6.89: μ (color coded) in the cNMSSM Scenario, $A_{\kappa(\mathrm{GUT})}/\lambda$ plane.

narrow band close to the exclusion bound for A_κ close to zero (Fig. 6.94). The mass quickly increases to values of about 1 TeV for small λ and large negative $A_{\kappa(\mathrm{GUT})}$.

For better illustration, the masses of the H_1 and A_1 as well as the branching ratios for $H_1 \to A_1A_1$ and $A_1 \to \tau\tau$ are shown in Figs. 6.96 to 6.99 for the restricted region of the parameter space which includes only the first and second benchmark point from Tab. 6.3. The A_1 mass is smaller than about 10 GeV in a thin band near the exclusion bound. Here, the $A_1 \to \tau\tau$ decay, elsewhere, the $A_1 \to b\bar{b}$ decay dominates.

The other Higgs bosons are heavy in this scenario. The H_2 and $H^\pm$ masses are about 1 TeV in the entire plane, whereas the H_3 mass can be as large as 2170 GeV in the unexcluded region (Fig. 6.93). The mass of the heavy pseudoscalar A_2 is always larger than about 1 TeV (Fig. 6.95).

Couplings In the entire plane, the H_1 couplings are Standard Model-like (Fig. 6.100). The couplings of the other neutral Higgs bosons (H_2, H_3, A_1, A_2) do not exceed about 10% of their Standard Model value in the unexcluded region. The $gb \to tH^-/g\bar{b} \to \bar{t}H^+$ cross section is about

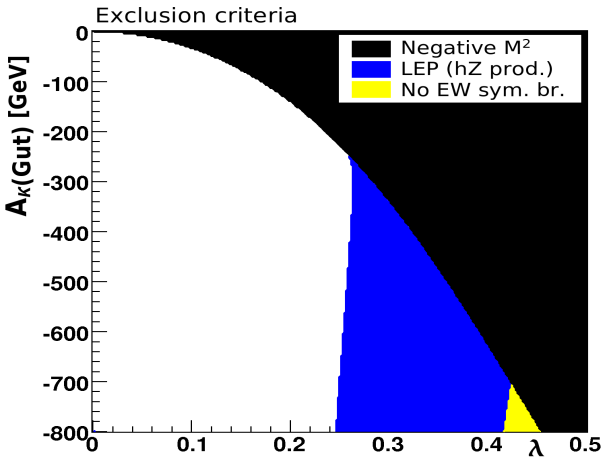

Fig. 6.90: Exclusion criteria in the cNMSSM Scenario, $A_{\kappa(\mathrm{GUT})}/\lambda$ plane.

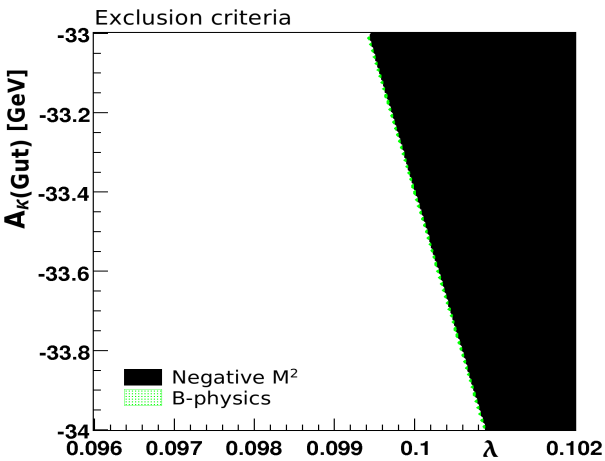

Fig. 6.91: Exclusion criteria in the cNMSSM Scenario, restricted $A_{\kappa(\mathrm{GUT})}/\lambda$ plane.

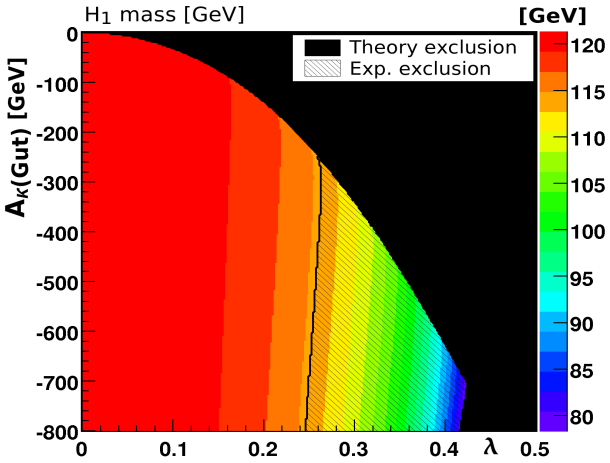

Fig. 6.92: H_1 mass (color coded) in the cNMSSM Scenario, $A_{\kappa(\mathrm{GUT})}/\lambda$ plane.

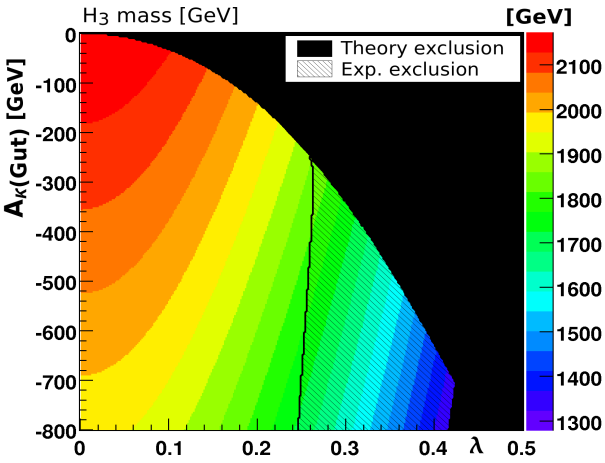

Fig. 6.93: H_3 mass (color coded) in the cNMSSM Scenario, $A_{\kappa(\mathrm{GUT})}/\lambda$ plane.

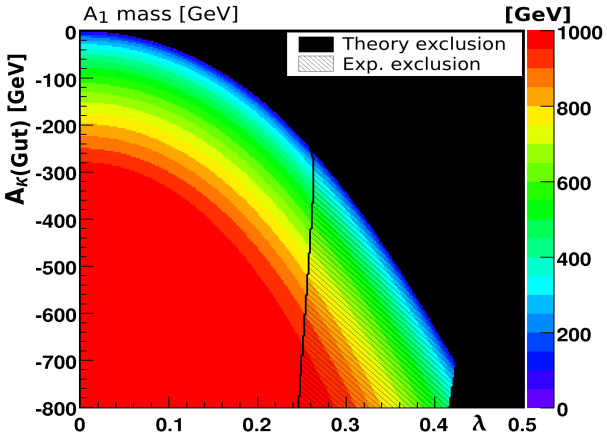

Fig. 6.94: A_1 mass (color coded) in the cNMSSM Scenario, $A_{\kappa(\mathrm{GUT})}/\lambda$ plane.

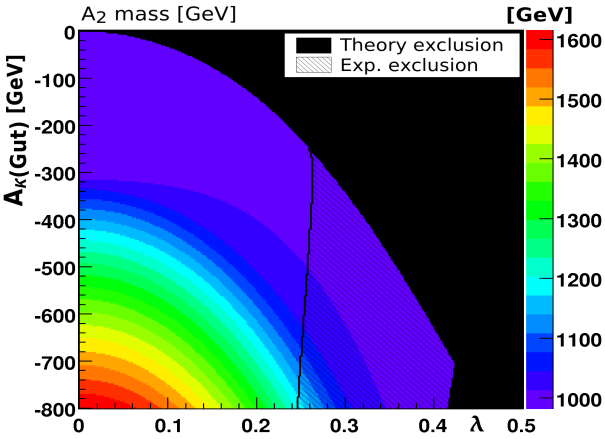

Fig. 6.95: A_2 mass (color coded) in the cNMSSM Scenario, $A_{\kappa(\mathrm{GUT})}/\lambda$ plane.

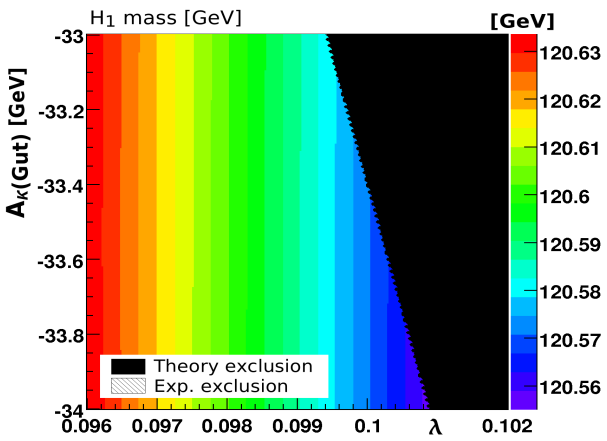

Fig. 6.96: H_1 mass (color coded) in the cNMSSM Scenario, restricted $A_{\kappa(\mathrm{GUT})}/\lambda$ plane.

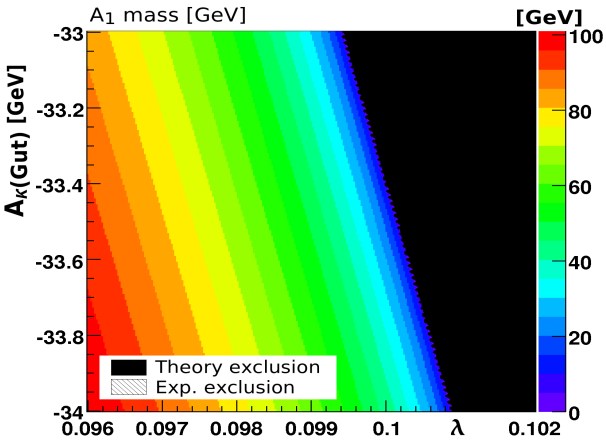

Fig. 6.97: A_1 mass (color coded) in the cNMSSM Scenario, restricted $A_{\kappa(\mathrm{GUT})}/\lambda$ plane.

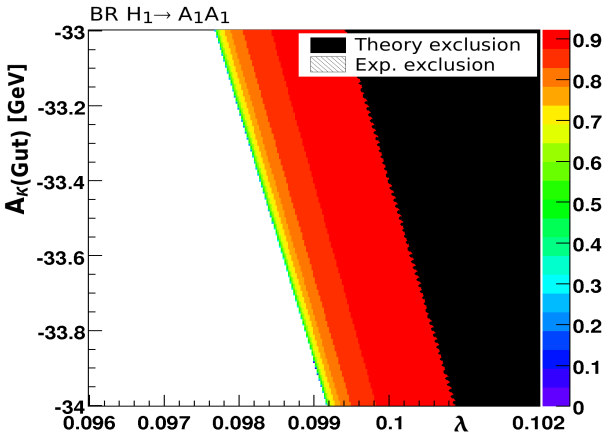

Fig. 6.98: $H_1 \to A_1A_1$ branching ratio (color coded) in the cNMSSM Scenario, restricted $A_{\kappa(\mathrm{GUT})}/\lambda$ plane.

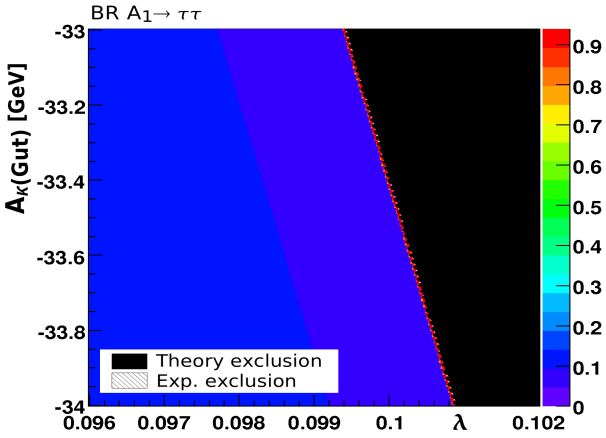

Fig. 6.99: $A_1 \to \tau\tau$ branching ratio (color coded) in the cNMSSM Scenario, restricted $A_{\kappa(\mathrm{GUT})}/\lambda$ plane.

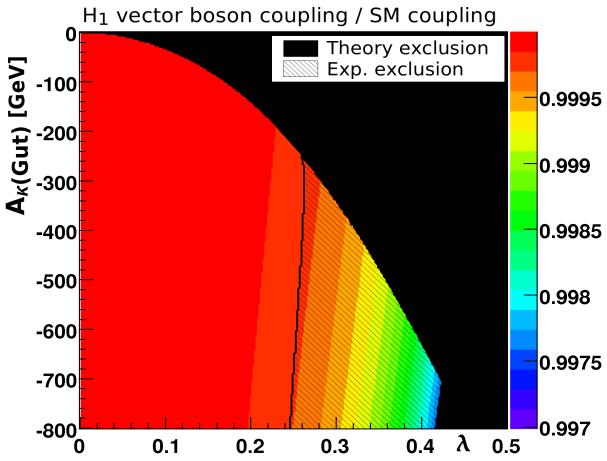

Fig. 6.100: H_1 vector boson coupling in the cNMSSM Scenario, $A_{\kappa(\mathrm{GUT})}/\lambda$ plane.

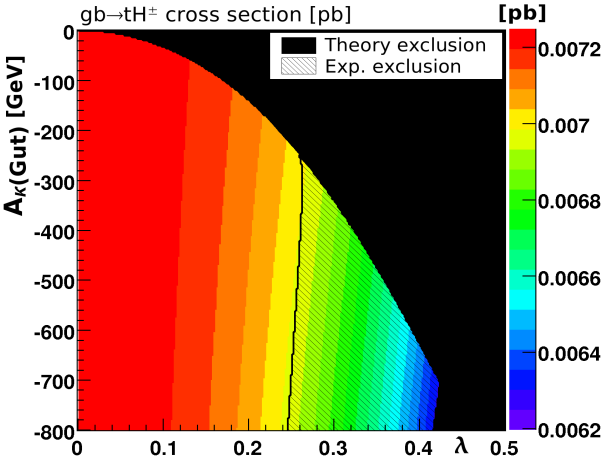

Fig. 6.101: $gb \to tH^-/g\bar{b} \to \bar{t}H^+$ cross section in the cNMSSM Scenario, $A_{\kappa(\mathrm{GUT})}/\lambda$ plane.

7 fb and thus negligible (Fig. 6.101).

Summary of the cNMSSM Scenario This cNMSSM plane consists of a large region with a Standard Model-like H_1. There is also a narrow band with a very light A_1, which includes both dominant $A_1 \to b\bar{b}$ and $A_1 \to \tau\tau$ decays. The other Higgs bosons are not promising for discovery.

6.6 Other interesting phenomenology types

An example of an experimentally very challenging phenomenology type not included in the benchmark scenarios presented in this thesis is a dominant $H_1 \to c\bar{c}$ decay, which can occur due to the suppression of various couplings [98]. In that case, also the most important production cross sections are reduced. Such model parameters will lead to hadronic final states that are very difficult to trigger on in ATLAS. Moreover, the decay of the Higgs boson to charm quarks will most probably not be efficiently separable from the huge QCD background processes at the LHC.

It is also possible that the NMSSM with parameters close to the decoupling limit that resembles the MSSM case is realized in nature. Then, both models will most probably be indistinguishable in the Higgs sector. The discovery potential for MSSM Higgs boson in ATLAS has already been studied in detail [83, 84, 93]. Moreover, possible CP-violation in the Higgs sector of the NMSSM [112] is not included in this work.

6.7 Summary of the benchmark scenarios

Seven interesting two-dimensional NMSSM planes within four different scenarios are described and proposed as possible benchmark planes for NMSSM Higgs boson searches.

- For the Reduced Couplings Scenario, λ/κ, A_λ/A_κ and $\tan\beta/\mu$ planes.
- For the Light A_1 Scenario, a λ/κ plane.
- For the Maximal M_{H_1} Scenario, λ/κ and A_λ/A_κ planes.
- For the cNMSSM Scenario, a $\lambda/A_{\kappa(\mathrm{GUT})}$ plane.

These planes cover the main, for the NMSSM typical phenomenology types. For some of these phenomenology types, a discovery of Higgs bosons at future experiments like the LHC might be difficult:

- Regions with very light scalar H_1.
- Regions where the masses of all seven Higgs bosons are below 300 GeV.
- Regions with reduced couplings of a scalar H_2 without decays to other Higgs bosons.
- Regions with dominant $H_1 \to A_1A_1 \to b\bar{b}b\bar{b}/b\bar{b}\tau\tau$ decays of an otherwise Standard Model-like scalar H_1.
- Regions with dominant $H_1 \to A_1A_1 \to \tau\tau\tau\tau$ decay of an otherwise Standard Model-like scalar H_1.
- A region with dominant $H_1 \to A_1A_1 \to \gamma\gamma\gamma\gamma$ decay of an otherwise Standard Model-like scalar H_1.

- Region with both $H_{1/2} \rightarrow A_1 A_1$ decays and reduced couplings.
- Regions where the mass of the lightest scalar Higgs boson is above the MSSM bound.

Also a scenario for the cNMSSM that is favored by theory is included. In some scenarios, the H_1, in others the H_2 resembles most the Standard Model Higgs boson. If a smaller set of benchmark planes is needed, the λ/κ planes of the Reduced Couplings Scenario and the Light A_1 Scenario might prove useful, since these two planes alone already cover the first six points in the above list [113].

Generally, the parameter regions with interesting and "typical" NMSSM phenomenology are often restricted to narrow bands or small islands close to theoretical or experimental exclusion bounds. Often, also the benchmark points from previous publications [99, 100] are found to be located in regions heavily restricted by various exclusion limits.

In the next chapter, the seven benchmark planes will now be used to evaluate the discovery potential of the ATLAS experiment for NMSSM Higgs bosons with the search channels previously studied by the ATLAS collaboration (Chap. 7).

7. Investigation of the discovery potential for NMSSM Higgs bosons

The discovery potential for SM and MSSM Higgs bosons is outlined in Chap. 5. As stated there, in both models the discovery of at least one Higgs boson at the LHC is highly probable if such a particle exists in nature. In this chapter, a detailed evaluation of the discovery potential for Higgs bosons of the NMSSM is presented. The study is performed for the benchmark scenarios that are described in Chap. 6 and is based on the published Monte Carlo studies of the ATLAS collaboration [5, 62, 72, 78, 82, 85, 87–92] that are reviewed in Chap. 5. At first, the applied method is described in detail. Afterwards, the discovery potential for NMSSM Higgs bosons is discussed. It is desirable that for any possible parameter combination that might be realized in nature, at least one Higgs boson can be observed. A special focus is given to the impact of systematic uncertainties on the background estimation.

7.1 The scanning method

For the evaluation of the discovery potential, the expected significance of every relevant search channel for every NMSSM Higgs boson is calculated. This is done for every scan point of the benchmark planes. The method used for this is specified in the following.

7.1.1 Calculation of NMSSM cross sections

At first, the production cross sections of all Higgs bosons in the NMSSM need to be calculated and to be multiplied with the relevant branching ratios for the NMSSM. The NMSSMTOOLS package [102–104] is used to calculate the Higgs boson masses, decay widths, branching ratios and the couplings relative to the respective couplings of a Standard Model Higgs boson with the same mass. To extract the couplings of the neutral Higgs bosons to gluons and the $H^{\pm}tb$ coupling of the charged Higgs bosons, the procedures of Apps. A and B are applied.

However, NMSSMTOOLS does not provide any production cross sections for the Higgs bosons of the NMSSM. For the neutral Higgs bosons, the production cross sections [66, 67] of a Standard Model Higgs boson of the same mass are therefore scaled to the NMSSM according to the relevant coupling[1]:

$$\sigma_{\mathrm{NMSSM}} = \sigma_{\mathrm{SM}} \cdot \frac{g^2_{\mathrm{NMSSM}}}{g^2_{\mathrm{SM}}} \tag{7.1}$$

This procedure can also be applied for the pseudoscalar Higgs bosons, as the differences in the couplings of pseudoscalar and scalar Higgs bosons are taken into account by g_{NMSSM}. Vector boson fusion and production in association with massive gauge bosons is negligible for the CP-odd Higgs bosons, as their couplings to vector bosons vanish at Born level. Only leading order cross sections are used for the following reasons. First of all, many studies on which the evaluation

[1] The couplings that have to be inserted into Eq. 7.1 are the gluon coupling for gluon fusion processes, the vector boson coupling for vector boson fusion and $W\phi$, $Z\phi$ production, the up-type fermion coupling for $tt\phi$ production and the down-type fermion coupling for $bb\phi$ production.

of the discovery potential is based do not take into account higher order effects. Moreover, a scaling of the gluon fusion cross section according to Eq. 7.1 is only justified in leading order, due to additional contributions to the heavy quark loop in next-to-leading order[2] [114].

For the charged Higgs bosons, the $gb \to tH^-/g\bar{b} \to \bar{t}H^+$ cross sections in leading order are taken from Ref. [115] and are modified according to the $H^\pm tb$ coupling obtained with NMSSMTOOLS. For $t\bar{t}$ production, a leading order cross section of 482 pb is assumed. In order to obtain the production rate of the charged Higgs bosons from top quark decays, the branching ratio $t \to H^+b/\bar{t} \to H^-\bar{b}$ is calculated with FeynHiggs [116]. For both production modes of the charged Higgs bosons, radiative corrections that depend on the exact parameter settings of the supersymmetric model are taken into account. For more details see App. B.

The top quark mass is set to 172 GeV. All branching ratios of the Higgs bosons are directly obtained from NMSSMTOOLS and are applied to the production cross sections if necessary.

7.1.2 Signal and background rates

For the estimation of the discovery potential of a search for the NMSSM Higgs bosons, both the expected number of signal and of background events that pass the signal selection need to be known. The expected numbers of background events are taken from published ATLAS Monte Carlo studies (Tab. 7.1) and scaled to the integrated luminosity used. The current results only include Standard Model background processes.

The expected number of totally produced signal events is derived from the NMSSM cross sections discussed above. Signal selection efficiencies that are taken from published ATLAS studies allow to calculate the expected number of signal events that pass the event selection.

All ATLAS studies included in this investigation are performed for a limited number of mass points. The selection efficiencies and background numbers for the exact masses of the NMSSM Higgs bosons are achieved from a linear interpolation between these points. An extrapolation is only done inside a mass range which is not too far away from the originally studied mass points, so that a reasonable behavior can still be expected. Especially, an extrapolation to regions with large background peaks, such as the Z^0 peak for the $H \to \tau\tau$ channel, is not performed. For Higgs bosons with masses outside the allowed mass range of a certain search channel, the significance is set to zero for that channel.

At last, the number of expected signal events is corrected for the effects of increased Higgs boson decay widths and for possible degeneracy of Higgs boson masses.

Corrections for large Higgs bosons widths

In the NMSSM, the natural line width of the Higgs bosons may be enhanced relative to the Standard Model case. Thus, a larger fraction of signal events may fall outside a mass window cut than in the Standard Model. The signal selection efficiency is then smaller than for the Standard Model case. To correct for this, the Higgs boson peak is described by a Voigt function[3] whose Breit-Wigner part is given by the natural line width, the Gaussian part by the detector resolution. The ratio k of the integrals of the Voigt function over the mass window for the SM (I_{SM}) and the NMSSM case (I_{NMSSM}) is used as a correction factor:

$$k = \frac{I_{\mathrm{NMSSM}}}{I_{\mathrm{SM}}} \tag{7.2}$$

If this yields $k > 1$, $k = 1$ is used instead in order to be purposely conservative.

[2] A direct calculation of the cross sections for each Higgs boson via suitable programs [66] on the basis of their couplings to up- and down-type fermions would be too time-consuming.

[3] The Voigt function is a convolution of a Gaussian and a Breit-Wigner function.

Corrections for degenerate Higgs boson masses

To correct for degenerate Higgs boson masses, the Higgs boson peaks are described by a Voigt function as before. The peaks are assumed to be indistinguishable if their separation is smaller 2σ.[4] Higgs bosons with overlapping mass windows are also considered indistinguishable to avoid a double counting of events. In this case, also Higgs bosons that have a separation larger than 2σ may be considered not to be separable in the following as a conservative estimate.

In case of inseparable peaks, the contributions from all Higgs bosons are added up for each boson's mass window. Only the highest observed significance is kept and assigned to the Higgs boson with the largest fraction of signal events in that mass window. In some cases two or three Higgs bosons contribute significantly to the same mass window. Such cases will be discussed in detail when they occur.

7.1.3 Significance calculation

For the significance calculation, the profile likelihood method [117] is used (see App. C). This method is chosen as it proved to be fast and reliable in a comparison of available methods. Moreover, it easily allows for the inclusion of systematic uncertainties and the combination of different channels. To claim a discovery, a significance of at least 5σ is required.

The data volume that is assumed for the significance calculation depends on the available studies for the different search channels:

- If only studies of a search channel at design luminosity exist, a data volume of 300 fb^{-1} is assumed in the following.
- If only low luminosity studies are available, 30 fb^{-1} are used.
- If both luminosity scenarios have been investigated, 30 fb^{-1} taken at low luminosity and 270 fb^{-1} taken at design luminosity are assumed.[5]

As a special case, the discovery potential for only 30 fb^{-1} is studied.

The search topologies considered in the evaluation of the discovery potential and the considered mass ranges are summarized in Tab. 7.1. All search topologies are considered for every NMSSM Higgs boson or allowed combination of NMSSM Higgs bosons. Within the scenarios examined in this thesis, the (VBF, $\phi\to\gamma\gamma$), the (GGF, $\phi\to\phi'\phi'\to\gamma\gamma\text{b}\bar{\text{b}}$) and the (GGF, $\phi\to\text{Z}\phi'\to\text{llb}\bar{\text{b}}$) channels do not show significances larger than 5σ with the considered integrated luminosity in the theoretically allowed and yet unexcluded regions for any of the NMSSM Higgs bosons. Also the inclusive $\phi\to\gamma\gamma$ analysis does not reach significances larger than 5σ for Higgs boson masses $\gtrsim 200$ GeV (referred to as $\text{A}\to\gamma\gamma$ mode in Tab. 7.1). In the above notation, ϕ (ϕ') refers to all neutral Higgs bosons of the NMSSM. In the following, ϕ will also be used to denote that the general search strategy is meant, and not the search for a specific Higgs boson.

7.1.4 Systematic uncertainties

In the evaluation of the discovery potential, results with and without systematic uncertainties on the background estimation are shown and compared. The inclusion of systematic uncertainties is only relevant for search topologies which have a discovery potential in the discussed scenarios

[4] For the Voigt function, this is calculated as 2·FWHM/2.355. In case of a negligible Higgs boson width, this corresponds to a 2σ separation of two Gaussians. To calculate the full width at half maximum of the Voigt function, the approximate formula from Ref. [118] is applied.

[5] This is preferred to taking the complete 300 fb^{-1} at design luminosity because signal-to-background ratios are usually higher in the low luminosity case.

Search Channel	**Mass Range [GeV]**	**Low Lumi.**	**Design Lumi.**	**Refs.**
VBF, H$\to\tau\tau$	110-150	30 fb^{-1}	-	[62]
VBF, H$\to$WW$\to$ll$\nu\nu$	110-200	30 fb^{-1}	-	[62]
VBF, H$\to$WW$\to$lνh	130-200	30 fb^{-1}	-	[62]
VBF, H$\to\gamma\gamma$	110-160	30 fb^{-1}	-	[82]
ttH, H$\to$b$\bar{\text{b}}$	70-150	30 fb^{-1}	270 fb^{-1}	[78]
GGF, H$\to$ZZ$\to$4l	120-420	30 fb^{-1}	270 fb^{-1}	[5]
GGF, H$\to$WW$\to$ll$\nu\nu$	140-200	30 fb^{-1}	270 fb^{-1}	[85]
WH, H$\to$WW$\to$ll$\nu\nu$	150-190	-	300 fb^{-1}	[5]
Inclusive H$\to\gamma\gamma$	70-160	-	300 fb^{-1}	[5]
Inclusive A$\to\gamma\gamma$	200-450	-	300 fb^{-1}	[5]
WH, ZH, ttH, H$\to\gamma\gamma$	70-150	-	300 fb^{-1}	[5]
bbH, H/A$\to\tau\tau\to$hh	450-800	30 fb^{-1}	-	[88]
GGF, bbH, H/A$\to\tau\tau\to$lνh	150-800	30 fb^{-1}	-	[87]
GGF, bbH, H/A$\to\mu\mu$	70-500	30 fb^{-1}	270 fb^{-1}	[89, 90]
GGF, H$\to$hh$\to\gamma\gamma$b$\bar{\text{b}}$	230-270 / 70-100	30 fb^{-1}	270 fb^{-1}	[5]
GGF, H$\to$ZA$\to$llb$\bar{\text{b}}$	200-250 / 70-100	30 fb^{-1}	270 fb^{-1}	[5]
gb$\to$H$^{\pm}$t, H$^{\pm}\to\tau\nu$	175-600	30 fb^{-1}	-	[92]
gb$\to$H$^{\pm}$t, H$^{\pm}\to$tb	190-400	30 fb^{-1}	-	[72]
t$\bar{\text{t}}\to$H$^{\pm}$bWb$\to\tau\nu$lνb$\bar{\text{b}}$	90-165	30 fb^{-1}	-	[5]
t$\bar{\text{t}}\to$H$^{\pm}$bWb$\to\tau\nu$q$\bar{\text{q}}$b$\bar{\text{b}}$	80-165	30 fb^{-1}	-	[91]

Tab. 7.1: Included search topologies with allowed mass ranges and integrated luminosities used for the two luminosity phases. The here given Higgs boson names (h, H, A) refer to the original studies. In this thesis, the search topologies are considered for all NMSSM Higgs bosons. For a more condensed notation in the limited space of this table, in the last four rows 't' and 'b' may refer both to quarks and to antiquarks, depending on the charge of the charged Higgs boson.

when the systematic uncertainties are neglected. Therefore, all other search topologies are excluded from this discussion.

For the (VBF, $\phi\to\tau\tau$), the (VBF, $\phi\to$WW), the (ttϕ, $\phi\to$b$\bar{\text{b}}$) and the (GGF, $\phi\to$WW$\to$ll+2ν) searches, an estimation of the background uncertainty can be found in the same references that the signal efficiencies and background numbers are taken from. These estimates are used in this work.

For the other search topologies, information on the background uncertainty is not included in the respective references. As an alternative approach, a method for the estimation of systematic uncertainties that assumes that the expected background numbers can be obtained from the sidebands is used. Reference [119] describes this method and also gives the expected relative factor of the number of events in the sideband in comparison to the number of background events in the signal region for the $\phi\to\gamma\gamma$ and (Wϕ, $\phi\to$WW$\to$ll$\nu\nu$) searches. As the number of background events in the signal region is known from the Monte Carlo studies for each search channel, the absolute number of events in the sideband and then the relative statistical error of the sideband estimation can be calculated with the help of this factor. Moreover, an estimation of the error of the fit from the sidebands to the signal region is provided. An estimation of the total background uncertainty is obtained by adding these two error contributions quadratically.

For the (GGF, $\phi\to$ZZ$\to$4l) and the charged Higgs boson searches, a rough estimate on sys-

Search Channel	Background Uncertainty	Refs.
VBF, $\phi\rightarrow\tau\tau$	10%	[62]
VBF, $\phi\rightarrow$WW	10%	[62]
ttϕ, $\phi\rightarrow$b$\bar{\text{b}}$	11.1% (80 GeV) - 4.8% (140 GeV)	[78]
GGF, $\phi\rightarrow$ZZ$\rightarrow$4l	10% ($<$ 200 GeV), 5% ($>$ 200 GeV)	[120]
GGF, $\phi\rightarrow$WW$\rightarrow$ll$\nu\nu$	5%	[85]
Wϕ, $\phi\rightarrow$WW$\rightarrow$ll$\nu\nu$	17.0%	[119]
Inclusive $\phi\rightarrow\gamma\gamma$	0.12% (80 GeV) - 0.15% (150 GeV)	[119]
Wϕ, Zϕ, ttϕ, $\phi\rightarrow\gamma\gamma$	6.7% (80 GeV) - 8.6% (140 GeV)	[119]
GGF, bbϕ, $\phi\rightarrow\tau\tau$	variation: 1%, 5%, 10%, 20%	-
GGF, bbϕ, $\phi\rightarrow\mu\mu$	variation: 1%, 5%, 10%	-
gb$\rightarrow$H$^{\pm}$t, H$^{\pm}\rightarrow\tau\nu$	10%	[121]
gb$\rightarrow$H$^{\pm}$t, H$^{\pm}\rightarrow$tb	10%	[121]
t$\bar{\text{t}}\rightarrow$H$^{\pm}bWb\rightarrow\tau\nu$l$\nu$b$\bar{\text{b}}$	10%	[121]
t$\bar{\text{t}}\rightarrow$H$^{\pm}bWb\rightarrow\tau\nu$q$\bar{\text{q}}b\bar{\text{b}}$	10%	[121]

Tab. 7.2: Systematic uncertainties on the background estimation and their references for all relevant search topologies. If the uncertainty depends on the Higgs boson mass, only the maximal and minimal values are listed. The corresponding Higgs boson masses are given in brackets. For a more condensed notation in the limited space of this table, in the last four rows 't' and 'b' may refer both to quarks and to antiquarks, depending on the charge of the charged Higgs boson.

tematic uncertainty based on the experience of the CSC[6] group leaders for these studies [120,121] is used in this thesis. For the (GGF, bbϕ, $\phi\rightarrow\tau\tau$) and (GGF, bbϕ, $\phi\rightarrow\mu\mu$) search topologies, the background uncertainty level is largely unknown up to now. Therefore, different values are investigated as examples.

In some cases, the background uncertainty depends on the mass of the Higgs boson. In that case, the uncertainties are given or calculated only for selected mass points. Like the signal selection efficiencies and the background numbers, the uncertainties for other Higgs boson mass values are obtained by a linear interpolation inside the allowed mass range. An overview of the background uncertainties for all relevant searches is given in Tab. 7.2.

7.2 Results of the scan

In the following, the results of the parameter scans over the seven benchmark planes from Chap. 6 are described. At first, the most important features of every benchmark plane are very shortly reviewed as a reminder. Afterwards, the 5σ discovery contours when systematic uncertainties are not taken into account are presented. Although in principle the discovery contours with systematic uncertainties are more relevant, the true sizes of the uncertainties that will have to be dealt with are not precisely known, and many of the here used values are only rough estimates. Therefore, the contours without inclusion of systematic uncertainties are presented at first. Unlike otherwise stated, the presented results are obtained for a data volume of 30+270 fb^{-1}. Then, detailed descriptions of the features of the relevant discovery contours will be given. The impact of the assumed background uncertainties is discussed afterwards. At last, the discovery potential for only 30 fb^{-1} will be discussed separately.

[6] Computing System Commissioning, an effort to test the ATLAS computing system and data processing chain.

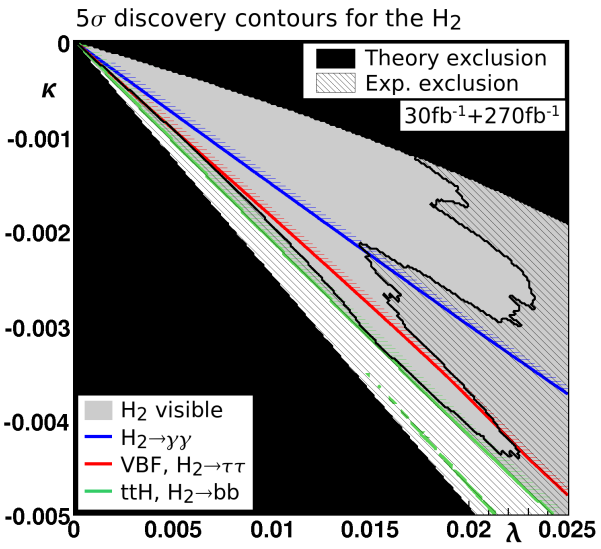

Fig. 7.1: 5σ discovery contours for the H_2 in the Reduced Couplings Scenario, λ/κ plane with 30+270 fb^{-1}. Systematic uncertainties are not included. The H_2 is observable in the grey region.
How the plot must be read: The colored (grayish) lines mark the region where the various analyses have a significance of 5σ. The colored (grayish) stripes indicate in which direction the significances are larger than 5σ.

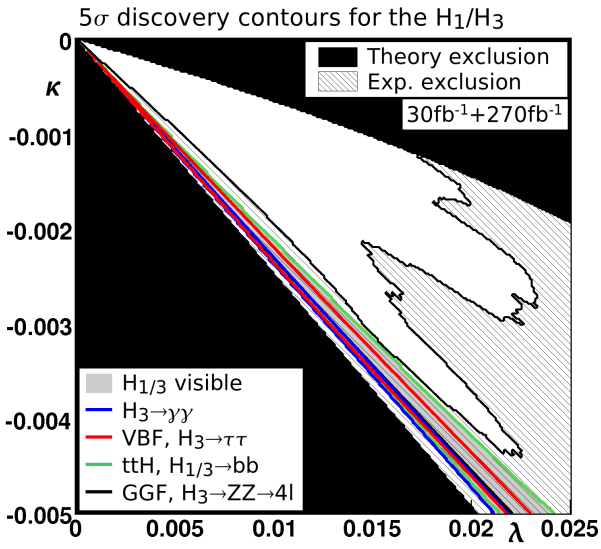

Fig. 7.2: 5σ discovery contours for the H_1 and H_3 in the Reduced Couplings Scenario, λ/κ plane with 30+270 fb^{-1}. Systematic uncertainties are not included. The H_1 or the H_3 is observable in the grey region. For details on how this plot must be read, see Fig. 7.1.

7.2.1 The Reduced Couplings Scenario

7.2.1.1 The λ/κ benchmark plane

In the λ/κ plane of the Reduced Couplings Scenario, the H_2 has a mass of about 115 to 120 GeV in the unexcluded region and is Standard Model-like in large parts of the parameter space. The smallest H_2 masses are obtained with small λ and large negative κ[7]. In an unexcluded region with large negative κ close to the lower exclusion bound, the couplings of H_2 are reduced to about 80% or less of their Standard Model value. The H_1 is very light in the region close to the upper exclusion bound, so that the decay $H_2 \rightarrow H_1 H_1$ is kinematically allowed. However, due to the small branching ratio for this decay mode of at most 6%, its effect on the discovery potential is negligible.

Discovery potential for the NMSSM Higgs bosons The discovery potential for the H_2 is shown in Fig. 7.1. The colored (grayish) lines mark the region where the various analyses have a significance of 5σ. The colored (grayish) stripes indicate in which direction the significances are larger than 5σ. In the grey region, the H_2 will be observable.

[7] In the following, terms like 'large κ' and 'small κ' will often be used to describe the position of regions inside the plane. Terms like 'large' and 'small' are then meant respectively to the κ range covered by the plane. The same is true also for the other Higgs sector parameters and other planes. Actually, the value of κ is in this plane very small compared to the full parameter space.

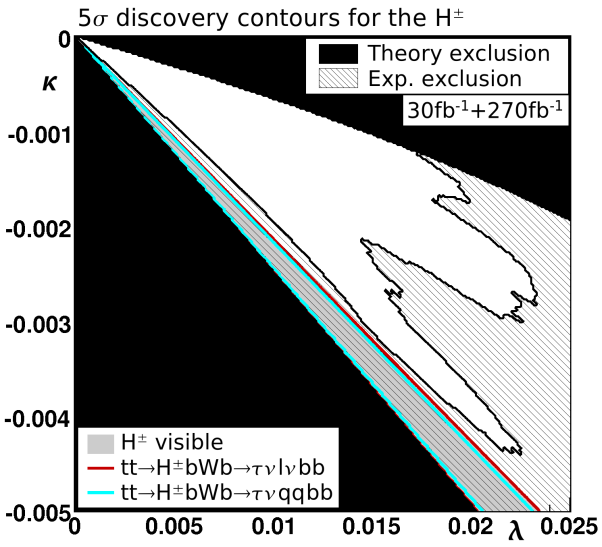

Fig. 7.3: 5σ discovery contours for the $H^{\pm}$ bosons in the Reduced Couplings Scenario, λ/κ plane with 30+270 fb^{-1}. For all charged Higgs boson searches, only the low luminosity case corresponding to 30 fb^{-1} is taken into account. Systematic uncertainties are not included. The $H^{\pm}$ bosons are observable in the grey region. For details on how this plot must be read, see Fig. 7.1.

The entire unexcluded region is covered by the ($tt H_2$, $H_2 \to b\bar{b}$) channel despite the reduced couplings. Also the (VBF, $H_2 \to \tau\tau$) and inclusive $H_2 \to \gamma\gamma$ channels contribute. In Fig. 7.2, the discovery potential for the H_1 and H_3 is shown. These Higgs bosons are visible only in the already excluded parameter region via the ($tt H_{1/3}$, $H_{1/3} \to b\bar{b}$), the (VBF, $H_3 \to \tau\tau$), the inclusive $H_3 \to \gamma\gamma$ and the (GGF, $H_3 \to ZZ \to 4l$) channels. Since the charged Higgs bosons are lighter than the top quark only in the excluded region, they can be detected via the corresponding searches only in this region of parameter space (Fig. 7.3). The $gb \to tH^-/g\bar{b} \to \bar{t}H^+$ cross section is too small to be of importance. Although the pseudoscalar Higgs bosons have experimentally accessible masses below 300 GeV in this scenario, they have highly reduced couplings and are therefore not visible. In short, in the λ/κ plane of the Reduced Couplings Scenario, only the H_2 is observable in the unexcluded region via the $tt H_2$, $H_2 \to b\bar{b}$, the VBF, $H_2 \to \tau\tau$ and the inclusive $H_2 \to \gamma\gamma$ searches. Some aspects of the discovery contours of these searches will be discussed in the following.

Specifics of the $tt\phi$, $\phi \to b\bar{b}$ channel For the ($tt\phi$, $\phi \to b\bar{b}$) channel, the mass peaks of all three scalar Higgs bosons are considered indistinguishable due to the large mass window of $M_\phi \pm 45$ GeV [78]. With such a large mass window, the Higgs boson peaks could only be considered separable if they are 90 GeV or more apart. This is larger than the allowed mass range from 70 GeV to 150 GeV of this search. In principle, mass peaks inside the allowed mass range might be more than 2σ apart, yet they cannot be considered as separate peaks in this work nevertheless as this would invoke a double counting of events due to the overlapping mass windows, as explained before. As a consequence, in this plane up to three Higgs bosons contribute to the excess of signal events when their masses are inside the allowed mass range.

For large λ and small negative κ, only the H_2 is inside the mass range of this analysis and can alone provide the necessary significance for a discovery. In the region where the H_2 couplings are reduced, significant contributions from the H_1, and for small λ and large negative κ close to the exclusion bound, also from the H_3, are added to the number of signal events. If this was

not the case, the H_2 alone would not be visible in the entire allowed region, but a narrow band very close to the exclusion bound would not reach significances above 5σ due to the reduced couplings. However, as the inverse variation of the couplings of the Higgs bosons is typical for the NMSSM, as explained in Chap. 6.2.1, such contributions of other Higgs bosons to the mass window can be expected to be common in the ($tt\phi$, $\phi\rightarrow b\bar{b}$) analysis, provided that these Higgs bosons have a low mass.

A significant excess of signal events is also present below the $H_2\rightarrow b\bar{b}$ discovery contour of Fig. 7.1, but there, the H_2 does not any longer provide the largest contribution to the signal events, so the discovery potential is assigned to the H_1 and, for even smaller λ and larger $|\kappa|$, to the H_3. Also in the excluded region, there is a thin line where the H_2 provides the largest contribution to this channel, however, a significance of 5σ is only achieved with the contributions from the H_1 and H_3. Regardless of which Higgs boson the discovery potential is assigned to, all three Higgs bosons contribute to the signal in the excluded region.

Specifics of the VBF, $\phi\rightarrow\tau\tau$ channel For the (VBF, $H_2\rightarrow\tau\tau$) channel, only the low luminosity phase is considered. With 30 fb^{-1}, the search for $H_2\rightarrow\tau\tau$ is the only sensitive channel and ensures the discovery of the H_2 in large parts of the parameter plane. The region with reduced couplings is not covered for that case. In addition to the reduction of the couplings, this channel suffers also from the fact that the H_2 mass decreases for small λ and large $|\kappa|$ to $\sim$115 GeV in the allowed region. Although this slightly increases the signal rate, the background contributions from the tails of the Z^0 peak grow significantly if the signal peak approaches the Z^0 mass [62]. Therefore, this search channel has its maximum discovery potential for masses from 120 to 130 GeV.

In large parts of the allowed parameter region, only the H_2 is inside the allowed mass range of the (VBF, $\phi\rightarrow\tau\tau$) analysis. However, there is a thin band in the unexcluded region close to the exclusion bound at large negative κ, where the H_3 is in principle light enough to be inside the allowed mass range of the channel. With respect to the mass resolution and to the mass window of $M_\phi - 10$ GeV $< M_\phi < M_\phi + 15$ GeV [62], the H_2 and the H_3 are well separated in the unexcluded region, so that there is no significant contribution from the H_3 to the mass window of the H_2. In the excluded region, the H_3 is visible in this channel. In this region, the H_2 and the H_3 are nearly degenerate, so that their contributions to the mass window are added. However, the contribution from the H_2 is small, and the H_3 alone would be observable in nearly the same region. The H_1 does not enter the allowed mass range of the $\phi\rightarrow\tau\tau$ channel in this parameter plane.

Specifics of the inclusive $\phi\rightarrow\gamma\gamma$ channel For different reasons, the inclusive search for $H_2\rightarrow\gamma\gamma$ covers a smaller region in this plane than the $H_2\rightarrow\tau\tau$ channel. The dominant contribution to the $H_2\rightarrow\gamma\gamma$ signal events stems from the gluon fusion process, and the coupling of the H_2 to gluons is slightly smaller than its Standard Model value in the entire plane. A significant reduction can be observed earlier than for the coupling to vector bosons when going to smaller λ and larger $|\kappa|$ (Fig. 6.18). Moreover, this channel is also sensitive to the decreasing H_2 mass, as the branching ratio of $H_2\rightarrow\gamma\gamma$ commonly has its maximum at a Higgs boson mass of about 126 GeV and then drops rapidly with decreasing Higgs boson mass [77] (see Fig. 5.4).

In principle, also the H_1 and the H_3 have accessible masses for the $\phi\rightarrow\gamma\gamma$ analysis in a part of the unexcluded region at small λ and large negative κ, but their signal rate is too small to be visible in the allowed region. As the mass resolution for the $\phi\rightarrow\gamma\gamma$ search is excellent ($\sim$1.1 to 1.7 GeV) [5], none of the signal peaks overlap. In the excluded region where the H_3 boson is visible in this channel, the $H_3\rightarrow\gamma\gamma$ branching ratio is enhanced due to a suppression of the $H_3\rightarrow b\bar{b}$ branching ratio. For the same reason, also the $H_3\rightarrow ZZ$ branching ratio is enhanced.

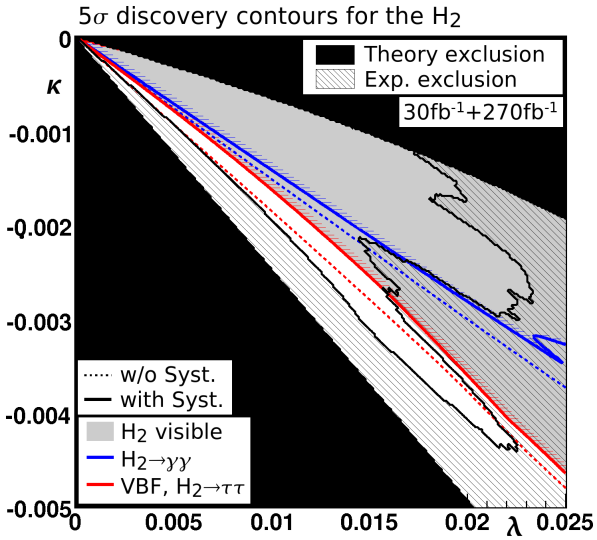

Fig. 7.4: 5σ discovery contours for the H_2 in the Reduced Couplings Scenario, λ/κ plane with 30+270 fb^{-1}. Systematic uncertainties are taken into account. For comparison, the results without systematic uncertainties are given by the dotted lines. The H_2 is observable in the grey region. For details on how this plot must be read, see Fig. 7.1.

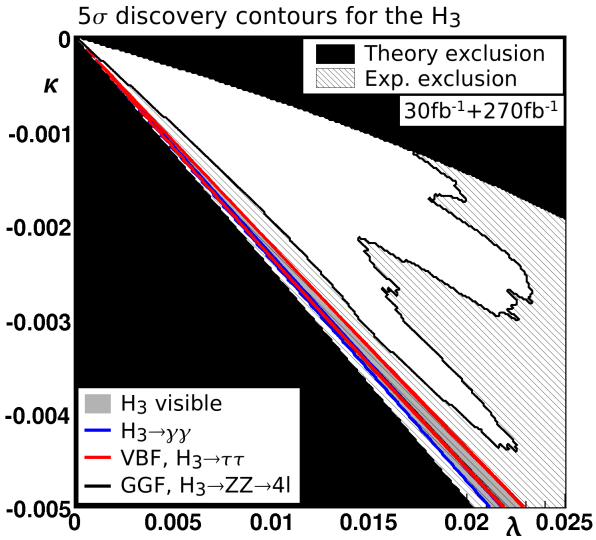

Fig. 7.5: 5σ discovery contours for the H_3 in the Reduced Couplings Scenario, λ/κ plane with 30+270 fb^{-1}. Systematic uncertainties are taken into account. The H_3 is observable in the grey region. For details on how this plot must be read, see Fig. 7.1.

Therefore, the contribution from the (GGF, $H_3 \to ZZ \to 4l$) channel occurs in about the same region.

Discovery potential with systematic uncertainties When systematic uncertainties are included, the ($tt H_2$, $H_2 \to b\bar{b}$) analysis does not reach the 5σ level any longer. Also the (VBF, $H_2 \to \tau\tau$) and the $H_2 \to \gamma\gamma$ searches lose some of their discovery potential (Fig. 7.4). The region with reduced couplings and with a low Higgs boson mass around 115 GeV is not covered any longer with 30+270 fb^{-1} of integrated luminosity. It is therefore crucial to either control the background uncertainties of the ($tt\phi$, $\phi \to b\bar{b}$) analysis very well, or to make sure that the (VBF, $\phi \to \tau\tau$) analysis can also be used for the design luminosity phase. This needs careful study of the central jet veto and the jet identification efficiencies in the presence of pile-up. Even if this should prove to be feasible, a deterioration of the signal selection efficiencies and/or the background suppression must be expected. Assuming low luminosity performance, about 150 fb^{-1} will be needed to cover the entire allowed parameter region with the (VBF, $\phi \to \tau\tau$) analysis when systematic uncertainties are taken into account.

Also a combination of the different search channels might yield an improvement. However, when the ($tt\phi$, $\phi \to b\bar{b}$), (VBF, $\phi \to \tau\tau$) (30 fb^{-1}), and $\phi \to \gamma\gamma$ channels are combined in the profile likelihood method, the region with reduced couplings can still not be covered completely.

In the excluded region, only the H_3 is visible when systematic uncertainties are included (Fig. 7.5). The charged Higgs bosons are not observable, as for the intermediate $\tan\beta$ of 5.7, the $H^{\pm}tb$ coupling is relatively small according to Eq. 2.60. The ($tt H_{1/3}$, $H_{1/3} \to b\bar{b}$) channel is also not observable. The deterioration of the discovery contours of the $H_3 \to \tau\tau$, $H_3 \to \gamma\gamma$ and $H_3 \to ZZ \to 4l$ searches is so small that it cannot be seen at the scale chosen for Fig. 7.5.

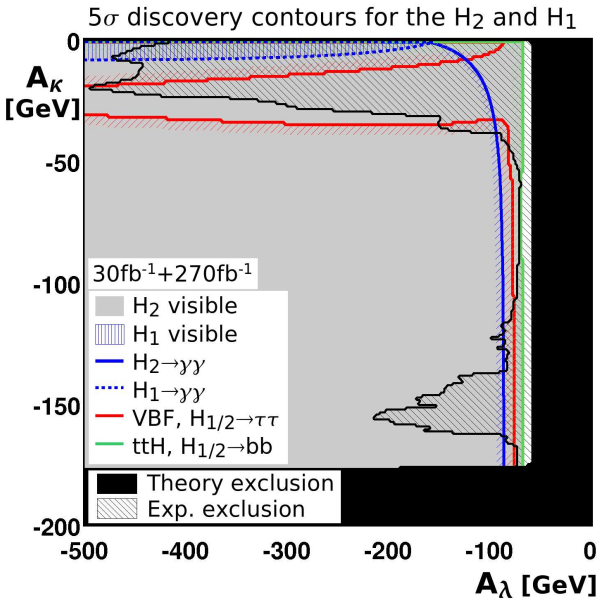

Fig. 7.6: 5σ discovery contours for the H_1 and H_2 in the Reduced Couplings Scenario, A_λ/A_κ plane with 30+270 fb^{-1}. The H_2, possibly with contributions from the H_1, is observable in the grey region. The H_1 is observable separately in the blue (dark grey) hatched region. Systematic uncertainties are not included. For details on how this plot must be read, see Fig. 7.1.

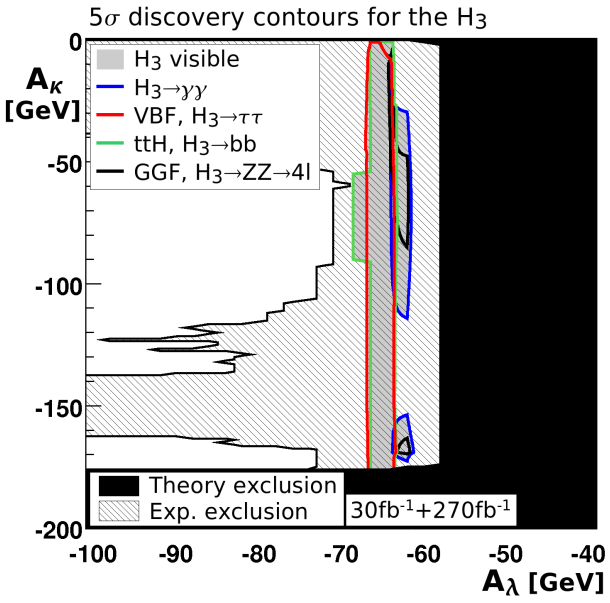

Fig. 7.7: 5σ discovery contours for the H_3 in the Reduced Couplings Scenario, A_λ/A_κ plane with 30+270 fb^{-1}. The H_3 is observable in the grey region. Systematic uncertainties are not included. For details on how this plot must be read, see Fig. 7.1.

Summary of the Reduced Couplings Scenario, λ/κ benchmark plane In this benchmark plane, only the H_2 will be observable in the unexcluded parameter region. To ensure a discovery, a good control of systematic uncertainties, especially in the (ttϕ, $\phi\to$b$\bar{\text{b}}$) channel, or a good detectability of the vector boson fusion signature under high luminosity conditions is needed. With 30 fb^{-1}, the (VBF, $\phi\to\tau\tau$) analysis allows a for discovery of the H_2 boson in a large part of the plane. A discrimination of the Standard Model from extended models from the number of discovered mass resonances will not be possible in this plane. More advanced methods need to be developed.

7.2.1.2 The A_λ/A_κ benchmark plane

In this plane, the H_2 has a mass around 115 to 124 GeV and is Standard Model-like in large parts of the parameter plane. There are two different unexcluded regions where its couplings are reduced. One is located at small negative $A_\lambda \approx 70$ GeV around $A_\kappa \approx 55$ GeV. In this region, the coupling of the H_2 to vector bosons is reduced to 80% of its Standard Model value, and its coupling to gluons is even more reduced. The second region with reduced couplings can be found at small negative $A_\kappa \gtrsim -30$ GeV. In this region, the couplings of the H_2 are about 70% of their Standard Model values. In that region, the mass of the otherwise lighter H_1 is around 110 GeV and its couplings are also about 70% of their Standard Model values. The other Higgs bosons are promising for a discovery only in the experimentally excluded region.

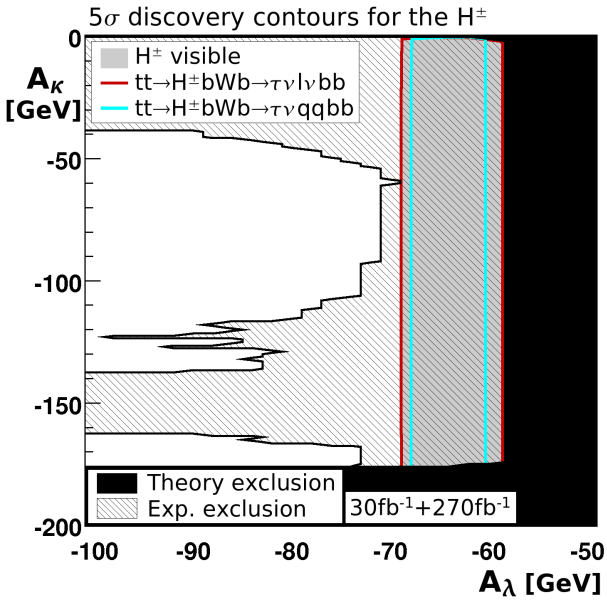

Fig. 7.8: 5σ discovery contours for the $H^{\pm}$ bosons in the Reduced Couplings Scenario, A_λ/A_κ plane with 30+270 fb^{-1}. For all charged Higgs boson searches, only the low luminosity case corresponding to 30 fb^{-1} is taken into account. The $H^{\pm}$ bosons are observable in the grey region. Systematic uncertainties are not included. For details on how this plot must be read, see Fig. 7.1.

Discovery potential for the NMSSM Higgs bosons The discovery potential for the H_1 and H_2 is shown in Fig. 7.6. For these Higgs bosons, the ($ttH_{1/2}$, $H_{1/2}\to b\bar{b}$), the (VBF, $H_{1/2}\to\tau\tau$) and the $H_{1/2}\to\gamma\gamma$ analyses contribute. For the latter search channel, the associated and the inclusive searches are both observable. However, since these channels are not disjoint, i.e. they partly use the same signal events and can thus not be added, only the discovery contours of the inclusive mode are shown, as they completely include the region where the associated channel can be observed.

The discovery contours for the H_3 are shown in Fig. 7.7. The H_3 is observable only in the excluded parameter region, as only there, it has sizeable couplings and is light enough. The (ttH_3, $H_3\to b\bar{b}$), the (VBF, $H_3\to\tau\tau$), the $H_3\to\gamma\gamma$ and (GGF, $H_3\to ZZ\to 4l$) channels contribute.

The charged Higgs bosons can be produced from top quark decays in the excluded region only, as in the λ/κ plane, and are not observable in the allowed parameter region (Fig. 7.8). The $gb\to tH^-/g\bar{b}\to\bar{t}H^+$ cross section is too low to be of importance. The pseudoscalar Higgs bosons have highly reduced couplings and are therefore is not observable throughout this plane.

Specifics of the $tt\phi$, $\phi\to b\bar{b}$ channel With the ($tt\phi$, $\phi\to b\bar{b}$) analysis, the entire unexcluded region can be covered. At medium and large negative $A_\kappa \lesssim -30$ GeV, only the H_2 contributes to the discovery potential of this search channel. As was explained for the λ/κ plane, this channel's mass window is with $M_\phi \pm 45$ GeV so large that the mass windows of different Higgs bosons in the allowed mass range of the search overlap. When the H_1 is heavy enough to be inside the mass range and its coupling to up-type fermions is sizeable, it contributes to the discovery potential of this search channel. This is the case for small negative $A_\kappa \gtrsim -30$ GeV. For very small negative $A_\kappa \gtrsim -10$ GeV, the contribution from the H_1 to the number of detected signal events inside the mass window is even larger than the contribution from the H_2. In parts of the excluded region ($A_\kappa \approx$ -60 to -70 GeV), the contribution from the H_3 is dominant. In this

channel, the H_1, H_2 and H_3 are assumed to be indistinguishable.

Specifics of the VBF, $\phi\to\tau\tau$ channel In the excluded region, there are two separated areas where the (VBF, $H_{1/2}\to\tau\tau$) channel is observable. At large and medium negative $A_\kappa \lesssim -30$ GeV, the H_2 is the only Higgs boson contributing to the excess of signal events in this channel. When going to smaller negative A_κ, the coupling of the H_2 to vector bosons decreases. Consequently, the signal rate of the H_2 alone becomes too low to be detected with a 5σ significance. However, for even smaller negative $A_\kappa \gtrsim -20$ GeV, the H_1 is heavier than 110 GeV and thus is inside the allowed mass range of this analysis[8]. Also its couplings are sizeable in that region. Thus, the H_1 contributes significantly to the observed excess of signal events, and the joint signal from the H_2 and the H_1 is observable with a significance above 5σ. For very small negative $A_\kappa \gtrsim -7$ GeV, the contribution from the H_1 is the dominant one as for the ($t\bar{t}\phi$, $\phi\to b\bar{b}$) channel. Also in this channel, the two Higgs bosons H_1 and H_2 are indistinguishable, so that only the existence of one Higgs boson can be confirmed experimentally by this search. Again, the $\phi\to\tau\tau$ channel will be the only channel in this plane that allows for the observation of Higgs bosons with 30 fb^{-1} only.

Specifics of the $\phi\to\gamma\gamma$ channels The $H_2\to\gamma\gamma$ analysis yields significances above 5σ in large parts of the parameter plane. However, the region with reduced couplings at small negative $A_\lambda \approx -70$ GeV is not covered. This region includes the original parameter point from Ref. [99], that is also included in the region with reduced couplings of the λ/κ plane shown before. The phenomenology of this region is therefore similar to the one that was described for the λ/κ plane: The $H_2\to\gamma\gamma$ channel suffers in this region from the decreasing H_2 mass which results in a smaller branching ratio of the $H_2\to\gamma\gamma$ decay, and from the reduced coupling to gluons that is more strongly reduced than the coupling to vector bosons. As a result, the (VBF, $H_2\to\tau\tau$) channel has the better discovery potential in this region. In contrast to that, the second region with reduced H_2 couplings at small negative $A_\kappa \gtrsim -30$ GeV is covered completely by the $H_2\to\gamma\gamma$ search. Although the coupling of the H_2 to gluons decreases when $|A_\kappa|$ becomes smaller, the H_2 mass increases up to 124 GeV. As the branching ratio of $H_2\to\gamma\gamma$ commonly has its maximum around 126 GeV, this channel retains its discovery potential in this region despite the reduced couplings. In short, if the Higgs boson masses are about 125 GeV, the $\phi\to\gamma\gamma$ channel is less affected by reduced couplings and has a better discovery potential than the $\phi\to\tau\tau$ search, for Higgs boson masses around 115 GeV, this behavior is reversed.

Also the $H_1\to\gamma\gamma$ search mode is not negligible and yields significances above 5σ at very small negative $A_\kappa \gtrsim -8$ GeV. Due to the excellent mass resolution of only 1.1 to 1.7 GeV [5] in the $\phi\to\gamma\gamma$ channel, the H_1 can, in contrast to the previously discussed searches, be distinguished from the H_2. Accordingly, there is a region (blue (dark grey) hatched in Fig. 7.6) where the H_1 and the H_2 are observable simultaneously in this channel with a mass difference of about 10 GeV. Such an observation of two separate mass resonances would be evidence for physics beyond the Standard Model.

Discovery potential with systematic uncertainties When systematic uncertainties on the background are taken into account, the ($t\bar{t}\phi$, $\phi\to b\bar{b}$) and the ($t\bar{t}\to\bar{t}H^+b/t\bar{t}\to tH^-\bar{b}$) analyses do not yield significances above 5σ any longer. Also the performance of the $\phi\to\tau\tau$, $\phi\to\gamma\gamma$ and $\phi\to ZZ\to 4l$ searches deteriorates (Figs. 7.9, 7.10). The contour of the $H_{1/2}\to\tau\tau$ search at

[8] The tails of signal peaks of Higgs bosons outside the allowed mass range might in principle contribute to the mass windows of Higgs bosons inside the mass range. In the scans shown in this thesis, such contributions are neglected as a conservative estimate. Including them would require the extrapolation of the signal efficiencies to masses outside the allowed mass range, which could give rise to large uncertainties in the results.

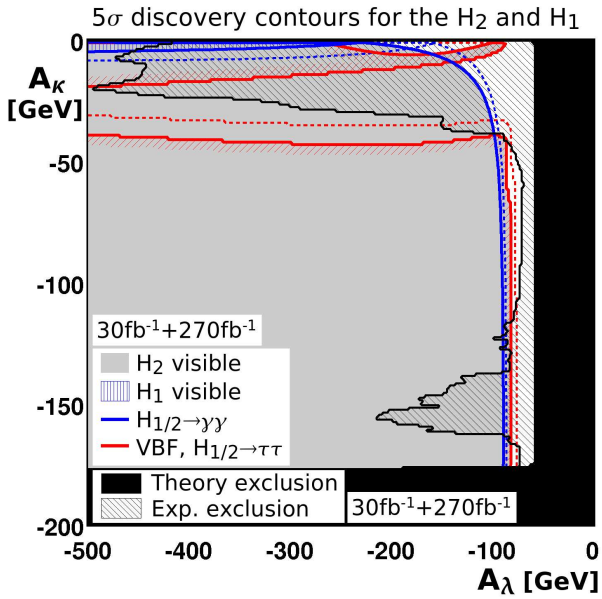

Fig. 7.9: 5σ discovery contours for the H_1 and H_2 in the Reduced Couplings Scenario, A_λ/A_κ plane with 30+270 fb^{-1}. Systematic uncertainties are taken into account. For comparison, the results without systematic uncertainties are given by the dotted lines. The H_2, possibly with contributions from the H_1, is observable in the grey region. The H_1 is observable separately in the blue (dark grey) hatched region. For details on how this plot must be read, see Fig. 7.1.

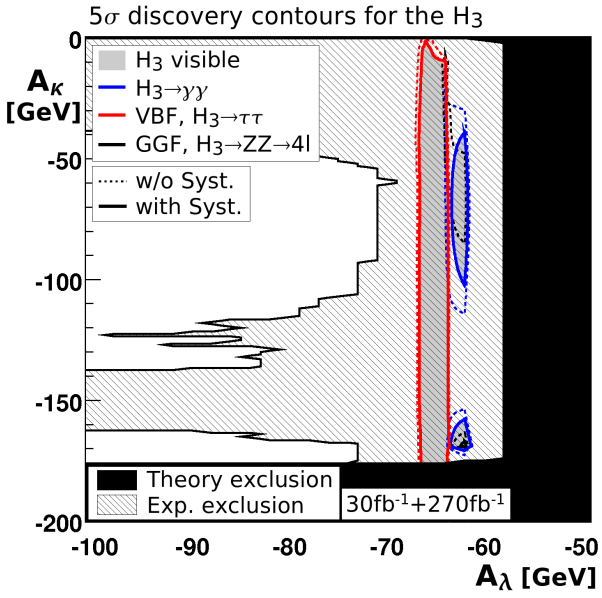

Fig. 7.10: 5σ discovery contours for the H_3 in the Reduced Couplings Scenario, A_λ/A_κ plane with 30+270 fb^{-1}. Systematic uncertainties are taken into account. For comparison, the results without systematic uncertainties are given by the dotted lines. The H_3 is observable in the grey region. For details on how this plot must be read, see Fig. 7.1.

$A_\kappa \approx -15$ GeV is unchanged by the consideration of systematic uncertainties as it marks the 110 GeV contour of the H_1 mass, where the H_1 enters the allowed mass range of this search.

The $H_2 \to \gamma\gamma$ channel still covers the entire region with reduced couplings at small negative $A_\kappa \gtrsim -30$ GeV. The parameter region where both the H_1 and the H_2 are observable simultaneously via the $H_{1/2} \to \gamma\gamma$ decay mode is still present, yet reduced in size. Also the $H_{1/2} \to \tau\tau$ channel is still of importance in this region. The dip in its discovery contour at $A_\kappa \approx -5$ GeV and $A_\lambda \approx -200$ GeV (Fig. 7.9) is a result of the large H_2 mass which reaches values above 124 GeV, while the H_1 mass is about 111 GeV. As the mass difference between the two resonances is thus relatively large in this region, their respective contributions to each other's mass windows are small, so that the discovery potential of this channel drops in this region.

Since the $\phi \to b\bar{b}$ search does not yield significances larger than 5σ, the region with reduced couplings at small negative $A_\lambda \approx -70$ GeV is not covered. The discussion on how the discovery potential of this region could be recovered is analogous to the discussion for the λ/κ plane, because both regions with reduced couplings are centered around the same, most critical point of Ref. [99].

Summary of the Reduced Couplings Scenario, A_λ/A_κ benchmark plane In a large part of this benchmark plane, the H_2 is the only observable Higgs boson. However, at small $|A_\kappa|$, also the H_1 contributes and in a small region with $|A_\kappa| \lesssim 8$ GeV also is simultaneously observable

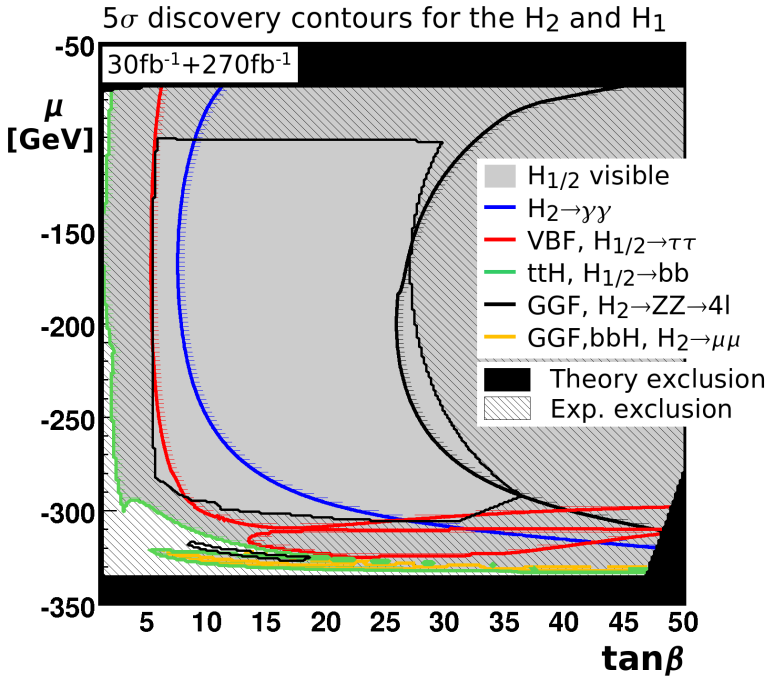

Fig. 7.11: 5σ discovery contours for the H_1 and H_2 in the Reduced Couplings Scenario, $\tan\beta/\mu$ plane with 30+270 fb^{-1}. Systematic uncertainties are not included. The H_1 or the H_2 is observable in the grey region. For details on how this plot must be read, see Fig. 7.1.

with the H_2. This would be a clear evidence for physics beyond the Standard Model. For this, the $\phi\to\gamma\gamma$ channel is of crucial importance due to its good mass resolution.

It is found that the region with reduced H_2 couplings and H_2 masses above 120 GeV can be covered without difficulty by the current ATLAS search strategies, whereas the region with reduced H_2 couplings and an H_2 mass of only 115 GeV poses problems. The phenomenology of the latter region has already been discussed for the λ/κ plane.

Also in this plane, an early discovery of a Higgs boson with only 30 fb^{-1} is only possible with the help of the (VBF, $\phi\to\tau\tau$) channel.

7.2.1.3 The $\mu/\tan\beta$ benchmark plane

In the $\tan\beta/\mu$ plane, the H_2 has, as in large parts of the entire scenario, approximately Standard Model-like couplings and a mass around 120 GeV. As before, close to the point from Ref. [99] at $\tan\beta = 5.7$ and $\mu = -284$ GeV, its couplings are reduced. The couplings of the other neutral Higgs bosons are highly suppressed in very large parts of the unexcluded region. However, a special feature of this benchmark plane is the small unexcluded region at large negative $\mu \approx -320$ GeV. In this region, the couplings of all neutral scalars have sizeable values. The couplings to gluons may even be enhanced compared to the Standard Model case, whereas the couplings to vector bosons and to up-type fermions are reduced. Moreover, all five neutral Higgs bosons have low, experimentally well accessible masses in that region. For large $\tan\beta$ values, the bbH_3 and bbA_3 couplings are heavily enhanced, and also the $H^\pm tb$ coupling is large. Also the mass of the charged Higgs bosons is in an experimentally accessible range.

In contrast to the other benchmark planes, the discovery potential for the H_1/H_2, for the $H_3/A_1/A_2$ and for the charged Higgs bosons will be discussed separately for the $\mu/\tan\beta$ plane of the Reduced Couplings Scenario, because this plane has a very complex phenomenology leading

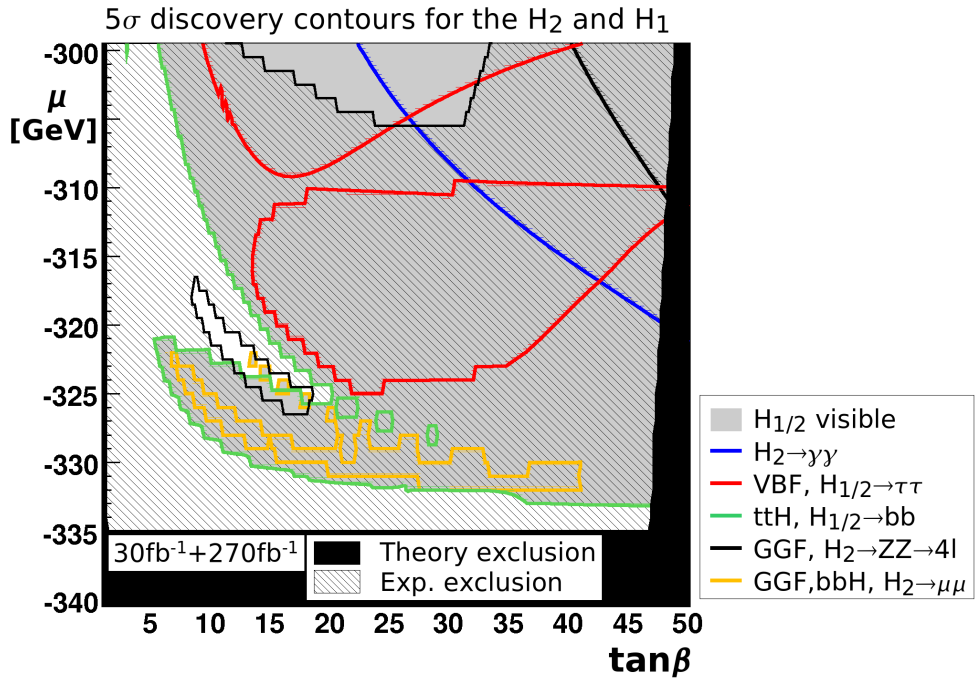

Fig. 7.12: 5σ discovery contours for the H_1 and H_2 in the Reduced Couplings Scenario, $\tan\beta/\mu$ plane with 30+270 fb^{-1}. Systematic uncertainties are not included. The H_1 or the H_2 is observable in the grey region. The shown part of the plane is restricted to large negative μ. For details on how this plot must be read, see Fig. 7.1.

to a large number of discovery contours.

Discovery potential for the H_1 and H_2 Figures 7.11 and 7.12 show the discovery potential for the H_1 and H_2. The large unexcluded region is totally covered by the ($ttH_{1/2}$, $H_{1/2}\to b\bar{b}$) mode. Also the (VBF, $H_{1/2}\to\tau\tau$) and inclusive and associated $H_2\to\gamma\gamma$ searches are of importance. At large $\tan\beta$, the (GGF, $H_2\to ZZ\to 4l$) search reaches significances above 5σ as well.

The phenomenology in the region with reduced couplings of the H_2 at $\mu\approx -280$ GeV is very similar to the one of the regions of the λ/κ and A_λ/A_κ planes that are also centered the around the point from Ref. [99]. It will therefore not be discussed in detail in this section.

The small unexcluded region at large negative $\mu\approx -320$ GeV has contributions from the $H_{1/2}\to b\bar{b}$ and the (GGF, bbH_2, $H_2\to\mu\mu$) channels. However, the searches for the H_1 and H_2 alone do not cover this region completely.

Specifics of the $ttH_{1/2}$, $H_{1/2}\to b\bar{b}$ channel In large parts of the parameter plane, the H_2 alone provides the necessary number of signal events for a 5σ discovery in the (ttH_2, $H_2\to b\bar{b}$) channel. Although the H_1 and A_1 in principle also have masses in the allowed mass range for this search in some areas, their couplings to up-type fermions are negligible in large parts of the parameter plane. However, there are relevant contributions from the H_1 for large negative μ. For example, at $\mu\approx -300$ GeV, the H_1 coupling to up-type fermions reaches about 45% of its Standard Model value and thus contributes to some extent to the discovery potential.

In and around the small unexcluded region at large negative $\mu\approx -320$ GeV, the situation is different. In this region, all neutral Higgs bosons have low masses ($M_{H_1}\approx 70$ GeV, $M_{H_2}\approx 115$ GeV, $M_{H_3}\approx 130$ GeV, $M_{A_1}\approx 80$ GeV, $M_{A_2}\approx 100$ GeV). The three scalar bosons have

reduced but sizeable couplings to up-type fermions and thus all contribute to the ($tt\phi$, $\phi \to b\bar{b}$) channel. With this combination, a 5σ significance is obtained despite the reduced couplings. The contributions from the pseudoscalar Higgs bosons are negligible as their couplings to up-type fermions are heavily suppressed in the relevant region. As stated before, this analysis is assumed not to be able to separate Higgs boson peaks whose masses are inside the allowed range. In Fig. 7.12, the small unexcluded region at $\mu \approx -320$ GeV is not completely covered. In the uncovered part, the H_3 provides the largest fraction of signal events in that channel, so that the discovery potential is in this region assigned to the H_3 instead to the H_1/H_2.

Specifics of the VBF, $H_{1/2} \to \tau\tau$ channel As in the A_λ/A_κ plane, the (VBF, $H_{1/2} \to \tau\tau$) analysis yields significances above 5σ in two separate regions. In the larger region at small and medium negative $\mu \gtrsim -310$ GeV, the H_2 contributes to the discovery potential alone. When $|\mu|$ becomes larger, the coupling of the H_2 to vector bosons decreases, so that its signal rate alone is not sufficient for a 5σ discovery. However, also the mass of the H_1 and the size of its couplings increase, so that in the second region at $\mu \lesssim -310$ GeV, the H_1 and the H_2 together provide the necessary signal events for a discovery. For $\mu \approx -320$ GeV, the H_1 even contributes the largest number of events to the observed signal excess. A similar behavior was already described for the A_λ/A_κ plane. In the $\mu/\tan\beta$ plane, in addition the H_3 contributes to the signal excess in a part of the covered area with $\mu \lesssim -290$ GeV.

The shapes of the discovery contours for this channel at small $\tan\beta$ are again mainly affected by the mass of the H_2, as for masses lower than about 114 GeV, the contributions from the Z^0 boson peak to the background level become so large that a discovery in this channel is impossible.

Specifics of the $H_2 \to \gamma\gamma$ channel Also in this benchmark plane, the inclusive mode covers a larger area than the associated mode. In contrast to the (VBF, $H_{1/2} \to \tau\tau$) channel, the shape of the discovery contour of the $H_2 \to \gamma\gamma$ channel is more bent, as it is mainly determined by the $H_2 \to \gamma\gamma$ branching ratio. The branching ratio is determined by the mass of the H_2 which increases with $|\mu|$, and the relevant coupling, which decreases slightly with $|\mu|$. The combination of these two effects results in the slightly bent shape of the discovery contour.

Specifics of the GGF, $H_2 \to ZZ \to 4l$ channel At large $\tan\beta$, also the (GGF, $H_2 \to ZZ \to 4l$) analysis yields significances above 5σ, as the $H_2 \to ZZ$ branching ratio is large enough to provide a discovery potential also for the relatively low H_2 masses around 120 GeV. For small and intermediate $|\mu|$, the bent discovery contour marks the line where the $H_2 \to ZZ$ branching ratio is $\sim$1.2%. The branching ratio is influenced by the mass of the H_2 which increases with $|\mu|$ and $\tan\beta$ in this plane. In the respective mass region, the $H_2 \to ZZ$ branching ratio increases with mass. For this reason, this channel is only observable at large $\tan\beta$. On the other hand, the discovery contour is also affected by the H_2 coupling to gluons via the production rate, which is maximal at small $|\mu|$ and large $\tan\beta$ and small at large $|\mu|$, so that at large $|\mu|$, a larger $H_2 \to ZZ$ branching ratio is required for a discovery. The combination of these two factors gives the final discovery contour.

Specifics of the GGF, bbH_2, $H_2 \to \mu\mu$ channel For very large negative $\mu \lesssim -320$ GeV, the coupling of the H_2 to gluons is enhanced (up to a factor of seven) with respect to the Standard Model. Its mass is about 70 GeV and thus inside the allowed mass range for the (GGF, bbH_2, $H_2 \to \mu\mu$) search channel. Therefore, a contribution from this analysis exists. Also the A_1 has a mass of about 80 GeV and an enhanced coupling to gluons. The chosen mass window is $M_\phi \pm 4$ GeV for such low masses [89], so that the mass windows of the H_2 and A_1 overlap if their masses

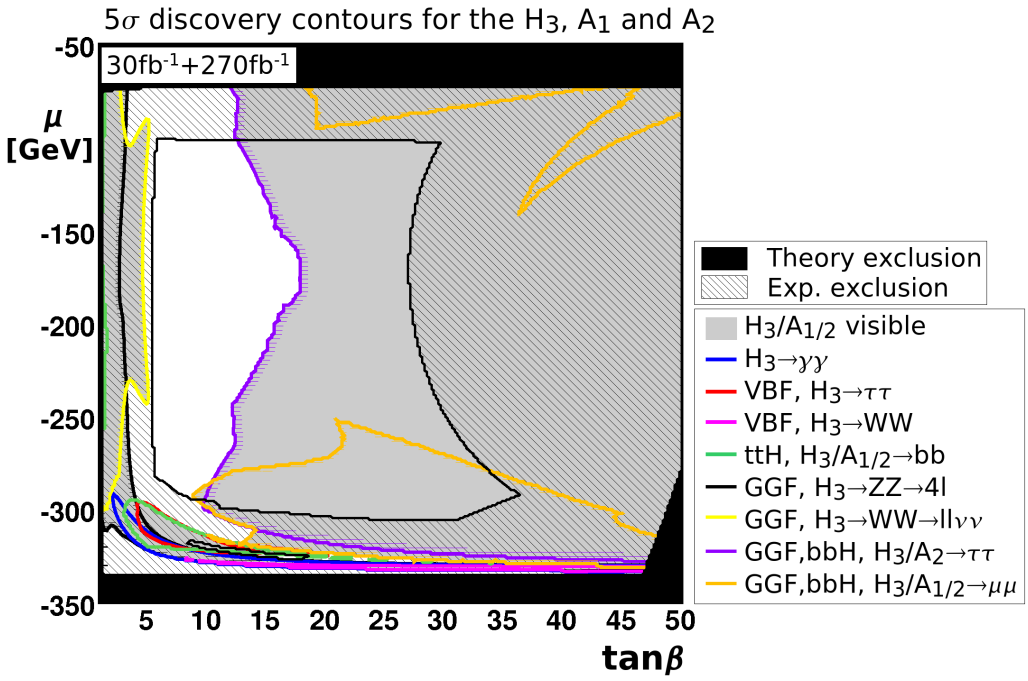

Fig. 7.13: 5σ discovery contours for the H_3, A_1 and A_2 in the Reduced Couplings Scenario, $\tan\beta/\mu$ plane with 30+270 fb^{-1}. Systematic uncertainties are not included. The H_3, A_1 or A_2 is observable in the grey region. For details on how this plot must be read, see Fig. 7.1.

are less then 8 GeV apart. As a consequence, in some parts of the covered region, contributions from these two Higgs bosons are added. The (GGF, bbϕ, $\phi\to\tau\tau$) analysis has no discovery potential in this region as results for that search are only available for masses larger than 150 GeV [87].

Discovery potential for the H_3, A_1 and A_2 The discovery potential for the H_3 and the pseudoscalar Higgs bosons is shown in Figs. 7.13 and 7.14. In the large unexcluded region, the searches for (GGF, bb$H_3/A_{1/2}$, $H_3/A_{1/2}\to\tau\tau/\mu\mu$) contribute significantly to the discovery potential, in particular at large $\tan\beta$. In the small allowed parameter region at large negative $\mu \approx -320$ GeV, also the (ttH_3, $H_3\to b\bar{b}$) and the (VBF, $H_3\to\tau\tau$) channels are observable. However, there are allowed regions where the H_3 will not be visible. The (GGF, $H_3\to$ZZ$\to$4l), the (GGF, $H_3\to$WW$\to$2l2ν) and the $H_3\to\gamma\gamma$ analyses yield significances above 5σ only in already excluded regions of the plane.

Specifics of the GGF, bb$H_3/A_{1/2}$, $H_3/A_{1/2}\to\mu\mu$ and GGF, bbH_3/A_2, $H_3/A_2\to\tau\tau$ channels The H_3 and the A_2 are nearly degenerate in this benchmark plane. Their contributions to the mass window add up both for the (GGF, bbH_3/A_2, $H_3/A_2\to\mu\mu$) and the (GGF, bbH_3/A_2, $H_3/A_2\to\tau\tau$) channel. Both search channels are affected by the couplings of the H_3 and A_2 to gluons, which are largest at large negative μ, but are also large for small $|\mu|$, and by the couplings to down-type fermions, that increase with $\tan\beta$ for both Higgs bosons. Thus, the gluon fusion production mode is dominant at low $\tan\beta$, the associated production with bottom quarks at large $\tan\beta$. Generally, the discovery potential of the two searches is better when the Higgs boson mass is lower, which is partly due to the smaller natural line width of lighter Higgs bosons [87,90]. At a fixed $\tan\beta$ value, the masses of the H_3 and A_2 are maximal at intermediate

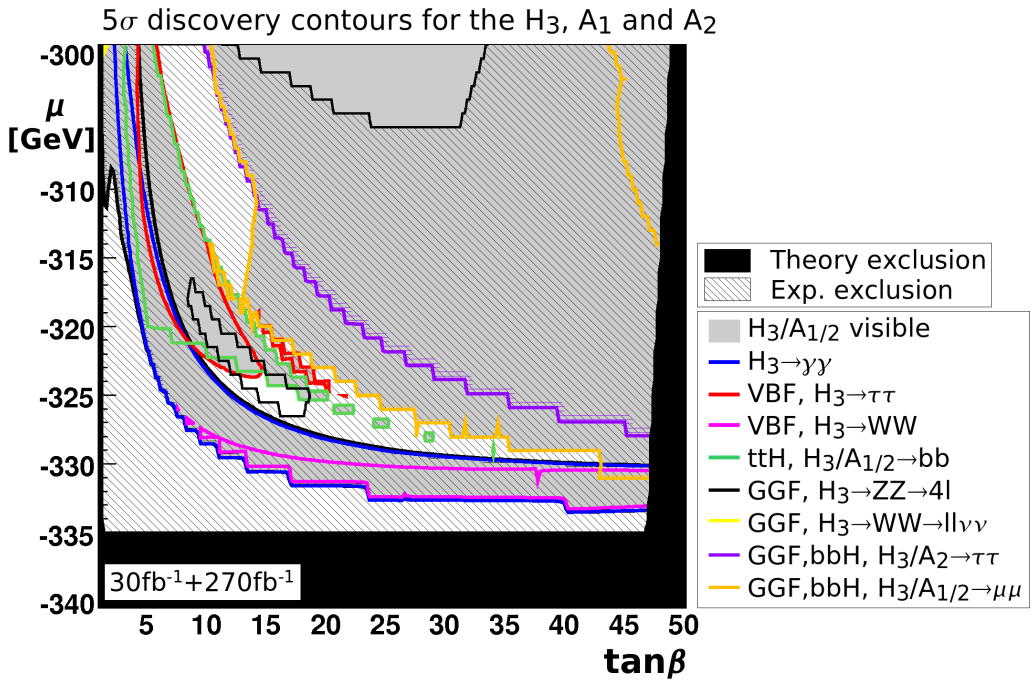

Fig. 7.14: 5σ discovery contours for the H_1, A_1 and A_2 in the Reduced Couplings Scenario, $\tan\beta/\mu$ plane with 30+270 fb^{-1}. Systematic uncertainties are not included. The H_3, A_1 or A_2 is observable in the grey region. The shown part of the plane is restricted to large negative μ. For details on how this plot must be read, see Fig. 7.1.

$|\mu|$. This and the influence of the couplings to gluons on the search channels explains the fact that the discovery potential of the searches is larger for small and for large $|\mu|$. However, masses larger than 500 GeV are not inside the allowed mass range of the $\phi\to\mu\mu$ analysis, whereas the $\phi\to\tau\tau$ analysis is applicable also for the largest mass values present in the parameter plane. For $\mu\approx -330$ GeV and $\tan\beta > 41$, also the A_1 is observable in the $A_1\to\mu\mu$ channel.

Specifics of the $tt H_3/A_{1/2}$, $H_3/A_{1/2}\to b\bar{b}$ channel As mentioned before, in and around the small unexcluded region at large negative $\mu\approx -320$ GeV, all scalar Higgs bosons contribute to the discovery potential in the $\phi\to b\bar{b}$ channel. The region where the H_3 provides the largest fraction of signal events can be seen in Fig. 7.14. Only at small, already excluded $\tan\beta < 2$, also the two pseudoscalar Higgs bosons contribute significantly to this channel, as their couplings to up-type fermions are Standard Model-like in that region.

Specifics of the VBF, $H_3\to\tau\tau$ channel For the (VBF, $H_3\to\tau\tau$) channel, there is a region at $\tan\beta < 20$ and large negative $\mu\approx -295$ GeV to -325 GeV where the H_3 is observable. In that region, its coupling to vector bosons is about 80% of its Standard Model value and thus larger than the couplings of the other scalar Higgs bosons, which also contribute to the signal excess.

Specifics of the GGF, $H_3\to WW\to 2l2\nu$ channel In the excluded region at small $\tan\beta\lesssim 5$, the (GGF, $H_3\to WW\to 2l2\nu$) channel reaches significances above 5σ, as in this area, the coupling of the H_3 to gluons is Standard Model-like, or, at very small $\tan\beta\approx 1$ even enhanced by 20% with respect to the Standard Model. The mass of the H_3 ranges from 160 to 175 GeV, which is optimal for a discovery via the $H_3\to WW$ decay, since the respective branching ratio is usually

maximal in that mass region (see Fig. 5.4).

The shape of the discovery contour of the (GGF, $H_3 \to WW \to 2l2\nu$) channel is determined by the H_3 mass via the $H_3 \to WW$ branching ratio and by the coupling of the H_3 to gluons. The H_3 mass is maximal for intermediate $|\mu|$ and large $\tan\beta$, whereas the H_3 coupling to gluons is minimal for intermediate $|\mu|$ and large $\tan\beta$. A combination of these effects leads to the observed discovery contour.

Although the (VBF, $H_3 \to WW$) search channel reaches larger significances than the (GGF, $H_3 \to WW$) channel for the Higgs boson of the Standard Model (see Fig. 5.6), the vector boson fusion channel is not relevant in this region as the H_3 coupling to vector bosons reaches only about $\sim$50% of its Standard Model value.

Specifics of the GGF, $H_3 \to ZZ \to 4l$ channel In the excluded region at small $\tan\beta \lesssim 3.5$, also the (GGF, $H_3 \to ZZ \to 4l$) search is visible, because it profits from the sizeable H_3 coupling to gluons like the (GGF, $H_3 \to WW \to 2l2\nu$) channel. However, for this channel, slightly smaller masses around 150 GeV would be more optimal than the here present H_3 masses from 160 to 175 GeV, as the $H_3 \to ZZ^*$ branching ratio is suppressed when the slightly lighter $W^\pm$ bosons can already be produced on their mass shell. The discovery area of the $H_3 \to ZZ$ channel is therefore restricted to smaller $\tan\beta$ values than the $H_3 \to WW \to 2l2\nu$ channel, where the coupling of the H_3 to gluons and thus its production rate is larger.

At large negative $\mu \approx -330$ GeV, there is another contribution from the $H_3 \to ZZ \to 4l$ analysis. The mass of the H_3 is about 130 GeV in that region. Both its couplings to gluons and to vector bosons are about 70% of their Standard Model value. Since the H_3 coupling to down-type fermions and thus the $H_3 \to b\bar{b}$ branching ratio is suppressed in that region, the $H_3 \to ZZ$ branching ratio is about twice as large as for a Standard Model Higgs boson with the same mass [77]. Therefore, this channel is visible despite the reduced couplings.

Specifics of the VBF, $H_3 \to WW$ and the $H_3 \to \gamma\gamma$ channels At large negative $\mu \approx -330$ GeV, also the $H_3 \to \gamma\gamma$ and the (VBF, $H_3 \to WW$) analyses yield large significances. As stated before, the mass of the H_3 is about 130 GeV in that region, and the $H_3 \to b\bar{b}$ branching ratio is suppressed. Both the H_3 couplings to gluons and to vector bosons are about 70% of their Standard Model values.

Similarly to the (GGF, $H_3 \to ZZ \to 4l$) analysis, these two searches have a discovery potential despite the reduced couplings due to the enhancement of the relevant branching ratios in this region. The $H_3 \to WW$ branching ratio reaches maximal values around 65% in this region, which is large, as for a Higgs boson mass of the Standard Model it would be only around 30% [77]. Also the $H_3 \to \gamma\gamma$ branching ratio is with maximally 0.55% large in this region.

Discovery potential for the $H^\pm$ bosons In Figs. 7.15 and 7.16, the discovery potential for the charged Higgs bosons in this parameter plane is shown. The $gb \to tH^-/g\bar{b} \to \bar{t}H^+$ cross section is sizeable for large $\tan\beta$, especially for large negative μ. Its minimal value is obtained for intermediate $|\mu|$. Above all, the $H^\pm \to \tau^\pm\nu$ decay is important for this production mode, but also $H^+ \to t\bar{b}/H^- \to \bar{t}b$ decays contribute to the discovery potential in the region where the production cross section is largest. This channel covers a smaller area than the search for the $H^\pm \to \tau^\pm\nu$ decay as it has to deal with large background processes.

The discovery potential of these searches is best for low masses of the charged Higgs bosons [72, 92], which, at fixed $\tan\beta$, are predicted for small and for large negative μ. Thus, the bent shape of the discovery contour of the ($gb \to tH^-/g\bar{b} \to \bar{t}H^+$, $H^\pm \to \tau^\pm\nu$) analysis is a combined result of the distributions of the $H^\pm$ boson mass and of the production cross section.

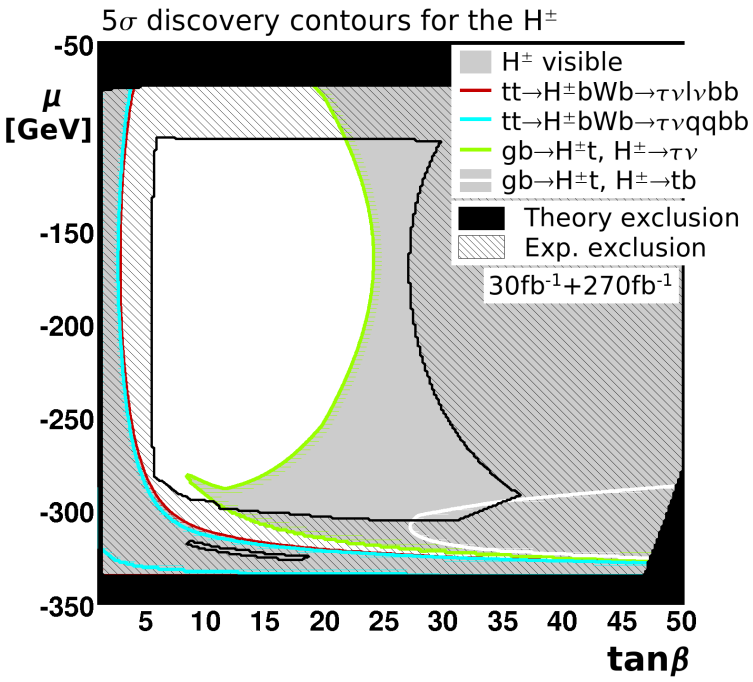

Fig. 7.15: 5σ discovery contours for the $H^{\pm}$ bosons in the Reduced Couplings Scenario, $\tan\beta/\mu$ plane. For all charged Higgs boson searches, only the low luminosity case corresponding to 30 fb^{-1} is taken into account. Systematic uncertainties are not included. The $H^{\pm}$ bosons are observable in the grey region. For details on how this plot must be read, see Fig. 7.1.

Moreover, there are regions in the plane in which the charged Higgs bosons are light enough to be produced in the decays of top quarks and are observable with the help of the respective analyses. A small part of the affected parameter region at $\mu \approx -320$ GeV is not yet excluded. The regions where discovery via $gb \to tH^-$ and $g\bar{b} \to \bar{t}H^+$ production and via decays from top quarks are possible are separated by a region where the charged Higgs bosons do not seem to be visible. This area corresponds to the so-called transition region (see Chap. 5.1), that is not included in the scans shown in this thesis[9]. However, Ref. [92] suggests that also in the transition region, the charged Higgs bosons are observable for large $\tan\beta$.

Observable Higgs bosons In Figs. 7.17 and 7.18, an overview of the number of discoverable Higgs bosons in the parameter plane is given. It is assumed that the $H_2 \to \gamma\gamma$, the (VBF, $H_{1/2} \to \tau\tau$) and the $H_2 \to ZZ \to 4l$ channels on the one hand and the (GGF, bbH_3/A_2, $H_3/A_2 \to \tau\tau$ $/\mu\mu$) channels on the other hand can be used to separate the mass peaks of the H_2 and the H_3/A_2. These channels have reasonable mass resolutions from 1.3 GeV to 45 GeV, depending on Higgs boson mass and channel (see Tab. 7.3). The mass resolutions are generally better for lighter Higgs bosons. It is assumed that in the $\phi \to b\bar{b}$ channel, Higgs boson peaks cannot be separated, as its mass window is with $M_\phi \pm 45$ GeV too large.

The mass resolutions are assumed be sufficient to separate the mass peaks of the H_2 and the H_3/A_2 which have a distance of minimally 15 GeV. This seems justified as in the region with the smallest mass separation around $\mu \approx -330$ GeV, the H_2 is visible only in the (VBF, $H_2 \to \tau\tau$)

[9] For the transition region, the calculation of the charged Higgs boson production cross section is not possible with the procedure used here(see App. B). Moreover, three of the four here included analyses [5, 72, 91] do not provide signal efficiencies and background numbers for this region.

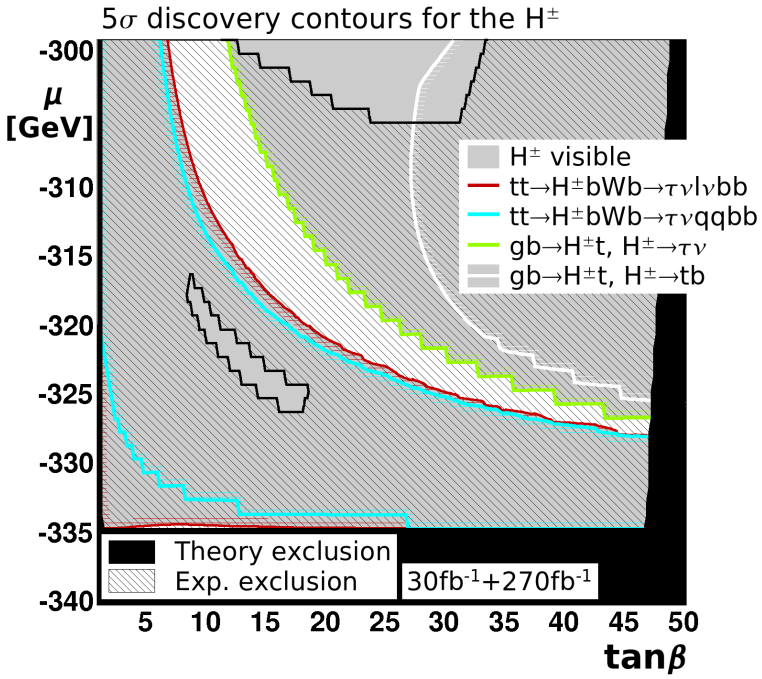

Fig. 7.16: 5σ discovery contours for the $H^{\pm}$ bosons in the Reduced Couplings Scenario, $\tan\beta/\mu$ plane. For all charged Higgs boson searches, only the low luminosity case corresponding to 30 fb^{-1} is taken into account. Systematic uncertainties are not included. The $H^{\pm}$ bosons are observable in the grey region. The shown part of the plane is restricted to large negative μ. For details on how this plot must be read, see Fig. 7.1.

Search Channel	**Mass Resolution at $M_\phi = 120$ GeV**	**Mass Resolution at $M_\phi = 450$ GeV**	**Refs.**
VBF, $\phi\to\tau\tau$	12 GeV	-	[62]
ttϕ, $\phi\to$b$\bar{\text{b}}$	20.5 GeV	-	[78]
GGF, $\phi\to$ZZ$\to$4l	1.3 GeV	6.0 GeV	[5]
Inclusive $\phi\to\gamma\gamma$	1.4 GeV	-	[5]
GGF, bbϕ, $\phi\to\tau\tau$	-	45 GeV	[87]
GGF, bbϕ, $\phi\to\mu\mu$	2.4 GeV	9 GeV	[89,90]

Tab. 7.3: Higgs boson mass resolutions for different search channels and two example Higgs boson masses. If no resolution is given, the respective Higgs boson mass lies outside the allowed mass range of the search channel.

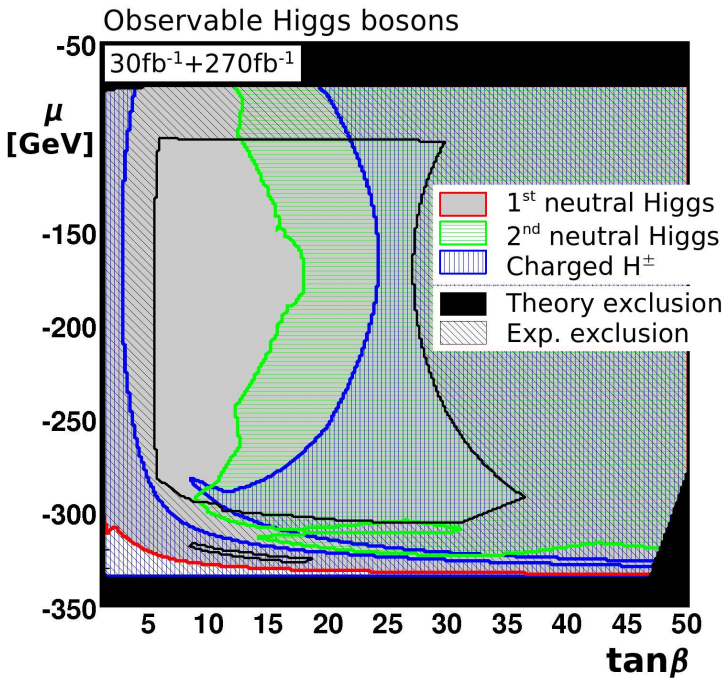

Fig. 7.17: Discoverable Higgs bosons in the Reduced Couplings Scenario, $\tan\beta/\mu$ plane with 30+270 fb^{-1}. Systematic uncertainties are not included. One neutral Higgs boson is observable in the grey region, two neutral Higgs bosons in the green (light grey) hatched region. The $H^{\pm}$ bosons are observable in the blue (dark grey) hatched region.

channel, whereas the H_3/A_2 bosons are only observable in the (GGF, bbH_3/A_2, $H_3/A_2 \to \mu\mu$) mode. For this case, the H_3/A_2 masses are small and thus the relevant mass resolutions are about 12 GeV for the $H_2 \to \tau\tau$ and about 2.4 GeV for the $H_3/A_2 \to \mu\mu$ channel. If the mass separation is smaller than 12 GeV+2.4 GeV$\lesssim$ 15 GeV, the Higgs bosons are considered indistinguishable. In other regions, the mass separations are also sufficiently large to guarantee a good separability with the given mass resolutions.

At small and medium $\tan\beta$, only one neutral Higgs boson, the H_2, is observable in the large unexcluded region, as it is the only Higgs boson with a mass and couplings that are accessible by the current ATLAS search strategies. In the small unexcluded region at large negative $\mu \approx -320$ GeV, in principle more than one neutral Higgs boson contributes to the discovery potential, but as the masses of the Higgs bosons are similar, the mass peaks are difficult to disentangle and only one neutral Higgs boson is considered measurable with the above assumptions. At larger $\tan\beta$ values, also a second Higgs boson peak from the degenerate H_3/A_2 bosons is observable. At large $\tan\beta \gtrsim 20$ or at large negative μ, the charged Higgs bosons are discoverable in addition. Thus, there are regions where only one neutral, two neutral, two neutral and the charged and one neutral and the charged Higgs bosons are observable, depending on the exact model parameters. The occurrence of more than one mass resonance or of an unknown charged particle would be evidence of physics beyond the Standard Model.

Discovery potential with systematic uncertainties In Fig. 7.19, the discovery potential of the (GGF, bbϕ, $\phi \to \tau\tau$) analysis is shown for different assumed values of systematic uncertainties on the background. This is not to be understood as a study of the systematic uncertainties in this channel, but rather as different examples for the behavior of the channel in the presence of

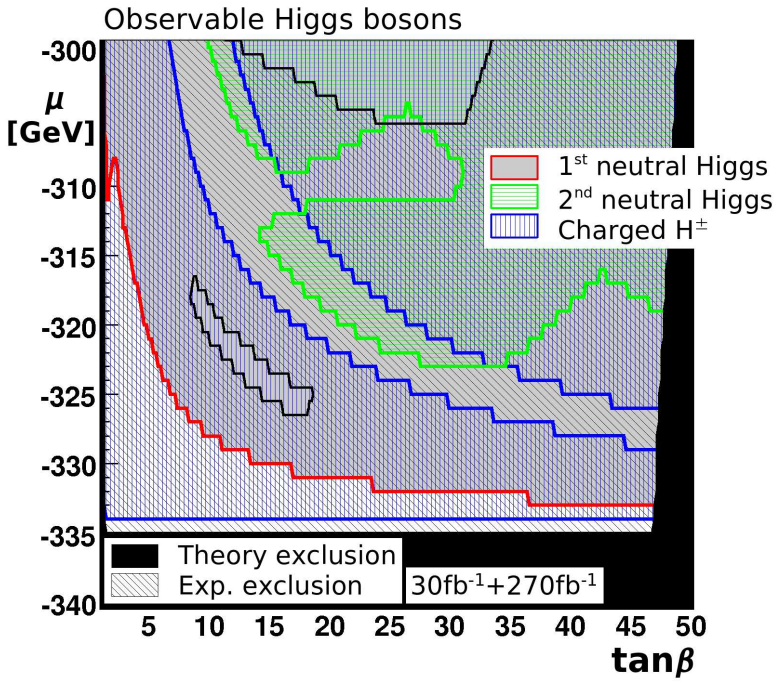

Fig. 7.18: Discoverable Higgs bosons in the Reduced Couplings Scenario, $\tan\beta/\mu$ plane with 30+270 fb^{-1}. Systematic uncertainties are not included. One neutral Higgs boson is observable in the grey region, two neutral Higgs bosons in the green (light grey) hatched region. The $H^{\pm}$ bosons are observable in the blue (dark grey) hatched region. The shown part of the plane is restricted to large negative μ.

systematic uncertainties, whose true size is unknown.

When systematic uncertainties are included, the discovery potential of this channel degrades most strongly at intermediate $|\mu|$ values, where the couplings of the H_3 and A_2 to gluons are small and their masses are large. The region at large negative μ is relatively insensitive to systematic uncertainties, as here, the couplings to gluons are especially large. In this region, the discovery potential of the channel is largely preserved even for uncertainties of 20%. Also the region where the Higgs bosons are heavier than 450 GeV has a stable discovery potential, because for such large masses, also the $\phi\rightarrow\tau\tau\rightarrow$hh channel contributes to the discovery potential. Thus, the number of selected signal events is increased in that region. This is also the reason for the hump at intermediate $|\mu| \approx 160$ GeV in the discovery contour with 20% uncertainty. The discovery contour at large negative $\mu \approx -320$ GeV is given by the allowed mass range of the search which requires masses larger than 150 GeV. Therefore, this contours is unchanged by the systematic uncertainties.

Similarly, Figs. 7.20 and 7.21 show the discovery potential of the (GGF, bbϕ, $\phi\rightarrow\mu\mu$) analysis in the presence of systematic uncertainties. This channel is very sensitive to systematic uncertainties in this benchmark plane, as already an uncertainty of 1% would significantly reduce the discovery potential. Assuming an uncertainty of 5%, only a very small region at $\mu \approx -330$ GeV still yields significances above 5σ. For 10% systematic uncertainty, the sensitivity of this channel is lost completely.

In Figs. 7.22 and 7.23, the discovery contours of the H_1 and H_2 are shown in the presence of systematic uncertainties. For the (GGF, bbϕ, $\phi\rightarrow\mu\mu$) search, a 10% uncertainty is assumed as an example value. Then, this channel will not be observable. Also the (ttϕ, $\phi\rightarrow$b$\bar{\text{b}}$) channel does not reach significances above 5σ, so that the region with reduced couplings at $\mu \approx$ -280

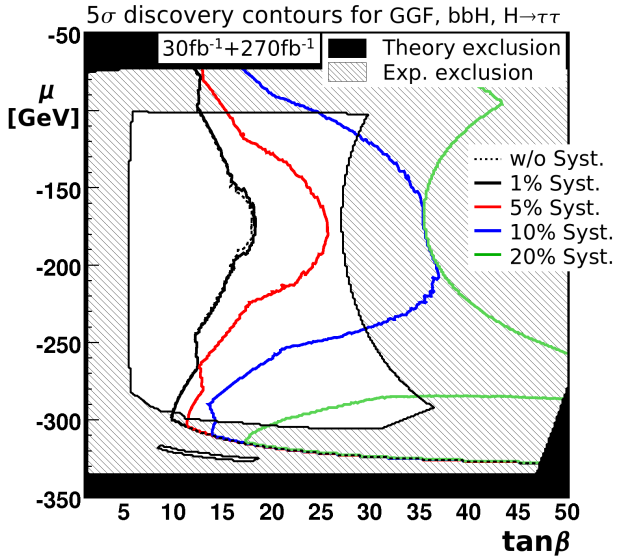

Fig. 7.19: 5σ discovery contours for all Higgs bosons in the (bbϕ, GGF, $\phi\to\tau\tau$) channel in the Reduced Couplings Scenario, $\tan\beta/\mu$ plane. Systematic uncertainties are varied as an example. The significances are larger than 5σ towards large $\tan\beta$.

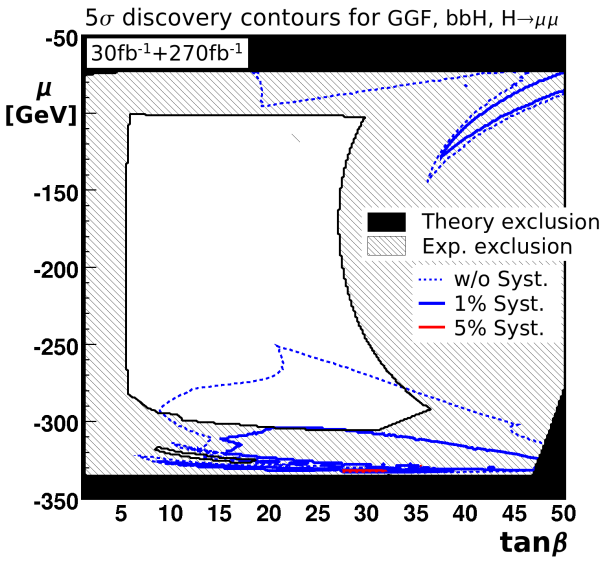

Fig. 7.20: 5σ discovery contours for all Higgs bosons in the (bbϕ, GGF, $\phi\to\mu\mu$) channel in the Reduced Couplings Scenario, $\tan\beta/\mu$ plane. Systematic uncertainties are varied as an example.

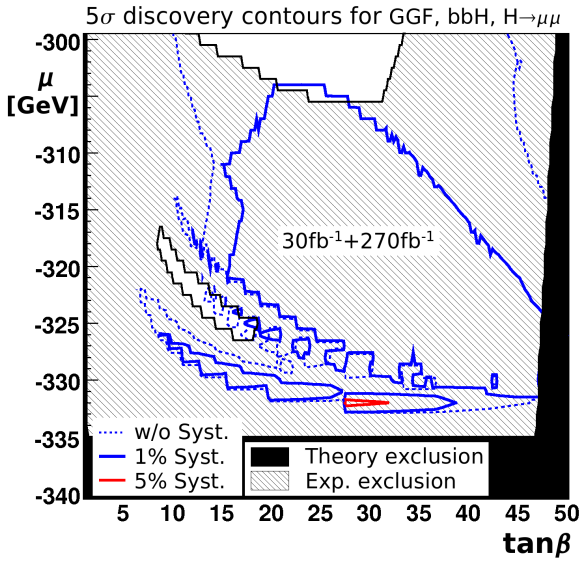

Fig. 7.21: 5σ discovery contours for all Higgs bosons in the (bbϕ, GGF, $\phi\to\mu\mu$) channel in the Reduced Couplings Scenario, $\tan\beta/\mu$ plane. Systematic uncertainties are varied as an example. The shown part of the plane is restricted to large negative μ.

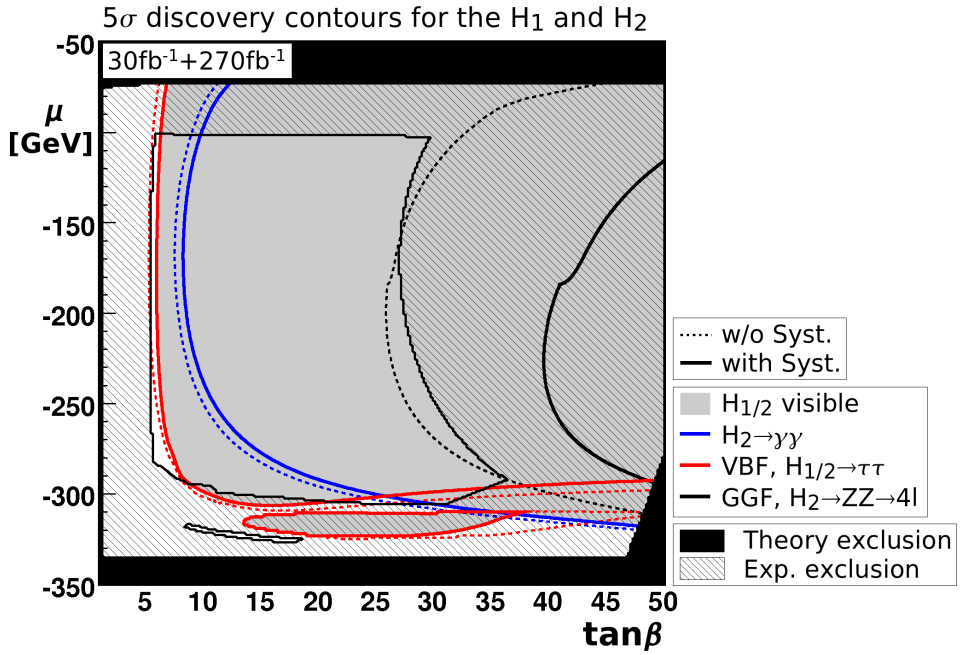

Fig. 7.22: 5σ discovery contours for the H_1 and H_2 in the Reduced Couplings Scenario, $\tan\beta/\mu$ plane with 30+270 fb^{-1}. Systematic uncertainties are taken into account. For comparison, the results without systematic uncertainties are given by the dotted lines. The H_1 or the H_2 is observable in the grey region. For details on how this plot must be read, see Fig. 7.1.

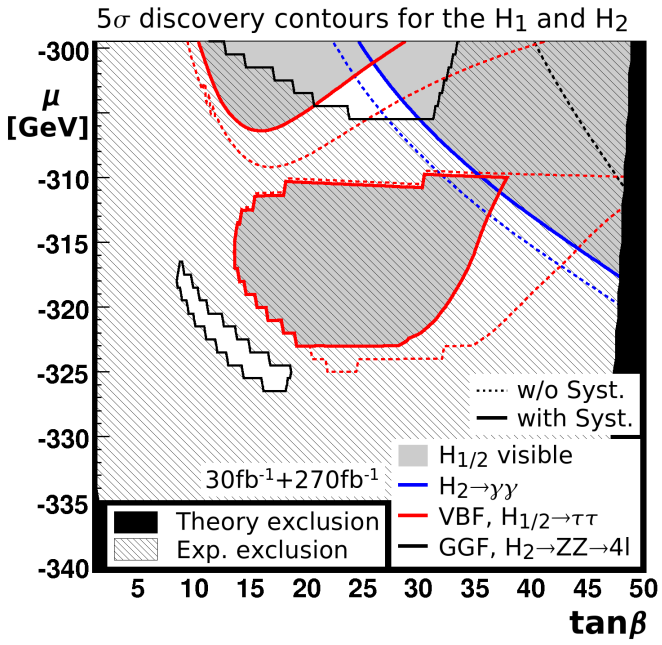

Fig. 7.23: 5σ discovery contours for the H_1 and H_2 in the Reduced Couplings Scenario, $\tan\beta/\mu$ plane with 30+270 fb^{-1}. Systematic uncertainties are taken into account. For comparison, the results without systematic uncertainties are given by the dotted lines. The H_1 or the H_2 is observable in the grey region. The shown part of the plane is restricted to large negative μ. For details on how this plot must be read, see Fig. 7.1.

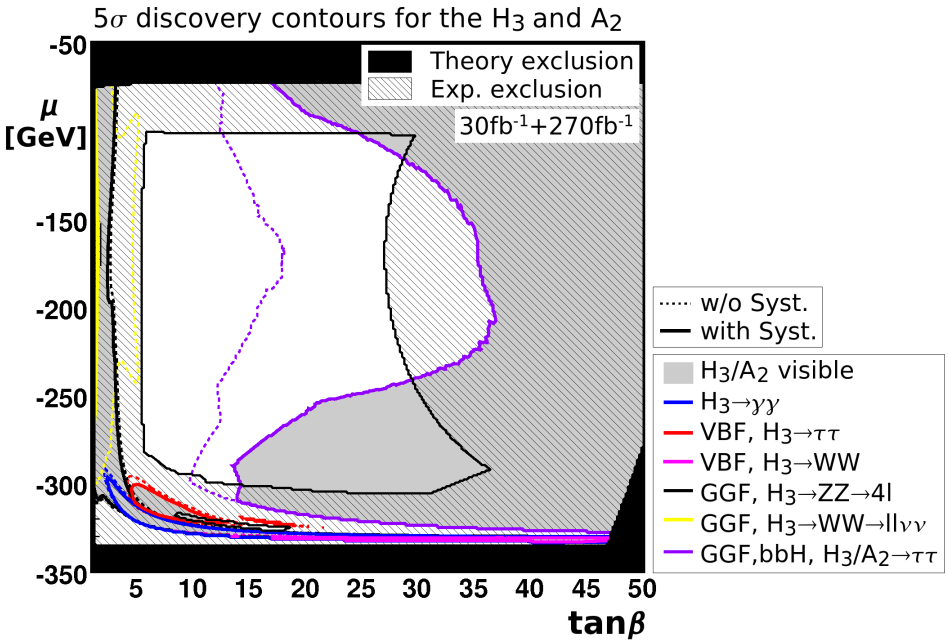

Fig. 7.24: 5σ discovery contours for the H_3 and A_2 in the Reduced Couplings Scenario, $\tan\beta/\mu$ plane with 30+270 fb^{-1}. Systematic uncertainties are taken into account. For comparison, the results without systematic uncertainties are given by the dotted lines. The H_3 or the A_2 is observable in the grey region. For details on how this plot must be read, see Fig. 7.1.

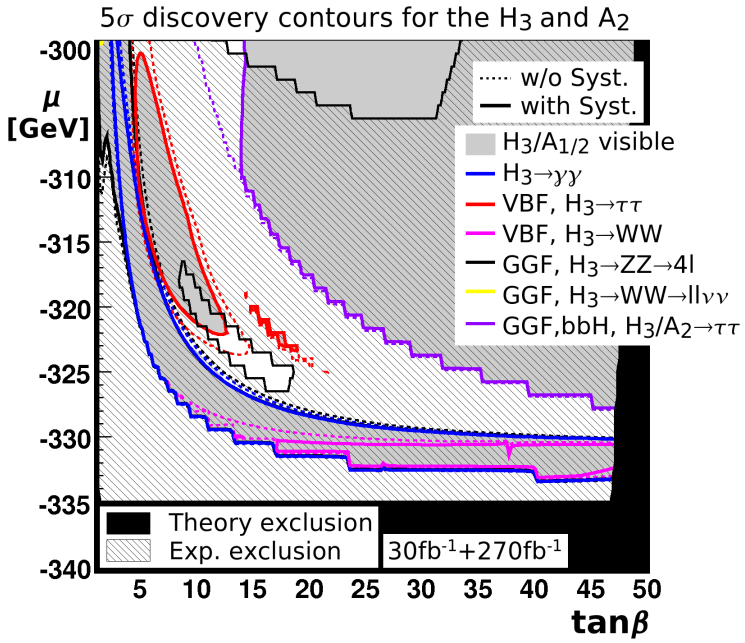

Fig. 7.25: 5σ discovery contours for the H_3 and A_2 in the Reduced Couplings Scenario, $\tan\beta/\mu$ plane with 30+270 fb^{-1}. Systematic uncertainties are taken into account. For comparison, the results without systematic uncertainties are given by the dotted lines. The H_3 or the A_2 is observable in the grey region. The shown part of the plane is restricted to large negative μ. For details on how this plot must be read, see Fig. 7.1.

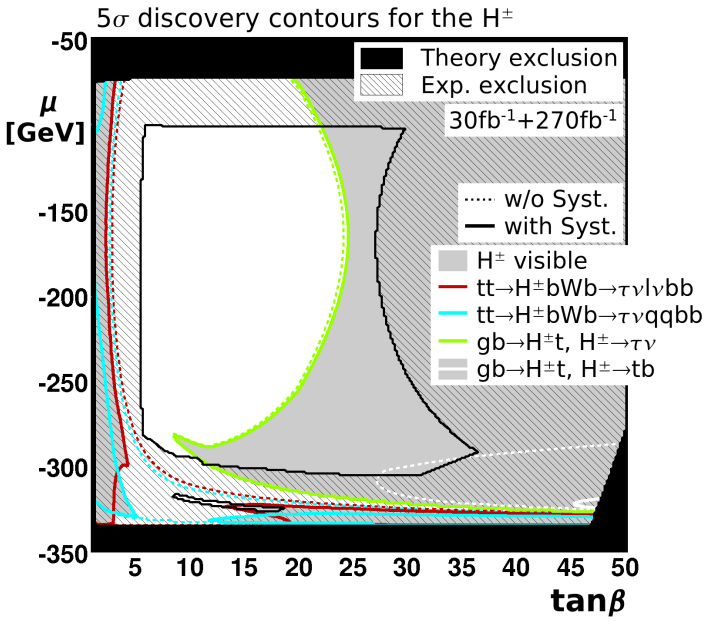

Fig. 7.26: 5σ discovery contours for the $H^{\pm}$ bosons in the Reduced Couplings Scenario, $\tan\beta/\mu$ plane with 30+270 fb^{-1}. For all charged Higgs boson searches, only the low luminosity case corresponding to 30 fb^{-1} is taken into account. Systematic uncertainties are taken into account. For comparison, the results without systematic uncertainties are given by the dotted lines. The $H^{\pm}$ bosons are observable in the grey region. For details on how this plot must be read, see Fig. 7.1.

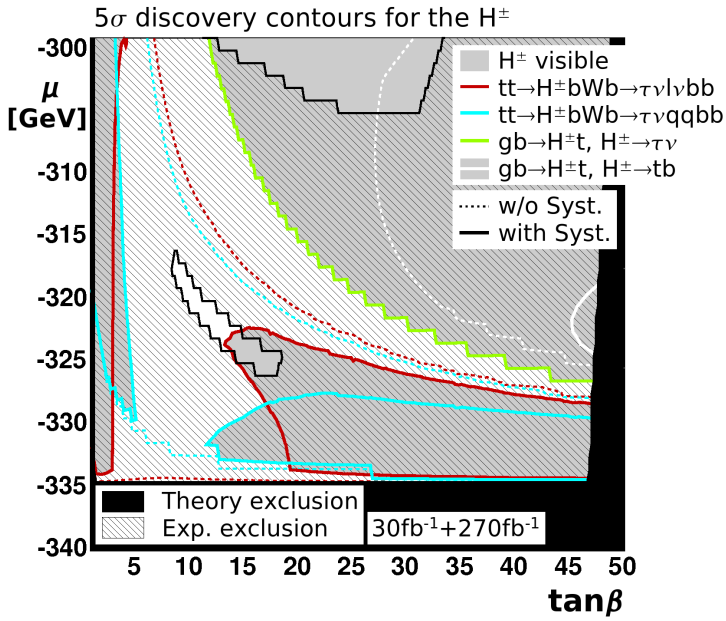

Fig. 7.27: 5σ discovery contours for the $H^{\pm}$ bosons in the Reduced Couplings Scenario, $\tan\beta/\mu$ plane with 30+270 fb^{-1}. For all charged Higgs boson searches, only the low luminosity case corresponding to 30 fb^{-1} is taken into account. Systematic uncertainties are taken into account. For comparison, the results without systematic uncertainties are given by the dotted lines. The $H^{\pm}$ bosons are observable in the grey region. The shown part of the plane is restricted to large negative μ. For details on how this plot must be read, see Fig. 7.1.

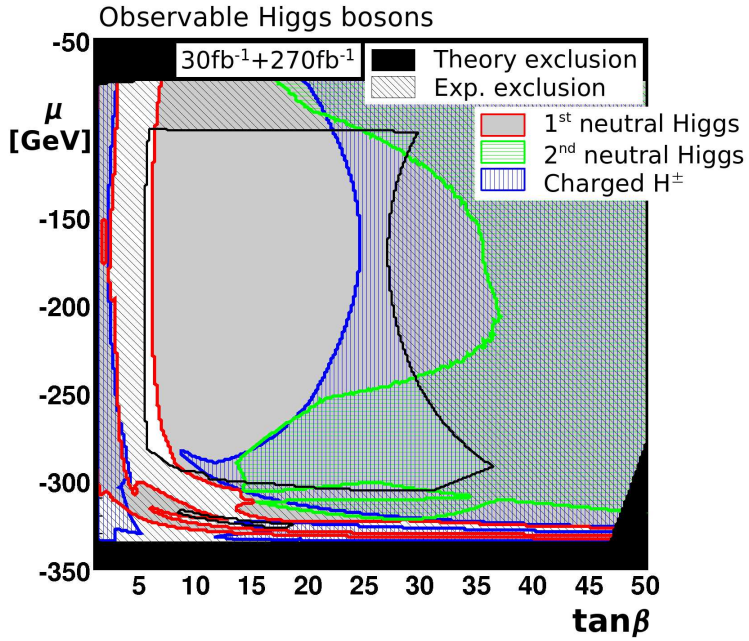

Fig. 7.28: Observable Higgs bosons in the Reduced Couplings Scenario, $\tan\beta/\mu$ plane with 30+270 fb^{-1}. For all charged Higgs boson searches, only the low luminosity case corresponding to 30 fb^{-1} is taken into account. Systematic uncertainties are taken into account. One neutral Higgs boson is observable in the grey region, two neutral Higgs bosons in the green (light grey) hatched region. The H$^{\pm}$ bosons are observable in the blue (dark grey) hatched region.

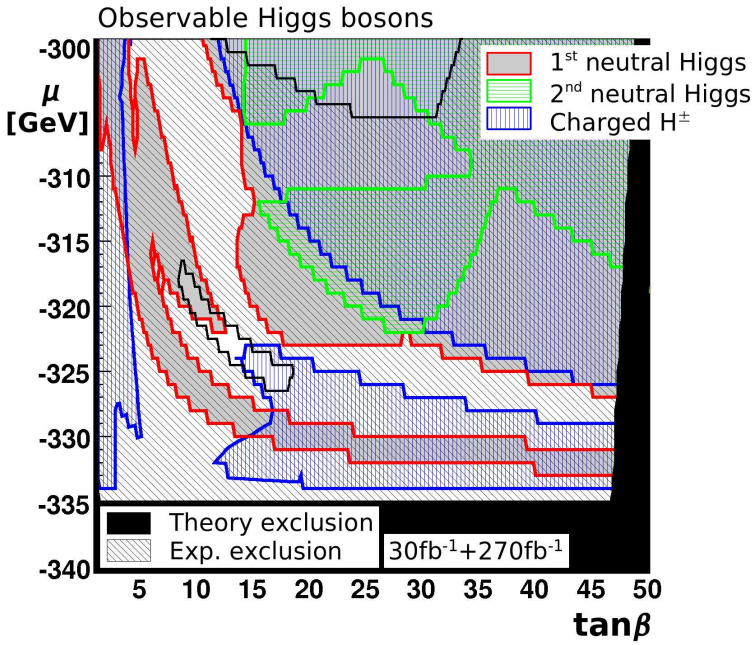

Fig. 7.29: Observable Higgs bosons in the Reduced Couplings Scenario, $\tan\beta/\mu$ plane with 30+270 fb^{-1}. For all charged Higgs boson searches, only the low luminosity case corresponding to 30 fb^{-1} is taken into account. Systematic uncertainties are taken into account. One neutral Higgs boson is observable in the grey region, two neutral Higgs bosons in the green (light grey) hatched region. The H$^{\pm}$ bosons are observable in the blue (dark grey) hatched region. The shown part of the plane is restricted to large negative μ.

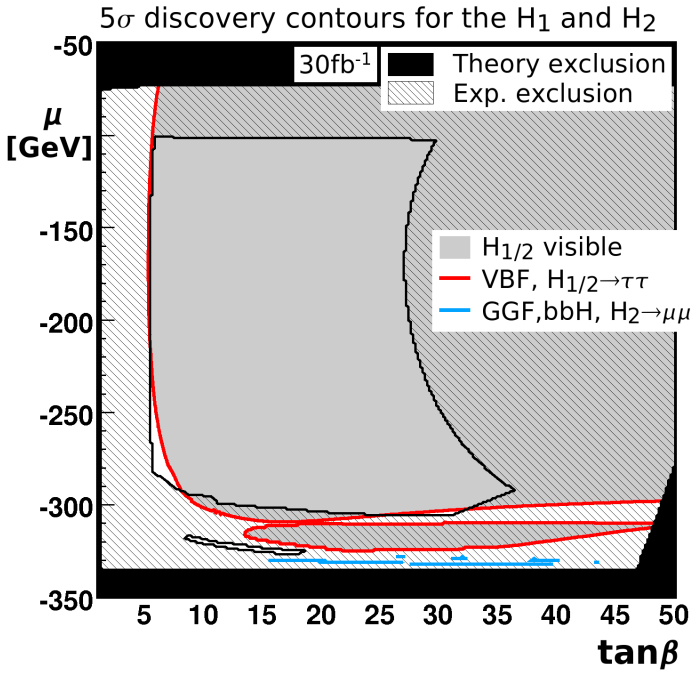

Fig. 7.30: 5σ discovery contours for the H_1 and H_2 in the Reduced Couplings Scenario, $\tan\beta/\mu$ plane with 30 fb^{-1}. Systematic uncertainties are not included. The H_1 or H_2 is observable in the grey region. For details on how this plot must be read, see Fig. 7.1.

GeV is not covered. This behavior has already been discussed for the λ/κ and for the A_λ/A_κ benchmark planes. The (GGF, $H_2 \to ZZ \to 4l$) analysis only reaches 5σ in the excluded region.

In Figs. 7.24 and 7.25, the discovery potential for the H_3 and A_2 in the presence of systematic uncertainties is shown. For both the (GGF, $bb\phi$, $\phi \to \mu\mu$) and (GGF, $bb\phi$, $\phi \to \tau\tau$) analyses, an uncertainty value of 10% is assumed as an example. As a result, the (GGF, $bb\phi$, $\phi \to \mu\mu$) channel is not observable. Also in this plane, the ($tt H_3/A_{1/2}$, $H_3/A_{1/2} \to b\bar{b}$) channel does not reach 5σ.

For the charged Higgs bosons (Figs. 7.26 and 7.27), the ($gb \to tH^-/g\bar{b} \to \bar{t}H^+$, $H^- \to b\bar{t}/H^+ \to t\bar{b}$) analysis loses some of its discovery potential in the presence of systematic uncertainties. It is then not observable in the unexcluded region. Charged Higgs boson detection from top quark decays will now only be possible for small and for large $\tan\beta$, but not for the intermediate $\tan\beta$ region, where the $H^\pm tb$ coupling is small (see Eq. 2.60).

In Figs. 7.28 and 7.29, the overall discovery potential in the presence of the systematic uncertainties is given. As explained before, the region with reduced couplings of the H_2 at $\mu \approx$ -280 GeV is not covered any longer. Also in a part of the small unexcluded region at large negative $\mu \approx -320$ GeV, the discovery of a Higgs boson does not seem to be possible. In this region, a combination of the results from different search channels might help. A combination of all relevant search modes for the neutral Higgs bosons in the profile likelihood and a similar combination for the charged Higgs boson searches give results that together totally cover the small unexcluded region also in the presence of systematic uncertainties.

Interestingly, in a part of the small unexcluded region at $\mu \approx -320$ GeV, the light charged Higgs bosons are the only observable mass resonances. Yet, in a large parameter region, in particular at large $\tan\beta$, two or three mass resonances of different NMSSM Higgs bosons are still observable.

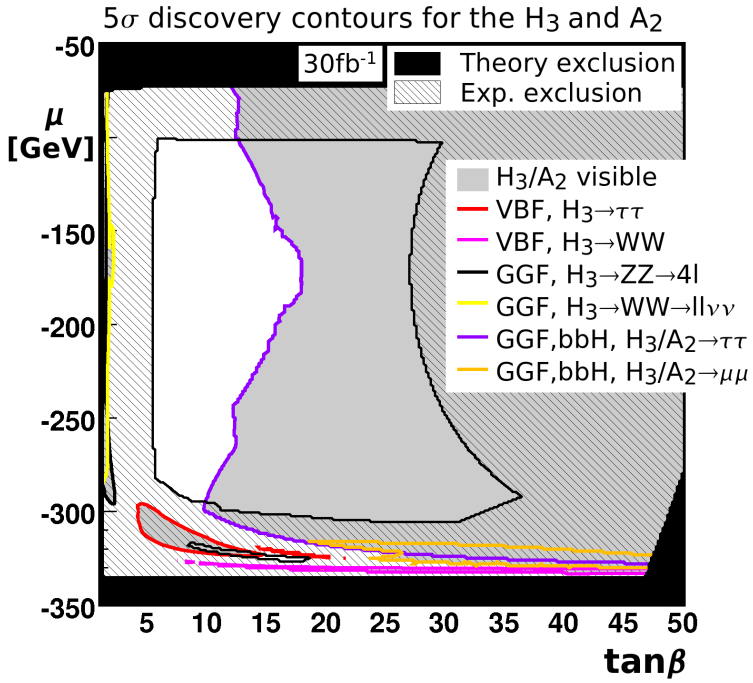

Fig. 7.31: 5σ discovery contours for the H_3 and A_2 in the Reduced Couplings Scenario, $\tan\beta/\mu$ plane with 30 fb^{-1}. Systematic uncertainties are not included. The H_3 or A_2 is observable in the grey region. For details on how this plot must be read, see Fig. 7.1.

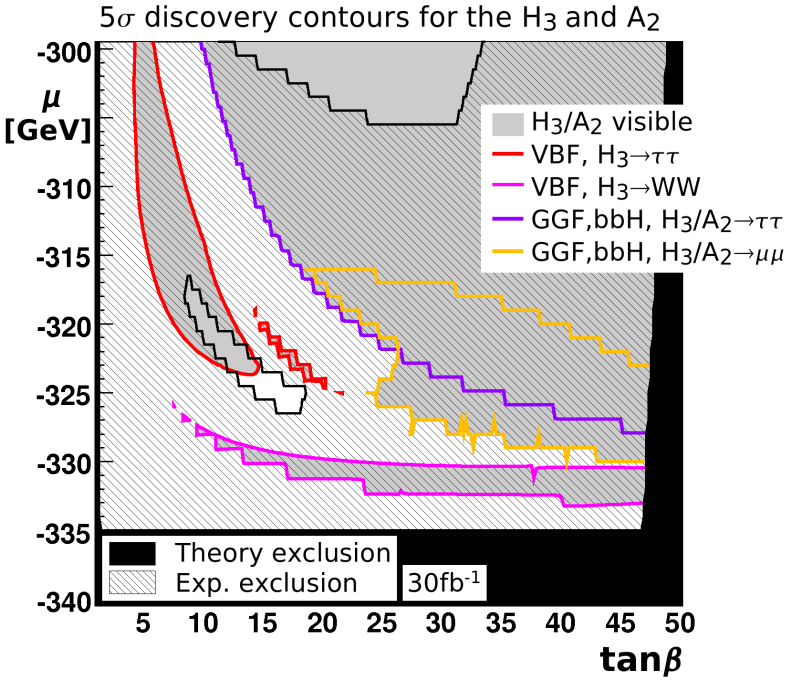

Fig. 7.32: 5σ discovery contours for the H_1 and A_2 in the Reduced Couplings Scenario, $\tan\beta/\mu$ plane with 30 fb^{-1}. Systematic uncertainties are not included. The H_3 or A_2 is observable in the grey region. The shown part of the plane is restricted to large negative μ. For details on how this plot must be read, see Fig. 7.1.

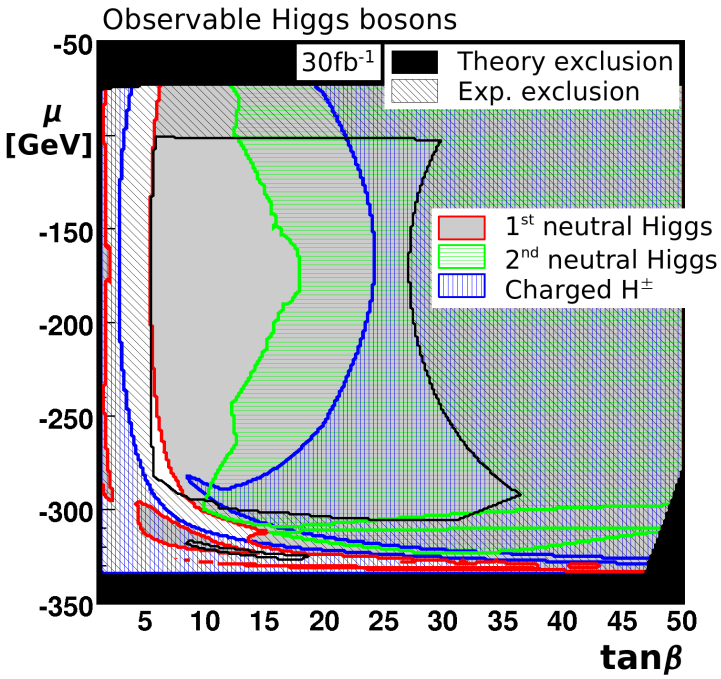

Fig. 7.33: Observable Higgs bosons in the Reduced Couplings Scenario, $\tan\beta/\mu$ plane with 30 fb^{-1}. Systematic uncertainties are not included. One neutral Higgs boson is observable in the grey region, two neutral Higgs bosons in the green (light grey) hatched region. The $H^{\pm}$ bosons are observable in the blue (dark grey) hatched region.

Discovery potential with 30 fb^{-1} The above discussion referred to the ATLAS discovery potential with an integrated luminosity of 30+270 fb^{-1}. In case only 30 fb^{-1} are available, the results of all vector boson fusion analyses, of the searches for the charged Higgs bosons and of the (GGF, bbϕ, $\phi\to\tau\tau$) analysis are unchanged, as for these channels, it is assumed in the above that they have no discovery potential at high luminosity. However, the $H_{2/3}\to\gamma\gamma$ and the (ttϕ, $\phi\to b\bar{b}$) searches are not observable with only 30 fb^{-1}. Also the $H_2\to ZZ$ search remains below 5σ now. The discovery potential of the (GGF, bbϕ, $\phi\to\mu\mu$) mode is restricted to the region with large couplings to gluons (Figs. 7.30 to 7.32).

Also with a data volume of only 30 fb^{-1}, at least one Higgs boson is observable in large parts of the parameter plane (Figs. 7.33, 7.34). To achieve this, the (VBF, $\phi\to\tau\tau$) channel has paramount importance. Only the region with reduced couplings of the H_2 at $\mu \approx -280$ GeV will not be covered by any search. For large $\tan\beta$, the detection of two or three mass resonances of NMSSM Higgs bosons will already be possible with 30 fb^{-1}. Again, in a part of the small unexcluded region at large negative $\mu \approx -320$ GeV, the charged Higgs bosons will be the only observable resonances.

Summary of the Reduced Couplings Scenario, $\mu/\tan\beta$ benchmark plane The $\mu/\tan\beta$ benchmark plane shows a rich phenomenology. In large parts, in particular at large $\tan\beta$, the detection of more than one mass resonance or of the charged Higgs bosons provides evidence for physics beyond the Standard Model. This is often already possible with only 30 fb^{-1}. The (VBF, $\phi\to\tau\tau$), the (bbϕ, GGF, $\phi\to\tau\tau$) and the charged Higgs boson searches are of critical importance to achieve this goal.

However, in large parts of the $\mu/\tan\beta$ plane, only one Higgs boson is observable. In these

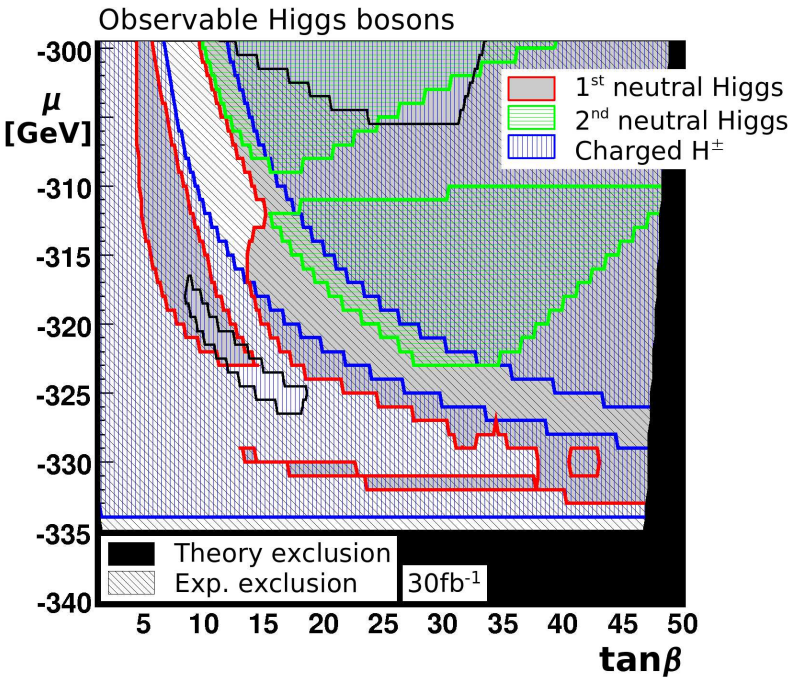

Fig. 7.34: Observable Higgs bosons in the Reduced Couplings Scenario, $\tan\beta/\mu$ plane with 30 fb^{-1}. Systematic uncertainties are not included. One neutral Higgs boson is observable in the grey region, two neutral Higgs bosons in the green (light grey) hatched region. The $\text{H}^{\pm}$ bosons are observable in the blue (dark grey) hatched region. The shown part of the plane is restricted to large negative μ.

regions, the distinction of the NMSSM from other models is more difficult. In the small unexcluded region at large negative $\mu \approx -320$ GeV, the discovery of a mass resonance is in parts only possible due to the combined contributions of three neutral scalar Higgs bosons with similar masses. Again, in the entire parameter plane with exception of the region with reduced couplings at $\mu \approx -280$ GeV, the discovery of a Higgs boson is already possible with 30 fb^{-1}.

7.2.1.4 Summary of the Reduced Couplings Scenario

In this scenario, various types of phenomenology were discussed. It was found that regions with reduced couplings of the most Standard Model-like Higgs boson can be covered by the currently available ATLAS search strategies if the mass of this Higgs boson is about 120 GeV or larger. If the Higgs boson is lighter with a mass around 115 GeV, a very good control of systematic uncertainties in the $\text{tt}\phi$, $\phi\text{b}\bar{\text{b}}$ channel or vector boson fusion analyses for the design luminosity phase are needed. Furthermore, it is possible to observe more than one Higgs bosons or the charged Higgs bosons in parts of the parameter space, in particular at large $\tan\beta$.

7.2.2 The Light A_1 Scenario

7.2.2.1 The λ/κ benchmark plane

In the λ/κ plane of the Light A_1 Scenario, the H_1 has a mass of about 90 to 120 GeV in the unexcluded region and Standard Model-like couplings. Since the A_1 is light, $\text{H}_1 \rightarrow \text{A}_1\text{A}_1$ decays are kinematically possible and often dominant. The H_2 has sizeable couplings in the excluded

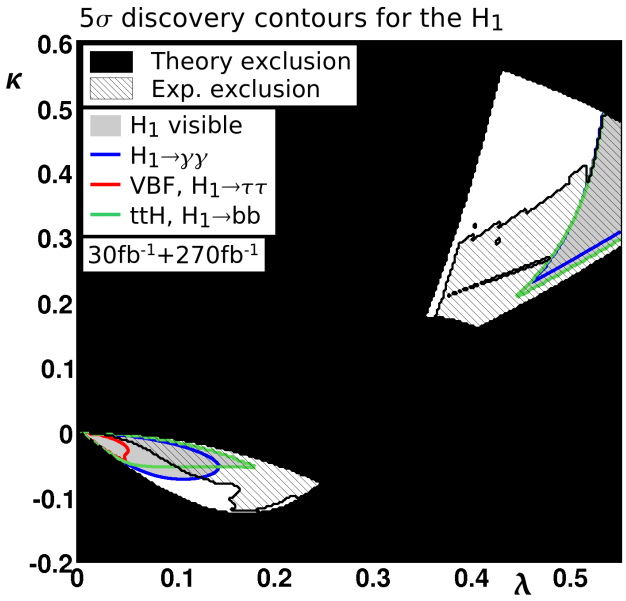

Fig. 7.35: 5σ discovery contours for the H_1 in the Light A_1 Scenario, λ/κ plane with 30+270 fb^{-1}. The H_1 is observable in the grey region. Systematic uncertainties are not included. For details on how this plot must be read, see Fig. 7.1.

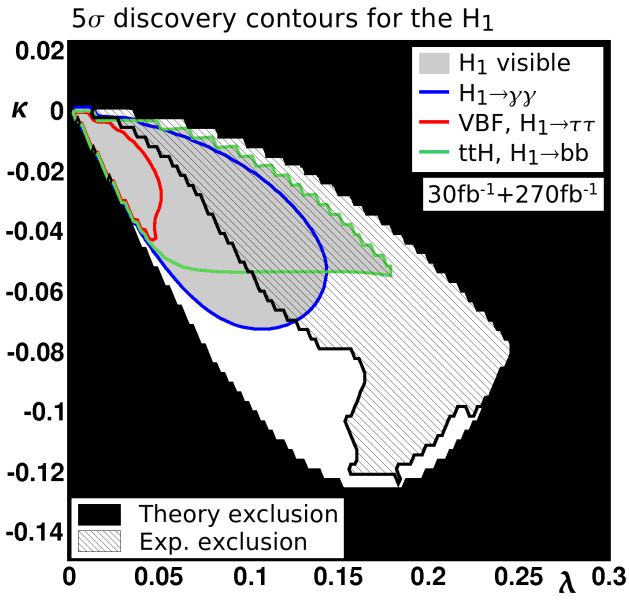

Fig. 7.36: 5σ discovery contours for the H_1 in the Light A_1 Scenario, λ/κ plane with 30+270 fb^{-1}. The H_1 is observable in the grey region. Systematic uncertainties are not included. The shown part of the plane is restricted to small λ and $|\kappa|$. For details on how this plot must be read, see Fig. 7.1.

region only. All other Higgs bosons are too heavy or have too heavily reduced couplings to be important for a discovery.

Discovery potential for the NMSSM Higgs bosons In the upper right hand unexcluded region, the branching ratio of the $H_1 \to A_1A_1$ decay is larger than 90%. In this case, the H_1 cannot be observed with the current ATLAS search strategies (Fig. 7.35), because these searches are designed for Higgs bosons of the Standard Model and the MSSM and thus do not look for such a phenomenology. The branching ratio of $H_1 \to A_1A_1$ drops for small λ and $|\kappa|$. Therefore, a discovery via the inclusive and associated $H_1 \to \gamma\gamma$, the VBF, $H_1 \to \tau\tau$ and the ttH_1, $H_1 \to b\bar{b}$ searches is possible in the lower left hand region when systematic uncertainties on the background are neglected (Fig. 7.36).

The H_2 contributes via the $H_2 \to \gamma\gamma$, the (VBF, $H_2 \to WW$), the (GGF, $H_2 \to ZZ \to 4l$) and the (GGF, $H_2 \to WW \to 2l2\nu$) channels in the excluded region only where it is light enough to be accessible (Fig. 7.37). All other Higgs bosons have either highly reduced couplings or are too heavy to be observed in this scenario. Therefore, only the H_1 is observable in this plane in the allowed region.

Specifics of the $\phi \to \gamma\gamma$ channels In contrast to the Reduced Couplings Scenario, where the coupling of the H_2 to gluons is reduced with respect to its Standard Model value in large parts of the parameter plane so that the $\phi \to \gamma\gamma$ channel is less important compared to the (VBF, $\phi \to \tau\tau$) channel, all couplings of the H_1 are Standard Model-like throughout the allowed parameter region of the λ/κ plane. The $H_1 \to \gamma\gamma$ search therefore has the largest discovery area among the considered searches. Its discovery contour is determined predominantly by the $H_1 \to \gamma\gamma$

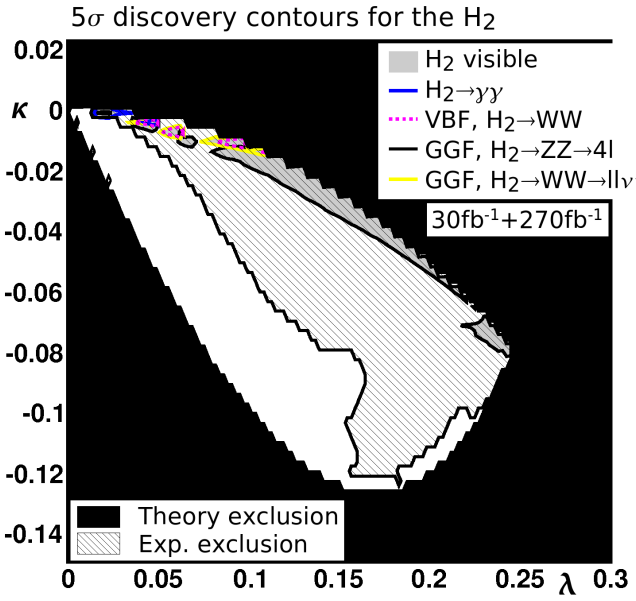

Fig. 7.37: 5σ discovery contours for the H_2 in the Light A_1 Scenario, λ/κ plane with 30+270 fb^{-1}. The H_1 is observable in the grey region. Systematic uncertainties are not included. The shown part of the plane is restricted to small λ and $|\kappa|$. For details on how this plot must be read, see Fig. 7.1.

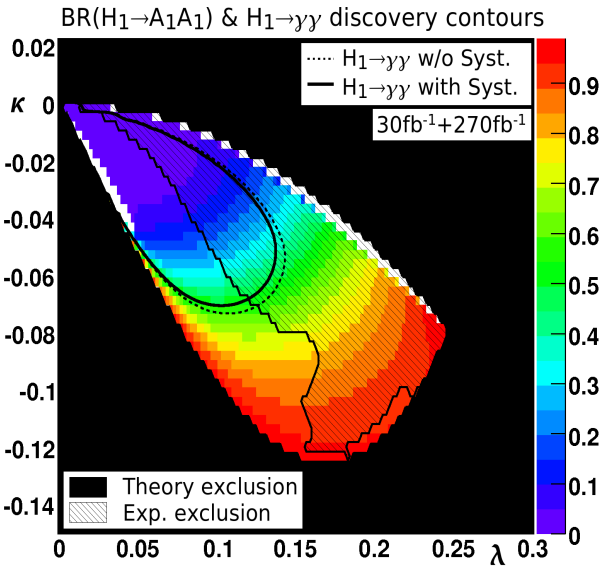

Fig. 7.38: The $H_1 \to A_1A_1$ branching ratio (color coded) in the Light A_1 Scenario, λ/κ plane. The discovery contours of the $H_1 \to \gamma\gamma$ channel for 30+270 fb^{-1} with and without systematic uncertainties are also shown. The shown part of the plane is restricted to small λ and $|\kappa|$.

branching ratio, which is in turn affected by both the H_1 mass and the $H_1 \to A_1A_1$ branching ratio. The $H_1 \to \gamma\gamma$ discovery contour marks in the allowed region approximately the line where the $H_1 \to A_1A_1$ branching ratio is 60% (Fig. 7.38). In this region, the mass of the H_2 is relatively stable. In the excluded region, however, the mass of the H_1 drops sharply at small $|\kappa|$, so that this channel does not reach 5σ also for smaller $H_1 \to A_1A_1$ branching ratios.

Specifics of the $tt\phi$, $\phi \to b\bar{b}$ channel The shape of the discovery contour is different for the (ttH_1, $H_1 \to b\bar{b}$) than for $H_1 \to \gamma\gamma$ analysis, as the $H_1 \to b\bar{b}$ branching ratio is not as sensitive to the Higgs boson mass, but is determined predominantly by the $H_1 \to A_1A_1$ branching ratio alone. In the unexcluded region, the (ttH_1, $H_1 \to b\bar{b}$) discovery contour marks approximately the line where the $H_1 \to A_1A_1$ branching ratio is 25%. In the excluded region, where the H_1 mass is smaller and the discovery potential of this search therefore is better, a 5σ significance can still be obtained for $H_1 \to A_1A_1$ branching ratios of about 65%.

Unlike in the Reduced Couplings scenario, where all Higgs bosons are relatively light, in the λ/κ plane effects from the overlap of Higgs boson peaks inside the mass windows of the analyses are negligible. Even for the ($tt\phi$, $\phi \to b\bar{b}$) analysis with its large mass window of $M_\phi \pm 45$ GeV, only four points of the scanning grid, which are located in the excluded region at very small λ and $|\kappa|$, are affected by an overlap of the H_1 and H_2 mass peaks. In the other regions, the H_2 is too heavy to contribute to the search channels for the light Higgs bosons.

Specifics of the VBF, $\phi \to \tau\tau$ channel In this plane, the (VBF, $H_1 \to \tau\tau$) channel is only observable for very low $H_1 \to A_1A_1$ branching ratios smaller than about 4%. The shape of this discovery contour is determined predominantly by the H_1 mass, as this analysis is very sensitive

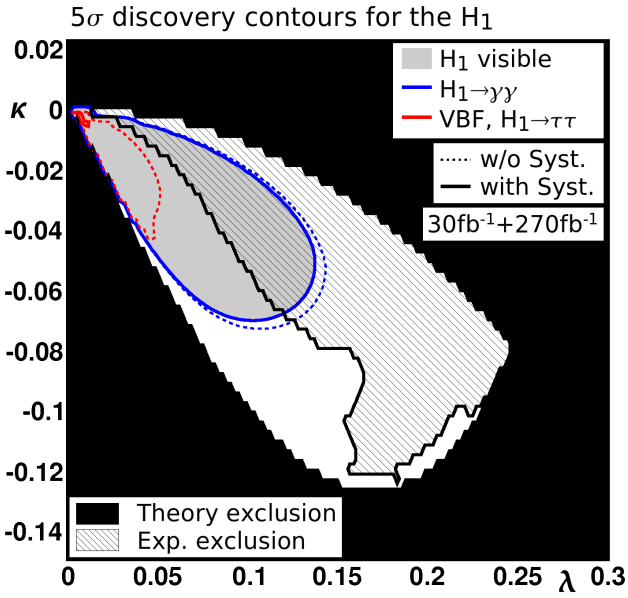

Fig. 7.39: 5σ discovery contours for the H_1 in the Light A_1 Scenario, λ/κ plane with 30+270 fb^{-1}. The H_1 is observable in the grey region. Systematic uncertainties are taken into account. For comparison, the results without systematic uncertainties are given by the dotted lines. The shown part of the plane is restricted to small λ and $|\kappa|$. For details on how this plot must be read, see Fig. 7.1.

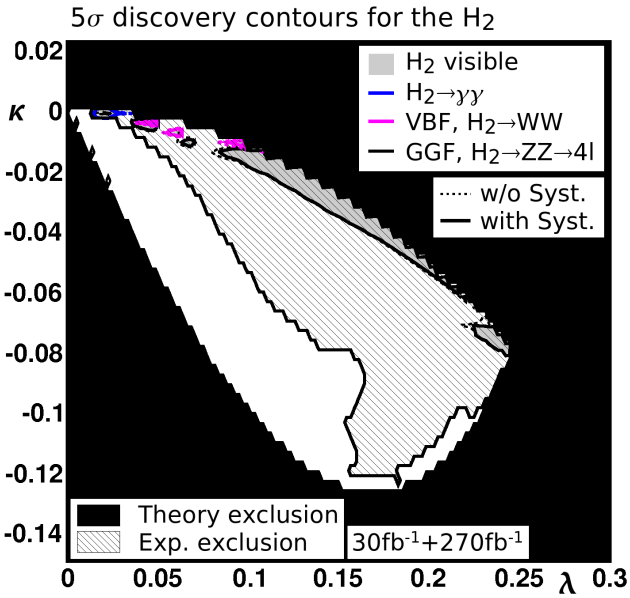

Fig. 7.40: 5σ discovery contours for the H_2 in the Light A_1 Scenario, λ/κ plane with 30+270 fb^{-1}. The H_2 is observable in the grey region. Systematic uncertainties are taken into account. For comparison, the results without systematic uncertainties are given by the dotted lines. The shown part of the plane is restricted to small λ and $|\kappa|$. For details on how this plot must be read, see Fig. 7.1.

to the separation of the signal peak from the Z^0 peak. In the relevant unexcluded region, the H_1 mass is maximally ∼118 GeV for very small λ and $|\kappa|$.

In case only 30 fb^{-1} of integrated luminosity are considered, this channel is the only observable search channel in the λ/κ parameter plane.

Discovery potential with systematic uncertainties When systematic uncertainties on the background levels are taken into account, the ($tt\bar{t}H_1/_2$, $H_1/_2 \to b\bar{b}$) and (GGF, $H_2 \to WW \to 2l2\nu$) analyses do not reach 5σ significances. The discovery contour of the $H_1 \to \gamma\gamma$ analysis is only slightly shifted (Figs. 7.39, 7.40). It now marks the 55% instead of the 60% line of the $H_1 \to A_1A_1$ branching ratio in the allowed parameter region (Fig. 7.38). Thus, the overall discovery potential in this benchmark plane therefore is quite stable with respect to background uncertainties.

However, the (VBF, $H_1 \to \tau\tau$) channel is very sensitive to the systematic uncertainties in the presence of $H_1 \to A_1A_1$ decays. Even without systematic uncertainties, it reaches maximally ∼5.3σ in this plane. Moreover, the H_1 mass of ∼118 GeV is in the relevant region slightly too small to yield an optimal discovery potential.

7.2.2.2 Summary of the Light A_1 Scenario

In this benchmark plane, the H_1 will be the only observable Higgs boson in the allowed parameter region. To fill the gaps in the current discovery potential which occur when the $H \to A_1A_1$ branching ratio is larger than about 60% to 55%, it is necessary to develop strategies to search

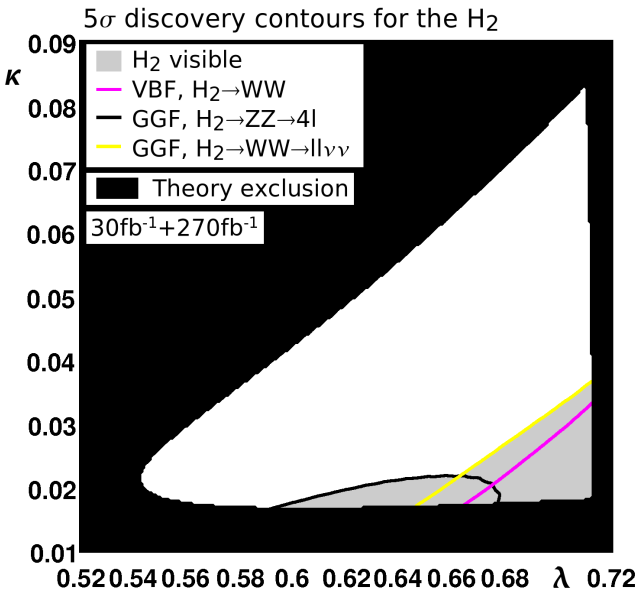

Fig. 7.41: 5σ discovery contours for the H_2 in the Maximal M_{H_1} Scenario, λ/κ plane with 30+270 fb^{-1}. Systematic uncertainties are not included. The H_2 is observable in the grey region. For details on how this plot must be read, see Fig. 7.1.

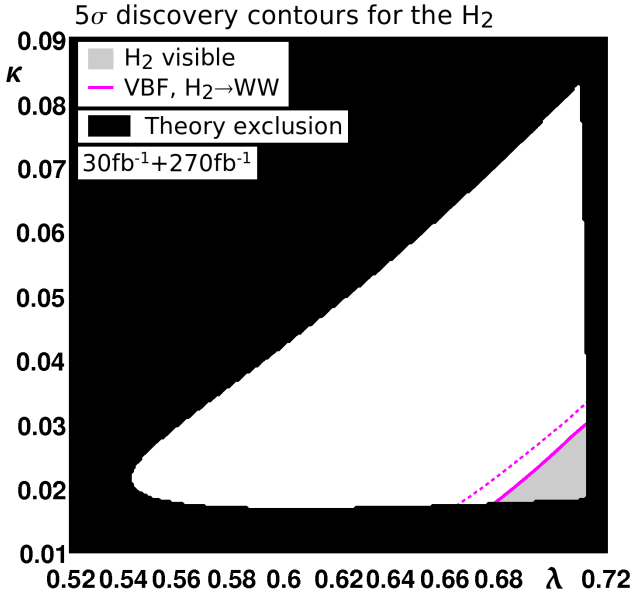

Fig. 7.42: 5σ discovery contours for the H_2 in the Maximal M_{H_1} Scenario, λ/κ plane with 30+270 fb^{-1}. Systematic uncertainties are taken into account. For comparison, the results without systematic uncertainties are given by the dotted lines. The H_2 is observable in the grey region. For details on how this plot must be read, see Fig. 7.1.

for the $H_1 \to A_1A_1$ topology. Regions with dominant $H_1 \to A_1A_1 \to b\bar{b}b\bar{b}/b\bar{b}\tau\tau$, $H_1 \to A_1A_1 \to \tau\tau\tau\tau$ and $H_1 \to A_1A_1 \to \gamma\gamma\gamma\gamma$ decays should be included in the considerations. Otherwise, a discovery of an NMSSM Higgs boson in ATLAS cannot be guaranteed, even if it exists in nature. One possible search channel will be investigated in Chap. 8.

For $H_1 \to A_1A_1$ branching ratios smaller than $\sim$55%, the $H_1 \to \gamma\gamma$ search is crucial for this scenario. Although its discovery potential is relatively stable under the influence of systematic uncertainties, it is nevertheless important to have these well under control to guarantee a good discovery potential also in the presence of a large $H_1 \to A_1A_1$ branching ratio.

For 30 fb^{-1}, only the (VBF, $H_1 \to \tau\tau$) channel will allow for the discovery of the H_1 in a small part of the parameter plane. Also for this channel, a good control of systematic uncertainties is of importance to maximize the discovery potential.

7.2.3 The Maximal M_{H_1} Scenario

7.2.3.1 The λ/κ benchmark plane

In this plane, the H_1 mass is at its maximal possible value of about 140 GeV for large λ and κ. The mass of the H_2 varies from about 135 to 195 GeV. Since the A_1 is very light, $H_1 \to A_1A_1$ and $H_2 \to A_1A_1$ decays are possible in the entire parameter plane. In addition, there is a significant variation of the couplings of the H_1 and H_2. All other Higgs bosons are not promising for discovery.

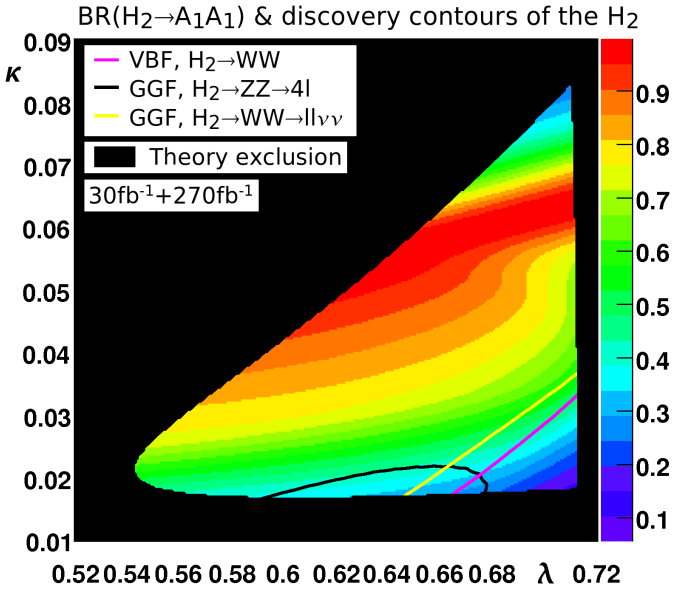

Fig. 7.43: The $H_2 \to A_1 A_1$ branching ratio (color coded) in the Maximal M_{H_1} Scenario, λ/κ plane. The discovery contours of different search channels for 30+270 fb^{-1} without systematic uncertainties are also shown.

Discovery potential for the NMSSM Higgs bosons In the benchmark plane discussed here, the H_1 is not observable with the current ATLAS search strategies, because in the region at large $\kappa \gtrsim 0.04$ where its couplings are sizeable, the branching ratio of the $H_1 \to A_1 A_1$ decay is larger than 80%. As discussed for the Light A_1 Scenario, for this situation new specialized searches need to be considered.

The discovery contours for the H_2 are shown in Fig. 7.41. For its mass, the searches for its decay to massive vector bosons are the most important ones, among these especially the (GGF, $H_2 \to ZZ \to 4l$) and (GGF, $H_2 \to WW \to ll\nu\nu$) searches. Their contours overlap, but do not cover the same region since their optimal mass ranges are different.

The $H_2 \to ZZ$ branching ratio is usually maximal at masses around 150 GeV, thus for the corresponding region, the (GGF, $H_2 \to ZZ \to 4l$) search is important. However, too large values of κ are not accessible by this search also if they provide optimal H_2 masses, because the coupling of the H_2 to gluons and thus its production rate becomes too low.

For masses larger than about 153 to 158 GeV, depending on the exact coupling to gluons at the scan point, the $H_2 \to WW$ branching ratio is large enough so that the $H_2 \to WW \to ll\nu\nu$ analysis yields significances above 5σ. Also the (VBF, $H_2 \to WW \to ll\nu\nu$) search contributes in a similar region with masses larger than 156 to 159 GeV. Thus, for the here present Higgs boson masses, the (GGF, $H_2 \to WW$) search covers a wider mass range than the (VBF, $H_2 \to WW$) analysis.

For these searches, the $H_2 \to A_1 A_1$ branching ratio up to which the discovery of the H_2 is still possible varies, as the discovery potential is also affected by the reduced couplings. However, it is roughly in the range of 40% to 60% (Fig. 7.43).

The other Higgs bosons are not observable in this plane because they have either heavily reduced couplings or are too heavy to be accessible as current studies in ATLAS show.

Discovery potential with systematic uncertainties When systematic uncertainties are included, only the (VBF, $H_2 \to WW$) channel allows for a Higgs boson discovery in a small region

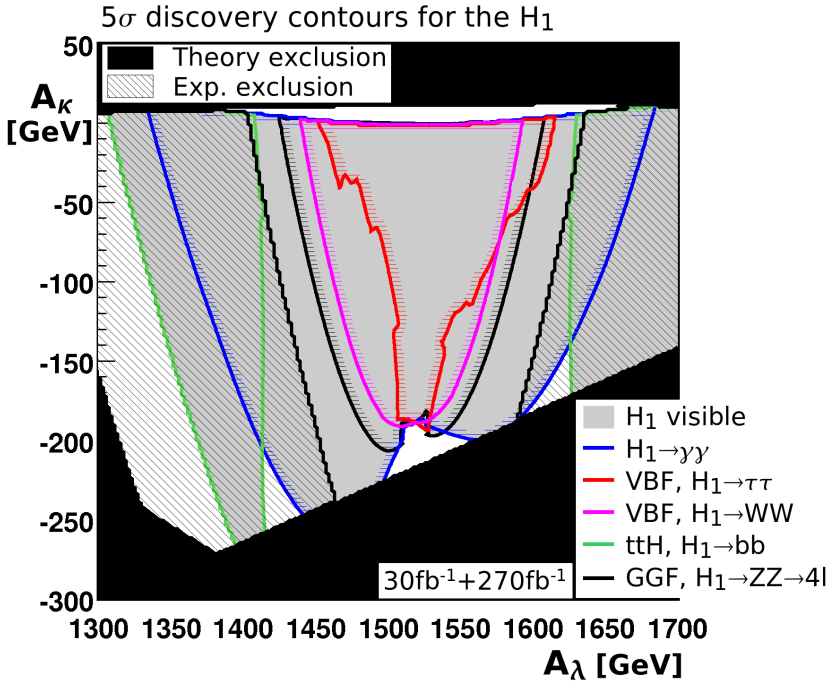

Fig. 7.44: 5σ discovery contours for the H_1 in the Maximal M_{H_1} Scenario, A_λ/A_κ plane with 30+270 fb^{-1}. Systematic uncertainties are not included. The H_1 is observable in the grey region. For details on how this plot must be read, see Fig. 7.1.

of the parameter plane (Fig. 7.42). The other channels are not observable. In the Standard Model, the (GGF, $\phi\to$ZZ$\to$4l) and the (GGF, $\phi\to$WW) modes preserve their good discovery potential also when systematic uncertainties are taken into account [5,85], but in this parameter region of the NMSSM, their signal rate is smaller due to the reduced couplings and the sizeable $H_2\to A_1A_1$ branching ratio.

Discovery potential with 30 fb^{-1} With 30 fb^{-1} of integrated luminosity, only the (VBF, $H_2\to$WW) channel will be observable in the same region that is shown in Fig. 7.42 since for this channel, always only the low luminosity scenario is taken into account.

Summary of the Maximal M_{H_1} Scenario, λ/κ benchmark plane In the λ/κ benchmark plane, the H_2 will be the only observable Higgs boson. The H_1 which is at its maximal possible mass value of 140 GeV will not be observable. The searches for Higgs boson decays to massive vector bosons are especially important. If systematic uncertainties are included or for only 30 fb^{-1}, the vector boson fusion production mode is of crucial importance.

7.2.3.2 The A_λ/A_κ benchmark plane

In this plane, the mass of the lightest scalar Higgs boson H_1 varies from ~114 to the maximal possible mass of 140 GeV in the allowed region. Also the H_2 is relatively light with masses ranging from 140 to 200 GeV. There is a large variation of the couplings of these two Higgs bosons. This means that in large parts of the parameter plane, their couplings are reduced with respect to the Standard Model case. As the A_1 is very light at small $|A_\kappa|$, $H_1\to A_1A_1$ and $H_2\to A_1A_1$ decays with partly significant branching ratios are possible in this region.

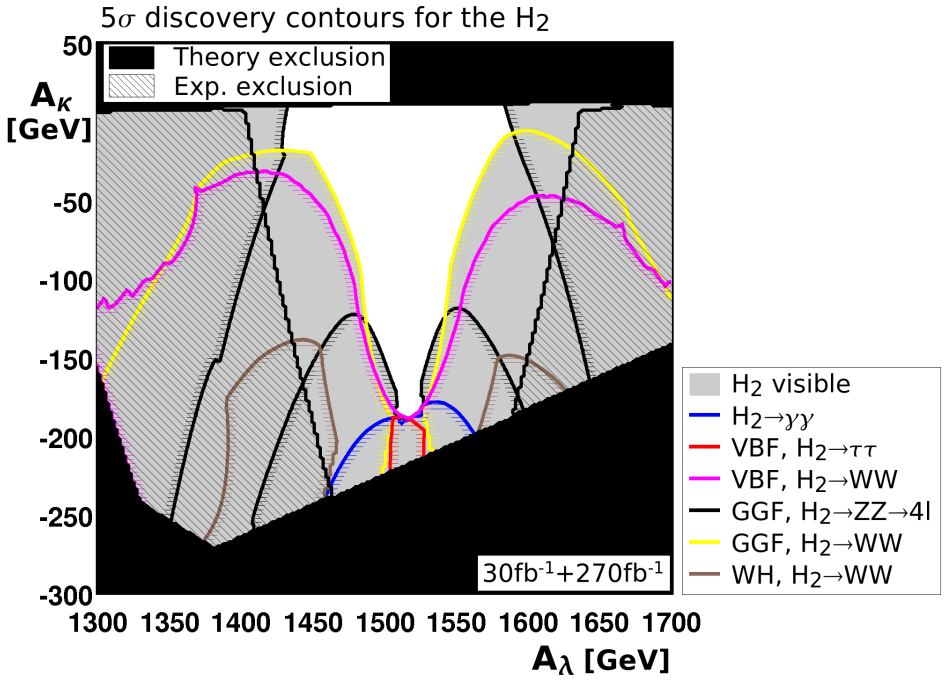

Fig. 7.45: 5σ discovery contours for the H_2 in the Maximal M_{H_1} Scenario, A_λ/A_κ plane with 30+270 fb^{-1}. Systematic uncertainties are not included. The H_2 is observable in the grey region. For details on how this plot must be read, see Fig. 7.1.

Discovery potential for the NMSSM Higgs bosons The discovery potential for the lightest scalar Higgs boson is shown in Fig. 7.44. In the unexcluded region, above all the inclusive and associated $H_1 \to \gamma\gamma$, the (GGF, $H_1 \to ZZ \to 4l$), the (VBF, $H_1 \to WW$) and the (VBF, $H_1 \to \tau\tau$) searches contribute to the discovery potential of the H_1. Near and in the excluded region, also the ($t\bar{t}H_1$, $H_1 \to b\bar{b}$) analysis yields significances larger than 5σ. The region with sizeable $H_1 \to A_1A_1$ decays at small $A_\kappa \gtrsim 0$ is not covered by any search. Moreover, in the region where the couplings of the H_1 are heavily reduced at $A_\lambda \approx 1550$ GeV and large negative $A_\kappa \lesssim -190$ GeV, this Higgs boson is also not observable. However, regions with only moderately reduced couplings can be covered without difficulty by the listed searches.

For the heavier H_2, in particular the (GGF, $H_2 \to ZZ \to 4l$), the (GGF, $H_2 \to WW \to 2l2\nu$) and the (VBF, $H_2 \to WW$) channels cover large parts of the parameter plane (Fig. 7.45). Also the inclusive and associated $H_2 \to \gamma\gamma$, the (VBF, $H_2 \to \tau\tau$) and the (WH_2, $H_2 \to WW$) searches are important in smaller regions. Around $A_\lambda \approx 1550$ GeV at small and intermediate negative $A_\kappa \gtrsim -190$ GeV, the couplings of the H_2 are heavily reduced. In this part of the parameter plane, it will not be observable. However, also for this Higgs boson, regions with only moderately reduced couplings can be covered without difficulty by the listed searches.

All other Higgs bosons have either highly reduced couplings or are too heavy to be observable in this benchmark plane.

Specifics of the $\phi \to \gamma\gamma$ channels Both the inclusive and the associated search modes for the $\phi \to \gamma\gamma$ decay yield significances above 5σ for the H_1 and H_2. As in the scenarios discussed before, the area covered by the associated search is fully contained in the area covered by the inclusive search. As these searches are not disjoint, only the discovery contour of the inclusive mode is shown and will be discussed in the following.

As in the scenarios before, the discovery contour for this search mode is above all determined by the branching ratio of the relevant Higgs bosons to photons. This branching ratio is usually maximal at a Higgs boson mass of about 126 GeV. At $A_\lambda \approx 1550$ GeV, where the H_1 is near its maximal allowed mass value of 140 GeV, this channel therefore loses some of its discovery potential. Moreover, for $A_\lambda \approx 1550$ GeV and large negative $A_\kappa \lesssim -190$ GeV, also the couplings of the H_1 are heavily reduced, so that this search mode is not visible there.

For similar reasons, this channel is important for the H_2 in the region where its mass is low, i.e. around $A_\lambda \approx 1550$ GeV and at large negative $A_\kappa \lesssim -190$ GeV. In this region, the H_2 also has a sizeable coupling to gluons.

There are two regions around $A_\kappa \approx -200$ GeV, where both the H_1 and the H_2 will be observable in this search mode. As was stated before, the mass resolution in this channel is with 1.1 to 1.7 GeV very good. Therefore, the mass peaks of the H_1 and H_2 can be separated in these regions.

Specifics of the GGF, $\phi \to ZZ \to 4l$ channel The Higgs boson branching ratio to a pair of Z^0 bosons commonly reaches a maximum for Higgs bosons masses of about 150 GeV, followed by a minimum for masses of about 160 to 170 GeV when the decay to a $W^\pm$ boson pair on its mass shell becomes possible, and then again increases with increasing Higgs boson mass (see Fig. 5.4). This behavior is mirrored by the shape of the discovery contours of the H_1 and H_2 in this channel. The (GGF, $H_1 \to ZZ \to 4l$) analysis benefits from an increasing mass of the lighter H_1 and thus covers the region where the H_1 mass and its couplings are maximal. For the H_2, the situation is more complicated. There are three separate areas where its discovery is possible in this channel. One area is located at intermediate $A_\lambda \approx 1550$ GeV where the mass of the H_2 is about 150 GeV, the other areas are at small and at large $A_\lambda \approx 1350/1650$ GeV, where the mass of the H_2 is larger than about 180 GeV. In these areas, the $H_2 \to ZZ$ branching ratio is large. They are separated by an area with $160 \lesssim M_{H_2} \lesssim 180$ GeV, where the relevant branching ratio is suppressed and the $H_2 \to ZZ$ decay therefore is not observable.

Specifics of the GGF, $\phi \to WW \to 2l2\nu$ channel This channel is only visible for the H_2, because the H_1 is too light to be of importance for this search mode. Unlike the (GGF, $\phi \to ZZ \to 4l$) search channel, this analysis covers the unexcluded parameter region where the H_2 is heavier than about 140 GeV and where its coupling to gluons is larger than 40% of its Standard Model value. For H_2 masses larger than about 190 GeV, the search channel is not observable as the $H_2 \to WW$ branching ratio drops due to the increasing $H_2 \to ZZ$ branching ratio. This is the case in the excluded region at small and at large $A_\lambda < 1400$ GeV/ $A_\lambda > 1600$ GeV. A similar deterioration for the (GGF, $H_2 \to ZZ \to 4l$) channel is not expected, as it has a good discovery potential also for large Higgs boson masses (see Fig. 5.6).

Since the (GGF, $H_2 \to WW \to 2l2\nu$) search suffers from the significant reduction of the H_2 couplings, especially at small negative $A_\kappa \gtrsim -20$ GeV, the channel is not visible there. Also the presence of $H_2 \to A_1A_1$ decays leads to a deterioration of the discovery potential.

Specifics of the VBF, $\phi \to WW$ channel Unlike the (GGF, $\phi \to WW \to 2l2\nu$) channel, the (VBF, $\phi \to WW$) search can also detect Higgs bosons with masses around 120 GeV and is therefore important for a possible discovery of the H_1. It provides significances larger than 5σ for this Higgs boson in the region where its mass and also its couplings are nearly maximal.

For the H_2 boson, this channel provides a discovery potential in a similar region than the (GGF, $H_2 \to WW \to 2l2\nu$) channel, as both analyses are mainly affected by the $H_2 \to WW$ branching ratio. However, as already observed for the λ/κ plane, this channel covers a slightly

smaller area than the gluon fusion mode, in particular at large $A_\kappa \approx -50$ GeV and intermediate $A_\lambda \approx 1450/1600$ GeV, where the couplings are significantly reduced.

Specifics of the Wϕ, $\phi\to$WW channel The A_λ/A_κ plane of the Maximal M_{H_1} Scenario is the only benchmark plane discussed in this thesis where the (WH_2, $\mathrm{H}_2\to$WW) search contributes to the discovery potential. It is important in the regions where the H_2 has a mass from about 150 to 170 GeV, so that the $\mathrm{H}_2\to$WW branching ratio is maximal, and where additionally the coupling of the H_2 to vector bosons is not too heavily reduced, i.e. larger than about 60% of its Standard Model value.

Specifics of the VBF, $\phi\to\tau\tau$ channel This channel is of special importance in the region where the couplings of the scalar Higgs bosons are largest, i.e. for intermediate $A_\lambda \approx 1550$ GeV. For small and intermediate negative $A_\kappa \gtrsim -190$ GeV, only the H_1 is visible and contributes alone to the signal events inside the mass window in a large part of the covered area. Its mass is with maximally 140 GeV still well accessible by this analysis. The observed asymmetry in the shape of the discovery contour of the H_1 is due to slightly larger vector boson fusion production cross sections at large A_λ to which the analysis is very sensitive. The complex shape of the contours is caused by the different contributions from the $\mathrm{H}_1\to\tau\tau\to$ll+4$\nu$ and $\mathrm{H}_1\to\tau\tau\to$lh+3$\nu$ channels, that are combined in the profile likelihood to obtain the significance. The purely leptonic channel has the best discovery potential for Higgs boson masses around 120 GeV, whereas the semileptonic channel yields the largest significances for a mass of 130 GeV [62].

At large negative $A_\kappa \lesssim -190$ GeV, the H_2 has large couplings and a mass close to 140 GeV, so it can be discovered in the (VBF, $\mathrm{H}_2\to\tau\tau$) channel in this region. The H_1 has a mass similar to the H_2 mass in that region and thus also contributes to the signal events inside the mass window. However, this is not a large contribution as the H_1 couplings are small.

Specifics of the ttϕ, $\phi\to$b$\bar{\text{b}}$ channel Unlike for example in the Reduced Couplings Scenario, the (ttϕ, $\phi\to$b$\bar{\text{b}}$) channel is only of minor importance in this benchmark plane. In large parts of the plane, the coupling of the H_1 to up-type fermions is reduced and thus the ttH_1 production cross section is smaller than in the Standard Model. Therefore only regions with H_1 masses that are optimal for the (ttϕ, $\phi\to$b$\bar{\text{b}}$) search channel, i.e. smaller than 115 GeV to 85 GeV, depending on the coupling to up-type fermions, can be covered by this search mode. This is mainly the case in the excluded region. Although approximately Standard Model-like couplings are obtained for intermediate $A_\lambda \approx 1500$ GeV and small $|A_\kappa| \lesssim 190$ GeV, the mass of the H_1 is about 140 GeV in that region. For this mass region, the $\mathrm{H}_1\to$b$\bar{\text{b}}$ branching ratio has decreased compared to smaller masses since the decay modes to massive vector bosons have gained importance.

Observable Higgs bosons In Fig. 7.46, an overview of how many Higgs bosons will be observable in the discussed benchmark plane is given. For this, is has been assumed that the H_1 and H_2 will be distinguishable if they are both observable either in the $\mathrm{H}_{1/2}\to\gamma\gamma$ channel or the $\mathrm{H}_{1/2}\to\mathrm{ZZ}\to$4l channel. These channels have a very good mass resolution of 1.1 to 3.0 GeV for Higgs boson masses smaller than 200 GeV [5]. This is assumed in this thesis to be sufficient to separate the mass peaks of the H_1 and H_2. The $\phi\to$WW searches are not considered for the Higgs boson distinction as the corresponding analyses do not reconstruct a Higgs boson mass. Including (VBF, $\phi\to\tau\tau$) in the above list of channels that can separate the Higgs boson mass peaks would not change the contours in Fig. 7.46.

In the entire plane with the exception of the region with frequent $\mathrm{H}_1\to\mathrm{A}_1\mathrm{A}_1$ decays at $A_\kappa \gtrsim 0$, the discovery of at least one neutral Higgs boson will be possible. In some parts of the

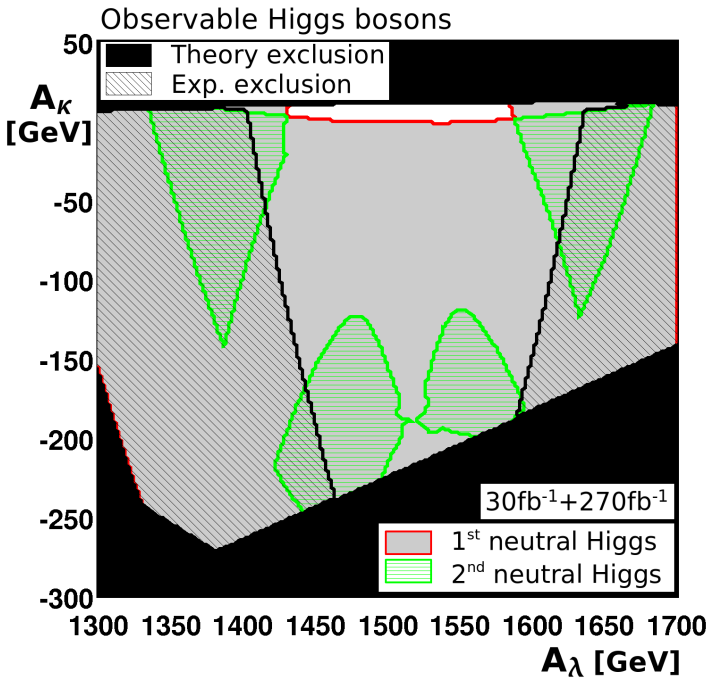

Fig. 7.46: Observable Higgs bosons in the Maximal M_{H_1} Scenario, A_λ/A_κ plane with 30+270 fb^{-1}. Systematic uncertainties are not included. One neutral Higgs boson is observable in the grey region, two neutral Higgs bosons in the green (light grey) hatched region.

parameter plane, but not near the maximal H_1 mass, also the existence of two neutral Higgs bosons can be experimentally confirmed. Such an observation would be evidence for physics beyond the Standard Model.

Discovery potential with systematic uncertainties In Figs. 7.47 and 7.48, the 5σ discovery contours of the H_1 and H_2 are shown in the presence of systematic uncertainties. Although the (ttH_1, $H_1 \to b\bar{b}$), (GGF, $H_2 \to WW$) and (WH_2, $H_2 \to WW$) channels do not contribute to the discovery potential any longer, the overall discovery potential in this parameter plane is only changed marginally when systematic uncertainties are included. The regions that where covered by the (ttH_1, $H_1 \to b\bar{b}$) and the (WH_2, $H_2 \to WW$) searches are also accessible by other analyses that retain their discovery potential. The regions in which the H_2 is not visible due to the loss of the (GGF, $H_2 \to WW$) channel and the deterioration in the (VBF, $H_2 \to WW$) channel are still covered by searches for the H_1. In this thesis, both $\phi \to WW$ searches are assumed not to be capable of separating the H_2 and the H_1 resonance peaks, so that the overall number of discoverable Higgs bosons is unchanged.

Discovery potential with 30 fb^{-1} When only 30 fb^{-1} of integrated luminosity are taken into account, the performance of the vector boson fusion searches is unchanged, as explained for the scenarios before (Figs. 7.49, 7.50). The regions where the (GGF, $H_{1/2} \to ZZ \to 4l$) and (GGF, $H_2 \to WW \to 2l2\nu$) searches can contribute to the discovery potential are reduced in size, and all other analyses do not yield significances sufficient to claim a discovery with 30 fb^{-1} in the unexcluded area of this benchmark plane.

Fig. 7.51 shows the overall discovery potential of the 30 fb^{-1} scenario. In parts of the plane, no Higgs boson will be observable, and only in a tiny region at $A_\kappa \approx -200$ GeV, two different

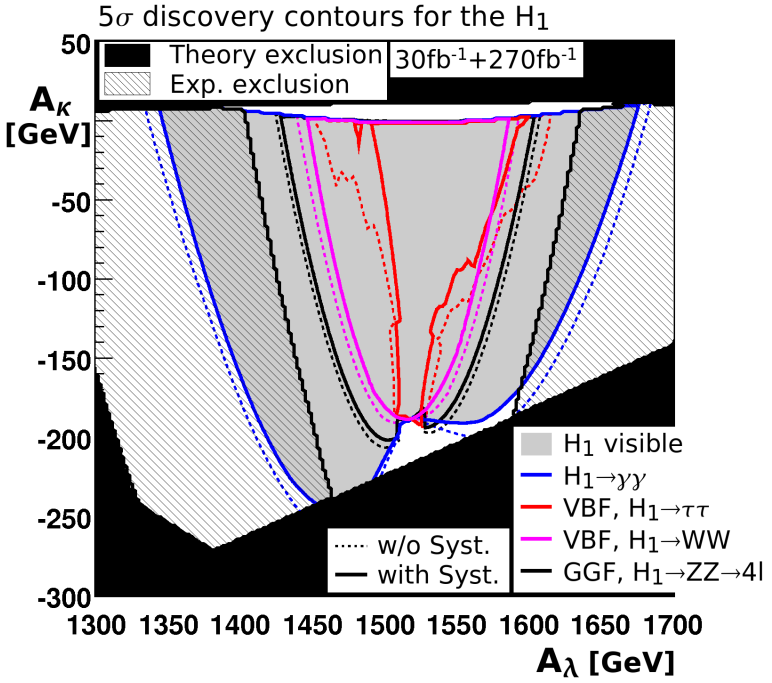

Fig. 7.47: 5σ discovery contours for the H_1 in the Maximal M_{H_1} Scenario, A_λ/A_κ plane with 30+270 fb^{-1}. Systematic uncertainties are taken into account. For comparison, the results without systematic uncertainties are given by the dotted lines. The H_1 is observable in the grey region. For details on how this plot must be read, see Fig. 7.1.

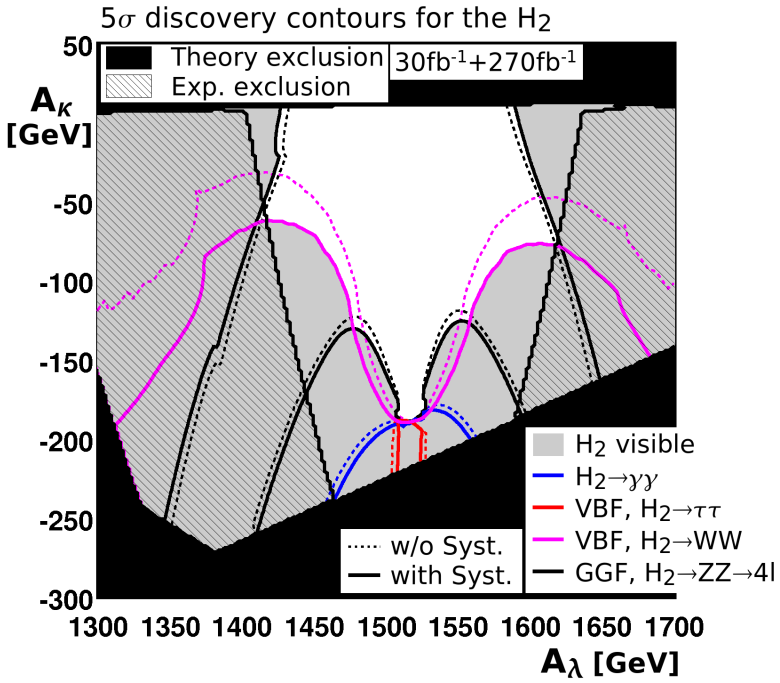

Fig. 7.48: 5σ discovery contours for the H_2 in the Maximal M_{H_1} Scenario, A_λ/A_κ plane with 30+270 fb^{-1}. Systematic uncertainties are taken into account. For comparison, the results without systematic uncertainties are given by the dotted lines. The H_2 is observable in the grey region. For details on how this plot must be read, see Fig. 7.1.

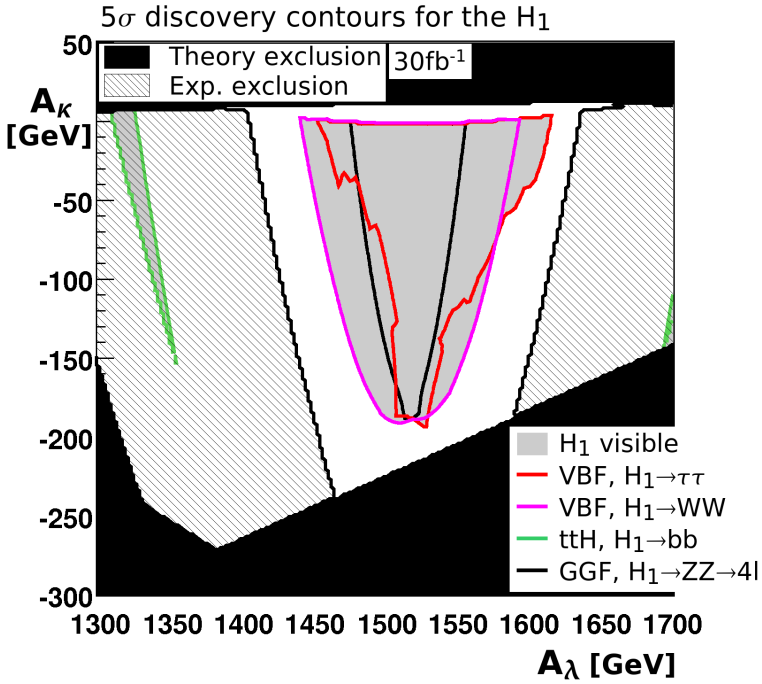

Fig. 7.49: 5σ discovery contours for the H_1 in the Maximal M_{H_1} Scenario, A_λ/A_κ plane with 30 fb^{-1}. Systematic uncertainties are not included. The H_1 is observable in the grey region. For details on how this plot must be read, see Fig. 7.1.

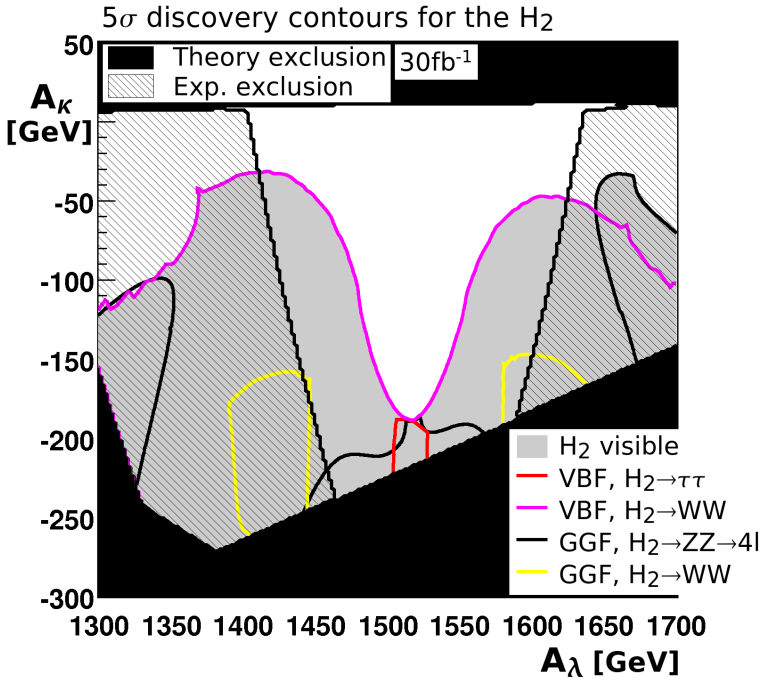

Fig. 7.50: 5σ discovery contours for the H_2 in the Maximal M_{H_1} Scenario, A_λ/A_κ plane with 30 fb^{-1}. Systematic uncertainties are not included. The H_2 is observable in the grey region. For details on how this plot must be read, see Fig. 7.1.

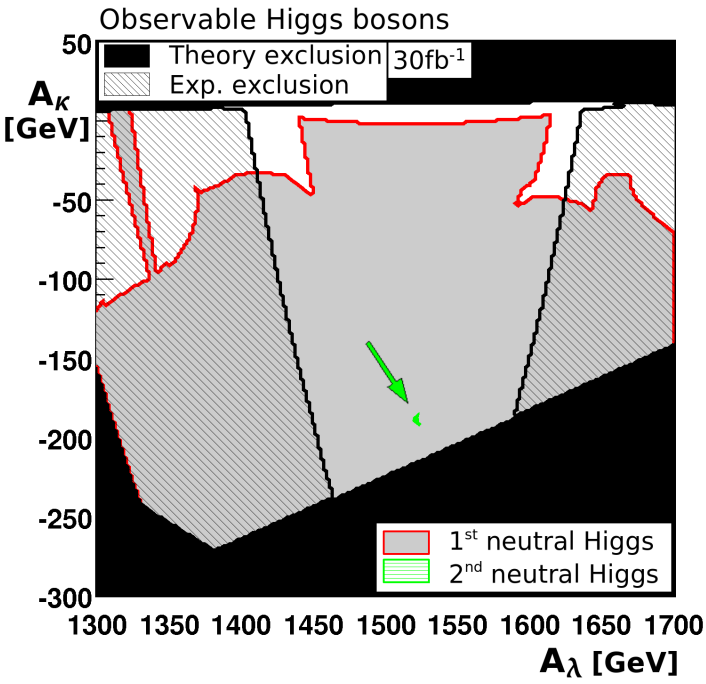

Fig. 7.51: Observable Higgs bosons in the Maximal M_{H_1} Scenario, A_λ/A_κ plane with 30 fb^{-1}. Systematic uncertainties are not included. One neutral Higgs boson is observable in the grey region, two neutral Higgs bosons in the green (light grey) region, pointed at by the green (light grey) arrow.

mass resonances are distinguishable. The shape and size of the regions where at least one Higgs boson can be discovered are dominated by the vector boson fusion modes.

Summary of the Maximal M_{H_1} Scenario, λ/κ benchmark plane This benchmark plane shows that for favorable model parameters, it is possible to observe the lightest scalar Higgs boson of the NMSSM when it has its maximal possible mass. Also the discovery potential for the H_2 is good. Although in large parts of the plane, the couplings of the H_1 and H_2 are significantly reduced, the discovery of at least one, in some regions even of two Higgs bosons, is possible without difficulties for Higgs boson masses of about 120 to 200 GeV in regions without $H_1 \to A_1A_1$ decay. A large variety of search channels contributes.

With only 30 fb^{-1}, only one Higgs boson is observable in large parts of the plane. Some regions, also without $H_{1/2} \to A_1A_1$ decays, are not covered for the low luminosity scenario. The vector boson fusion searches for $\phi \to \tau\tau$ and $\phi \to$WW decays are particularly important.

7.2.3.3 Summary of the Maximal M_{H_1} Scenario

In this scenario the phenomenology of the NMSSM with an H_1 at its maximal possible mass is investigated. It is found that it is possible to observe such an H_1 with the currently available ATLAS analysis strategies if its branching ratio to a pair of light pseudoscalars is sufficiently small.

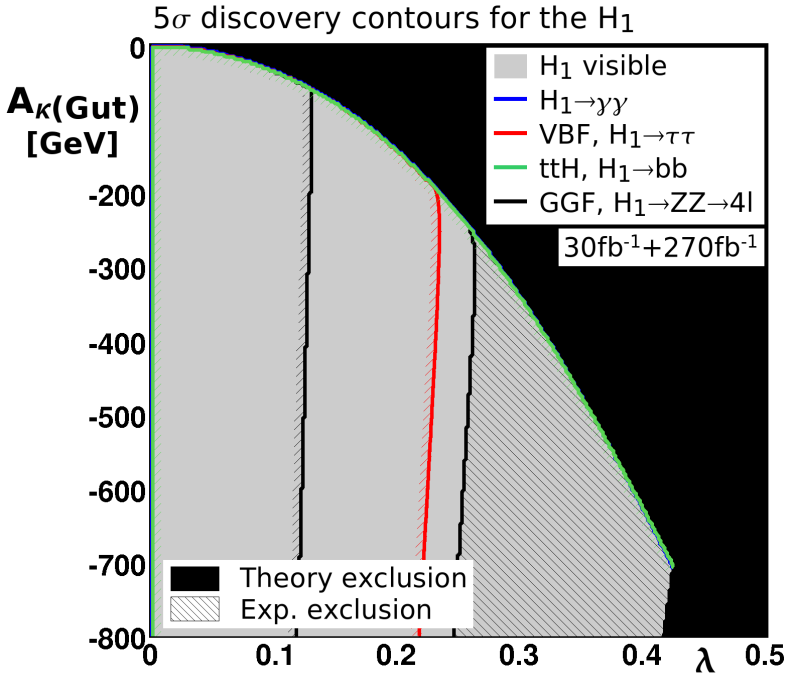

Fig. 7.52: 5σ discovery contours for the H_1 in the cNMSSM Scenario, $\lambda/A_{\kappa(\mathrm{GUT})}$ plane with 30+270 fb^{-1}. Systematic uncertainties are not included. The H_1 is observable in the grey region. The blue (dark grey) line is almost completely covered by the green (light grey) line. For details on how this plot must be read, see Fig. 7.1.

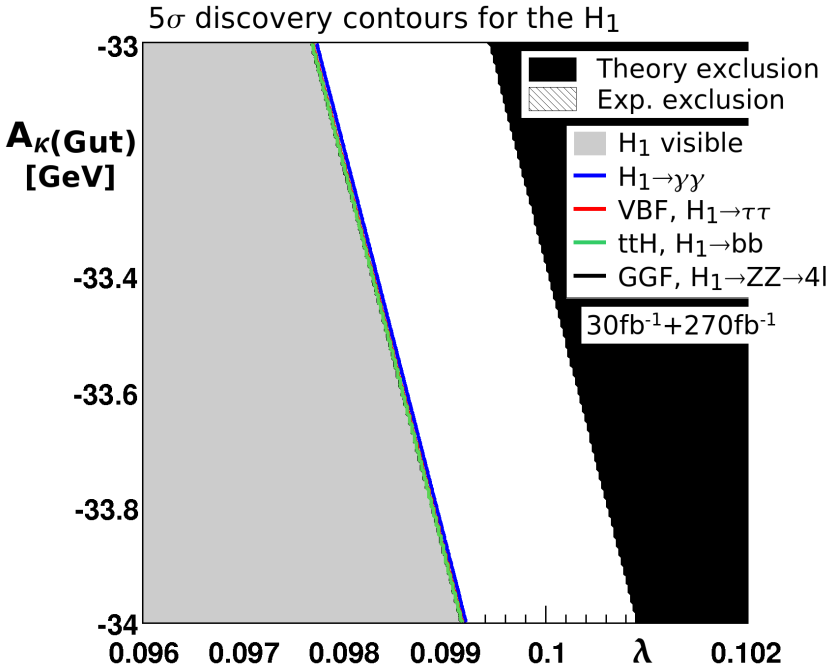

Fig. 7.53: 5σ discovery contours for the H_1 in the cNMSSM Scenario, in the restricted $\lambda/A_{\kappa(\mathrm{GUT})}$ plane with 30+270 fb^{-1}. Systematic uncertainties are not included. The H_1 is observable in the grey region. For details on how this plot must be read, see Fig. 7.1.

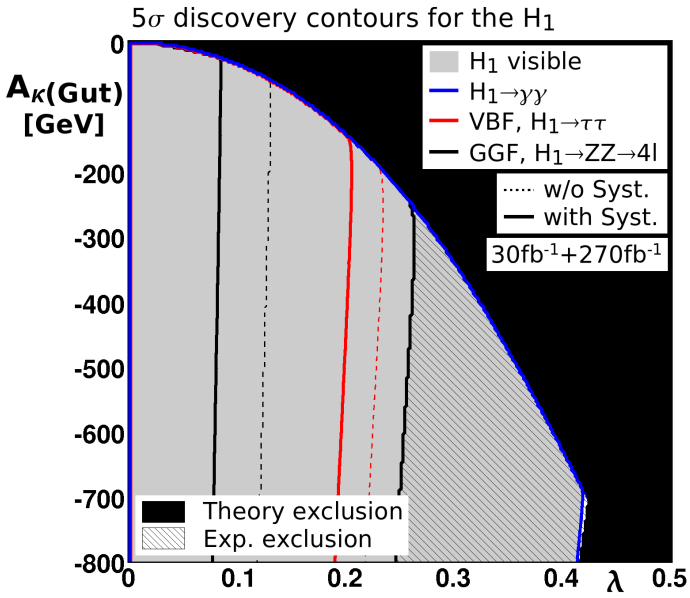

Fig. 7.54: 5σ discovery contours for the H_1 in the cNMSSM Scenario, $\lambda/A_{\kappa(\mathrm{GUT})}$ plane with 30+270 fb^{-1}. Systematic uncertainties are taken into account. For comparison, the results without systematic uncertainties are given by the dotted lines. The H_1 is observable in the grey region. For details on how this plot must be read, see Fig. 7.1.

7.2.4 The cNMSSM Scenario

7.2.4.1 The $\lambda/A_{\kappa(\mathrm{GUT})}$ benchmark plane

In this parameter plane of the constrained NMSSM, the H_1 has a mass of about 114 to 120 GeV in the unexcluded region. It is Standard Model-like in large parts of the parameter plane, but at small A_κ, there is a narrow band with very low A_1 masses, so that the $H_1 \to A_1A_1$ decay is dominant. The other Higgs bosons either have very large masses or heavily reduced couplings.

Discovery potential for the NMSSM Higgs bosons The discovery contour for the H_1 is shown in Fig. 7.52. The ($tt H_1$, $H_1 \to b\bar{b}$) and the $H_1 \to \gamma\gamma$ searches cover nearly the entire parameter plane. The H_1 is also visible in the (VBF, $H_1 \to \tau\tau$) search for H_1 masses larger than 116 GeV, and in the (GGF, $H_1 \to ZZ \to 4l$) channel for masses larger than 120 GeV. This behavior is also expected for a Standard Model Higgs boson. As all other Higgs bosons are either too heavy or have reduced couplings in this plane, the H_1 is the only Higgs boson which is observable in this scenario.

In the narrow band where $H_1 \to A_1A_1$ decays are dominant, no NMSSM Higgs boson will be observable with the current ATLAS search strategies (Fig. 7.53). Accordingly, new search strategies are needed in this region. A similar phenomenology was already discussed for the Light A_1 Scenario.

Discovery potential with systematic uncertainties When systematic uncertainties are included, the ($tt\phi$, $\phi \to b\bar{b}$) channel is not observable any longer, as it is the case for all scenarios discussed before. However, nearly the entire plane is still covered by the $H_1 \to \gamma\gamma$ search (Fig. 7.54). In contrast, the (VBF, $H_1 \to \tau\tau$) search only yields significance above 5σ for H_1 masses larger than about 118 GeV, and the (GGF, $H_1 \to ZZ \to 4l$) channel for masses larger than about 121 GeV.

Discovery potential with 30 fb^{-1} In this plane, only the vector boson fusion, $H_1 \rightarrow \tau\tau$ channel will be observable with 30 fb^{-1}.

7.2.4.2 Summary of the cNMSSM Scenario This parameter plane is added to the set of benchmark planes to provide an example of Higgs boson physics in a constrained model of the NMSSM. The investigated parameter plane can be divided into a region with a purely Standard Model-like behavior, where only the H_1 is observable, and a region with dominant $H_1 \rightarrow A_1A_1$ decays, where no Higgs boson discovery is possible with the current ATLAS search strategies.

7.3 Conclusions on the discovery potential for NMSSM Higgs bosons

A detailed evaluation of the ATLAS discovery potential for NMSSM Higgs bosons within seven benchmark planes of four different scenarios is performed. With 300 fb^{-1} and when systematic uncertainties are neglected, at least one light, neutral Higgs boson is found to be observable in unexcluded regions without a light A_1. In addition, the light neutral scalar is observable in regions where the $H_{1/2} \rightarrow A_1A_1$ branching ratio is smaller than about 40% to 60%, depending on the Higgs boson mass and the relevant couplings. Depending on the scenario, the observable Higgs boson may be the H_1 or the H_2. In some regions of the parameter space, such a discovery is only possible due to additional contributions from one or two other neutral Higgs bosons with similar masses to the mass window of the respective analysis channel. If the NMSSM with parameters leading to a large $H_{1/2} \rightarrow A_1A_1$ branching ratio is realized in nature, new searches for the decay chains $H_{1/2} \rightarrow A_1A_1 \rightarrow b\bar{b}b\bar{b}/\tau\tau b\bar{b}$, $H_{1/2} \rightarrow A_1A_1 \rightarrow 4\tau$ and $H_{1/2} \rightarrow A_1A_1 \rightarrow 4\gamma$ are needed to guarantee the discovery of at least one Higgs boson at the LHC. A possible analysis for the $H_{1/2} \rightarrow A_1A_1 \rightarrow 4\tau$ case will be presented in Chap. 8.

When systematic uncertainties are included, the otherwise quite important $tt\phi$, $\phi \rightarrow b\bar{b}$ search does not yield significances above 5σ. Then, Higgs boson discovery in regions with reduced couplings of an otherwise Standard Model-like Higgs boson is challenging if its mass is about 115 GeV. In such a region, a good understanding of systematic uncertainties, a combination of different search channels and, if possible, an extension of the vector boson fusion searches also to the high luminosity case might help. For larger masses, reduced couplings do not pose problems for the discovery of at least one NMSSM Higgs boson. There is also a region where only the light charged, but no neutral Higgs bosons, are discoverable.

In some regions of the parameter space, two or three Higgs bosons are observable also when systematic uncertainties are taken into account. This is especially the case for large $\tan\beta$ values. More than three mass resonances from NMSSM Higgs bosons are not observable simultaneously within the benchmark planes considered in this thesis. For the separation of nearby mass peaks of the neutral Higgs bosons, the $\phi \rightarrow \gamma\gamma$, $\phi \rightarrow ZZ \rightarrow 4l$ and $\phi \rightarrow \mu\mu$ search channels are most important due to their good mass resolutions.

When only 30 fb^{-1} of integrated luminosity are used, the vector boson fusion analyses are crucial for the discovery of a light neutral Higgs boson. In numerous parameter planes, these channels are the only means for an early Higgs boson discovery. Moreover, these channels have a stable discovery potential also in the presence of systematic uncertainties if $H_{1/2} \rightarrow A_1A_1$ decays are not allowed. At large $\tan\beta$, also the ($bb\phi$, GGF, $\phi \rightarrow \tau\tau$) mode contributes. The charged Higgs boson searches are also relevant. However, in parts of the parameter space, no Higgs boson will be observable with a data volume of 30 fb^{-1}. Yet, for favorable parameter combinations, the discovery of two or three different mass resonances will already be possible with 30 fb^{-1}.

The $H^{\pm} \rightarrow W^{\pm}h$ channel is not considered in this study for technical reasons[10], although

[10] For the necessary two-dimensional interpolation of the signal efficiencies, background numbers etc. with $M_{H^{\pm}}$ and M_h, at least three separate mass combinations would be needed as an input. Unfortunately, Ref. [72] provides

Refs. [72, 122] suggest that it has a good discovery potential for the NMSSM, especially for low $\tan\beta$ and $M_{H^\pm} \approx 160$ GeV. In such regions, this channel might allow for the observation of the charged Higgs bosons and an additional neutral Higgs boson, that would otherwise be more difficult. However, to fill the observed gaps in the discovery potential for the discussed scenarios i.e. for the Reduced Couplings Scenario and Light A_1 Scenario, this channel is not helpful, as either the $H^\pm \to W^\pm h$ decay is forbidden in the relevant region, or the mass of the charged Higgs bosons is too large for a discovery.

If the mass resonances of more than one Higgs boson or of the charged Higgs bosons are observed experimentally, physics beyond the Standard Model with its one, neutral Higgs boson can be established. However, a distinction of the NMSSM from other models, such as the MSSM, is often challenging. Also in the case when only one neutral mass resonance is found, the distinction between the SM, MSSM and NMSSM is of interest. The discrimination of these models needs complex studies, which are beyond the scope of this thesis. Approaches for distinguishing the NMSSM from the MSSM with the help of the ILC can for example be found in Refs. [44, 123].

only two mass combinations.

8. A sensitivity study for the vector boson fusion process, $H_1 \rightarrow A_1 A_1 \rightarrow 4\tau \rightarrow 4\mu + 8\nu$

As a result of the evaluation of the discovery potential for NMSSM Higgs bosons at the ATLAS experiment in Chap. 7, it is found that the currently available ATLAS search strategies that are designed for Standard Model and MSSM Higgs bosons cannot completely cover the parameter space of the NMSSM. Especially, $H_{1/2} \rightarrow A_1 A_1$ decays that are dominant in sizeable parts of the NMSSM parameter space are not looked for by these searches. Accordingly, the SM and MSSM searches are only sensitive to a light scalar Higgs boson of the NMSSM if its branching ratio to a pair of pseudoscalars, $H_{1/2} \rightarrow A_1 A_1$, is smaller than about 40-60%. Therefore, it is rewarding to investigate the possibility to directly observe the $H_{1/2} \rightarrow A_1 A_1$ decay at the LHC. As this would provide evidence for the existence of two yet unknown particles, such an observation would be a clear evidence for physics beyond the Standard Model.

Several promising searches for a scalar Higgs boson decaying to a pair of light pseudoscalars have been suggested. The $H_1 \rightarrow A_1 A_1 \rightarrow 2\tau 2b$ channel is proposed in Refs. [97, 124] and has been studied by the ATLAS collaboration [125]. The H_1 is here assumed to be produced in vector boson fusion as this allows for good background suppression due to the clear signature. However, this channel is very sensitive to the shape of possibly large tails in the $b\bar{b}\tau\tau$ invariant mass distribution of the $t\bar{t}$ background process and thus experimentally challenging.

In Ref. [126], a search for the WH, $H_1 \rightarrow A_1 A_1 \rightarrow 4b$ process is suggested. Here, the $W^{\pm}$ boson which is produced in association with the Higgs boson has to decay leptonically to provide a trigger signature and to suppress large QCD background processes. An excellent b-tagging performance is essential. This channel has not been studied by the ATLAS collaboration so far.

Furthermore, it can be searched for the $H_1 \rightarrow A_1 A_1 \rightarrow 4\gamma$ decay chain. However, experience from the Tevatron suggests that it is challenging to separate the four photons of the final state, as they are produced in very collimated pairs [127].

The work presented here is the first study of the vector boson fusion, $H_1 \rightarrow A_1 A_1 \rightarrow 4\tau$ process with the ATLAS experiment. Although the vector boson fusion production cross section is usually about an order of magnitude smaller than the gluon fusion cross section, vector boson fusion production is studied here since its clear signature helps to suppress the background processes. Presently, only the case that all four τ-leptons decay to muons is considered. In contrast to electrons or τ-jets, collimated muon pairs as they are expected in this channel can easily be separated and are able to fulfill standard isolation requirements.

The mass of the pseudoscalar Higgs boson must be very small ($\lesssim 10$ GeV) to obtain a sizeable cross section for this process. Corresponding regions are included in the Light A_1 Scenario and the cNMSSM Scenario as described in Chap. 6. There are also several benchmark points from Refs. [47, 99] that lead to such a phenomenology.

The aim of this study is to give an estimation of the discovery potential for this search channel. The fast ATLAS detector simulation ATLFAST [54] is used. At first, the main features of the signal and possible background processes are described. A special emphasis is put on the Higgs boson mass reconstruction. Finally, a cut analysis for the selection of signal events is presented.

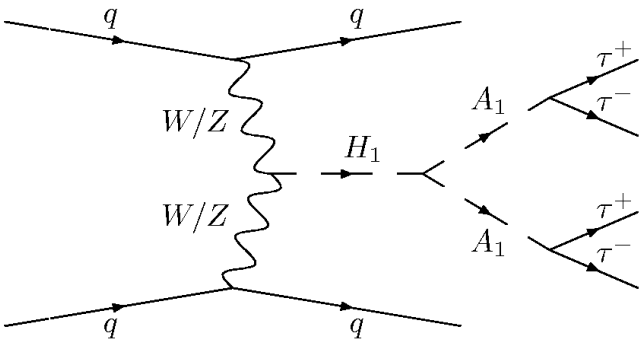

Fig. 8.1: The signal process: The scalar Higgs boson H_1 is produced in vector boson fusion and decays to a pair of light pseudoscalars with dominant decays to τ-leptons.

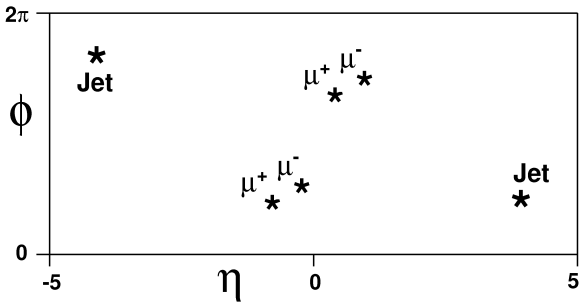

Fig. 8.2: The typical signature of the signal process. The decay products of the τ-leptons, here four isolated muons, form close pairs in the central region of the detector. Often, one of the muons is not detected. Moreover, the two tagging jets lie in the forward and backward region of the detector. There is typically no considerable jet activity in the central region.

8.1 The signal process

The signal process (Fig. 8.1) features the typical signature of a vector boson fusion process (Fig. 8.2). The two tagging jets lie in the forward and backward hemispheres of the detector. Additional jet production between the tagging jets is suppressed. As the detectability of these typical features depends on the presence of pile-up, it is assumed that only 30 fb^{-1} of integrated luminosity collected during the low-luminosity phase of the LHC are available for this search. The decay products of the Higgs bosons typically lie in the central detector region. As the τ-leptons decay already in the beam pipe due to their short lifetime of $2.9 \cdot 10^{-13}$ s [14], only their decay products reach the detector. The decay products of the two τ-leptons from the same pseudoscalar Higgs boson typically lie close to each other in the detector. The neutrinos from the τ-decays give rise to a large missing momentum.

In the experimentally most simple case $H_1 \to A_1 A_1 \to 4\tau \to 4\mu + 8\nu$, all four τ-leptons decay to muons. Only this case is considered here for several reasons. Since muons do not deposit considerable energy in the calorimeters, also muons from a very close pair can be classified as isolated[1]. Decay channels including electrons or hadronic τ-jets need more consideration, because considerable energy can be deposited in the calorimeters and might destroy the isolation

[1] In ATLFAST, a muon is defined as isolated if no energy clusters (formed by a cone jet algorithm with R=0.4) are found in the calorimeter within a radius of R=0.4 around the muon, and when the sum of the transverse energy of all calorimeter cells within a radius of R=0.2 around the muon is less than 10 GeV.

M_{H} [GeV]	100	105	110	115	120	125	130	135	140
VBF cross section [pb]	5.03	4.82	4.62	4.42	4.28	4.09	3.97	3.85	3.65

Tab. 8.1: The vector boson fusion production cross section for a light scalar Higgs boson with Standard Model-like couplings, for selected Higgs boson masses [66, 67].

	Typical cross sections for VBF, $H_1 \to A_1A_1 \to 4\tau \to 4\mu + 8\nu$	
$M_{\mathrm{H_1}}$	$M_{\mathrm{A_1}} < 10$ GeV	$M_{\mathrm{A_1}} > 10$ GeV
100 GeV	3.33 fb	0.026 fb
105 GeV	3.19 fb	0.025 fb
110 GeV	3.05 fb	0.024 fb
115 GeV	2.91 fb	0.023 fb
120 GeV	2.83 fb	0.022 fb
125 GeV	2.70 fb	0.021 fb
130 GeV	2.62 fb	0.021 fb
135 GeV	2.54 fb	0.020 fb
140 GeV	2.41 fb	0.019 fb

Tab. 8.2: Estimates for typical NMSSM signal cross sections, assuming BR($H_1 \to A_1A_1$)= 90%. For M_{A}<10 GeV, BR($A_1 \to \tau\tau$) is assumed to be 90%, for M_{A}>10 GeV, to be 8%.

of nearby muons. The possibility to separate nearby electrons and/or τ-jets or to find non-isolated muons inside a shower from an electron or τ-jet needs careful study with the full ATLAS detector simulation.

Furthermore, muons show a high identification efficiency ($\gtrsim$ 90% for $p_T > 6$ GeV) [6] and a good momentum resolution (see Tab. 3.1). An identification efficiency for the leptons is not included in ATLFAST. Therefore, an overall probability of 90% for each muon to be found is assumed in this study. The η and p_T dependence of the identification efficiency is neglected, as it is quite uniform for muons with $p_T > 5$ GeV with the exception of a degradation of the performance at $\eta \approx 0$ [6]. This identification probability is included in all figures and numbers shown in this chapter.

However, as the branching ratio of the decay $\tau \to \mu\nu_\tau\bar{\nu}_\mu$ is only 17.36% [14], the total signal cross section is heavily reduced by requiring four muons. The vector boson fusion production cross section of a light scalar with a mass of 115 GeV and Standard Model-like couplings is 4.42 pb (Tab. 8.1). The branching ratio of the $H_1 \to A_1A_1$ decay is assumed here to be 90%, which, judging from the benchmark scenarios in Chap. 6, is a typical value if λ and κ are not too small. If the A_1 is light enough ($M_{\mathrm{A}} \lesssim 10$ GeV) its branching ratio to a pair of τ-leptons, $A_1 \to \tau\tau$ is typically $\sim$ 90%. With the above numbers, 2.9 fb is then a typical cross section for the $H_1 \to A_1A_1 \to 4\tau \to 4\mu + 8\nu$ signal process (Tab. 8.2). This corresponds to only $\sim$ 90 produced events for a data volume of 30 fb^{-1}. It is therefore crucial to efficiently suppress the partly much more prevalent background without removing too many signal events. If M_{A} is larger than about 10 GeV, the $A_1 \to b\bar{b}$ decay is dominant and the cross section of the signal process is too small to be observable (less than one expected event for 30 fb^{-1}).

As can be seen from Tab. 8.1, the vector boson fusion production cross section is largest for small masses of the scalar Higgs boson. It can thus be expected that this channel is most important for a light scalar Higgs boson, as for example for the H_1 of the NMSSM which has to be lighter than about 145 GeV [43]. The exact cross section at a specific parameter point

may vary from the values in Tab. 8.2. In fact, in the parameter regions of the Light A_1 and the cNMSSM Scenario where the $A_1 \rightarrow \tau\tau$ decay is dominant, its branching ratio is about 90% to 93% and the $H_1 \rightarrow A_1A_1$ branching ratio can be as large as 98%, so that the actual production cross sections in these scenarios are slightly larger than the listed ones.

The transverse momentum of the stable leptons in this channel is rather low, since a large part of the energy is carried away by the eight neutrinos in the final state. Therefore, not in all cases all four muons will be identified. In order to keep a sizeable signal rate, only three muons will be required by the analysis. It is therefore possible, at least in principle, that events where only three of the four τ-leptons decay to muons, and the forth τ-lepton decays to an electron or to hadrons, pass the selection criteria. However, the produced shower particles must have sufficiently low energy not to spoil the isolation of the nearby muon. In principle, the overall cross section for the $H_1 \rightarrow A_1A_1 \rightarrow 4\tau \rightarrow 1e+3\mu+8\nu$ channel is a factor of four larger than the cross section of the $H_1 \rightarrow A_1A_1 \rightarrow 4\tau \rightarrow 4\mu+8\nu$ channel, and the $H_1 \rightarrow A_1A_1 \rightarrow 4\tau \rightarrow h+3\mu+7\nu$ cross section is even a factor of $\sim$15 larger. These additional contributions to the signal might be significant, however, as the invoked isolation issues are not well described by ATLFAST, they are neglected here to obtain a conservative estimate.

In order to significantly reduce the impact of fake muons, which are not described adequately by ATLFAST, a minimum p_T for all muons of 6 GeV is required. In addition, the muons must lie inside the pseudorapidity coverage $|\eta| < 2.5$ of the Inner Detector. According to Ref. [6], fake muons from cavern background and pile-up effects can be efficiently rejected by requiring $p_T > 5$ GeV and by using a muon identification algorithm which combines the information from the Inner Detector and the Muon Spectrometer. However, it would be useful to study the influence of the muon fake rate on the Higgs boson search in this channel with the full detector simulation.

In spite of the eight neutrinos in the final state and the possibility that one muon might remain unrecognized, it is still possible to reconstruct the mass of the scalar Higgs boson with the help of the collinear approximation [80] which is also used for mass reconstruction in the VBF, $H \rightarrow \tau\tau$ channel [62]. The method for mass reconstruction will be described in detail in Chap. 8.4.

Some aspects of the kinematics of the signal process depend on both the masses of the scalar H_1 and the pseudoscalar A_1 (Fig. 8.3). The number of muons that can be detected in the event increases with increasing mass of the scalar Higgs boson, as its mass adds to the energy that is shared between its decay products. Due to their larger p_T, they more easily pass the required 6 GeV threshold. Also for a low mass of the pseudoscalar Higgs boson, the number of muons found is slightly larger. Nevertheless, even for large scalar Higgs boson masses, only a few events possess three or even four muons. The mean separation of the decay products of the pseudoscalar is sensitive to the mass of the pseudoscalar Higgs boson, as well as the invariant mass of the visible decay products in the detector (Fig. 8.3).

8.2 Background processes

Generally, background processes show a signature similar to the signal. For this study, processes that can have at least three muons in the final state are considered. These can either be produced as isolated muons in decays of vector bosons, or in jets originating from bottom quarks. Only a small fraction of the latter muon type passes the isolation requirements [128].

Two light jets that can replace the tagging jets of the vector boson fusion processes are required in the final state. Also possible b-jets can be misidentified as light jets, as the b-tagging

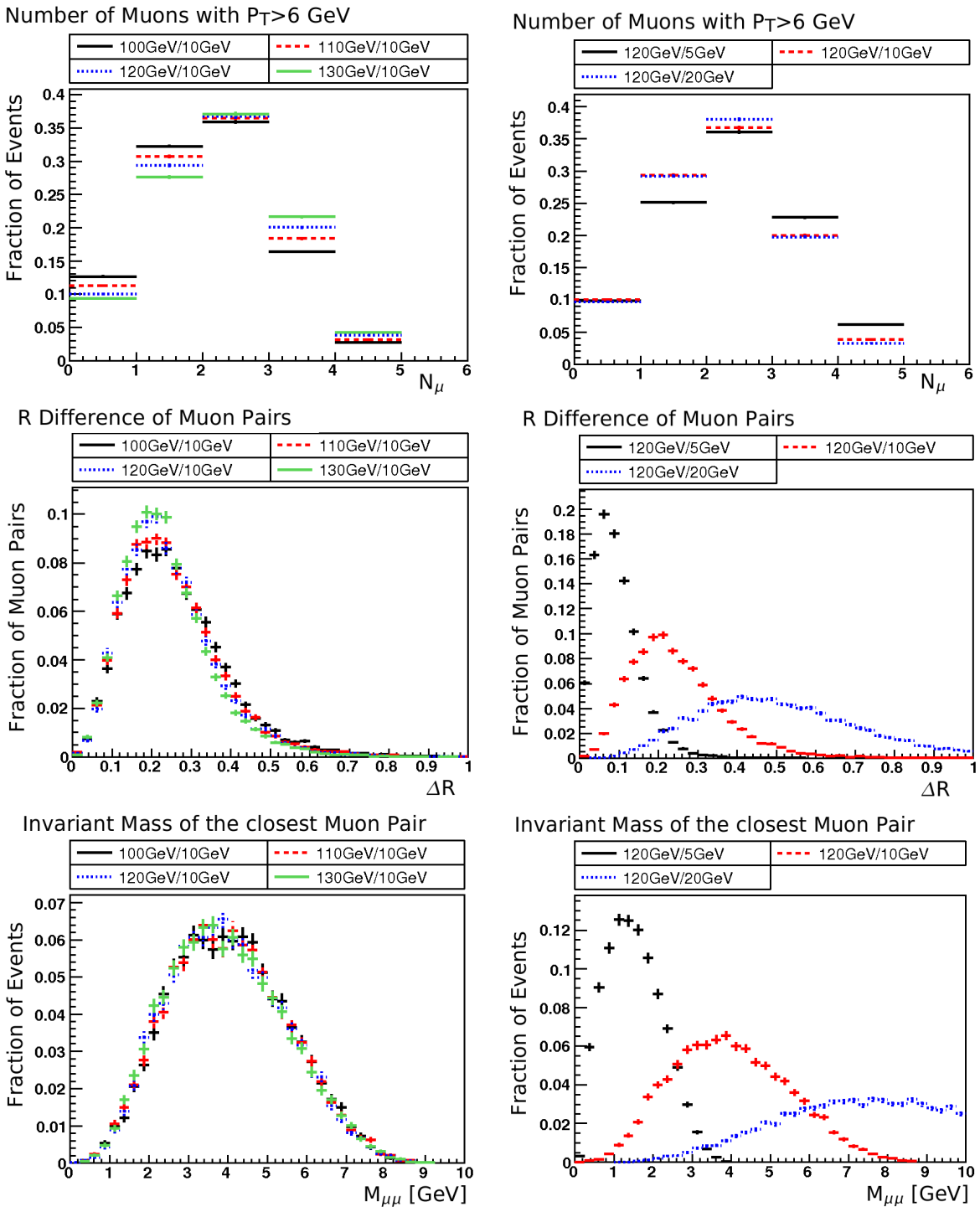

Fig. 8.3: Typical features of the signal process (ATLFAST). Left hand column: For different masses of the scalar boson. Right hand column: For different masses of the pseudoscalar boson. In the legend, the masses are given in the form $M_{\mathrm{H}}/M_{\mathrm{A}}$. First row: Number of muons with $p_T > 6$ GeV found in the events. The identification efficiency of 90% is included. Second row: Difference in R of the muon pairs with the smallest ΔR separation, and if four muons are found, also of the remaining muon pair. Third row: Invariant mass of the muon pair with the smallest ΔR separation in the event.

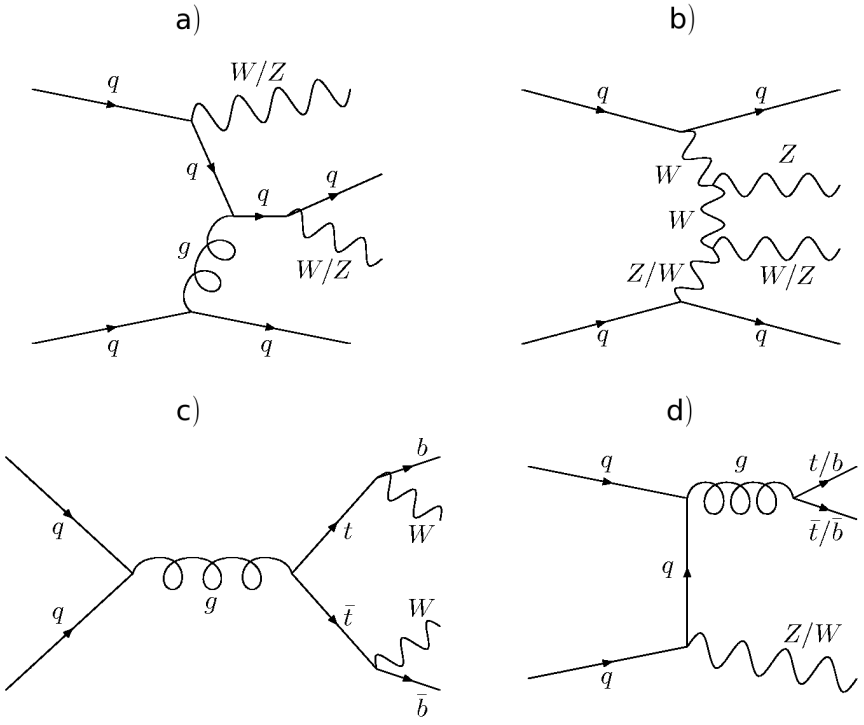

Fig. 8.4: Example Feynman diagrams for background processes to the $H_1 \rightarrow A_1 A_1 \rightarrow 4\tau \rightarrow 4\mu + 8\nu$ channel. a) ZZjj/WZjj (QCD) production b) ZZjj/WZjj (EW) production c) Top quark pair production d) $Zb\bar{b}/Zt\bar{t}$ production.

efficiency in ATLAS is expected to be 60%[2] for a light jet rejection factor of 100 [6]. The missing transverse momentum can either originate from neutrinos from the decay chains of vector bosons and heavy quarks or from a mismeasurement.

The invariant mass of the muon pair originating from the same pseudoscalar Higgs boson is used as a powerful discriminant variable in the cut selection. For signal events, it is lower than the mass of the pseudoscalar Higgs boson, and thus much lower than the Z^0 mass. For background processes including Z^0 bosons, it is therefore crucial to fully consider the Z^0/photon interference.

It is also possible that a final state with three or more leptons occurs in processes including supersymmetric particles. These processes are neglected here. In the following, the most important Standard Model background processes are shortly reviewed.

ZZjj and WZjj production The production of two vector bosons in association with two jets is the main background processes for this search channel. The muons in the final state come from the vector boson decays, either directly via $Z^{(*)}/\gamma^* \rightarrow \mu\mu$ and $W \rightarrow \mu\nu$, or indirectly from τ-leptons, $Z^{(*)}/\gamma^* \rightarrow \tau\tau$ and $W \rightarrow \tau\nu$ with subsequent $\tau \rightarrow \mu + 2\nu$ decay. The missing momentum can originate from neutrinos produced in the W boson and/or τ-lepton decays or from a mismeasurement, as for example for the $Z^{(*)}/\gamma^* \rightarrow \mu\mu$ process that does not include a neutrino.

The most frequent type of events includes two vertices of the strong interaction (Fig. 8.4a). Such processes are denoted as ZZjj/WZjj (QCD) in the following. However, also purely electroweak (EW) processes exist. Although these have a smaller production cross sections than the QCD events, they include diagrams with a structure similar to the vector boson fusion signal

[2] Also for this ATLFAST study, a b-tagging efficiency of 60% is used.

process, as eg. in Fig. 8.4b. Also here, the vector bosons are radiated off the initial quarks which then produce jets that are similar to the vector boson fusion tagging jets. The decay products of the vector bosons are expected to lie in the central region of the detector. Also here, there is no color flow between the quark lines, hence jet production in the central detector region is suppressed. The signature of these events is thus similar to the signal and they are more difficult to suppress than QCD events.

Since the invariant mass of the lepton pairs is small in signal events, as stated earlier, contributions from off-shell Z^*/γ^* bosons are crucial for the correct evaluation of the expected background rate after the cut selection. A lepton pair originating from a Z boson on its mass shell can be very easily removed by an invariant mass cut without losing any signal events.

$t\bar{t}$ production An example diagram for the production of top quark pairs is shown in Fig. 8.4c. In this study, it is assumed that top quarks decay only Standard Model-like, i.e. via t→Wb. Two muons and neutrinos that produce missing momentum can originate from the decays of the two W bosons. The third muon and an additional neutrino can be produced in the decay of a bottom quark. Usually, these muons are not isolated, as they occur in a hadronic showering process, however, due to the huge number of $t\bar{t}$ events, a considerable number of these muons pass the isolation criteria nevertheless. The tagging jets can be faked by b-jets that are misidentified as light jets, or by jets from additional gluon radiation in the event.

$Zt\bar{t}$ and $Wt\bar{t}$ production In these processes, an additional vector boson is produced in association with a top quark pair (Fig. 8.4d). Unlike for $t\bar{t}$ events, here all three required muons can come from vector boson decays.

$Zb\bar{b}$ and $Wb\bar{b}$ production In these processes, one or two muons can originate from the decays of the vector bosons. One or even two muons can then be produced in the b-quark decays. Again, these processes might not be negligible as their cross sections are much larger than the signal cross section. As before, the b-jets in the event or additional jets from gluon radiation might be selected as tagging jets.

8.3 Monte Carlo samples

In this chapter, the Monte Carlo samples that are used for this study are described. While two samples are taken from the common Monte Carlo production of the ATLAS collaboration, most samples had to be produced especially for this study, as the characteristics of the search channel are rather uncommon. For example, samples from the ATLAS production which include Z^0 bosons have a too large generator cut on the invariant mass of the leptons from the Z^0 decay, which is not acceptable here as the Z/γ interference needs to be fully included.

The cross sections, filter efficiencies and numbers of generated events for the background processes are listed in Tab. 8.4. The exact signal cross section depends on the NMSSM model parameters. Information on the signal samples can be found in Tab. 8.3. As next-to-leading order cross sections are not available for all background processes used here, leading order cross sections are used throughout this study.

The program mainly used for matrix element generation in this study is MadGraph / MadEvent [129]. From the common ATLAS Monte Carlo production, also samples produced with MC@NLO [130] and Alpgen [131] are utilized. The CTEQ6L1 (CTEQ6M for MC@NLO) parton distribution functions [132] are used.

MadGraph/MadEvent automatically generates all Feynman diagrams and the corresponding

$H_1 \to A_1 A_1 \to 4\tau \to 4\mu + 8\nu$			
M_H	M_A	Generated events	Total cross section
100 GeV	5 GeV	49,999	3.33 fb
100 GeV	10 GeV	49,996	3.33 fb
110 GeV	5 GeV	49,992	3.05 fb
110 GeV	10 GeV	49,993	3.05 fb
120 GeV	5 GeV	49,996	2.83 fb
120 GeV	10 GeV	49,993	2.83 fb
120 GeV	20 GeV	49,994	0.022 fb
130 GeV	5 GeV	49,998	2.62 fb
130 GeV	10 GeV	49,995	2.62 fb

Tab. 8.3: Leading order cross sections and number of produced events for the signal samples. The cross sections are taken from Tab. 8.2.

Process/Sample	Gen. events	Total cross section	Filtered events	Filter eff.	Filtered cross section	Data volume
ZZjj (QCD), ZZ$\to 4\mu$	116,852	715 fb	20,352	17.4%	125 fb	163 fb^{-1}
ZZjj (QCD), ZZ$\to 2\mu\, 2\tau$	52,255	454 fb	3,049	5.83%	26 fb	115 fb^{-1}
ZZjj (QCD), ZZ$\to 4\tau$	34,999	46 fb	598	1.71%	0.8 fb	760 fb^{-1}
ZZjj (EW), ZZ$\to 4\mu$	20,000	1.4 fb	7,630	38,1%	0.5 fb	14 ab^{-1}
WZjj (QCD), WZ$\to 3\mu\,\nu$	113,684	478 fb	66,266	58.3%	279 fb	238 fb^{-1}
WZjj (QCD), WZ$\to 2\mu\,\tau\,\nu$	71,588	431 fb	11,896	16.6%	72 fb	166 fb^{-1}
WZjj (QCD), WZ$\to 2\tau\,\mu\,\nu$	81,579	248 fb	4,112	5.04%	12.5 fb	329 fb^{-1}
WZjj (QCD), WZ$\to 3\tau\,\nu$	70,524	244 fb	1,114	1.58%	3.9 fb	289 fb^{-1}
WZjj (EW), WZ$\to 3\mu\,\nu$	16,000	2.4 fb	15,189	94.9%	2.3 fb	6.7 ab^{-1}
$t\bar{t}$	34,752,112	482 pb	-	-	482 pb	78 fb^{-1}
Z$t\bar{t}$, Z$\to 2\tau/2\mu$	38,635	134 fb	14,217	36.8%	49 fb	288 fb^{-1}
W$t\bar{t}$, W$\to\tau\nu/\mu\nu$	20,632	146 fb	4,802	23.3%	34 fb	141 fb^{-1}
Z$b\bar{b}$, Z$\to 2\tau/2\mu$	7,023,014	237 pb	114,810	1.63%	3.9 pb	30 fb^{-1}
W$b\bar{b}$, W$\to\tau\nu/\mu\nu/e\nu$	-	29 fb	19,750	20.8%	562 fb	35 fb^{-1}

Tab. 8.4: Numbers of generated and filtered events, leading order cross sections and filter efficiencies for the background samples. On the $t\bar{t}$ sample from the ATLAS production, no filter is applied. For the W$b\bar{b}$ sample, the exact number of generated events is unknown as it originates from the ATLAS production, but can in principle be inferred from the filter efficiency. On this sample, a special filter has been applied (see App. D). The cross sections of different final states of the same process are not equal due to a different behavior of the light muons and heavier τ-leptons at the Z/γ interference. Moreover, the number of diagrams for final states with same-flavour leptons is larger.

program code for a requested final state. The compilation and run times of the code strongly depend on the number of diagrams. A practical limit on the number of diagrams that MadGraph/MadEvent can still handle is approximately 100.000 [133]. To reduce the number of Feynman diagrams included in the generation to a manageable level, a special physics model [136] containing only the relevant couplings is used to produce the signal samples. Several samples for different Higgs boson mass combinations (M_{H} = 100, 110, 120, 130 GeV, M_{A}= 5, 10, 20) GeV were produced. For $M_{\mathrm{A}} \lesssim 4$ GeV, the decay $\mathrm{A}_1 \to \tau\tau$ is kinematically forbidden. For masses $\gtrsim 10$ GeV, the $\mathrm{A}_1 \to \mathrm{b\bar{b}}$ decay is dominant and the total signal cross section drops rapidly. The mass point M_{A}=20 GeV is therefore only added to study the dependence of the signal kinematics on the mass of the pseudoscalar boson.

In order to take into account the Z^0/γ interference in the background samples, final states including muons or τ-leptons, but not W and Z bosons, are specified in MadGraph. The decay of the vector bosons is thus simulated by MadGraph, and also processes with identical final states, but other intermediate particles, are taken into account. To reduce the number of diagrams of a single generation job to a reasonable value, distinct final states of background processes with many diagrams have been generated separately (e.g. 4μjj, $2\mu 2\tau$jj, 4τjj for ZZjj, see Tab. 8.4). Nevertheless, the ZZjj (EW) process still has too many diagrams to be calculable. Therefore, for this process, possible contributions of interacting sea charm quarks from the protons are neglected. Compared to the contributions from up, down and strange quarks, these are believed to be negligible for that process [133]. For all background processes, no diagrams containing Higgs bosons are included.

For ZZjj and WZjj production, the light jets are included in the matrix element generation (in the form of partons), since this is preferable to the generation of these jets in the parton shower, which on average produces jets with too low p_T. Additionally, different generator cuts where applied to the samples. These cuts influence to some extent the selection efficiencies for the different samples. Further details are given in App. D.

For all samples used in this study, Herwig [52] and the included parton shower generator are used for further processing of the samples[3]. The correct treatment of spin correlations in the decays of τ-leptons is ensured by the decay library Tauola [134]. All τ-leptons in the signal process are forced to decay to muons by Tauola. For background processes, possible τ-leptons in the final state could decay in all possible ways. Additional photon radiation is described by Photos [135].

In this study, the detector simulation and the event reconstruction are performed by AtlFast [54]. Filter algorithms are applied to most background samples (see App. D). Herwig, Tauola, Photos, AtlFast and the filter algorithms are called within releases 12.0.6 ($\mathrm{Wb\bar{b}}$) and 12.0.7 (other samples) of the ATLAS software framework Athena.

8.4 Mass reconstruction

The mass of the scalar Higgs boson in the $\mathrm{H}_1 \to \mathrm{A}_1\mathrm{A}_1 \to 4\tau \to 4\mu + 8\nu$ channel can be reconstructed in spite of the presence of eight neutrinos in the final state if the following assumptions hold:

- The mass and the transverse momentum of the scalar Higgs boson are sufficiently large to give a considerable boost to its decay products. The directions of flight of the A_1, of the two τ-leptons from its decay, of the two muons and of the four neutrinos from the τ-lepton

[3] Herwig is preferred to Pythia [51] as it shows a better stability with the interface of the ATLAS software framework to MadGraph. Moreover, this gives a coherent picture, as the samples from the ATLAS production used here are also produced with Herwig. In the ATLAS production, Herwig is generally used for the description of vector boson fusion processes.

decays are then nearly parallel (Fig. 8.6). This is called the collinear approximation [80,81]. In Fig. 8.5, the distance in $R = \sqrt{\eta^2 + \phi^2}$ of the A_1 to the muons from its decay on generator level is shown for different H_1 and A_1 masses. The mean distance is about $\Delta R \approx 0.2$ and thus reasonably small. The collinear approximation improves for large masses of the scalar boson, as the boost of the decay products from the H_1 is then enhanced. In the rest frame of the A_1, the two τ-leptons are emitted back-to-back. The larger the mass of the A_1 is, the less kinetic energy it carries due to energy conservation. Therefore, the boost of the A_1 is smaller when the mass of the A_1 is larger, and the angle between the decay products from the τ-lepton is larger.

- The missing transverse momentum originates exclusively from the neutrinos from the decay chain of the Higgs boson. Additional sources, eg. from mismeasurement or miscalibration, are neglected.
  In Fig. 8.5, the difference of the total p_T of all neutrinos from the decay chain of the H_1 boson on generator level and the reconstructed missing momentum is shown. The resolution of the missing momentum is about 6 GeV for all mass combinations. The reconstructed missing momentum is on average about 1.5 GeV higher than the p_T sum of the neutrinos. This is due to the fact that muons with very low p_T can remain undetected. These muons contribute to the reconstructed missing momentum, but are not taken into account by the p_T sum of the neutrinos. As less muons are detected for low masses of the scalar Higgs boson (see Fig. 8.3), the shift is then more pronounced. The contrary is true for the mass of the pseudoscalar Higgs boson, as the number of detected muons increases with decreasing pseudoscalar mass.

- The masses of the final state leptons and the pseudoscalar A_1 are neglected compared to the typical mass of the scalar Higgs boson. The A_1 can have masses up to 10 GeV if the $A_1 \rightarrow \tau\tau$ decay is dominant. Also samples with an A_1 mass of 20 GeV are considered. Since the approximation of negligible mass does not seem to be well fulfilled for these cases, a degradation of the mass resolution for large A_1 masses is expected.

If the above requirements are met, the Higgs boson mass can be reconstructed from the momentum vectors of the final state muons and the missing momentum vector.

According to the collinear approximation, the direction of flight of the pseudoscalar Higgs boson is parallel to the direction of the visible muons from its decay. In practice, the two muons are never perfectly parallel. Thus, it must be decided which muons come from the decay of the same A_1. To do that, the muon pair with the smallest distance in R is taken as coming from one A_1, the other two, regardless of their distance, are assumed to come from the other A_1. In the frequent case that only three muons are detected in the event, only one muon is assigned to the second A_1. Muons that are assigned to the same A_1 are then combined by addition of their four-momentum vectors to a dimuon object with momentum $\vec{p}_{\mu\mu}$. The direction of the momentum of this object or, if only three muons are found in the event, of the visible single muon is taken to be the direction of flight of the corresponding pseudoscalar A_1.

To reconstruct also the absolute value of the momentum of the pseudoscalar, the momentum sum of the four neutrinos from its decay needs to be determined. According to the collinear approximation, all the neutrinos should have the same direction of flight, which is assumed to be identical to the direction of the momentum of the corresponding dimuon or single muon. The known p_{Tmiss} vector can then be projected on this direction (Fig. 8.6). The projection gives the total transverse momentum of all neutrinos from the decay of the pseudoscalar boson. Although the missing momentum vector has an unknown component in z-direction, the z-component of the neutrino momentum can be calculated from the requirement that the neutrino momentum must

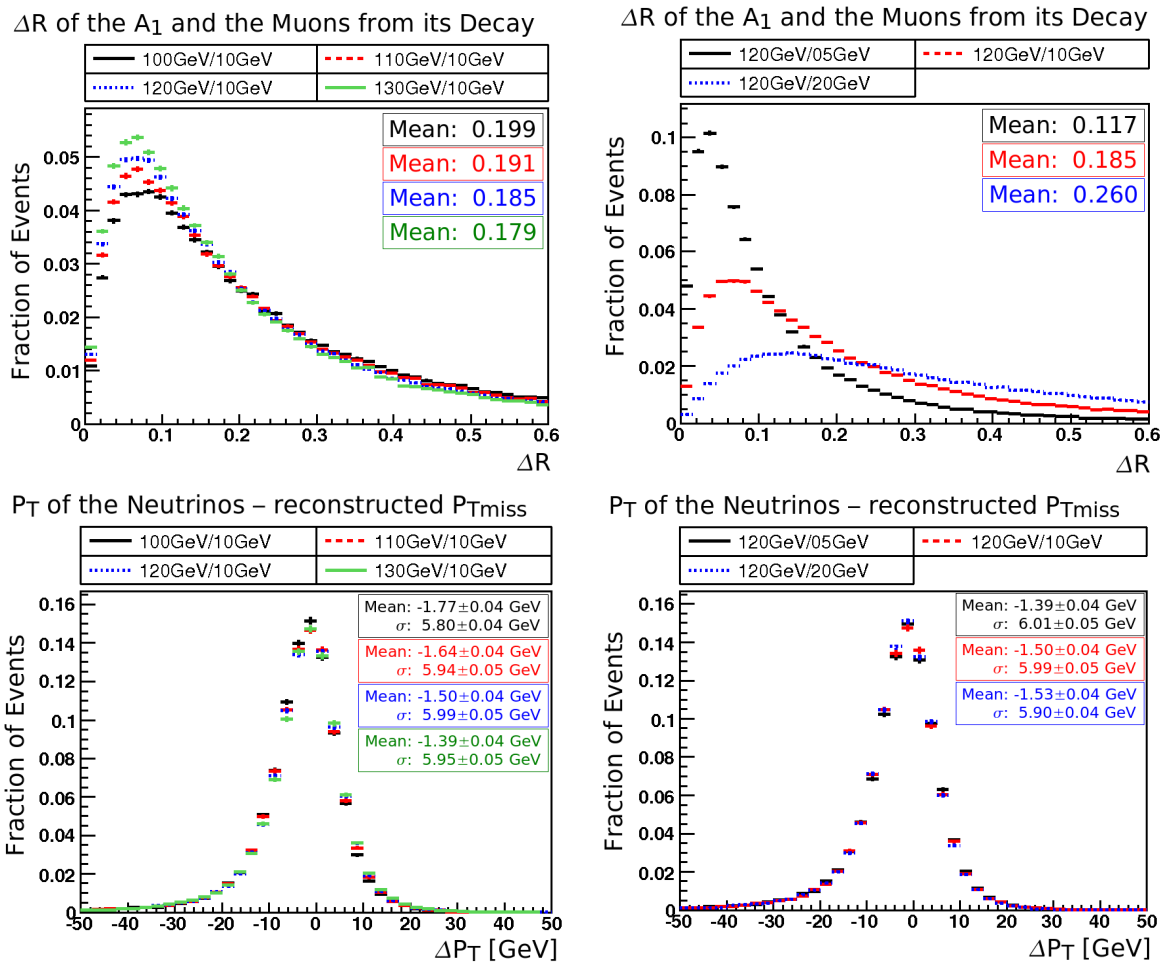

Fig. 8.5: Figures on the quality of the assumptions made for the mass reconstruction. Left hand column: For different masses of the scalar boson. Right hand column: For different masses of the pseudoscalar boson. In the legend, the masses are given in the form $M_{\mathrm{H}}/M_{\mathrm{A}}$. First row: ΔR separation between the true A_1 and the muons from its decay. Second row: Total transverse momentum of the neutrinos from the A_1 decay minus the reconstructed missing transverse momentum.

have the same direction as the dimuon or single muon vector, whose z-component is measured in the detector. The total momentum vector of the four neutrinos can then be added to the dimuon vector to obtain the momentum vector of the pseudoscalar Higgs boson. The invariant mass of the two pseudoscalar bosons corresponds to the scalar Higgs boson mass.

To formulate this algorithm mathematically, the quantities x_1 and x_2 are defined as the visible muons' energy fraction of the original pseudoscalar's total energy:

$$x_1 = E_{\mu\mu_1}/E_{\mathrm{A}_{1,1}}, \qquad x_2 = E_{\mu\mu_2}/E_{\mathrm{A}_{1,2}} \tag{8.1}$$

The subscript $\mu\mu$ denotes the properties of the dimuon system. For simplicity, it is here and in the following also used for the case that only a single muon can be assigned to one pseudoscalar. As the masses of the muons and the pseudoscalar Higgs bosons A_1 are assumed to be negligible and the directions of muons, neutrinos and pseudoscalars to be the same, x_1 and x_2 also give the corresponding fraction of the total momentum and of the single momentum components of the muons. By definition, only values from zero to one are physically meaningful.

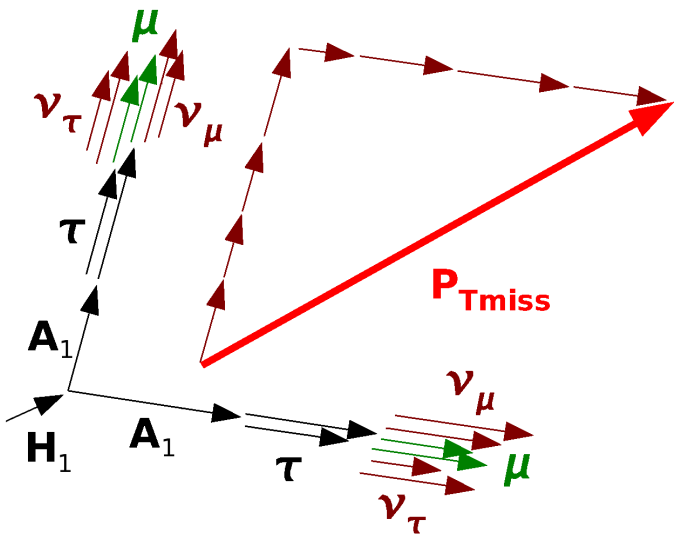

Fig. 8.6: Momentum diagram for the collinear approximation. The pseudoscalar bosons A_1 are boosted strongly so that their decay products are approximately parallel to their original directions. The missing transverse momentum vector can be projected on the direction of the visible decay products, i.e. the muons, to obtain the momentum of the neutrinos from the decay chain of each pseudoscalar boson.

Now, the momentum conservation in the transverse plane is exploited:

$$\vec{p}_{T\mathrm{A}_{1,1}} + \vec{p}_{T\mathrm{A}_{1,2}} = \frac{\vec{p}_{T\mu\mu_1}}{x_1} + \frac{\vec{p}_{T\mu\mu_2}}{x_2} = \vec{p}_{T\mu\mu_1} + \vec{p}_{T\mu\mu_2} + \vec{p}_{Tmiss} \tag{8.2}$$

From this, x_1 and x_2 can be extracted:

$$x_1 = \frac{p_{x\mu\mu_1} p_{y\mu\mu_2} - p_{y\mu\mu_1} p_{x\mu\mu_2}}{p_{y\mu\mu_2} p_{xmiss} - p_{x\mu\mu_2} p_{ymiss} + p_{x\mu\mu_1} p_{y\mu\mu_2} - p_{y\mu\mu_1} p_{x\mu\mu_2}} \tag{8.3}$$

$$x_2 = \frac{p_{x\mu\mu_1} p_{y\mu\mu_2} - p_{y\mu\mu_1} p_{x\mu\mu_2}}{p_{x\mu\mu_1} p_{ymiss} - p_{y\mu\mu_1} p_{xmiss} + p_{x\mu\mu_1} p_{y\mu\mu_2} - p_{y\mu\mu_1} p_{x\mu\mu_2}} \tag{8.4}$$

In Fig. 8.7, the reconstructed x_1 and x_2 are shown. As expected, these quantities lie in the physical range between zero and one for most events. For large masses of the pseudoscalar Higgs boson A_1, the distribution broadens slightly as the collinear approximation deteriorates.

The invariant mass of the pseudoscalar Higgs boson pair, i.e. the scalar Higgs boson mass, is then given by

$$\begin{aligned} m^2_{\mathrm{A}_1\mathrm{A}_1} &= (p_{\mathrm{A}_{1,1}} + p_{\mathrm{A}_{1,2}})^2 \\ &= 2\left(p_{\mathrm{A}_{1,1}} \cdot p_{\mathrm{A}_{1,2}} + m^2_{\mathrm{A}_1}\right) \\ &= 2\left(\frac{p_{\mu\mu_1} \cdot p_{\mu\mu_2}}{x_1 x_2} + m^2_{\mathrm{A}_1}\right) \\ &= \frac{m^2_{\mu\mu,\mu\mu} - m^2_{\mu\mu_1} - m^2_{\mu\mu_2}}{x_1 x_2} + 2m^2_{\mathrm{A}_1} \end{aligned} \tag{8.5}$$

Here, $m_{\mu\mu,\mu\mu}$ denotes the 4-muon invariant mass of the two dimuon objects. Since the mass of the pseudoscalar is assumed to be negligible, the mass of the dimuon objects, $m_{\mu\mu}$, should also be negligible. It then follows

$$m_{\mathrm{A}_1\mathrm{A}_1} \approx \frac{m_{\mu\mu,\mu\mu}}{\sqrt{x_1 x_2}} \tag{8.6}$$

The performance of the mass reconstruction is shown in Fig. 8.7, both on generator and on ATLFAST level. The mass resolution on generator level is about 6.8% to 10% for masses of the pseudoscalar Higgs boson from 5 to 10 GeV and worsens for decreasing scalar boson mass and increasing pseudoscalar boson mass, as then, the collinear approximation is less valid. Also a mass shift of several GeV can be observed. It can to some extent be explained by the neglected mass of the pseudoscalar Higgs boson. On reconstruction level, the mass resolution degrades slightly due to the experimental resolution of the muon momenta, and above all, the missing transverse momentum. The mass resolution is now about 8.7% to 11.3% for $M_{\mathrm{A}} = 5$ to 10 GeV.

As can be seen from Eq. 8.5, the mass shift is not only small for negligible A_1 mass, but also if the A_1 is given by the invariant mass of the dimuon vector divided by the geometric mean of the x_1 and x_2:

$$m_{\mathrm{A}_1} \approx \frac{m_{\mu\mu_{1,2}}}{\sqrt{x_1 x_2}} \tag{8.7}$$

Fig. 8.8 shows this quantity for different masses of the pseudoscalar Higgs boson. The mean value is approximately equal to the mass of the pseudoscalar boson, so that the mass shift due to the neglected A_1 mass is canceled to some extend by these terms. It is possible to calculate the quantity $\frac{m_{\mu\mu_{1,2}}}{\sqrt{x_1 x_2}}$ for all muon pairs found, and to include it in the mass reconstruction. The result of such an approach is shown in Fig. 8.9. The mass resolution is unchanged by this, whereas the shift of the mean value is enlarged by 0.7 GeV. This is to be expected as the additional terms are, according to Eq. 8.5, subtracted from the $\frac{m^2_{\mu\mu,\mu\mu}}{x_1 x_2}$ term. As the overall performance of the algorithm is not improved by this approach, it is not pursued here any further.

As the invariant mass of one A_1 should be given by only the muons and neutrinos of its decay, but not by the neutrinos from the decay of the other A_1 in the event, a more physical estimation of the A_1 mass is given by

$$m_{\mathrm{A}_1} \approx \frac{m_{\mu\mu_{1,2}}}{x_{1,2}} \tag{8.8}$$

This quantity becomes equal to Eq. 8.7 if $x_1 = x_2$. As can be seen in Fig. 8.8, the mean value of this quantity is smaller than for the quantity from Eq. 8.7, however, the distribution is not as broad and features an edge near the nominal A_1 mass. Studying the potential of this quantity for the measurement of the A_1 mass might be promising.

Furthermore, the observed shift of the reconstructed mass is partly due to the large fraction of events where one muon escapes undetected. In principle, such a muon should contribute to the missing momentum and thus not produce a shift. However, ATLFAST has no muon identification included, such that a probability of 90% for detecting muons with $p_T > 6$ GeV is assumed and applied to the samples after the event reconstruction. Muons that are not taken account due to this identification probability are also not added to p_{Tmiss} by ATLFAST. As a consequence, such a muon is not considered at all in the mass reconstruction. In contrast to that, muons that are not identified by ATLFAST due to a very low p_T are included in the missing momentum. Furthermore, in the real experiment, muons will deposit several GeV of their energy in the calorimeters. This energy will also not be taken into account in the missing momentum calculation if the muon is undetected. Moreover, for the VBF, $\mathrm{H}\rightarrow\tau\tau$ channel, a mass shift has been observed with the full dectector simulation due to a bias in the missing momentum measurement [56]. A similar effect could also apply to this channel. It would therefore be interesting also to study the influence of the undetected muon and the missing momentum on the mass reconstruction with the full detector simulation. Yet the influence of the here observed shift of the reconstructed mass on the number of selected signal events is negligible because only a soft cut on the reconstructed mass is performed in the signal selection (see next chapter).

The described method for the mass reconstruction only works well if the dimuon momentum

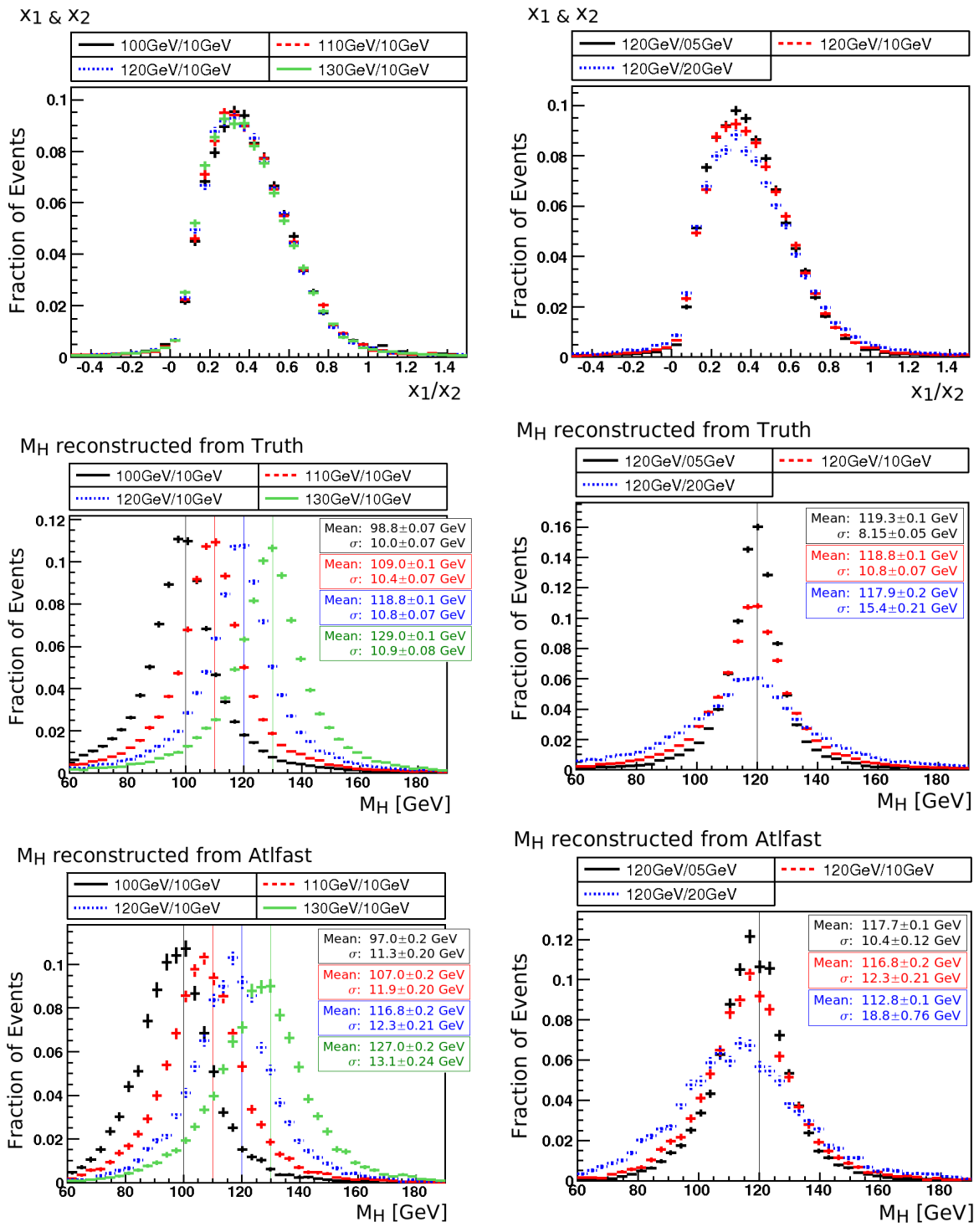

Fig. 8.7: Features of the mass reconstruction. Left hand column: For different masses of the scalar boson. Right hand column: For different masses of the pseudoscalar boson. In the legend, the masses are given in the form $M_{\mathrm{H}}/M_{\mathrm{A}}$. First row: x_1 and x_2. Second row: Mass of the scalar Higgs boson calculated from truth quantities. The shown mass resolution and shift is not influenced by the experimental resolution and thus inherent to the algorithm used. Third row: Mass of the scalar Higgs boson calculated from ATLFAST quantities.

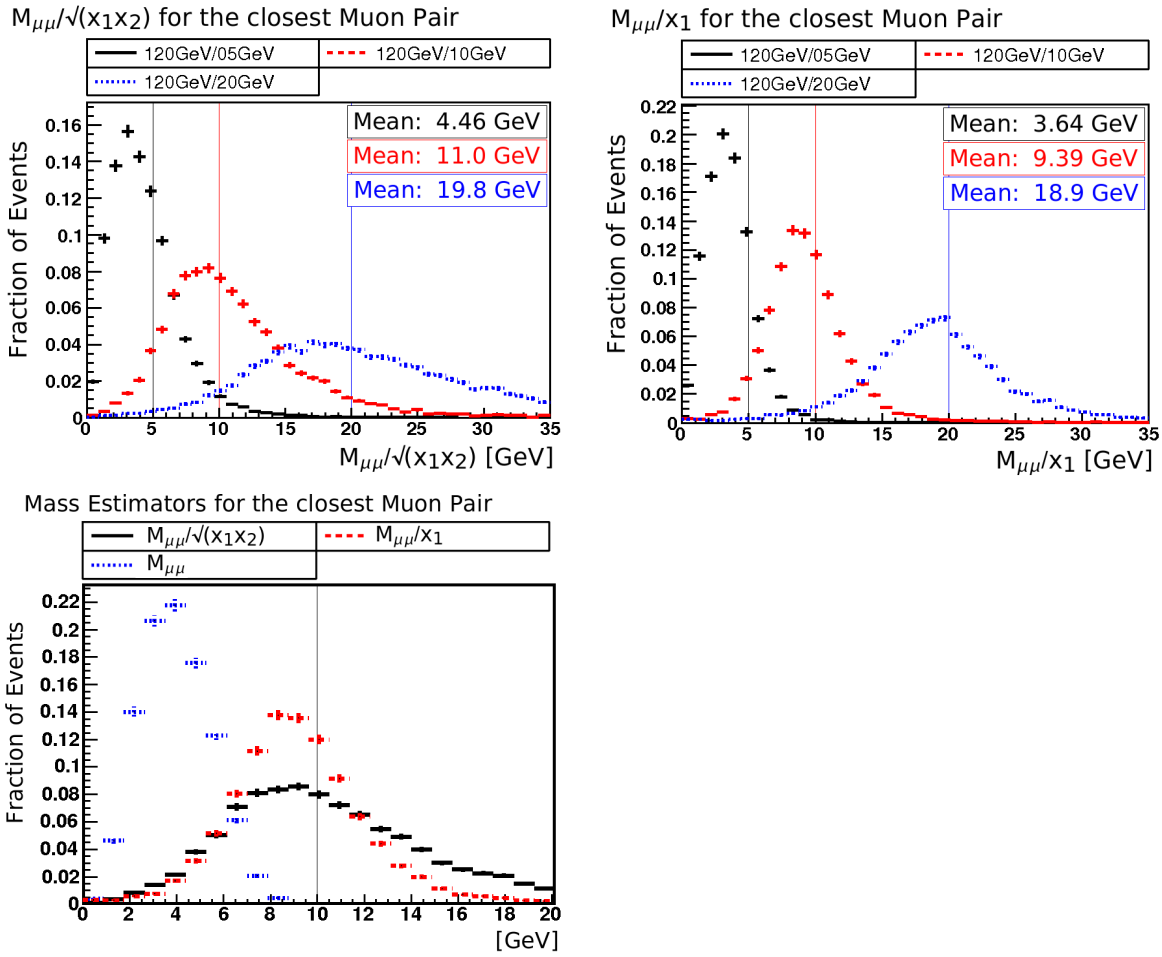

Fig. 8.8: Different quantities for estimating the mass of the pseudoscalar Higgs boson. In the legend, the masses are given in the form $M_{\mathrm{H}}/M_{\mathrm{A}}$. First row, left hand side: $M_{\mu\mu}/\sqrt{x_1x_2}$ for all found muon pairs for different masses of the pseudoscalar Higgs boson. First row, right hand side: $M_{\mu\mu}/x_1$ for the closest dimuon pair in the event for different masses of the pseudoscalar Higgs boson. Second row: Comparison of $M_{\mu\mu}/\sqrt{x_1x_2}$, $M_{\mu\mu}/x_1$ and $M_{\mu\mu}$ for M_{H}=120 GeV and M_{A}=10 GeV.

vectors are not back-to-back in the transverse plane. Otherwise, the projection of the missing momentum is ambiguous. Although in practice the dimuon vectors are never exactly back-to-back, the mass resolution worsens for angles $\phi_{\mu\mu,\mu\mu}$ near 180°. An example is shown in Fig. 8.10. Commonly, a cut like $\cos\phi_{\mu\mu,\mu\mu} \geq -0.9$ is applied to ensure a good quality of the mass resolution (eg. Ref. [62]).

8.5 Signal selection with the cut analysis method

This chapter addresses the question whether the here discussed channel is suitable for a Higgs boson discovery at the LHC. For this goal, it is necessary to select as many signal events as possible from the available data, while rejecting a large fraction of background events. For the signal selection, a cut analysis method is used. A set of cut requirements on characteristic distributions that are different for signal and background events is applied to the events. All events that do not pass at least one of the cut requirements are assumed to be background-like

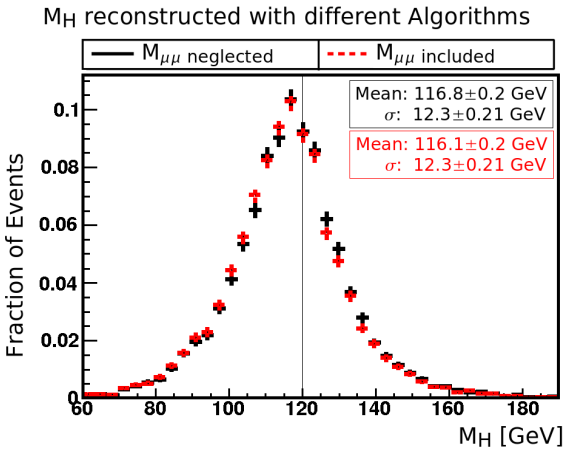

Fig. 8.9: Comparison of two approaches for the mass reconstruction. For the black curve, the invariant mass of the muon pairs is neglected. For the red curve, it is taken into account for all found muon pairs.

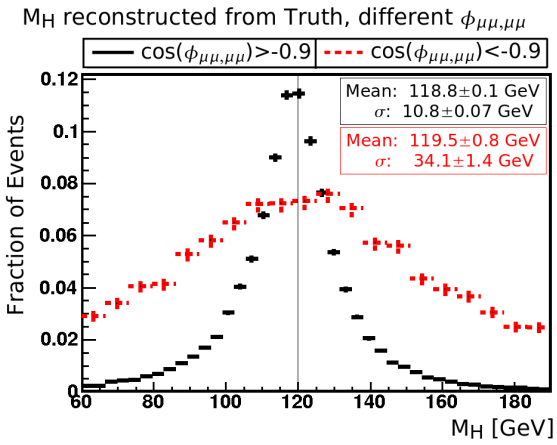

Fig. 8.10: The reconstructed Higgs boson mass for different angles $\phi_{\mu\mu,\mu\mu}$ between the dimuon objects. If the dimuon objects are back-to-back ($\cos(\phi_{\mu\mu,\mu\mu}) < -0.9$), the mass resolution degrades.

and are rejected.

As usually done for vector boson fusion analyses, the results of the cut analysis are given for a data volume of 30 fb^{-1}, which corresponds approximately to the complete foreseen low luminosity phase of the LHC. As the production rate of the signal process is with only ∼90 expected events very low, some cuts, eg. on the p_T of the tagging jets, have to be significantly softer than in previous vector boson fusion searches at the ATLAS experiment [62] in order to retain enough signal events for a discovery after the selection. The selection cuts have been optimized for a scalar Higgs boson mass of 120 GeV.

8.5.1 Selection strategy

In principle, four muons from the decays of the pseudoscalar Higgs bosons are expected in the final state. However, since the p_T of these leptons is frequently very low, only in about 5% of the events, all four leptons can be experimentally detected (Fig. 8.3). It is therefore favorable to require only three leptons to be found in order to keep a sizeable signal rate. As mentioned in Chap. 8.1, possible contributions from the $H_1 \to A_1 A_1 \to 4\tau \to 1e + 3\mu + 8\nu$ and $H_1 \to A_1 A_1 \to 4\tau \to h + 3\mu + 7\nu$ channels to the number of signal events are neglected here as a conservative estimate, because the involved isolation issues are not adequately described by ATLFAST. If only two leptons would be required, the number of available events would be even larger, but the Higgs boson mass reconstruction would not be possible for all selected events, as at least one muon from each pseudoscalar must be detected. Moreover, this would significantly enhance the relevant background rates.

ATLFAST does not include a realistic muon identification, but uses truth information for this task. Therefore, a muon identification probability of 90% has been applied for every muon, as was mentioned before. In the rare case that more than four muons are found in the event, only the four muons with the highest p_T are considered in the analysis.

For triggering, either two muons with p_T >10 GeV or one muon with p_T>20 GeV are needed. Otherwise, the event would not pass the trigger and not be written to storage. To avoid having a large number of lepton fakes, a minimum transverse momentum of 6 GeV for the remaining

leptons is required. Furthermore, all leptons must lie inside $|\eta| < 2.5$ to ensure that a combined reconstruction algorithm using information from the Inner Detector and the muon system can be used for a good suppression of fake muons. This is especially of importance, as fake muons eg. from cavern background or pile-up are not included in the ATLFAST samples, which might otherwise lead to a too optimistic estimation of the discovery significance.

For signal events, the p_T of the muons is on average lower than for all important background processes (Fig. 8.11). It therefore proved to be advantageous also to do a cut on the maximum transverse momentum of the muons. With the help of this additional requirement, the selection efficiency for events from vector boson production is reduced to up to 30%, while only about 3% of the signal cross section is lost.

In summary, the cuts requirements on the found muons are:

$$\begin{array}{rcll} p_{T,\mu 1} & > & 20 \text{ GeV} & \text{or} \\ p_{T,\mu 1} & > & 10 \text{ GeV} & \text{and} \quad p_{T,\mu 2} > 10 \text{ GeV} \\ p_{T,\mu 3} & > & 6 \text{ GeV} & \\ |\eta_\mu| & < & 2.5 & \\ p_{T,\mu 1} & < & 120 \text{ GeV} & \\ p_{T,\mu 2} & < & 50 \text{ GeV} & \\ p_{T,\mu 3} & < & 30 \text{ GeV} & \end{array} \tag{8.9}$$

As described in the mass reconstruction chapter, the identified muons are grouped into dimuon objects. At first, the muon pair with the smallest separation in ΔR is assumed to come from the same pseudoscalar boson and a dimuon object is created from these muons by four-vector addition. This object will for convenience be named 'first dimuon' in the following. The remaining two muons will be treated likewise and be named 'second dimuon' in the following. In the frequent case that only three muons are found in the event, the third muon alone takes the place of the second dimuon. For a short notation, the term 'second dimuon' can refer either to the combination of the two remaining muons or to the third muon alone, depending on the number of muons found in the event.

In $H_1 \to A_1 A_1 \to 4\tau \to 4\mu$ events, the muons from the decay of the pseudoscalar bosons are boosted strongly and thus lie close to each other, as explained in the discussion of the collinear approximation. Therefore, it is here required that the two muons that are grouped to the first dimuon are closer together than a certain ΔR_{match}. This helps to suppress all relevant background processes (Fig. 8.11). As discussed before, the separation of the muons depends on the mass of the pseudoscalar boson (see Fig. 8.3). Therefore, the exact cut value is chosen in dependence on the mass assumption for the A_1. Moreover, in events containing an off-shell Z^*/γ^* boson, the two muons often lie even closer together due to the vanishing mass of the photon. These background processes can be reduced by also requiring a minimal separation. Yet, for low A_1 masses, this cut needs to be soft as otherwise too many signal events are lost.

$$\begin{array}{rcl} M_A = 5 \text{ GeV} & : & 0.02 < \Delta R_{\text{match}} < 0.3 \\ M_A = 10 \text{ GeV} & : & 0.06 < \Delta R_{\text{match}} < 0.6 \end{array} \tag{8.10}$$

The b-jet veto is efficient for suppressing all background processes containing top or bottom quarks. It rejects all events that have at least one b-jet with minimal transverse momentum $p_{T,\text{bveto}}$ inside a pseudorapidity range given by η_{bveto}. In ATLFAST, a b-tagging efficiency of 60% is assumed. As b-tagging is only possible with the tracking capabilities of the Inner Detector which covers the pseudorapidity range $|\eta| < 2.5$, only b-jets inside this range can be identified

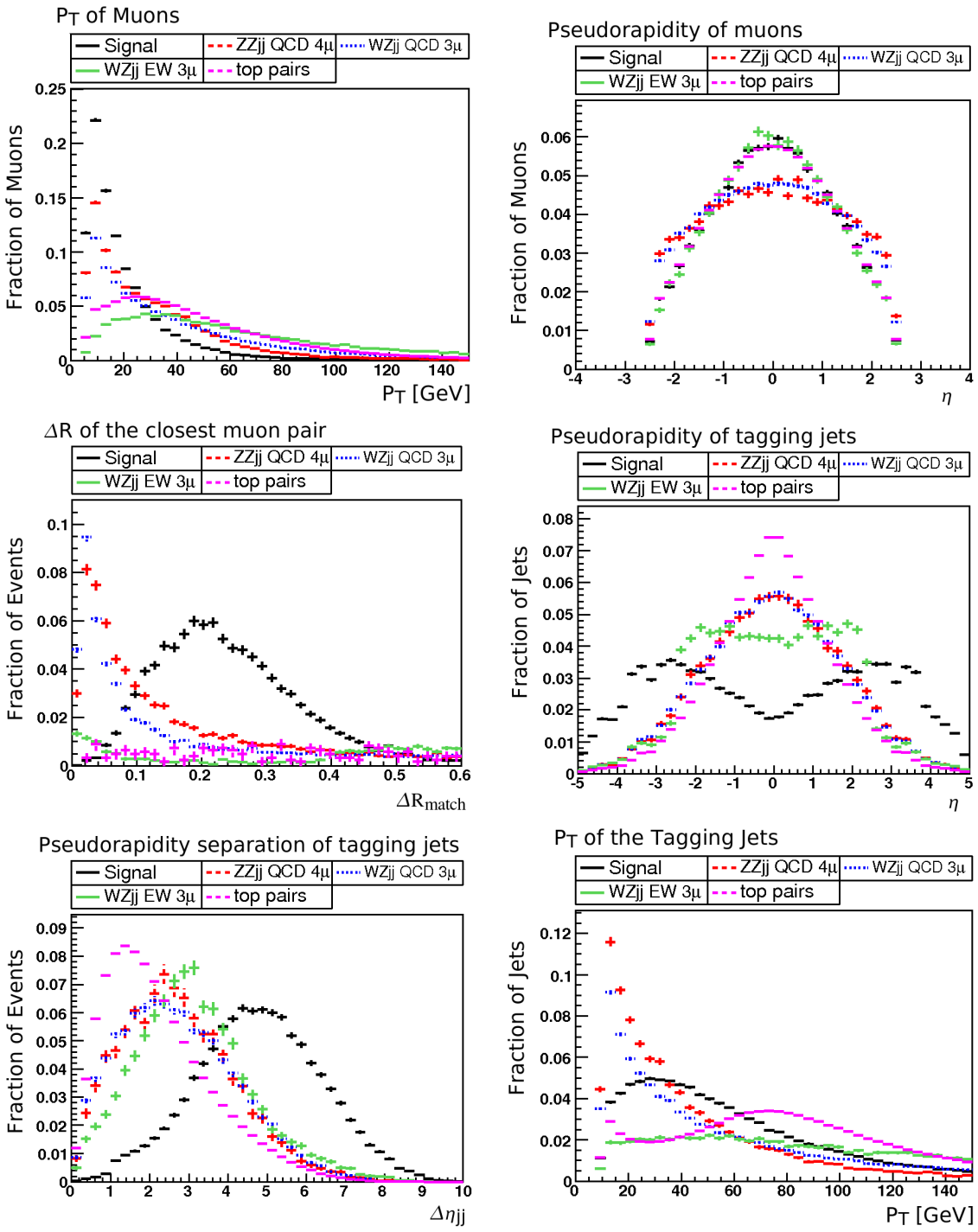

Fig. 8.11: Distributions for the signal with M_{H}=120 GeV and M_{A}=10 GeV and example background processes (ZZjj (QCD) with four directly produced muons in the final state, WZjj (QCD) and WZjj (EW) with three muons, top pair production). All distributions are shown without any cuts, as the statistics for the background processes quickly decreases during the cutflow. All diagrams are normalized to one including over- and underflow bins. First row, left hand side: Transverse momentum of all muons found in the event. First row, right hand side: Pseudorapidity of all muons found in the event. Second row, left hand side: ΔR separation of the closest muon pair that is grouped into the first dimuon object. Second row, right hand side: Pseudorapidity of the tagging jets. Last row, left hand side: Pseudorapidity separation of the tagging jets. Last row, right hand side: Transverse momentum of the tagging jets.

and rejected.

$$\begin{aligned} p_{T,\text{bveto}} &> 20 \text{ GeV} \\ |\eta_{\text{bveto}}| &< 2.5 \end{aligned} \tag{8.11}$$

The typical vector boson fusion signature contains the two tagging jets in the forward and backward region of the detector. Due to the calorimeter coverage of the ATLAS detector, jets outside $|\eta| < 5$ are not detectable any more. Such jets are not taken into account in this analysis.

To identify the tagging jets, in this analysis the jets with the highest p_T in each detector hemisphere are selected. Accordingly, the chosen jets have to be in different hemispheres ($\eta_{\text{jet1}} \cdot \eta_{\text{jet2}} < 0$), and no explicit cut on that is performed. The tagging jets are required to have a minimum separation in pseudorapidity, $\Delta\eta_{\text{jets}}$. This cut is efficient to suppress all background processes from QCD production, especially top pair production (Fig. 8.11). For these processes, the jets lie preferably in the central region of the detector and thus typically have a small separation.

$$\begin{aligned} \Delta\eta_{\text{jets}} &> 2.5 \\ |\eta| &< 5 \end{aligned} \tag{8.12}$$

The tagging jets in signal events typically have a large transverse momentum. Thus, a cut on $p_{T,\text{jet1}}$ and $p_{T,\text{jet2}}$ is suitable to suppress the ZZjj/WZjj background processes, since the production cross sections of these processes diverge for small jet energy (Fig. 8.11).

$$\begin{aligned} p_{T,\text{jet1}} &> 30 \text{ GeV} \\ p_{T,\text{jet2}} &> 20 \text{ GeV} \end{aligned} \tag{8.13}$$

The $A_1 \to \tau\tau$ decay is only important for A_1 masses of at most $\sim$10 GeV. The mass of the dimuon objects, which corresponds to the invariant mass of the matched muon pair, has to be smaller than the mass of the pseudoscalar Higgs boson, as the pseudoscalar decays not only to the muons from its decay chain, but also to four neutrinos. Only very few signal events have an invariant dimuon mass larger than 8 GeV (3 GeV) for M_{A}=10 GeV (M_{A}=5 GeV). This can be used to efficiently reject muon pairs originating from on-shell Z^0 bosons. However, background processes containing off-shell Z^*/γ^* bosons can also have very low invariant dimuon masses (Fig. 8.12). To reduce such background events, also a minimum dimuon mass is required. For light pseudoscalar masses around 5 GeV, the signal peak is close to the background peak, so that only a moderate cut is chosen here.

$$\begin{aligned} M_{\text{A}} = 5 \text{ GeV} &: 0.5 \text{ GeV} < M_{\mu\mu} < 3 \text{ GeV} \\ M_{\text{A}} = 10 \text{ GeV} &: 1.5 \text{ GeV} < M_{\mu\mu} < 8 \text{ GeV} \end{aligned} \tag{8.14}$$

As this cut is only meaningful if two muons are combined to a dimuon object, it is applied only to the first dimuon, which always consists of two muons.

For signal events, the isolated muons lie in the central region and the tagging jets in the forward and backward region of the detector. Thus, the muons typically lie between the tagging jets in terms of η. As shown in Fig. 8.11, the muons are more central in signal events than in vector boson production. Therefore, the dimuon objects are required to lie between the tagging jets in terms of pseudorapidity.

$$\eta_{\text{min,jet}} < \eta_{\mu\mu} < \eta_{\text{max,jet}} \tag{8.15}$$

Also the invariant mass of the two dimuon objects, which corresponds to the invariant mass of the three or four muons in the event, has discriminating power. For ZZjj events, there is a peak

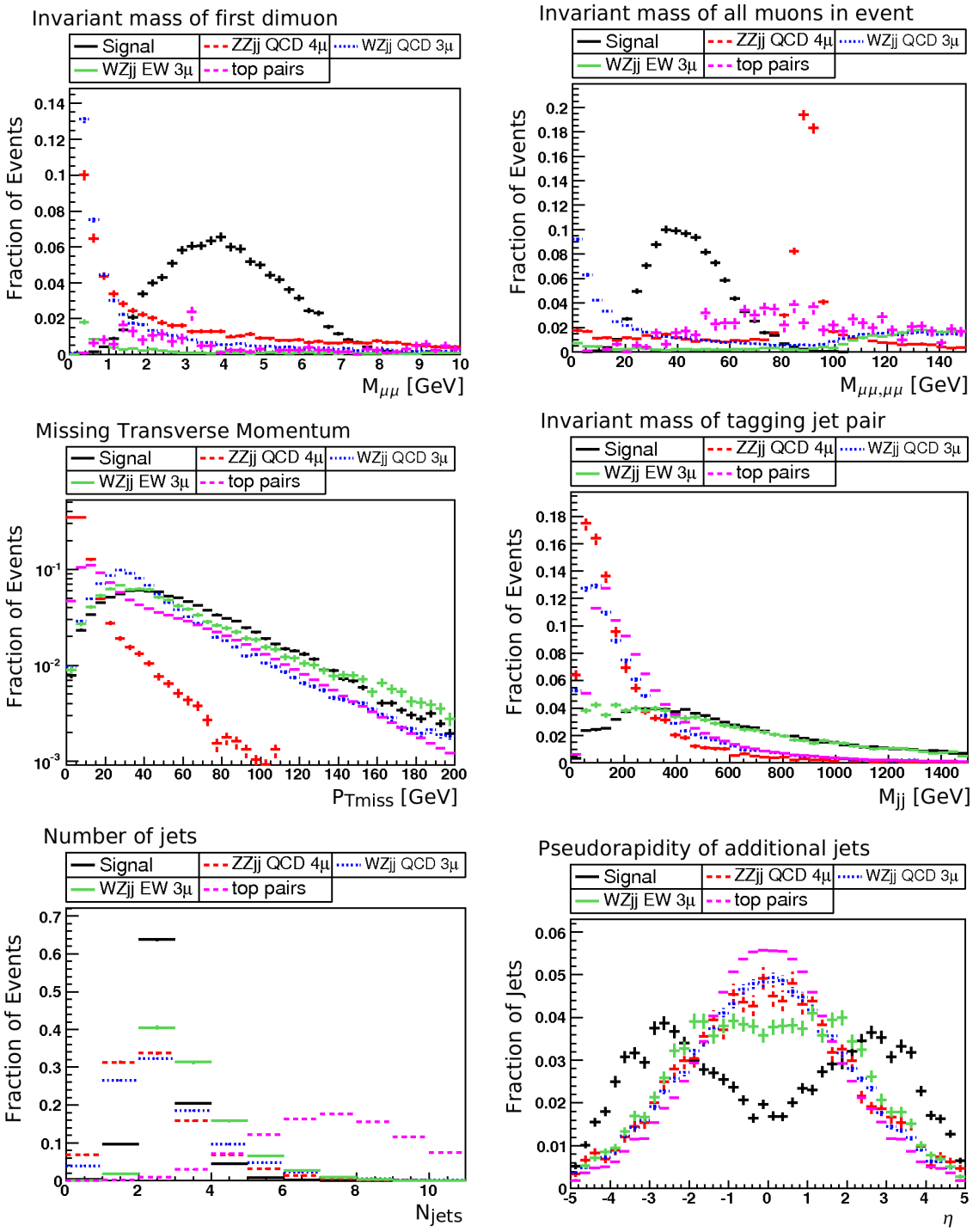

Fig. 8.12: Distributions for the signal with M_{H}=120 GeV and M_{A}=10 GeV and example background processes (ZZjj (QCD) with four directly produced muons in the final state, WZjj (QCD) and WZjj (EW) with three muons, top pair production). All distributions are shown without any cuts, as the statistics for the background processes quickly decreases during the cut flow. All diagrams are normalized to one including over- and underflow bins. First row, left hand side: Mass of the first dimuon object, i.e. invariant mass of the closest muon pair. First row, right hand side: Invariant mass of all three or four muons found in the event. Second row, left hand side: Missing transverse momentum. Second row, right hand side: Invariant mass of the tagging jets. Last row, left hand side: Total number of jets found in the event. Last row, right hand side: Pseudorapidity of additional jets other than the tagging jets.

at the Z boson mass because the invariant mass can be dominated by one muon pair if the other one has low momentum, for example if it originates an off-shell Z^*/γ^* boson. As the cut on the invariant dimuon mass is only done for the closest muon pair, not all such events are removed by the previous cuts. Moreover, if one muon pair comes from an off-shell Z^*/γ^* boson and the additional muon, for example from the decay of a W boson, has low momentum, a low invariant mass is the result (Fig. 8.12). Therefore, it is required:

$$20 \text{ GeV} < M_{\mu\mu,\mu\mu} < 80 \text{ GeV} \tag{8.16}$$

Furthermore, signal events have a considerable amount of missing momentum due to the eight neutrinos in the final state. ZZjj events with a subsequent decay of the Z bosons into muons do not contain any neutrinos and thus usually have low missing momentum. Furthermore, also events with only one neutrino such as WZjj production or with two neutrinos from top quark decays on average have a lower missing momentum than signal events (Fig. 8.12). Accordingly,

$$p_{Tmiss} > 30 \text{ GeV} \tag{8.17}$$

is required.

For QCD background processes, the invariant mass of the jet pair selected as tagging jets is on average lower than for signal events (Fig. 8.12). Therefore, a cut on this quantity can reject a fraction of these background events. Moreover, the cut is efficient to suppress jet production from hadronic Z or W boson decays.

$$M_{\text{jj}} > 200 \text{ GeV} \tag{8.18}$$

The so-called central jet veto [69–71] exploits the fact that in purely electroweak processes, additional jet production in the central region is suppressed in contrast to processes with gluon exchange. Here, events which have an additional jet other than the tagging jets with $p_{T,\text{cjv}}$ and $|\eta_{\text{cjv}}|$ are rejected by the veto.

$$\begin{aligned} |\eta_{\text{cjv}}| &< 2.5 \\ p_{T,\text{cjv}} &> 20 \text{ GeV} \end{aligned} \tag{8.19}$$

This cut is especially effective to suppress top quark pair production due to the large number of central jets in these events (Fig. 8.12), but also helps to reduce the number of ZZjj (QCD) and WZjj (QCD) events.

In WZ and ZZ production, all muons are often very collimated (Fig. 8.13). Therefore, a minimal separation $\Delta R_{\mu\mu,\mu\mu}$ of the two dimuon objects is required. Furthermore, a large number of background events has a large $\Delta R_{\mu\mu,\mu\mu}$ separation, in particular from top pair production.

$$0.6 < \Delta R_{\mu\mu,\mu\mu} < 3.0 \tag{8.20}$$

As was argued in the discussion of the mass reconstruction, the mass resolution degrades if the two dimuon objects are back-to-back in the transverse plane. To prevent this, these events are not considered. In addition, this cut is also effective to suppress all relevant background processes (Fig. 8.13), for which the dimuon objects are more often back-to-back than for signal events.

$$\cos(\phi_{\mu\mu,\mu\mu}) > -0.9 \tag{8.21}$$

Furthermore, x_1 and x_2 must be in the physical range. For background processes, this is frequently not the case because the assumption for the calculation of x_1 and x_2, that the muons stem from the decay of the same, collinear particle is here not always well fulfilled (Fig. 8.13).

$$0 < x_{1,2} < 1 \tag{8.22}$$

Cut		**Signal $H_1 \to A_1 A_1 \to 4\tau \to 4\mu + 8\nu$**							
		M_H=120 GeV				M_H=100 GeV			
		M_A=10 GeV		M_A=5 GeV		M_A=10 GeV		M_A=5 GeV	
		[fb]	#	[fb]	#	[fb]	#	[fb]	#
None		2.83	85	2.83	85	3.33	100	3.33	100
3 muons	(8.9)	0.59	17.8	0.72	21.6	0.54	16.2	0.66	19.8
ΔR_{match}	(8.10)	0.58	17.5	0.69	20.6	0.53	15.8	0.63	19.0
b-veto	(8.11)	0.57	17.0	0.67	20.0	0.51	15.4	0.62	18.5
$\Delta\eta_{\text{jets}}$	(8.12)	0.47	14.1	0.55	16.5	0.43	12.8	0.51	15.2
$p_{T,\text{jet1,2}}$	(8.13)	0.39	11.6	0.44	13.3	0.35	10.5	0.42	12.5
$M_{\mu\mu}$	(8.14)	0.37	11.2	0.42	12.5	0.34	10.2	0.39	11.6
$\eta_{\mu\mu}$	(8.15)	0.35	10.5	0.39	11.7	0.31	9.4	0.36	10.8
$M_{\mu\mu,\mu\mu}$	(8.16)	0.34	10.2	0.38	11.4	0.30	9.0	0.35	10.4
p_{Tmiss}	(8.17)	0.29	8.8	0.32	9.5	0.26	7.7	0.30	8.9
M_{jj}	(8.18)	0.29	8.6	0.31	9.4	0.25	7.6	0.29	8.8
CJV	(8.19)	0.27	8.0	0.29	8.6	0.23	6.9	0.27	8.0
$\Delta R_{\mu\mu,\mu\mu}$	(8.20)	0.26	7.7	0.28	8.3	0.22	6.7	0.26	7.9
$\phi_{\mu\mu,\mu\mu}$	(8.21)	0.25	7.4	0.27	8.0	0.22	6.6	0.26	7.7
$x_{1,2}$	(8.22)	0.24	7.1	0.26	7.8	0.20	6.1	0.25	7.4
Mass window	(8.23)	0.22	6.7	0.25	7.5	0.20	5.9	0.24	7.2

Tab. 8.5: Cut flow for signal events and M_H = 120/100 GeV and M_A = 10/5 GeV. Both the selected cross section and the number of expected signal events for 30 fb^{-1} are listed.

At last, a mass window cut around the assumed scalar Higgs boson mass is done. Here, a large window is chosen in order to accommodate many signal events to obtain a sizeable signal rate after the cut selection.

$$M_H - 30 \text{ GeV} < M_{H,\text{reco}} < M_H + 30 \text{ GeV} \tag{8.23}$$

For the background processes, the reconstructed mass distribution is basically flat (Fig. 8.13). Accordingly, many events have a reconstructed mass which is very different to the mass assumption for the scalar boson. Thus, also with a large mass window, still a significant fraction of the background events can be rejected.

8.5.2 Results of the signal selection

The results of the cut selection for each background process and the signal process are given in Tabs. 8.5 to 8.8. For the signal process, the cut flows for four mass combinations (M_H=120 GeV, 100 GeV and M_A=10 GeV, 5 GeV) are shown as examples. Slightly more events are selected for M_A=5 GeV than for M_A=10 GeV, as the number of detected muons is larger for this case (Fig. 8.3). In addition, the mass resolution is slightly better (Fig. 8.7). For low masses of the scalar boson the number of selected events is lower although the initial cross section is larger since on average less muons are detected in an event.

The ZZjj (QCD) process is heavily suppressed by the selection cuts. The number of expected events is reduced to zero within the available Monte Carlo statistics while five or more cuts remain to be done. For the ZZjj (QCD) process with four directly produced muons (i.e. not from τ-lepton decays) in the final state, this corresponds to less than 0.55 expected events at 95% confidence level according to Poisson statistics, for the ZZjj (QCD) process with two muons and two τ-leptons, to less than 0.77 expected events at 95% confidence level. These small numbers

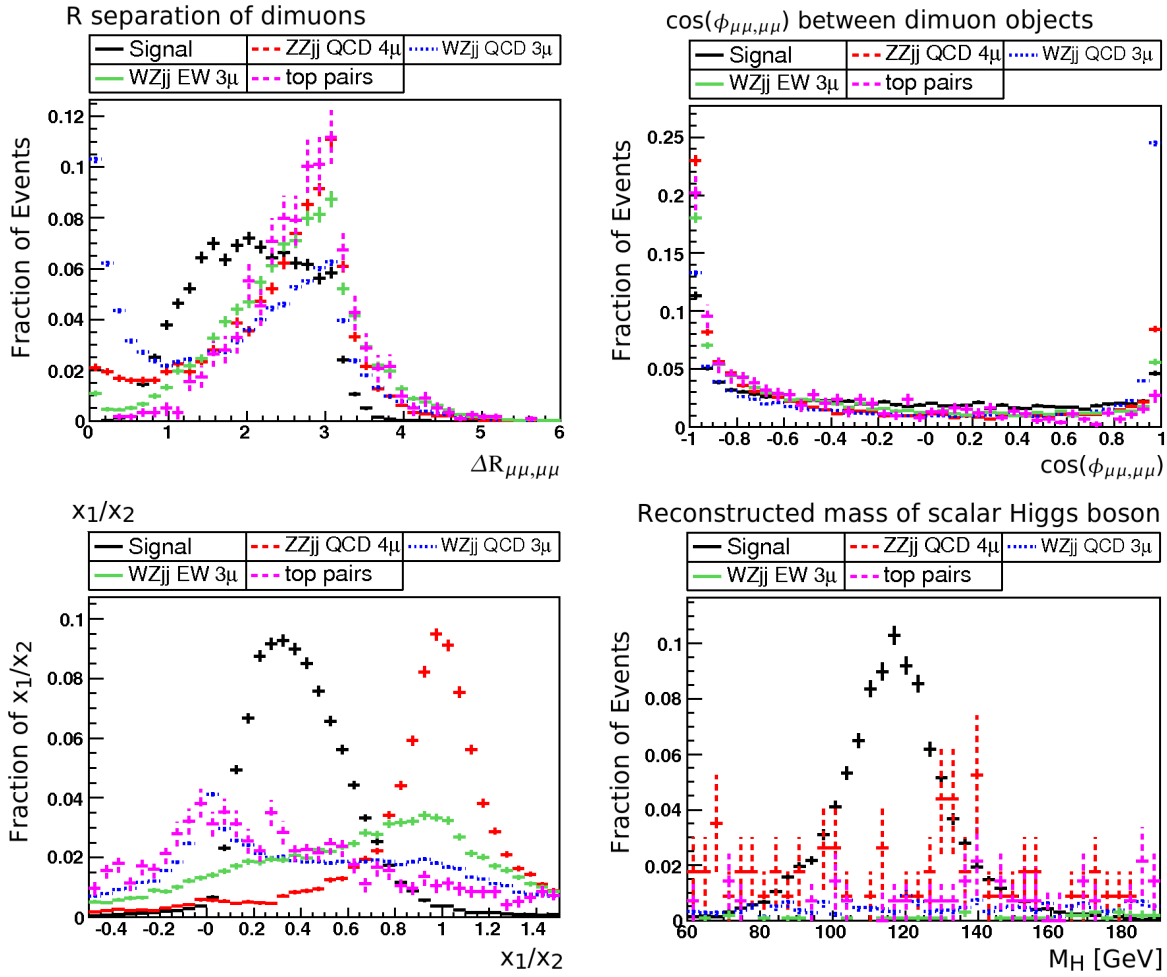

Fig. 8.13: Distributions for the signal with M_{H}=120 GeV and M_{A}=10 GeV and example background processes (ZZjj (QCD) with four directly produced muons in the final state, WZjj (QCD) and WZjj (EW) with three muons, top pair production). All distributions are shown without any cuts, as the statistics for the background processes quickly decreases during the cut flow. All diagrams are normalized to one including over- and underflow bins. First row, left hand side: R separation of the two dimuon objects. First row, right hand side: Cosine of the angle $\phi_{\mu\mu,\mu\mu}$ between the dimuon objects in the transverse plane. Last row, left hand side: x_1 and x_2 as defined for the mass reconstruction. Last row, right hand side: Reconstructed mass of the scalar Higgs boson.

Cut		ZZjj QCD						ZZjj EW		WZjj EW	
		4μ		$2\mu 2\tau$		4τ		4μ		4μ	
120 GeV/10 GeV		[fb]	#	[fb]	#	[fb]	#	[fb]	#	[fb]	#
None		125	3750	26	780	0.8	24	0.5	15	2.3	69
3 muons	(8.9)	52	1571	3.7	112	0.03	1.0	0.15	4.4	0.31	9.4
ΔR_{match}	(8.10)	29	864	1.4	42	0.005	0.16	0.08	2.3	0.06	1.7
b-veto	(8.11)	28	844	1.3	40	0.005	0.16	0.07	2.2	0.05	1.6
$\Delta\eta_{\text{jets}}$	(8.12)	4.2	125	0.20	6.1	0.001	0.04	0.03	0.94	0.03	0.89
$p_{T,\text{jet1,2}}$	(8.13)	1.4	43	0.09	2.6	0	0	0.02	0.73	0.03	0.76
$M_{\mu\mu}$	(8.14)	0.78	23	0.06	1.8	0	0	0.01	0.29	0.01	0.44
$\eta_{\mu\mu}$	(8.15)	0.39	12	0.009	0.26	0	0	0.008	0.24	0.01	0.32
$M_{\mu\mu,\mu\mu}$	(8.16)	0.13	3.9	0.009	0.26	0	0	0.002	0.06	0.004	0.13
p_{Tmiss}	(8.17)	0	0	0.009	0.26	0	0	0.0002	0.006	0.003	0.10
M_{jj}	(8.18)	0	0	0	0	0	0	0.0002	0.006	0.003	0.10
CJV	(8.19)	0	0	0	0	0	0	0.0002	0.006	0.002	0.08
$\Delta R_{\mu\mu,\mu\mu}$	(8.20)	0	0	0	0	0	0	0.0002	0.006	0.002	0.06
$\phi_{\mu\mu,\mu\mu}$	(8.21)	0	0	0	0	0	0	0.0002	0.006	0.0005	0.01
$x_{1,2}$	(8.22)	0	0	0	0	0	0	0	0	0.0002	0.005
Mass window	(8.23)	0	0	0	0	0	0	0	0	0.0002	0.005
		negligible		negligible		negligible		negligible		negligible	
120 GeV/5 GeV		0	0	0	0	0	0	0	0	0.0002	0.005
		negligible		negligible		negligible		negligible		negligible	

Tab. 8.6: Cut flow for ZZjj events with cuts for $M_{\text{H}} = 120$ GeV and $M_{\text{A}} = 10$ GeV. Both the selected cross section and the number of expected signal events for 30 fb^{-1} are listed. In the last two rows, the final results of the selection for $M_{\text{H}} = 120$ GeV and $M_{\text{A}} = 5$ GeV are given. All channels are assumed to be negligible.

are assumed to be sufficiently reduced by the remaining five cuts to be negligible. This is independent of the mass hypothesis for the scalar Higgs boson, since only the mass window, which is the last cut in the cut flow, depends on this mass.

For the WZjj (QCD) process, only the final states with two or three directly produced muons are of importance, as the other processes are heavily suppressed by the requirement that at least three muons must be found in the event. From the sample with three directly produced muons, only one Monte Carlo event remains after the cut on x_1 and x_2, which is very efficient to suppress this class of background processes. This event has a reconstructed Higgs boson mass of about 61 GeV (520 GeV) for the selection for M_{A}=10 GeV (M_{A}=5 GeV) and is thus removed by the mass window cut for all here studied mass hypotheses. For the WZjj (QCD) process with two directly produced muons in the final state, the selection for M_{A}=10 GeV reduces the number of Monte Carlo events to zero when four cuts still remain to be done. However, as one Monte Carlo event passes the selection for M_{A}=5 GeV, this channel is not neglected also for the M_{A}=10 GeV hypothesis in order not to be overly optimistic. Nevertheless, it seems reasonable that the suppression of this background process is more efficient for the M_{A}=10 GeV case, as it can better reject events containing an off-shell Z^*/γ^* boson. The selected background event for the M_{A}=5 GeV hypothesis has a reconstructed Higgs boson mass of about 92 GeV. Thus, it is selected by all hypotheses on M_{H} studied here except for M_{H}=130 GeV.

The suppression of the electroweak ZZjj and WZjj production by the cuts on the tagging jets is not as efficient as for the QCD processes. Yet, not all diagrams belonging to the class of

Cut		WZjj QCD							
		$3\mu\nu$		$2\mu\tau\nu$		$\mu 2\tau\nu$		$3\tau\nu$	
120 GeV/10 GeV		[fb]	#	[fb]	#	[fb]	#	[fb]	#
None		279	8370	72	2160	12.5	375	3.9	117
3 muons	(8.9)	82	2450	10	299	0.91	27	0.14	4.2
ΔR_{match}	(8.10)	30	899	3.0	91	0.16	4.6	0.03	0.84
b-veto	(8.11)	29	874	3.0	89	0.16	4.6	0.03	0.84
$\Delta\eta_{\text{jets}}$	(8.12)	4.8	145	0.47	14	0.03	0.91	0.01	0.32
$p_{T,\text{jet1,2}}$	(8.13)	1.9	58	0.22	6.5	0.009	0.27	0.004	0.11
$M_{\mu\mu}$	(8.14)	1.2	35	0.13	3.8	0	0	0	0
$\eta_{\mu\mu}$	(8.15)	0.76	23	0.05	1.6	0	0	0	0
$M_{\mu\mu,\mu\mu}$	(8.16)	0.24	7.2	0.02	0.54	0	0	0	0
p_{Tmiss}	(8.17)	0.17	5.1	0.02	0.54	0	0	0	0
M_{jj}	(8.18)	0.14	4.3	0.02	0.54	0	0	0	0
CJV	(8.19)	0.06	1.9	0	0	0	0	0	0
$\Delta R_{\mu\mu,\mu\mu}$	(8.20)	0.04	1.3	0	0	0	0	0	0
$\phi_{\mu\mu,\mu\mu}$	(8.21)	0.03	1.0	0	0	0	0	0	0
$x_{1,2}$	(8.22)	0.004	0.13	0	0	0	0	0	0
Mass window	(8.23)	0	0	0	0	0	0	0	0
		< 0.013	< 0.39	< 0.018	< 0.54	negligible		negligible	
120 GeV/5 GeV		0	0	0.006	0.18	0	0	0	0
		< 0.013	< 0.39	< 0.028	< 0.85	negligible		negligible	

Tab. 8.7: Cut flow for WZjj events with cuts for $M_{\text{H}} = 120$ GeV and $M_{\text{A}} = 10$ GeV. Both the selected cross section and the number of expected signal events for 30 fb^{-1} are listed. In the last two rows, the final results of the selection for $M_{\text{H}} = 120$ GeV and $M_{\text{A}} = 5$ GeV are given. The limits correspond to a 95% confidence interval according to the Poisson distribution. The WZjj $\to 2\tau 1\mu$, $\to 3\tau$ channels are assumed to be negligible.

electroweak ZZjj and WZjj production have a structure that is similar to vector boson fusion production, so that the characteristic features are not as pronounced here as for the signal. Furthermore, the features of the muons in this class of background events are very distinct from the signal, so that an efficient suppression of these background events is still possible. Moreover, the production cross section is small. For these reasons, it is found that less than $\sim$0.02 events are expected after the signal selection at 95% confidence level according to the Poisson distribution for both the ZZjj and WZjj background processes. This is regarded to be negligible. Although here, only the final states with four (ZZjj) and three (WZjj) directly produced muons are explicitly studied, all other final states are assumed to be negligible as well, because the number of events that pass the requirements that three muons have to be found is even smaller for these final states than for the processes studied here.

For top quark pair production, also in association with vector bosons, all available Monte Carlo events are rejected by the analysis at the central jet veto step. This veto is very efficient to suppress this class of background processes due to the large number of central jets in these events. With a modified selection where no requirements on the muons other than their existence are made, the selection efficiency of the central jet veto for $\text{t}\bar{\text{t}}$ events is about 25%. This cut is largely independent of the muon selection. Moreover, only about 20% of the $\text{t}\bar{\text{t}}$ events pass the requirements for a sensible mass reconstruction (x_1, x_2 physical, dimuons not back-to-back). This number seems reasonable to use as an estimate of the efficiency also for the

Cut		**$t\bar{t}$**		**$Zt\bar{t}$**		**$Wt\bar{t}$**		**$Zb\bar{b}$**		**$Wb\bar{b}$**	
120 GeV/10 GeV		[fb]	#	[fb]	#	[fb]	#	[fb]	#	[fb]	#
None		482000	14M	49	1470	34	1020	3900	117k	562	16860
3 muons	(8.9)	12	374	2.3	68	1.6	47	128	3840	0.17	5.1
$\Delta R_{\mathrm{match}}$	(8.10)	2.4	71	0.65	20	0.46	14	32	979	0.09	2.6
b-veto	(8.11)	1.1	32	0.17	5.2	0.12	3.6	28	856	0.03	0.85
$\Delta\eta_{\mathrm{jets}}$	(8.12)	0.29	8.7	0.07	2.0	0.05	1.5	0.88	26	0	0
$p_{T,\mathrm{jet1,2}}$	(8.13)	0.11	3.3	0.04	1.2	0.03	0.85	0.07	2.0	0	0
$M_{\mu\mu}$	(8.14)	0.06	1.7	0.01	0.4	0.007	0.21	0	0	0	0
$\eta_{\mu\mu}$	(8.15)	0.04	1.2	0.007	0.21	0.007	0.21	0	0	0	0
$M_{\mu\mu,\mu\mu}$	(8.16)	0.01	0.42	0.007	0.21	0.007	0.21	0	0	0	0
p_{Tmiss}	(8.17)	0.01	0.42	0.007	0.21	0.007	0.21	0	0	0	0
M_{jj}	(8.18)	0.01	0.42	0.007	0.21	0.007	0.21	0	0	0	0
CJV	(8.19)	0	0	0	0	0	0	0	0	0	0
$\Delta R_{\mu\mu,\mu\mu}$	(8.20)	0	0	0	0	0	0	0	0	0	0
$\phi_{\mu\mu,\mu\mu}$	(8.21)	0	0	0	0	0	0	0	0	0	0
$x_{1,2}$	(8.22)	0	0	0	0	0	0	0	0	0	0
Mass window	(8.23)	0	0	0	0	0	0	0	0	0	0
		negligible		negligible		negligible		negligible		negligible	
120 GeV/5 GeV		0	0	0	0	0	0	0	0	0	0
		negligible		negligible		negligible		negligible		negligible	

Tab. 8.8: Cut flow for events from top and bottom quark production with cuts for $M_{\mathrm{H}} = 120$ GeV and $M_{\mathrm{A}} = 10$ GeV. Both the selected cross section and the number of expected signal events for 30 fb^{-1} are listed. In the last two rows, the final results of the selection for $M_{\mathrm{H}} = 120$ GeV and $M_{\mathrm{A}} = 5$ GeV are given. All channels are assumed to be negligible.

complete selection, as similar efficiencies of these cuts also have been observed for the WZjj QCD background processes after the full cut selection. If these efficiencies are applied to the expected number of events before the central jet veto cut, only 0.02 $t\bar{t}$ events are predicted to remain before the mass window cut is performed. The cut on $\Delta R_{\mu\mu,\mu\mu}$ is not taken into account for this estimation. Although such an estimation might be too optimistic due to possible correlations of the cut variables, it seems justifiable to consider $t\bar{t}$ production and also the similar $Wt\bar{t}$ and $Zt\bar{t}$ production processes negligible[4].

Events from bottom quark pair production in association with vector bosons can be suppressed very efficiently and thus also are assumed to be negligible. The selection efficiencies of the $Zb\bar{b}$ and $Wb\bar{b}$ processes listed in Tab. 8.8 are not directly comparable due to very different generator cuts on these samples.

To calculate the significance of this search as a discovery channel, the profile likelihood method[5] (see App. C) is used. For many mass combinations, the total number of selected background events is zero due to the limited Monte Carlo statistics. The profile likelihood method is suitable for this case also, as it takes into account Poisson fluctuation of the expected signal

[4] From the common ATLAS Monte Carlo production, also samples for $t\bar{t}t\bar{t}$ and $t\bar{t}b\bar{b}$ production are available. These processes are also found to be negligible for this analysis.

[5] Both the WZjj (QCD) processes with three and with two directly produced muons are considered to be non-negligible for this search. As the sample with two directly produced muons corresponds to a smaller data volume than the one with three muons (Tab. 8.4), the scale factor that relates the number of selected Monte Carlo events to the expected number of background events is taken from this sample in the calculation of the significances with the profile likelihood method. This is a conservative estimate.

M_{H}	M_{A}	Selected signal events	Selected background events	Significance
100 GeV	5 GeV	7.2	0.18	4.68
100 GeV	10 GeV	5.9	0	4.69
110 GeV	5 GeV	7.4	0.18	4.75
110 GeV	10 GeV	6.5	0	4.93
120 GeV	5 GeV	7.5	0.18	4.79
120 GeV	10 GeV	6.7	0	5.01
130 GeV	5 GeV	7.6	0	5.34
130 GeV	10 GeV	6.3	0	4.85

Tab. 8.9: Number of selected signal and background events after the cut selection for 30 fb^{-1}. The significances are calculated with the profile likelihood method, taking into account Poisson fluctuation of both signal and background numbers that arise from the limited size of the data samples (see App. C).

and background event numbers [137].

The total numbers of selected signal and background events and the significances for different Higgs boson mass combinations are listed in Tab. 8.9. All significances are close to or slightly above the 5σ level that is commonly required for a discovery. Accordingly, this channel has a good discovery potential for a light scalar Higgs boson and the light pseudoscalar Higgs boson from its decay. The significances are higher for larger M_{A}, if $M_{\mathrm{A}} \lesssim 10$ GeV.

As this study is performed with the fast detector simulation ATLFAST, the influence of falsely identified muons that might enhance the expected background numbers has not been taken into account. On the other hand, the number of signal events might also be enhanced by contributions from the $H_1 \to A_1A_1 \to 4\tau \to 1e+3\mu+8\nu$ and $H_1 \to A_1A_1 \to 4\tau \to h+3\mu+7\nu$ processes. Both issues should be studied with the full GEANT detector simulation.

As mentioned before, in the relevant parameter regions of the Light A_1 and the cNMSSM Scenario, the branching ratios of the $H_1 \to A_1A_1$ and $A_1 \to \tau\tau$ decays are slightly larger than assumed in Tab. 8.2, so that the actual production cross sections and thus the expected significances are slightly larger in these scenarios than the here listed ones. The discovery contours of this new search channel for the two scenarios are shown in Figs. 8.14 and 8.15. In the λ/κ plane of the Light A_1 Scenario, the channel reaches significances above 5σ in the right hand unexcluded region if the $A_1 \to \tau\tau$ decay is dominant and if $M_H \gtrsim 105$ GeV. In the left hand unexcluded region, the $H_1 \to A_1A_1$ branching ratio is slightly smaller than in the right hand unexcluded region, and the mass of the scalar Higgs boson is smaller than about 110 GeV in the region where the $A_1 \to \tau\tau$ decay is dominant. Therefore, only four points of the scanning grid have significances larger than 5σ. Also in the cNMSSM Scenario, the channel has a good discovery potential in the region with dominant $A_1 \to \tau\tau$ decay.

8.6 Conclusions on the VBF, $H_1 \to A_1A_1 \to 4\tau \to 4\mu + 8\nu$ process

In this chapter, a detailed description of the features of the VBF, $H_1 \to A_1A_1 \to 4\tau \to 4\mu + 8\nu$ process is presented. The reconstruction of the mass of the scalar Higgs boson is possible with the help of the collinear approximation. Throughout the relevant mass range of the pseudoscalar Higgs boson ($M_{\mathrm{A}} \approx 5$ - 10 GeV), the mass resolution is found to be about 10% , depending on M_{A} and M_{H}. The observed slight shift can only be realistically studied with the help of the full

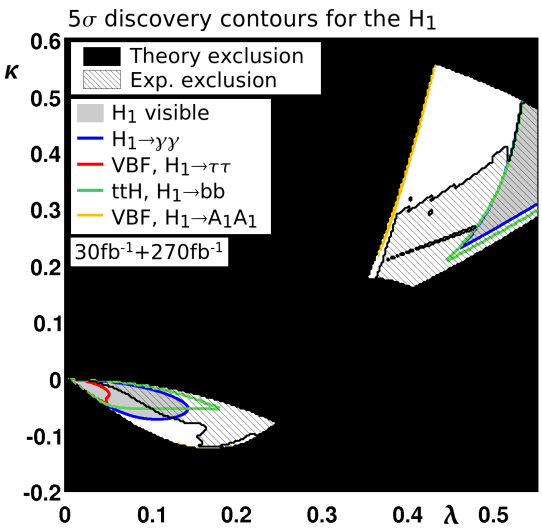

Fig. 8.14: 5σ discovery contours for the H_1 in the Light A_1 Scenario, λ/κ plane with 30+270 fb^{-1}. For the $H_1 \to A_1 A_1$ search, only 30 fb^{-1} are taken into account. The H_1 is observable in the grey region. Systematic uncertainties are not included. For details on how this plot must be read, see Fig. 7.1.

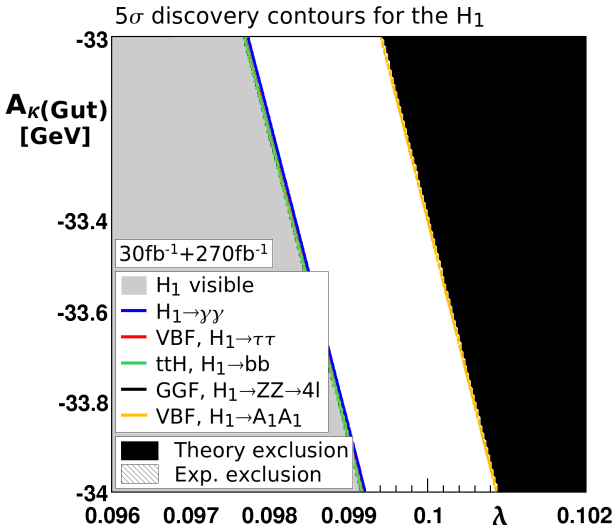

Fig. 8.15: 5σ discovery contours for the H_1 in the cNMSSM Scenario, $\lambda/A_{\kappa(\mathrm{GUT})}$ plane with 30+270 fb^{-1}. For the $H_1 \to A_1 A_1$ search, only 30 fb^{-1} are taken into account. Systematic uncertainties are not included. The H_1 is observable in the grey region. For details on how this plot must be read, see Fig. 7.1.

simulation, but is not relevant for the estimation of the discovery potential in this channel as the chosen mass window is large.

Furthermore, a cut analysis method for the signal selection is presented. The clear features of the vector boson fusion process and of the muons in signal events are exploited to efficiently remove the main background processes such as vector boson and top quark pair production. Although in total only about 90 signal events are produced with an integrated luminosity of 30 fb^{-1}, significances around 5σ can be obtained. A discovery of the light scalar and light pseudoscalar Higgs bosons in parameter regions of the NMSSM where the studied decay chain is dominant seems to be possible. Thus, the $H_1 \to A_1 A_1 \to 4\tau$ search mode closes large parts of those gaps of the discovery potential in the λ/κ plane of the Reduced Couplings Scenario and the $\lambda/A_{\kappa(\mathrm{GUT})}$ plane of the cNMSSM Scenario where the $A_1 \to \tau\tau$ decay is dominant.

9. Summary

The identification of the tagging jets originating from the scattered quarks is one of the most important issues of vector boson fusion analyses. Therefore, the performance of jet reconstruction at the ATLAS experiment is studied with focus on vector boson fusion events over the full pseudorapidity range of the ATLAS detector in the first part of this thesis. The cone jet algorithm with a size parameter of R=0.4 run on topological clusters is shown to be the best choice among the studied cone jet algorithms and is therefore now used in many ongoing ATLAS studies. However, the observed purity, in particular for central jets with low p_T, degrades significantly already in the presence of a pile-up which corresponds to a luminosity of $10^{33}\text{cm}^{-2}\text{s}^{-1}$.

The discovery potential for NMSSM Higgs bosons at the ATLAS experiment is evaluated in the second part of this thesis. The NMSSM as an extended supersymmetric model solves the so-called hierarchy problem that is present in Standard Model. Moreover, it contains a dark matter candidate and can accommodate the unification of the gauge couplings at a large energy scale. Due to an additional supersymmetric gauge singlet field, it also solves the μ-problem of the Minimal Supersymmetric Standard Model and thus constitutes a very appealing theory for the description of nature.

The Higgs sector of the NMSSM is complex since it contains in total seven Higgs bosons and is at Born level described by six parameters. Therefore, only individual benchmark points for the NMSSM were available in the past. With this thesis, an effort to develop two-dimensional benchmark planes inside this six-dimensional parameter space is done in order to guide future experimental search strategies. Such planes are of paramount importance for a realistic evaluation of the discovery potential for NMSSM Higgs bosons, as unlike points, they provide a smooth variation of the model parameters and can give a better feeling for the position and size of regions of a certain phenomenology, also with respect to the exclusion bounds.

In total, seven benchmark planes within four different benchmark scenarios are developed. These planes are designed to contain the most important phenomenology types of the Higgs sector of the NMSSM, such as reduced couplings of the Higgs bosons to fermions and bosons with respect to the Standard Model. In addition, also dominant $H_{1/2} \rightarrow A_1 A_1$ decays of a light scalar Higgs boson are included. In such regions, the discovery of the NMSSM Higgs bosons is partly much more challenging than in the Standard Model, as the production rates for the relevant signal processes can be heavily reduced. Furthermore, regions with the maximal theoretically allowed mass for the lightest scalar Higgs boson of about 140 GeV are also investigated.

The seven benchmark planes prove to be highly useful for the investigation of the discovery potential for NMSSM Higgs bosons with the help of a scanning method. All seven Higgs bosons and the twenty most relevant ATLAS search strategies are considered.

It is shown that in regions of the parameter space where the $H_{1/2} \rightarrow A_1 A_1$ branching ratio is smaller than 40% to 60%, depending on the size of the relevant couplings for the production of the scalar Higgs boson, at least one light scalar Higgs boson of the NMSSM can be discovered if systematic uncertainties are negligible. Furthermore, in parts of the parameter space of the NMSSM, not only the discovery of one neutral Higgs boson, but also of the charged Higgs bosons or of more than one neutral Higgs boson is possible. Such an observation would be a clear evidence for physics beyond the Standard Model. In this study, up to two neutral Higgs

bosons and the charged Higgs bosons are found to be observable simultaneously for favorable parameter settings.

In addition, the critical importance of the vector boson fusion search channels for an early Higgs boson discovery with a data volume of only 30 fb^{-1}, that is present for the Standard Model and the MSSM, can be confirmed also for the NMSSM case.

Still, in parameter regions where the most Standard Model-like Higgs boson has a mass around 115 GeV and its couplings are significantly reduced, the discovery of at least one Higgs boson will only be possible if the systematic uncertainties in the ttH, $H \to b\bar{b}$ channel are very well under control. As an alternative, the possibility to use vector boson fusion searches also for the high luminosity phase of the LHC could be studied.

In parameter regions with dominant $H_{1/2} \to A_1 A_1$ decays, no Higgs bosons are observable with ATLAS search strageties for SM and MSSM Higgs bosons. Therefore, the discovery potential for the vector boson fusion, $H_1 \to A_1 A_1 \to 4\tau$ channel at the ATLAS experiment is evaluated for the first time. The scalar Higgs boson is here assumed to be produced in vector boson fusion as the clear signature of this production mode is an excellent means for the suppression of the partly much more prevalent background processes. A special emphasis is put on the reconstruction of the mass of the scalar Higgs boson, which proved to be possible with the help of the collinear approximation. In spite of the very complex final state, mass resolutions of about 10% can be obtained. The developed cut selection method retains a sufficiently large number of signal events to yield significances around 5σ with 30 fb^{-1} if the $H_1 \to A_1 A_1 \to 4\tau$ decay chain is dominant, while the expected background level is smaller than one event at 95% confidence level. In regions of the parameter space with dominant $H_1 \to A_1 A_1 \to 4\tau$ decay, the gaps in the ATLAS discovery potential for NMSSM Higgs bosons are largely filled by this search mode. Thus, a clarification of the fundamental question how elementary particles acquire their mass will be possible also if such parameter settings are realized in nature.

Bibliography

[1] S. Weinberg, Phys. Rev. Lett. **19** (1967) 1264.

A. Salam, "Elementary Particle Theory", ed. N. Svartholm, Stockholm: Almqvist and Wiksell (1968) 367.

[2] S. Abachi *et al.* [D0 Collaboration], Phys. Rev. Lett. **74** (1995) 2632 [arXiv:hep-ex/9503003].

F. Abe *et al.* [CDF Collaboration], Phys. Rev. Lett. **74** (1995) 2626 [arXiv:hep-ex/9503002].

[3] LEP Electroweak Working Group webpage, `http://lepewwg.web.cern.ch/LEPEWWG`.

[4] LHC Study Group, CERN-AC-DI-FA-90-06.

[5] ATLAS Collaboration, CERN-LHCC-99-014/CERN-LHCC-99-015.

[6] ATLAS Collaboration, "The ATLAS Experiment at the CERN Large Hadron Collider", to appear.

[7] CMS Collaboration, CERN-LHCC-2006-001/CERN-LHCC-2006-021.

[8] P. W. Higgs, Phys. Lett. **12** (1964) 132.

G. S. Guralnik, C. R. Hagen and T. W. B. Kibble, Phys. Rev. Lett. **13** (1964) 585.

P. W. Higgs, Phys. Rev. **145** (1966) 1156.

[9] H. P. Nilles, M. Srednicki and D. Wyler, Phys. Lett. B **120** (1983) 346.

J. M. Frere, D. R. T. Jones and S. Raby, Nucl. Phys. B **222** (1983) 11.

J. P. Derendinger and C. A. Savoy, Nucl. Phys. B **237** (1984) 307.

J. R. Ellis, J. F. Gunion, H. E. Haber, L. Roszkowski and F. Zwirner, Phys. Rev. D **39** (1989) 844.

M. Drees, Int. J. Mod. Phys. A **4** (1989) 3635.

F. Franke and H. Fraas, Int. J. Mod. Phys. A **12** (1997) 479 [arXiv:hep-ph/9512366].

[10] P. Ramond, Phys. Rev. D **3** (1971) 2415.

A. Neveu and J. H. Schwarz, Nucl. Phys. B **31** (1971) 86.

J. L. Gervais and B. Sakita, Nucl. Phys. B **34** (1971) 632.

[11] J. Wess and B. Zumino, Nucl. Phys. B **70** (1974) 39.

A. Salam and J. A. Strathdee, Nucl. Phys. B **76** (1974) 477.

[12] F. Halzen and A. D. Martin, "Quarks & Leptons: An Introductory Course in Modern Particle Physics", John Wiley & Sons Inc., 1984.

[13] M. Schumacher, PhD thesis, BONN-IR-99-19.

[14] W. M. Yao *et al.* [Particle Data Group], J. Phys. G **33** (2006) 1.

[15] J. Goldstone, Nuovo Cim. **19** (1961) 154.
J. Goldstone, A. Salam and S. Weinberg, Phys. Rev. **127** (1962) 965.

[16] M. Spira and P. M. Zerwas, arXiv:hep-ph/9803257.

[17] B. W. Lee, C. Quigg and H. B. Thacker, Phys. Rev. Lett. **38** (1977) 883.

[18] S. Weinberg, Phys. Rev. Lett. **36** (1976) 294.

[19] K. Riesselmann, arXiv:hep-ph/9711456.

[20] R. Barate *et al.* [LEP Working Group for Higgs boson searches], Phys. Lett. B **565** (2003) 61 [arXiv:hep-ex/0306033].

[21] M. J. G. Veltman, Acta Phys. Polon. B **8** (1977) 475.

[22] T. T. E. Group *et al.* [CDF and D0 Collaborations], arXiv:0803.1683 [hep-ex].

[23] S. Sarkar, Rept. Prog. Phys. **59** (1996) 1493 [arXiv:hep-ph/9602260].

[24] M. Drees, arXiv:hep-ph/9611409.

[25] H. P. Nilles, Phys. Rept. **110** (1984) 1.

[26] H. Murayama, arXiv:hep-ph/0002232.

[27] A. Dobado, M. J. Herrero and S. Penaranda, Eur. Phys. J. C **12** (2000) 673 [arXiv:hep-ph/9903211].

[28] S. P. Martin, arXiv:hep-ph/9709356.

[29] M. Drees, R. M. Godbole and P. Roy, Theory and Phenomenology of Sparticles, World Scientific, 2004.

[30] S. R. Coleman and J. Mandula, Phys. Rev. **159** (1967) 1251.
R. Haag, J. T. Lopuszanski and M. Sohnius, Nucl. Phys. B **88** (1975) 257.

[31] J. R. Ellis, J. S. Hagelin, D. V. Nanopoulos, K. A. Olive and M. Srednicki, Nucl. Phys. B **238** (1984) 453.
J. R. Ellis, arXiv:hep-ph/9812235.

[32] A. Brignole, G. Degrassi, P. Slavich and F. Zwirner, Nucl. Phys. B **631** (2002) 195 [arXiv:hep-ph/0112177].
G. Degrassi, S. Heinemeyer, W. Hollik, P. Slavich and G. Weiglein, Eur. Phys. J. C **28** (2003) 133 [arXiv:hep-ph/0212020].

[33] M. S. Carena, S. Heinemeyer, C. E. M. Wagner and G. Weiglein, arXiv:hep-ph/9912223.
M. S. Carena, J. R. Ellis, A. Pilaftsis and C. E. M. Wagner, Nucl. Phys. B **586** (2000) 92 [arXiv:hep-ph/0003180].
M. S. Carena, S. Heinemeyer, C. E. M. Wagner and G. Weiglein, Eur. Phys. J. C **26** (2003) 601 [arXiv:hep-ph/0202167].

[34] J. E. Kim and H. P. Nilles, Phys. Lett. B **138** (1984) 150.

[35] D. J. Miller, R. Nevzorov and P. M. Zerwas, Nucl. Phys. B **681** (2004) 3 [arXiv:hep-ph/0304049].

[36] S. Baffioni, J. Gunion, D. J. Miller, A. Pilaftsis and D. Zerwas, published in: E. Accomando *et al.*, arXiv:hep-ph/0608079, pp. 193-204.

[37] S. Weinberg, Phys. Rev. Lett. **40** (1978) 223.

F. Wilczek, Phys. Rev. Lett. **40** (1978) 279.

[38] K. Hagiwara *et al.* [Particle Data Group], Phys. Rev. D **66** (2002) 010001.

[39] S. A. Abel, S. Sarkar and P. L. White, Nucl. Phys. B **454** (1995) 663 [arXiv:hep-ph/9506359].

Y. B. Zeldovich, I. Y. Kobzarev and L. B. Okun, Zh. Eksp. Teor. Fiz. **67** (1974) 3 [Sov. Phys. JETP **40** (1974) 1].

[40] A. Vilenkin, Phys. Rept. **121** (1985) 263.

[41] C. Panagiotakopoulos and K. Tamvakis, Phys. Lett. B **446** (1999) 224 [arXiv:hep-ph/9809475].

[42] R. Dermisek, J. F. Gunion and B. McElrath, Phys. Rev. D **76** (2007) 051105 [arXiv:hep-ph/0612031].

R. Dermisek and J. F. Gunion, Phys. Rev. D **75** (2007) 075019 [arXiv:hep-ph/0611142].

[43] T. Elliott, S. F. King and P. L. White, Phys. Rev. D **49** (1994) 2435 [arXiv:hep-ph/9308309].

[44] G. A. Moortgat-Pick, S. Hesselbach, F. Franke and H. Fraas, JHEP **0506** (2005) 048 [arXiv:hep-ph/0502036].

[45] A. H. Chamseddine, R. Arnowitt and P. Nath, Phys. Rev. Lett. **49** (1982) 970.

R. Barbieri, S. Ferrara and C. A. Savoy, Phys. Lett. B **119** (1982) 343.

J. R. Ellis, D. V. Nanopoulos, K. A. Olive and K. Tamvakis, Nucl. Phys. B **221** (1983) 524.

[46] J. R. Ellis, J. F. Gunion, H. E. Haber, L. Roszkowski and F. Zwirner, Phys. Rev. D **39** (1989) 844.

U. Ellwanger, M. Rausch de Traubenberg and C. A. Savoy, Phys. Lett. B **315** (1993) 331 [arXiv:hep-ph/9307322].

U. Ellwanger, M. Rausch de Traubenberg and C. A. Savoy, Z. Phys. C **67** (1995) 665 [arXiv:hep-ph/9502206].

U. Ellwanger, M. Rausch de Traubenberg and C. A. Savoy, Nucl. Phys. B **492** (1997) 21 [arXiv:hep-ph/9611251].

[47] A. Djouadi *et al.*, arXiv:0801.4321 [hep-ph].

[48] S. Heinemeyer, W. Hollik, F. Merz and S. Penaranda, Eur. Phys. J. C **37** (2004) 481 [arXiv:hep-ph/0403228].

[49] LHCb Collaboration, CERN-LHCC-98-4.

[50] P. Giubellino [ALICE Collaboration], Nucl. Instrum. Meth. A **344** (1994) 27.

[51] T. Sjostrand, S. Mrenna and P. Skands, JHEP **0605** (2006) 026 [arXiv:hep-ph/0603175].

[52] G. Corcella *et al.*, JHEP **0101** (2001) 010 [arXiv:hep-ph/0011363].

G. Marchesini, B. R. Webber, G. Abbiendi, I. G. Knowles, M. H. Seymour and L. Stanco, Comput. Phys. Commun. **67** (1992) 465.

[53] "GEANT - Detector Description and Simulation Tool", CERN Program Library Long Writeup W5013.

[54] D. Cavalli *et al.*, ATL-PHYS-INT-2007-005.

E. Richter-Was, D. Froidevaux and L. Poggioli, ATL-PHYS-98-131.

[55] M. Röder, M. A. Pleier, E. von Törne, N. Wermes, ATL-COM-PHYS-2008-025.

[56] I. Rottländer, diploma thesis, BONN-IB-2005-03.

[57] C. Cojocaru *et al.* [ATLAS Liquid Argon EMEC/HEC Collaboration], Nucl. Instrum. Meth. A **531** (2004) 481 [arXiv:physics/0407009].

[58] G. C. Blazey *et al.*, arXiv:hep-ex/0005012.

[59] S. D. Ellis and D. E. Soper, Phys. Rev. D **48** (1993) 3160 [arXiv:hep-ph/9305266].

S. Catani, Y. L. Dokshitzer, M. H. Seymour and B. R. Webber, Nucl. Phys. B **406** (1993) 187.

[60] M. Cacciari and G. P. Salam, Phys. Lett. B **641** (2006) 57 [arXiv:hep-ph/0512210].

[61] I. Abt *et al.* [H1 Collaboration], Nucl. Instrum. Meth. A **386** (1997) 348.

[62] S. Asai *et al.*, Eur. Phys. J. C **32S2** (2004) 19 [arXiv:hep-ph/0402254].

[63] S. Menke, personal communication.

[64] K. Lohwasser, personal communication.

[65] I. Tsukerman, ATL-COM-PHYS-2007-083.

M. Schmitz, personal communication.

[66] M. Spira, Fortsch. Phys. **46** (1998) 203 [arXiv:hep-ph/9705337]. Programs are available at `http://people.web.psi.ch/spira/proglist.html`.

[67] B. Mellado *et al.*, ATL-COM-PHYS-2007-024.

[68] T. Hahn, S. Heinemeyer, F. Maltoni, G. Weiglein and S. Willenbrock, arXiv:hep-ph/0607308.

[69] D. L. Rainwater and D. Zeppenfeld, JHEP **9712** (1997) 005 [arXiv:hep-ph/9712271].

[70] D. L. Rainwater, D. Zeppenfeld and K. Hagiwara, Phys. Rev. D **59** (1999) 014037 [arXiv:hep-ph/9808468].

[71] V. D. Barger, R. J. N. Phillips and D. Zeppenfeld, Phys. Lett. B **346** (1995) 106 [arXiv:hep-ph/9412276].

[72] K. A. Assamagan, Y. Coadou and A. Deandrea, Eur. Phys. J. direct C **4** (2002) 9 [arXiv:hep-ph/0203121].

[73] A. Belyaev, D. Garcia, J. Guasch and J. Sola, Phys. Rev. D **65** (2002) 031701 [arXiv:hep-ph/0105053].

[74] D. Dicus, T. Stelzer, Z. Sullivan and S. Willenbrock, Phys. Rev. D **59** (1999) 094016 [arXiv:hep-ph/9811492].

[75] J. Alwall, arXiv:hep-ph/0503124.

[76] M. S. Carena, D. Garcia, U. Nierste and C. E. M. Wagner, Nucl. Phys. B **577** (2000) 88 [arXiv:hep-ph/9912516].

[77] A. Djouadi, J. Kalinowski and M. Spira, Comput. Phys. Commun. **108** (1998) 56 [arXiv:hep-ph/9704448].

[78] J. Cammin and M. Schumacher, ATL-PHYS-2003-024.

[79] S. Cucciarelli *et al.*, CERN-CMS-NOTE-2006-119.

[80] R. K. Ellis, I. Hinchliffe, M. Soldate and J. J. van der Bij, Nucl. Phys. B **297** (1988) 221.

[81] D. L. Rainwater, arXiv:hep-ph/9908378.

[82] K. Cranmer, B. Mellado, W. Quayle and S. L. Wu, ATL-PHYS-2003-036.

[83] M. Schumacher, ATL-COM-PHYS-2004-070.

[84] M. Schumacher, arXiv:hep-ph/0410112.

[85] K. Jakobs and T. M. Trefzger, ATL-PHYS-2000-015.

[86] K. Cranmer, B. Mellado, W. Quayle and S. L. Wu, ATL-PHYS-2004-034.

[87] D. Cavalli and G. Negri, ATL-PHYS-2003-009.

[88] J. Thomas, ATL-PHYS-2003-003.

[89] S. González, E. Ros, M. A. Vos, ATL-PHYS-2002-021.

[90] D. Cavalli and P. Bosatelli, ATL-PHYS-2000-001.

[91] C. Biscarat and M. Dosil, ATL-PHYS-2003-038.

[92] B. Mohn, M. Flechl and J. Alwall, ATL-PHYS-PUB-2007-006.

[93] M. Schumacher, published in: E. Accomando *et al.*, arXiv:hep-ph/0608079, pp. 110-116.

[94] M. Dührssen, S. Heinemeyer, H. Logan, D. Rainwater, G. Weiglein and D. Zeppenfeld, Phys. Rev. D **70** (2004) 113009 [arXiv:hep-ph/0406323].

[95] D. K. Ghosh, R. M. Godbole and D. P. Roy, Phys. Lett. B **628** (2005) 131 [arXiv:hep-ph/0412193].

[96] M. Lehmacher, diploma thesis, BONN-IB-2006-02.

[97] U. Ellwanger, J. F. Gunion, C. Hugonie and S. Moretti, arXiv:hep-ph/0401228.

[98] D. J. Miller and S. Moretti, arXiv:hep-ph/0403137.

[99] U. Ellwanger, J. F. Gunion and C. Hugonie, JHEP **0507** (2005) 041 [arXiv:hep-ph/0503203].

[100] U. Ellwanger and C. Hugonie, Mod. Phys. Lett. A **22** (2007) 1581 [arXiv:hep-ph/0612133].

[101] A. Djouadi and R. Godbole, personal communication.

[102] U. Ellwanger, J. F. Gunion and C. Hugonie. The program package can be downloaded at `http://www.th.u-psud.fr/NMHDECAY/nmssmtools.html`.

[103] U. Ellwanger and C. Hugonie, Comput. Phys. Commun. **175** (2006) 290 [arXiv:hep-ph/0508022].

U. Ellwanger, J. F. Gunion and C. Hugonie, JHEP **0502** (2005) 066 [arXiv:hep-ph/0406215].

[104] U. Ellwanger and C. Hugonie, Comput. Phys. Commun. **177** (2007) 399 [arXiv:hep-ph/0612134].

[105] J. Abdallah *et al.* [DELPHI Collaboration], Eur. Phys. J. C **31** (2004) 421 [arXiv:hep-ex/0311019].

G. Abbiendi *et al.* [OPAL Collaboration], Eur. Phys. J. C **35** (2004) 1 [arXiv:hep-ex/0401026].

[106] LEP Collaboration, arXiv:hep-ex/0107031.

LEP Susy Working Group, LEPSUSYWG Note/02-04.1.

[107] B. Abbott *et al.* [D0 Collaboration], Phys. Rev. Lett. **83** (1999) 4937 [arXiv:hep-ex/9902013].

V. M. Abazov *et al.* [D0 Collaboration], Phys. Rev. Lett. **88** (2002) 171802 [arXiv:hep-ex/0108018].

A. A. Affolder *et al.* [CDF Collaboration], Phys. Rev. Lett. **84** (2000) 5704 [arXiv:hep-ex/9910049].

A. A. Affolder *et al.* [CDF Collaboration], Phys. Rev. Lett. **88** (2002) 041801 [arXiv:hep-ex/0106001].

[108] S. Schael *et al.* [The LEP Collaborations], Eur. Phys. J. C **47** (2006) 547 [arXiv:hep-ex/0602042].

[109] F. Domingo and U. Ellwanger, JHEP **0712** (2007) 090 [arXiv:0710.3714 [hep-ph].

[110] M. S. Carena, H. E. Haber, S. Heinemeyer, W. Hollik, C. E. M. Wagner and G. Weiglein, Nucl. Phys. B **580** (2000) 29 [arXiv:hep-ph/0001002].

[111] J. Hamann, S. Hannestad, M. S. Sloth and Y. Y. Y. Wong, Phys. Rev. D **75** (2007) 023522 [arXiv:astro-ph/0611582].

[112] K. S. Babu and S. M. Barr, Phys. Rev. D **49** (1994) 2156 [arXiv:hep-ph/9308217].

N. Haba, M. Matsuda and M. Tanimoto, Phys. Rev. D **54** (1996) 6928 [arXiv:hep-ph/9512421].

N. Haba, Prog. Theor. Phys. **97** (1997) 301 [arXiv:hep-ph/9608357].

[113] I. Rottländer and M. Schumacher, published in: N. E. Adam *et al.*, arXiv:0803.1154, pp. 71-76.

[114] M. Spira and S. Heinemeyer, personal communication.

[115] T. Plehn, Phys. Rev. D **67** (2003) 014018 [arXiv:hep-ph/0206121].

[116] S. Heinemeyer, W. Hollik and G. Weiglein, Comput. Phys. Commun. **124** (2000) 76 [arXiv:hep-ph/9812320].

G. Degrassi, S. Heinemeyer, W. Hollik, P. Slavich and G. Weiglein, Eur. Phys. J. C **28** (2003) 133 [arXiv:hep-ph/0212020].

S. Heinemeyer, W. Hollik and G. Weiglein, Eur. Phys. J. C **9** (1999) 343 [arXiv:hep-ph/9812472].

[117] W. A. Rolke and A. M. Lopez, arXiv:physics/0606006.

W. A. Rolke, A. M. Lopez and J. Conrad, Nucl. Instrum. Meth. A **551** (2005) 493 [arXiv:physics/0403059].

[118] J. J. Olivero and R. L. Longbothum, J. Quant. Spectrosc. Radiat. Transfer **17** (1977) 233

[119] M. Dührssen, ATL-PHYS-2003-030.

[120] Estimate from a discussion with E. Paganis.

[121] Estimate from a discussion with M. Flechl.

[122] M. Drees, M. Guchait and D. P. Roy, Phys. Lett. B **471** (1999) 39 [arXiv:hep-ph/9909266].

[123] C. Blochinger, F. Franke and H. Fraas, Nucl. Instrum. Meth. A **472** (2001) 144 [arXiv:hep-ph/0008167].

[124] N. E. Adam, V. Halyo, M. Herquet and S. Gleyzer, published in: N. E. Adam *et al.*, arXiv:0803.1154, pp. 85-89.

[125] S. Baffioni, D. Zerwas, talks in the ATLAS Higgs working group meeting.

[126] K. Cheung, J. Song and Q. S. Yan, Phys. Rev. Lett. **99** (2007) 031801 [arXiv:hep-ph/0703149].

[127] B. A. Dobrescu, G. L. Landsberg and K. T. Matchev, Phys. Rev. D **63** (2001) 075003 [arXiv:hep-ph/0005308].

[128] M. Rast, diploma thesis, BONN-IB-2008-02.

[129] J. Alwall *et al.*, JHEP **0709** (2007) 028 [arXiv:0706.2334 [hep-ph]].

F. Maltoni and T. Stelzer, JHEP **0302** (2003) 027 [arXiv:hep-ph/0208156].

T. Stelzer and W. F. Long, Comput. Phys. Commun. **81** (1994) 357 [arXiv:hep-ph/9401258].

[130] S. Frixione, P. Nason and B. R. Webber, JHEP **0308** (2003) 007 [arXiv:hep-ph/0305252].

S. Frixione and B. R. Webber, JHEP **0206** (2002) 029 [arXiv:hep-ph/0204244].

S. Frixione and B. R. Webber, arXiv:hep-ph/0506182.

[131] M. L. Mangano, M. Moretti, F. Piccinini, R. Pittau and A. D. Polosa, JHEP **0307** (2003) 001 [arXiv:hep-ph/0206293].

[132] J. Pumplin, D. R. Stump, J. Huston, H. L. Lai, P. Nadolsky and W. K. Tung, JHEP **0207** (2002) 012 [arXiv:hep-ph/0201195].

[133] M. Herquet, personal communication.

[134] S. Jadach, Z. Was, R. Decker and J. H. Kuhn, Comput. Phys. Commun. **76** (1993) 361.

S. Jadach, J. H. Kuhn and Z. Was, Comput. Phys. Commun. **64** (1990) 275.

[135] E. Barberio and Z. Was, Comput. Phys. Commun. **79** (1994) 291.

E. Barberio, B. van Eijk and Z. Was, Comput. Phys. Commun. **66** (1991) 115.

[136] The model was implemented by M. Herquet.

[137] G. Cowan, personal communication.

G. Cowan, "Statistical significance estimation with Poisson uncertainty in the expected signal and background", to appear.

[138] U. Ellwanger, personal communication.

[139] A. Stuart, J. K. Ord und S. Arnold, "Advanced Theory of Statistics, Volume 2A", London Oxford University Press, 1999.

A. Calculation of the Higgs boson couplings to gluons

Like the couplings to massive vector bosons and fermions, also the couplings of the neutral Higgs bosons to gluons are calculated by NMHDECAY [103]. However, these directly calculated values do not include relevant radiative QCD corrections that are significant above all for the couplings of the pseudoscalar Higgs bosons to gluons [138]. In order to obtain an estimate for these couplings that includes radiative corrections, the couplings relative to their Standard Model value are extracted from the partial widths of the H→gg decay[1]:

$$\frac{g^2_{\mathrm{Hgg,NMSSM}}}{g^2_{\mathrm{Hgg,SM}}} = \frac{\Gamma(H \to gg)_{\mathrm{NMSSM}}}{\Gamma(H \to gg)_{\mathrm{SM}}}. \tag{A.1}$$

The partial widths of the Standard Model Higgs boson are taken from HDECAY [77]. A calculation of the gluon couplings from the known couplings to up-type and down-type fermions with a suitable program, eg. with HIGLU [66], is in principle also possible, but this method is too time-consuming to be used in the parameter scans presented here.

For a comparison of the gluon couplings from NMHDECAY and HIGLU, NMHDECAY is run in the decoupling limit. In this limit, it effectively calculates parameter points of the MSSM. The results of such a comparison for selected parameter points in the $\mathrm{M_h}$max Scenario of the MSSM and for selected Higgs bosons are shown in Tab. A.1. The first two rows list the couplings of the lightest scalar Higgs boson for very low and very high M_A. For these points, the agreement between NMHDECAY and HIGLU is reasonable.

For the third point, the coupling of the pseudoscalar Higgs boson to gluons that is directly calculated by NMHDECAY only has about half the size of the coupling calculated with HIGLU. In contrast to that, the prediction from HIGLU is correctly reproduced by the coupling calculated from the partial widths. The difference is due to sizeable radiative corrections [138]. A similar behavior is observed for many different parameter points of the MSSM.

In Tab. A.2, the gluon couplings directly calculated by NMHDECAY and obtained from the partial widths are compared for two exemplary NMSSM points in the λ/κ plane of the Reduced Couplings Scenario. Here, HIGLU is not listed as it does not include NMSSM physics. The first

[1] To obtain a reasonable behavior, the number of flavors running in the quark loop is set to five in NMHDECAY. The default value is three.

MSSM Point		**Higgs boson**	**Higgs boson mass**	**Gluon coupling / SM value**		
				NMHDECAY		HIGLU
$\tan\beta$	M_A			direct	from widths	
3	50 GeV	h	48 GeV	1.353	1.350	1.212
3	1000 GeV	h	116 GeV	0.976	0.951	1.000
3	380 GeV	A	380 GeV	0.328	0.615	0.618

Tab. A.1: Comparison of the gluon couplings calculated by NMHDECAY and HIGLU for selected parameter points in the $\mathrm{M_h}$max Scenario of the MSSM and for selected Higgs bosons.

NMSSM Point		**Higgs boson**	**Higgs boson mass**	**Gluon coupling / SM value** NMHDECAY	
λ	κ			direct	from widths
0.016	-0.0034	H_1	99 GeV	0.454	0.442
0.016	-0.0034	H_2	114 GeV	0.552	0.538
0.016	-0.0034	H_3	144 GeV	0.971	0.950
0.016	-0.0034	A_1	98 GeV	0.040	0.060
0.016	-0.0034	A_2	133 GeV	0.334	0.510
0.015	-0.0014	H_1	35 GeV	0.123	0.128
0.015	-0.0014	H_2	118 GeV	0.933	0.911
0.015	-0.0014	H_3	270 GeV	0.384	0.380
0.015	-0.0014	A_1	66 GeV	0.0057	0.0084
0.015	-0.0014	A_2	268 GeV	0.123	0.203

Tab. A.2: Comparison of the gluon couplings calculated by directly by NMHDECAY and from the partial widths for selected parameter points in the λ/κ-plane of the Reduced Couplings Scenario of the NMSSM.

point listed is the benchmark point taken from Ref. [99]. A similar comparison was done also for other parameter points in all NMSSM benchmark scenarios from Chap. 6. The differences between the directly calculated values and the values from the partial widths are smaller than about 3% for the scalar Higgs bosons if their masses are in the for a discovery most promising range from about 114 to 800 GeV. Accordingly, for the calculation of the couplings of the scalar Higgs bosons to gluons, it is not critical which of the two approaches is used. However, for the couplings of the pseudoscalar Higgs bosons, also in the NMSSM, relevant differences of up to 50% between the two approaches are observed. As in the MSSM limit, the couplings calculated from the partial widths are here preferable. In the thesis at hand, the couplings to gluon as obtained from the partial widths are utilized for this reason.

As the calculation of the couplings is the same in NMSPEC [104] and NMHDECAY, the above discussion holds for NMSPEC as well. For the couplings to vector bosons and to up-type and down-type fermions, the values directly calculated by NMHDECAY and by other programs specialized for the SM and MSSM [66] are in good agreement.

B. Calculation of $H^{\pm}$ production cross sections

The $gb \to tH^-/g\bar{b} \to \bar{t}H^+$ production process The coupling of the charged Higgs bosons to heavy fermions, $H^{\pm}tb$, is not directly calculated by the programs from the NMSSMTOOLS package [102]. Therefore, the best way to obtain the coupling is from the partial widths of the $H^+ \to t\bar{b}$ decay [138]:

$$\frac{g^2_{H^{\pm}tb,NMSSM}}{g^2_{H^{\pm}tb,MSSM}} = \frac{\Gamma(H^+ \to t\bar{b})_{NMSSM}}{\Gamma(H^+ \to t\bar{b})_{MSSM}}. \tag{B.1}$$

The partial width of the $H^+ \to t\bar{b}$ decay for the MSSM is calculated with NMHDECAY [103] in the decoupling limit. With Eq. B.1, no absolute coupling sizes can be obtained, but only the coupling relative to its value in the MSSM. As the charged Higgs boson couplings in the MSSM vary depending on the chosen MSSM parameters, a designated point in the MSSM is chosen as fixed reference point to be used in the calculation.

As a next step, the $gb \to tH^-/g\bar{b} \to \bar{t}H^+$ production cross section of the MSSM is scaled to the NMSSM case according to the coupling:

$$\sigma_{NMSSM} = \sigma_{MSSM} \cdot \frac{g^2_{H^{\pm}tb,NMSSM}}{g^2_{H^{\pm}tb,MSSM}}. \tag{B.2}$$

For a consistent calculation, the MSSM cross sections used in Eq. B.2 must be valid for the same fixed MSSM reference point that is used in the calculation of the $H^{\pm}tb$ coupling.

In this thesis, the $gb \to tH^-/g\bar{b} \to \bar{t}H^+$ cross sections are taken from Ref. [115]. These cross sections do not include supersymmetric radiative corrections. The influence of such radiative corrections is sizeable for large $\tan\beta$ and negligible for small $\tan\beta$. For a small $\tan\beta$ of about 2.5 GeV, the partial widths of the $H^+ \to t\bar{b}$ decay obtained with NMHDECAY in the MSSM limit is largely independent of the chosen parameter settings and corresponds to the partial widths without supersymmetric radiative corrections. The MSSM reference point is therefore chosen to be in the $M_h$max Scenario at $\tan\beta$=2.5[1]. For any other scenario with the same $\tan\beta$, the same results would have been achieved. As for such a parameter point, the influence of the radiative corrections is negligible, the cross section from Ref. [115] are applicable.

The final NMSSM production cross section obtained with Eq. B.2 include the effects of the radiative corrections appropriate for each scan point, as the partial width of the $H^+ \to t\bar{b}$ decay in the NMSSM is calculated including these corrections. For a correct treatment of the radiative corrections, the above procedure is also needed if the charged Higgs bosons of the NMSSM and MSSM are assumed to be identical.

The procedure described above can only be applied if the mass of the charged Higgs bosons is heavier than the sum of the top quark mass and the bottom quark mass, since otherwise, the branching ratio of the $H^+ \to t\bar{b}$ decay vanishes. Then, it is not possible to calculate the $gb \to tH^-/g\bar{b} \to \bar{t}H^+$ production cross sections. Moreover, such parameter points may be in the problematic transition region (see Chap. 5.1). For these reasons, the production cross sections are then set to zero.

[1] The second parameter of the Higgs sector is not fixed in order to obtain different masses of the charged Higgs bosons.

Charged Higgs boson production from top quark decays To calculate cross sections for charged Higgs boson production from top quark decays, the $t\bar{t}$ production cross section is assumed to be 482 pb at leading order. The correct branching ratio of the $t \to H^+b$ decay must be applied to this number. This branching ratio is not calculated by the NMSSMTOOLS package. Moreover, as for such low masses, the $H^+ \to t\bar{b}$ decay is forbidden, the $H^{\pm}tb$ coupling cannot be obtained, and no scaling of MSSM branching ratios is possible.

In the NMSSM, the charged Higgs bosons are changed only marginally to with respect to the MSSM. For example, $H^+ \to t\bar{b}$ branching ratios calculated with NMHDECAY in the MSSM limit and for the NMSSM case are equal for identical parameter settings. For this reason, it is assumed here that the $t \to H^+b$ branching ratios obtained for the MSSM with FeynHiggs [116] are applicable to the NMSSM as well.

However, the $t \to H^+b$ branching ratio may vary significantly depending on the chosen MSSM parameters. In principle, the branching ratios for different charged Higgs boson masses therefore have to be calculated separately for every benchmark scenario from Chap. 6. However, only in the Reduced Couplings Scenario, the charged Higgs bosons are light enough to be produced in top quark decays, so that only for this scenario, the branching ratios are relevant. For the λ/κ and the A_λ/A_κ plane, the calculation of the charged Higgs boson production cross section from top quark decays is straightforward, since the features of the charged Higgs bosons to a good approximation do not depend on λ, κ, A_λ and A_κ. Thus, the same set of branching ratios can be used for every scan point in these planes, depending only on the mass of the charged Higgs boson.

For the $\tan\beta/\mu$ plane, the situation is more complicated, as the $t \to H^+b$ branching ratio does not only depend on the charged Higgs boson mass, but also on the two scan parameters $\tan\beta$ and μ. Here, a two-dimensional extrapolation depending on the charged Higgs boson mass and on $\tan\beta$ is done, so that the influence of $\tan\beta$ on the branching ratio is taken into account. Yet, a three-dimensional extrapolation also in dependence of μ would be too time-consuming to be used for the parameter scans. Therefore, $\mu = -284$ GeV is used for the calculation of the branching ratios independently of the actual value of μ in the scan. This value for μ is also used for the λ/κ and the A_λ/A_κ plane of the Reduced Couplings Scenario. Reasons why this choice seems justified will be given in the following.

The charged Higgs bosons are light enough to be produced in top quark decay in the $\tan\beta/\mu$ plane only at quite large negative μ or at small $\tan\beta$ (see Fig. 7.15). At large $\tan\beta$, the entire region where $t \to H^+b$ decays are allowed has $|\mu|$ values larger than 284 GeV. This means that the branching ratio used here is smaller than the actual one, so the utilized choice for μ is a conservative estimate in this region.

For small $|\mu|$, the $t \to H^+b$ decay is only possible for $\tan\beta \lesssim 6$. In this region, varying μ only changes the branching ratio on the per mill level. The relative difference between branching ratios for the different μ-values used in the scan is less than 3% of their absolute value.

Moreover, the impact of a variation of the $t \to H^+b$ branching ratio on the observed discovery contours of the affected search modes is generally small. Changing the branching ratio so much that the overall cross section for charged Higgs boson production from top quark decays is half its actual value only leads to a shift of the discovery contours of about $\Delta\tan\beta = 0.5$ in the low $\tan\beta$ region[2]. At high $\tan\beta$[3], the shift is significantly smaller than $\Delta\mu = 1$ GeV. Yet, the actual changes in the branching ratio due to μ are even much smaller.

[2] In this region, the discovery contour is approximately parallel to the μ-axis. For this reason, the shift is given here in terms of a deviation in $\tan\beta$.

[3] In this region, the discovery contour is approximately parallel to the $\tan\beta$-axis. For this reason, the shift is given here in terms of a deviation in μ.

C. The profile likelihood method

In this thesis, the profile likelihood method is used for significance calculation. In the following, the method will be reviewed based on Refs. [117, 137]. The presented method also takes into account the Poisson fluctuations in estimates of both signal and background levels that arise from limited data samples.

In particle physics, the question if claiming a discovery, eg. of a new particle, is justified, often arises. In statistics, such a problem falls under the heading of hypothesis testing. The probability of claiming a false discovery, i.e. when the signal excess is only due to statistical fluctuations of the background, has to be very small. Commonly, it is to be required to be smaller than $2.88 \cdot 10^{-7}$, which corresponds to a 5σ discovery. Such a low probability is needed because normally, the mass of the new particle to be discovered is unknown, so that a fluctuation that could fake a signal can occur everywhere in the possible mass range. The probability for a single fluctuation therefore has to be multiplied with the number of possible mass bins to get the total probability for claiming a false discovery.

The profile likelihood method is based on the frequently used method of a likelihood ratio test. In a general problem, there is measured data, i.e. n independent observations $X = (X_1, ..., X_n)$. This data is assumed to be distributed according to the probability density $f(x|\pi, \theta)$, which depends on k parameters $\pi = (\pi_1, ..., \pi_k)$, that are of interest to the researcher, but also of l nuisance parameters $\theta = (\theta_1, ...\theta_l)$, that are part of the possible parameter space. The full likelihood function $L(\pi, \theta|X)$ is then given by

$$L(\pi, \theta|X) = \prod_{i=1}^{n} f(X_i|\pi, \theta) \tag{C.1}$$

It gives a measure for the probability that the measured data is achieved with given π and θ. Normally, the goal of the measurement is to check whether the data is consistent with the assumed value for π or not. In case of particle physics experiments, this normally means testing the null hypothesis $H_0 : \pi \in \pi_0$ (no signal found). If this test fails, the existence of a signal is confirmed. The likelihood ratio test is defined by

$$\lambda(\pi_0|X) = \frac{\sup\left(L(\pi_0, \theta|X)\right)}{\sup\left(L(\pi, \theta|X)\right)} \tag{C.2}$$

The supremum in the denominator refers to the full parameter space, whereas the supremum in the numerator refers only to the subspace with $\pi = \pi_0$. Accordingly, the ratio is small if parameter points in an alternative hypothesis exist that are more likely to describe the measured data than all parameter points in the null hypothesis H_0. Then, the null hypothesis is rejected.

In the next step, this method is applied to a more concrete example typical for particle physics, which is the search for a rare decay with an only approximately known expected background. As an assumption, x events are observed in the signal region, for example inside a mass window, and a total of y events in the background region. The background region can for example be the sidebands of a mass distribution. The true signal rate is to be μ. The true background rate in the signal region is b and plays the role of a nuisance parameter, as it is not

the parameter of interest to be measured, but influences the measured data. As the probability that a background event falls into the background region divided by the probability that it falls into the signal region is defined as τ. The total number of background events expected in the background region is then equal to τb. Moreover, if not measured data, but Monte Carlo data samples are used, τ can be interpreted as a scale factor that relates the effective integrated luminosity of the Monte Carlo background sample to that of the real data. Here, it is assumed that τ can be determined with negligible uncertainty.

If the number of observed events in the signal region is small, it is adequately described by a Poisson distribution. The probability density for the number of events in the signal region is then:

$$X \sim Pois(\mu + b), \tag{C.3}$$

Similarly, the probability density for the number of events in the background region is

$$Y \sim Pois(\tau b) \tag{C.4}$$

Large capital letters X, Y here denote random variables, whereas x, y denote realizations, i.e. observed values, of these random variables. According to Eq. C.1, the likelihood function for the measured data x, y is then given by the multiplication of X and Y:

$$L(x, y|\mu, b) = \frac{(\mu + b)^x}{x!} e^{-(\mu+b)} \cdot \frac{(\tau b)^y}{y!} e^{-\tau b} \tag{C.5}$$

The likelihood test ratio is then:

$$\lambda(\mu_0|x, y) = \frac{L(\mu_0, \hat{b}(\mu_0)|x, y)}{L(\hat{\mu}, \hat{b}|x, y)} \tag{C.6}$$

Here, $\hat{\mu}$, $\hat{b}$ and $\hat{b}(\mu)$ are the maximum likelihood estimators for which the supremum is obtained. As the denominator runs of over the full parameter space, μ and b are maximized separately to obtain a maximum value. In the numerator, a hypothesis μ_0 (normally the null hypothesis, which here corresponds to $\mu = 0$) is made. Therefore, $\hat{b}(\mu_0)$ is maximized only for this hypothesis μ_0. Here, it becomes clear why this method is called the profile likelihood method: The likelihood function in the numerator is only taken over the profile with μ_0 of the total parameter space given by μ and b. The maximum likelihood estimators can be found by requiring the derivative of the logarithm[1] of the likelihood function to be zero. For the here discussed case, they are given by:

$$\hat{\mu} = x - y/\tau \tag{C.7}$$

$$\hat{b} = y/\tau \tag{C.8}$$

$$\hat{b}(\mu) = \frac{x + y - (1 + \tau)\mu + \sqrt{(x + y - (1 - \tau)\mu)^2 + 4(1 + \tau)y\mu}}{2(1 + \tau)} \tag{C.9}$$

In the case of the null hypothesis $\mu = 0$, the formulas corresponding to Eqs. C.5 and C.9 are easier:

$$L(x, y|0, b) = \frac{b^x}{x!} e^{-b} \cdot \frac{(\tau b)^y}{y!} e^{-\tau b} \tag{C.10}$$

$$\hat{b}(0) = (x + y)/(1 + \tau) \tag{C.11}$$

[1] As the logarithms is a monotonous function, it does not alter the position of the maximum.

Plugging the maximum likelihood estimators into the likelihood test ratio from Eq. C.6 then yields:

$$\lambda(0|x,y) = \frac{\left(\frac{x+y}{1+\tau}\right)^{x+y} \tau^{y}}{x^{x} y^{x}} \tag{C.12}$$

In the next step, a general theorem (eg. Ref. [139]) is used: If the null hypothesis is true, then $-\log\lambda(\pi_0|X)$ has a χ^2-distribution in the limit of a large sample size. The number of degrees of freedom of the χ^2-distribution is given by the differences between the number of free parameters in the null hypothesis and the total number of free parameters, which is here equal to one. Accordingly, the function

$$-2\log\lambda(0|x,y) = 2\left(x\log(x) + y\log(y) - (x+y)\log\left(\frac{x+y}{1+\tau}\right) - y\log(\tau)\right) \tag{C.13}$$

has a χ^2_1-distribution. It can be shown that the significance can then be obtained by (see eg. [137]):

$$\text{Significance} = \sqrt{-2\log\lambda(0|\text{x},\text{y})} \tag{C.14}$$

In this model, the relative systematic uncertainties on the background, Δ, can be easily incorporated. To do so, it is assumed that the systematic uncertainty is obtained from a measurement of the sidebands. The number of events expected in the sidebands (background region) is given by τb and the absolute statistical uncertainty on this number is given by $\sqrt{\tau b}$. This uncertainty determines the relative uncertainty Δ of the number of the expected background events.

$$\sqrt{\tau b} = \Delta \cdot \tau b \tag{C.15}$$

From this results the following expression for τ, that can be used in Eq. C.13 for the calculation of the significance in the presence of systematic background uncertainties, can be derived:

$$\tau = \frac{1}{\Delta^2 b} \tag{C.16}$$

Moreover, the method can be easily transferred to multiple channels by calculating Eq. C.13 for every channel and instead of Eq. C.14 taking the square-root of the sum of the calculated values.

In the case of limited sample sizes, it may happen that all available events of a sample, eg. the background sample, are rejected in the signal selection (y=b=0). For this case, Eq. C.13 is not directly useable as not all logarithmic terms are well defined. Yet, $\lambda(0)$ can then be simplified to [137]:

$$\log\lambda(0) = -\mu\log(1+\tau). \tag{C.17}$$

Thus, the significance in this case only depends on the expected number of selected signal events μ and the size of the background sample, that is given by τ. The statistical fluctuations on the number of selected events (for this example eg. zero background events) is fully taken into account.

In Refs. [117], the profile likelihood method has been proven to have good coverage. Its main advantage is that it is very fast and reliable and thus very well suited for the calculation of significances for example in parameter scans with many scan points.

D. Generator cuts for the vector boson fusion, $H_1 \rightarrow A_1A_1 \rightarrow 4\tau \rightarrow 4\mu + 8\nu$ study

In this appendix, the details of the generator cuts and filters applied to the Monte Carlo samples that are used for the vector boson fusion, H→AA→4τ→4μ+8ν study are described. It must be taken care that the generator cuts and filters do not remove any events that might otherwise have passed the signal selection. On the other hand, generator and filter cuts that are suitably chosen help to optimize the run times of the Monte Carlo programs and the needed storage. An overview of all samples, the event generators and the generator cuts is given in Tab. D.1.

In the matrix element, radiation of collinear light jets and of jets with low energy is divergent. Therefore, a minimum cut on the p_T of the jets and their respective separation (ΔR or $\Delta\eta$) is required on the generator level for all processes containing light jets.

Moreover, since muons are treated as massless in MadGraph/MadEvent, there is a divergency at the photon peak for processes with Z/γ→$\mu\mu$. Therefore, a cut on the invariant mass of the muon pair in the order of twice the muon mass is applied to the affected samples. Such a $M_{\mathrm{ll}} > 0.2$ GeV cut improves the unweighting efficiency to about a factor of 100 to 1000, depending on the process, and should not remove any physical events.

Furthermore, generator cuts on the p_T of the leptons in the final state are applied to the signal samples to further improve the unweighting efficiency. Care must be taken that no events that could pass the trigger requirement for the muons (one muon with $p_T > 20$GeV, or two muons with $p_T > 10$ GeV) and the selection cuts (three muons with $p_T > 6$ GeV) are removed. MadGraph only foresees cuts on the lepton with highest p_T and on all generated leptons, but not on the lepton with second-highest or third-highest p_T. To avoid a bias of the analysis results, a security margin for resolution effects must always be included for cuts on the generator level.

For processes where only three leptons in the final state are produced (ZWjj), all of these must have $p_T > 6$ GeV at the reconstruction step to pass the cut selection. A generator cut of $p_T > 4$ GeV can therefore be safely applied to all leptons. Regardless whether one muon with $p_T > 20$GeV or two muons with $p_T > 10$ GeV trigger the event, it is true for all triggered events that one muon must have a p_T of at least 10 GeV. Thus, a p_T cut of 8 GeV on the generator level is safe for the hardest lepton.

For processes with four leptons in the final state (ZZjj), one of the leptons can even be undetected, and the event passes the selection criteria nevertheless. Therefore, one of the leptons may have arbitrarily small momentum, and no p_T cut on all leptons is acceptable. However, still the trigger must be passed, so one lepton is here required to have a p_T larger than 8 GeV at the generator level.

Also b-jets (as in the $t\bar{t}$, $Zb\bar{b}$, $Zt\bar{t}$, $Wt\bar{t}$, $Wb\bar{b}$ processes) could in principle produce muons that could trigger the event. These muons are not yet present at the generator level, as they are produced in the decay of the bottom quark. It is assumed here that maximally two muons originate from b-jets in a single event. Then, at least the lepton with the highest p_T of the leptons present at the generator level should have a reconstructed p_T of 6 GeV or more, resulting in a $p_T > 4$ GeV generator cut for that lepton. In the samples from the ATLAS production ($t\bar{t}$, $Wb\bar{b}$) no generator cut on the leptons is performed.

Process	**Generator**	**Generator cuts**	**Filter**	**Remark**
Hjj→AAjj→ 4τ jj→4μ 8ν jj	MadGraph, special model	$p_{T\mathrm{jet}} > 10$ GeV $\Delta\eta_{\mathrm{jetjet}} > 1$	-	$M_{\mathrm{A}}, M_{\mathrm{H}}$ varied
ZZjj (QCD)	MadGraph	$p_{T\mathrm{jet}} > 10$ GeV $\lvert\eta_{\mathrm{jet}}\rvert < 7$ $\Delta R_{\mathrm{jetjet}} > 0.3$ $p_{T,1\mathrm{lepton}} > 8$ GeV $M_{\mathrm{ll}} > 0.2$ GeV	3-lepton	-
ZZjj (EW)	MadGraph	$p_{T\mathrm{jet}} > 10$ GeV $\lvert\eta_{\mathrm{jet}}\rvert < 7$ $\Delta R_{\mathrm{jetjet}} > 1.0$ $p_{T,1\mathrm{lepton}} > 8$ GeV $M_{\mathrm{ll}} > 0.2$ GeV	3-lepton	-
WZjj (QCD)	MadGraph	$p_{T\mathrm{jet}} > 10$ GeV $\lvert\eta_{\mathrm{jet}}\rvert < 7$ $\Delta R_{\mathrm{jetjet}} > 0.3$ $p_{T\mathrm{l}} > 4$ GeV $p_{T,1\mathrm{lepton}} > 8$ GeV $M_{\mathrm{ll}} > 0.2$ GeV	3-lepton	-
WZjj (EW)	MadGraph	$p_{T\mathrm{jet}} > 15$ GeV $\lvert\eta_{\mathrm{jet}}\rvert < 7$ $\Delta R_{\mathrm{jetjet}} > 1.0$ $M_{\mathrm{jetjet}} > 100$ GeV $p_{T\mathrm{l}} > 4$ GeV $p_{T,1\mathrm{lepton}} > 8$ GeV $\lvert\eta_{\mathrm{l}}\rvert < 3$ $M_{\mathrm{ll}} > 0.2$ GeV	3-lepton	- -
$t\bar{t}$	MC@NLO	-	-	Common ATLAS production
$Zt\bar{t}$	MadGraph	$p_{T\mathrm{jet}} > 10$ GeV $\lvert\eta_{\mathrm{jet}}\rvert < 7$ $\Delta R_{\mathrm{jetjet}} > 0.3$ $p_{T,1\mathrm{lepton}} > 4$ GeV $M_{\mathrm{ll}} > 0.2$ GeV	3-lepton	-
$Wt\bar{t}$	MadGraph	$p_{T\mathrm{jet}} > 10$ GeV $\lvert\eta_{\mathrm{jet}}\rvert < 7$ $\Delta R_{\mathrm{jetjet}} > 0.3$ $p_{T,1\mathrm{lepton}} > 4$ GeV $M_{\mathrm{ll}} > 0.2$ GeV	3-lepton	-
$Zb\bar{b}$	MadGraph	$p_{T\mathrm{b}} > 5$ GeV $p_{T,1\mathrm{lepton}} > 4$ GeV $M_{\mathrm{ll}} > 0.2$ GeV	3-lepton	
$Wb\bar{b}$	Alpgen	$p_{T\mathrm{b}} > 12$ GeV $\Delta R_{\mathrm{bb}} > 0.2$	special	Common ATLAS production

Tab. D.1: Overview of the used samples with generator information and the applied filters.

Generally, the cuts for the electroweak ZWjj/ZZjj processes are chosen more strictly than for the other processes, as good unweighting efficiencies are especially desirable here due to long generation times.

Moreover, to the MadGraph background samples, a 3-lepton filter that requires at least three stable leptons (electrons or muons) with $p_T > 5$ GeV to be found within $|\eta| < 2.7$ is applied.

On the $Wb\bar{b}$ sample from the ATLAS production, a special filter is run. It requires two leptons to be found within $|\eta| < 2.7$. Electrons must have $p_T > 14$ GeV, muons $p_T > 5$ GeV to be counted for the filter. Additionally, there must be at least two leptons with equal charge in the event. As in the cut analysis, at least three muons are required, two of them have to have the same charge. Thus, the filter does not remove events relevant for this study, and the sample is useable.

Acknowledgement

Finishing this thesis would not have been possible without the help and guidance of many people. I would like to use the opportunity to thank at least some of them with a few sentences, although doing so is clearly little compared to how much I have profited from my last years with ATLAS.

First of all, I would like to thank my supervisor Prof. Dr. Norbert Wermes for the possibility to work on the intriguing topics of my thesis, for his reliable support, and also for being able to spend six months at CERN. Apart from that, I am very grateful to Prof. Dr. Markus Schumacher, who always found the time for discussions with me, for his friendly and competent mentoring.

The work on the benchmark scenarios and the correct scaling of the NMSSM cross sections required much input and numerous discussions with colleagues from theory. In this context, I am especially grateful to Abdelhak Djouadi, Rohini M. Godbole, Sally Dawson, Ulrich Ellwanger, Sven Heinemeyer and Michael Spira. Furthermore, I would like to thank Michel Herquet for his help with MadGraph.

During my work on this thesis, I always appreciated the friendly working climate in the Bonn group. Therefore, I wish to cordially thank all my colleagues for a great time. I would like to especially point out our system administrators Jan Schumacher, Duc Bao Ta and Nicolas Möser who all helped me a lot in case of technical problems, and Matthias Röder, who allowed me to use his highly convenient plotting tool.

Furthermore, I would also like to thank the entire Pixel community for a most interesting and enjoyable time in Geneva, and for learning how to make a decent cheese fondue.

At last, but not at all least, I am very grateful to my family and friends for their support, and of course to Christian, to whom I owe so much.